Electrohydrodynamic transport in compressible nanoporous packed beds

zur Erlangung des akademischen Grades eines
DOKTORS DER INGENIEURWISSENSCHAFTEN (DR.-ING.)

der Fakultät für Chemieingenieurwesen und Verfahrenstechnik des
Karlsruher Instituts für Technologie (KIT)

genehmigte
DISSERTATION

von
Dipl.-Ing. Bastian Schäfer
aus Bad Neuenahr-Ahrweiler, Deutschland

Referent: Prof. Dr.-Ing. Hermann Nirschl
Korreferent: Prof. Dr.-Ing. Clemens Posten
Tag der mündlichen Prüfung: 19.02.2010

Acknowledgements

It was a pleasure for me to work with all the wonderful people at the Institute for Mechanical Process Engineering and Mechanics in Karlsruhe. First, I would like to thank my supervisor Prof. Hermann Nirschl for his scientific support, enthusiasm and straightforwardness. He gave me the freedom to develop my own scientific objectives and created the general framework for me so that I find my own way in the scientific world. I would like to express my gratitude to Prof. Clemens Posten for doing the second review of my thesis.

This work would not have been possible without the extensive support by my colleagues in Prof. Nirschl's team, the workshops, the laboratories and the administration. My colleagues supported me with great ideas and created a warm atmosphere, making it a pleasure to work at the institute. I would like to show my special gratitude to Friedhelm Flügel for the outstanding support in realizing new experimental setups and solving unexpected experimental problems, even on Sunday evenings. I am grateful to Harald Anlauf and Prof. Werner Stahl for their advice and to Franky Ruslim for proofreading this thesis.

I would like to thank Martin Hecht and Jens Harting for their help in the numerical part of this thesis. My student collaborators helped my to collect the experimental and numerical data presented in this thesis. Thank you for the hard work.

I am grateful to the German Science Foundation (DFG) for financial support of my work within the priority program "Nano- & Microfluidics" (SPP 1164).

I owe my deepest gratitude to my family for always backing me. And last but not least I would like to thank my wife Bhawna for being my biggest fan and my greatest critic.

Düsseldorf, April 2010

Contents

1 Introduction

In nanoporous structures, fluid flow and charge transport are closely interrelated due to the presence of electrochemical double layers (**EDLs**) on the solid-liquid interfaces. This interaction, which is referred to as electrohydrodynamic transport (**EHT**), is only relevant for systems with small dimensions and large specific surface areas. Since nanotechnology is a new and growing field in research with promising commercial potential, much attention has been paid to the behavior and the control of liquids in nanoscale systems during the last decade. However, little is known on the transport in nanoporous packed beds (**PBs**). These are irregular and deformable porous systems composed of densely packed colloidal particles with pore structures that depend on the physicochemical properties of the EDLs. The academic and industrial applications of EHT in nanoporous PBs range from micro- and nanofluidics to chemical engineering processes: Electroosmotic micropumps can be used to drive liquids in micro-fluidic systems without requiring any moving parts. Consequently, they are inexpensive and robust and can be manufactured in small dimensions. In electroosmotic soil remediation, an electric field is applied to the ground via several pairs of electrodes. The electric field drives the heavy metal ions towards the cathode, from were the can be extracted. Electrowashing is a similar approach to cleaning porous particles: The electric field draws the ions even from dead-end pores to open cavities, from where they are sheared off by a pressure-driven flow.

Although there are many promising applications of EHT, it is not sufficiently understood for irregular structures. Hence, there is a need for new measurement techniques, models, and numerical methods. The aim of this study is to understand how physicochemical and structural parameters affect the fluid flow and charge transport in nanoporous PBs.

1.1 Physical background

Colloidal ceramic particles in aqueous suspensions are charged due to dissociation reactions taking place on their surfaces and thus attract counter-ions from the surrounding liquid. This accumulation of ions in the EDL causes an interaction of fluid flow and charge transport: if the mobile counter-ions are sheared off by a pressure-driven flow, they constitute the so-called streaming current (see figure 1-1 a). Analogously, an externally applied electric field accelerates the counter-ions as well as the adjacent water molecules, resulting in an electroosmotic flow (see figure 1-1 b). These electrokinetic transport phenomena depend on the particle charge, the ionic strength, and the pore structure of the compressible PBs. The pore structures of the PBs, which are formed by filtration of colloidal suspensions, are determined by the state of agglomeration of the particles in the suspensions. The agglomeration depends on the particle charge and the ionic strength, as described by the Derjaguin-Landau-Verwey-Overbeek (**DLVO**) theory. Agglomerated suspensions form loosely structured PBs with large pores between the agglomerates (see figure 1-1 c), while unagglomerated suspensions lead to dense and homogenous structures (see figure 1-1 d).

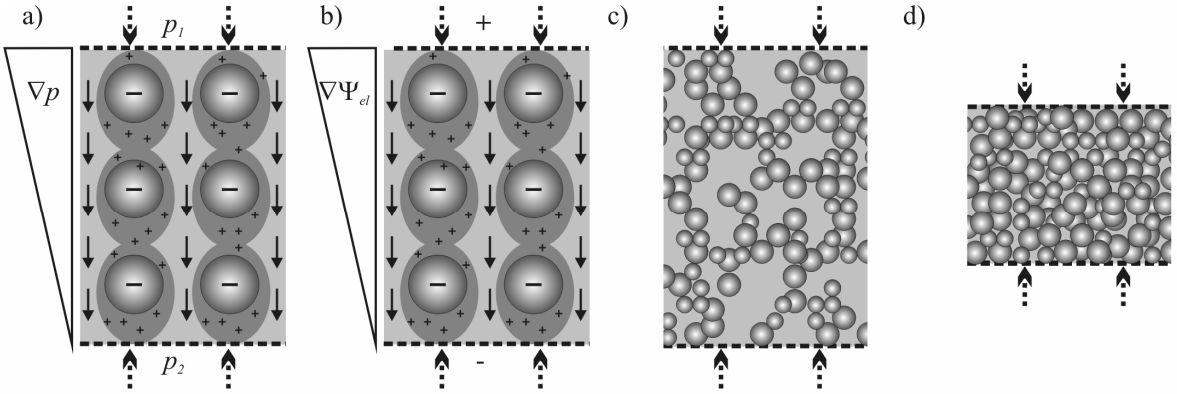

Figure 1-1: Illustration of a streaming current driven by a pressure gradient ∇p (a), electroosmosis driven by an electrical gradient $\nabla\Psi_{el}$ (b), a loosely structured PB resulting from agglomerated particles (c), and a densely structured PB resulting from unagglomerated particles (d).

1.2 Approach

The aim of this study is to understand the influence of structural and physicochemical properties on the mass and charge transport in nanoporous PBs. Since these are closely interrelated and can be driven both by hydraulic and electrical gradients, the following questions arise:

- How does the structure of a PB depend on the agglomeration of the particles, the particle size and the compression acting on the PBs.
- How is the hydraulic permeability affected by physicochemical properties of the PB? Is this influence restricted to structural changes or is there an additional electroviscous influence? What are the differences between macroporous and nanoporous PBs?
- How does the electric conductivity of a PB depend on the pore structure? How strong is the contribution of surface conductivity to the total electric conducutivity of nanoporous packed beds?
- How do the physicochemical properties affect the electroosmotic flow and streaming potential in a PB. What is the contribution of structural changes? How does surface conductivity influence the EOF? Is it possible to distinguish between elektrochemical and structural influences on electrohydrodynamic transport?

Most of the questions are addressed experimentally: In an electro-compression-permeability cell, PBs are compressed between two membranes in a round tube. The surface charge of the Boehmite particles ranges from -40 mV to 60 mV and ionic strengths from 0.02 mol/L to 0.2 mol/L. The number-rated mean diameters of the different particle classes are 24 nm, 73 nm and 130 nm. The compressive load acting on the PBs is increased from 1 bar to 4 bar to reveal the influence of the pore structure on the EHT. In the experimental range, the DLVO theory and Smoluchowski's assumption of a thin double layer are valid. The experimental results are explained with a capillary model, where the complex porous structure is replaced by a hypothetical set of cylindrical capillaries.

Furthermore, the agglomeration of the particles and the formation of the PBs are simulated with a combination of molecular dynamics and stochastic rotation dynamics. This mesoscopic approach includes the DLVO interactions, Brownian motion and the hydrodynamics of the fluid. The permeability of the resulting PBs is investigated with via lattice Boltzmann simulations.

1.3 Outline

The following chapter gives an overview of the theoretical background and an introduction to the state-of-the-art described in current literature. The subchapters are organized in a bottom-up manner. Starting from the origin and structure of the EDL, the DLVO theory for the stability of suspensions against agglomeration is explained. The agglomeration of the particles affects the structure and the compressibility of PBs formed by filtering the suspension. Chapter 2.5 introduces to the EHT in nanoporous PBs by discussing the relevant transport coefficients. The following subchapter gives an overview of the simulation methods for colloidal systems and their applicability to the formation of PBs and the EHT.

Chapter 3 describes the experimental part of the thesis. The first subchapter introduces the apparatuses, namely the electro-compression-permeability cell, the Nutsche filter, the AcoustoSizer and the Nanotrac. The description of the materials includes the particles, the electrolyte solution, the preparation of the suspension and the membranes. The experimental results reported in chapter 3.3 are categorized similarly to chapter 2 and the final subchapter summarizes the experimental investigations.

The fourth chapter deals with the numerical simulation of the agglomeration of the particles as well as the formation and permeation of the PBs. The description of the simulation methods includes the assumptions, the simplifications, and the boundary conditions used for implementing the filtration process. It is followed by the verification of the simulation methods and the discussion of the results.

The thesis ends with a summary of the experimental and numerical results and suggestions for future research.

2 Fundamentals and state-of-the-art

In nanoporous packed beds (**PBs**), fluid flow and charge transport are closely interrelated and are thus referred to as electrohydrodynamic transport (**EHT**). The interaction is caused by the acceleration of ions in the electrochemical double layers (**EDL**), which are formed on the surfaces of charged particles. Ions dragged along by a pressure-driven flow constitute an electric current, while ions accelerated by electric fields effect a liquid flow. Consequently, it is important to understand the origin and structure of the EDL (see chapter 2.1). The properties of the EDL control the agglomeration of the particles in colloidal suspensions, as described by the Derjaguin-Landau-Verwey-Overbeek (**DLVO**) theory (see chapter 2.2). The agglomeration affects the pore structure and the compressibility of the PBs, which are formed by filtration of the suspensions (see chapter 2.3 and 2.4). The pore structure and the physicochemical properties of the EDL determine the EHT as described in chapter 2.5, where the subchapters treat the pressure-driven flow, the electroosmotic flow, the streaming current, the electric conduction, the streaming potential and the electroviscous flow retardation. These phenomena can be approached with various simulation methods, which are reviewed in chapter 2.6.

2.1 Origin and structure of the electrochemical double layer

While EDLs are present on most solid-liquid interfaces, they are important only for systems with small dimensions and large specific surface areas. Ceramic particles in aqueous suspensions carry a surface charge due to association and dissociation reactions on the particle surface, which is marked by S in the following chemical equations [Hunter, R. J. 1993, Lyklema, J. 1993]:

$$\mathrm{SOH+H_2O \rightleftarrows SO^- + H_3O^+}, \qquad (2\text{-}1)$$

$$\mathrm{SOH+H_2 0 \rightleftarrows SOH_2^+ + OH^-}. \qquad (2\text{-}2)$$

The equilibrium of these reactions depends on the concentration of the participating ions, namely hydroxide (OH^-) and oxonium (H_3O^+) ions. At a low pH value, where the concentration of oxonium ions is high and the concentration of hydroxide ions is low, the particle surface is protonated and thus carries a positive charge. Analogously, particles are negatively charged in suspensions with a high pH value. The surface

charge is zero at a material-specific pH value, which is called isoelectric point (**IEP**). In addition, certain ions can specifically adsorb on the particle surface and thus constitute an additional charge [Hunter, R. J. 1993, Lyklema, J. 1993], but such ions are not considered in this study.

The charged particles attract oppositely charged counter-ions from the surrounding liquid, thus forming EDLs. Together, the particles and the EDLs are electroneutral. Figure 2-1 shows the distribution of the ions and the electric potential Ψ_{el} in the EDLs according to the Gouy-Chapman-Stern model. This is a simple but pragmatic model with sharp borders between the layers, which do not exist in reality. The particle surface, including the associated hydroxide and oxonium ions, carries the charge density σ_0 and the potential Ψ_0. It is surrounded by the inner Helmholtz layer, a charge free zone between the particle surface and the inner Helmholtz plane. The inner Helmholtz plane is formed by ions that are specifically adsorbed due to their chemical affinity to the surface, often against an electrostatic repulsion. It has the charge density σ_i and the potential Ψ_i. The outer Helmholtz layer is a charge free zone between the inner and the outer Helmholtz plane, which marks the beginning of the diffuse layer.

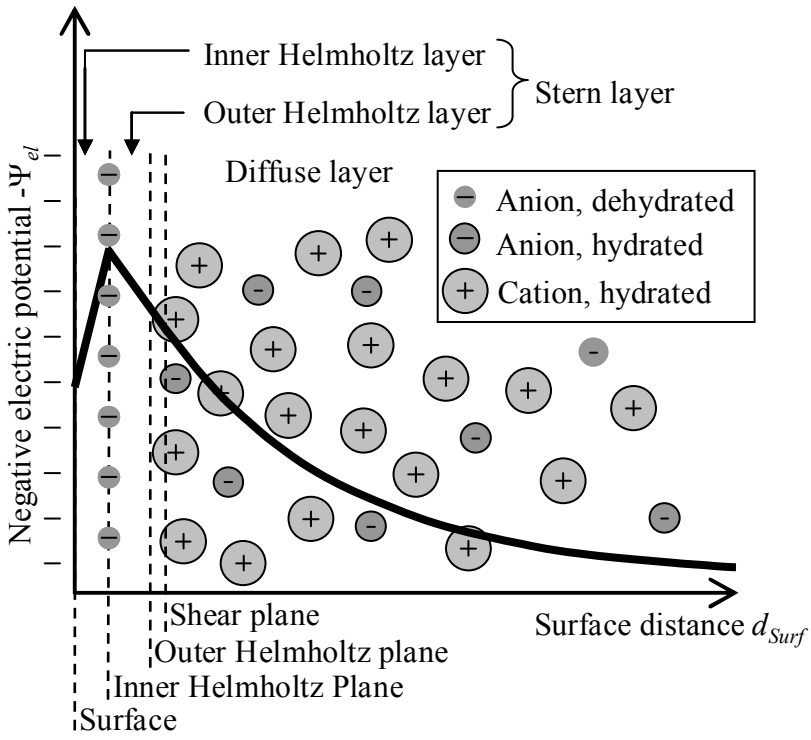

Figure 2-1: Model of the EDL formed on a solid-liquid interface. The electric potential Ψ_{el} is defined with respect to the potential in the bulk solution [Lyklema, J. 1995, Delgado, A. V., et al. 2007].

The inner and outer Helmholtz layer taken together are also called Stern layer. Although no hydrodynamic flow can develop within the stagnant Stern layer, it can be electrically conducting [Hunter, R. J. 1993, Lyklema, J. 1993]. The diffuse layer is a cloud of electrostatically attracted counter-ions with the charge density σ_d and the potential Ψ_d.

The distribution of the ions in the diffuse layer depends on the equilibrium of convection and diffusion. Although simulations reveal that the diffuse layer is deformed by electric or hydraulic gradients [Keller, F., et al. 2009, Mattke, T. 1999, Mattke, T. and Kecke, H. J. 1998] and even the diameters of the co- and counter-ions affect the ion distribution [Kerisit, S., et al. 2006], this is beyond the scope of most studies on agglomeration and EHT. Alternatively, the Poisson-Boltzmann equation is a good approximation for ionic strengths up to about 1 mol/L [Wang, M. and Chen, S. Y. 2008, Wang, M., et al. 2008]. For spherical particles, the Debye-Hückel approximation to the Poisson-Boltzmann equation yields an exponential decrease of the electric potential in the diffuse layer [Hunter, R. J. 1993, Lyklema, J. 1993]

$$\Psi_{el} = \Psi_d \frac{d_P/2}{d_P/2 + d_{Surf}} e^{-\kappa d_{Surf}}, \tag{2-3}$$

with the particle diameter d_P, the distance from the particle surface d_{Surf}, and the reciprocal Debye length [Hunter, R. J. 1993, Lyklema, J. 1993]

$$\kappa = \left(\frac{2 \cdot F_F^2 \cdot I}{\varepsilon_{rel} \cdot \varepsilon_0 \cdot R \cdot T} \right)^{\frac{1}{2}}. \tag{2-4}$$

The latter depends on the ionic strength I and the temperature T, with the Faraday constant F_F, the relative permittivity of the liquid ε_{rel}, the vacuum permittivity ε_0, and the gas constant R. The ionic strength [Hunter, R. J. 1993, Lyklema, J. 1993]

$$I = \frac{1}{2} \sum_i c_i z_i^2 \tag{2-5}$$

depends on the concentrations c_i and valencies z_i of all ionic species i in the solution. In the regime of this study, Smoluchowski's assumption of a thin EDL applies since $\kappa d_P \gg 1$. The EDL is thus sufficiently characterized by the reciprocal Debye length κ

and the zeta potential ζ, which is defined as the potential difference between the bulk solution and the shear plane that occurs if the EDL is sheared off by hydraulic or electric forces. The zeta potential, which is sometimes called electrokinetic potential, is a good approximation to the potential of the diffuse layer Ψ_d since the shear plane is very close to the outer Helmholtz plane. The zeta potential is more relevant for practical applications than the surface charge density σ_0 and can be determined much easier, for example by analyzing the electrosonic amplitude [Lyklema, J. 1995, Delgado, A. V., et al. 2007].

2.2 Stability of suspensions against agglomeration

The EHT is mainly affected by the zeta potential, the ionic strength, and the agglomeration of the particles in the suspension from which the PB is formed. The agglomeration itself also depends on the zeta potential and the ionic strength: According to the DLVO theory, colloidal particles agglomerate due to the van-der-Waals attraction if the electrostatic Coulomb repulsion is not strong enough to constitute an energy barrier between the particles. The DLVO potential Ψ_{DLVO} with its material-specific maxima and minima results from superposing the attractive and repulsive potentials [Derjaguin, B. V. and Landau, L. 1941, Verwey, E. J. W. and Overbeek, J. T. G. 1948]:

- London-van-der-Waals forces are attractive or repulsive forces between the particles, which are induced by transitory dipoles and have a range of 5 to 10 nm. The other van-der-Waals forces, namely the Kesom-van-der-Waals force and the Debye-van-der-Waals force, are negligible for particle interactions. For round particles, integration of the London-van-der-Waals force leads to the van-der-Waals potential

$$\Psi_{vdW}\left(d_C\right) = -\frac{A_H}{12}\left[\frac{d_P^2}{d_C^2 - d_P^2} + \frac{d_P^2}{d_C^2} + 2\ln\left(\frac{{d_C}^2 - d_P^2}{d_C^2}\right)\right], \tag{2-6}$$

  with the Hamaker constant A_H, and the center-to-center distance d_C [Hamaker, H. C. 1937, Lyklema, J. 2005, Hecht, M. 2007].

- The potential Ψ_{Coul} of the electrostatic Coulomb force between spherical and equally charged particles and for ions with identical valency is

$$\Psi_{Coul}\left(d_C\right) = \pi\varepsilon_{rel}\varepsilon_0 \left[\frac{2 + d_P\kappa}{1 + d_P\kappa} \cdot \frac{4k_BT}{z_ie} \tanh\left(\frac{z_ie\zeta}{4k_BT}\right)\right]^2 \frac{{d_P}^2}{d_C} \exp\left(-\kappa\left[d_C - d_P\right]\right). \qquad (2\text{-}7)$$

  It depends on the modulus of the zeta potential ζ and on the reciprocal Debye length κ, with the elementary charge e, and the Boltzmann constant k_B [Bocquet, L., et al. 2002, Hecht, M., et al. 2005].

- The Born repulsion reflects Pauli's principle, which forbids outer electrons of one atom from entering occupied orbitals of another atom and thus keeps the particles from penetrating each other. The Born potential Ψ_{Born} increases steeply for small distances [Israelachvili, J. N. 1992]:

$$\Psi_{Born}\left(d_C\right) = 3 \cdot 10^{-14}\,\mathrm{J} \cdot \exp\left(\frac{d_P - d_C}{0,02\,\mathrm{nm}}\right). \qquad (2\text{-}8)$$

Figure 2-2 shows typical plots of the DLVO potential for illustrative combinations of surface charge and ionic strength.

- For a low zeta potential or a high ionic strength, the van-der-Waals force is stronger than the Coulomb force at every inter-particle distance. The resulting DLVO potential has only one minimum at a short distance, below which the Born repulsion dominates. Consequently, the particles agglomerate to attain a state of low potential energy. The relatively stable agglomerates are here referred to as primary agglomerates.

- At a low ionic strength and a high or intermediate zeta potential, the Coulomb force is stronger than the van-der-Waals force for a certain range of the inter-particle distance. The resulting maximum of the DLVO potential forms an energy barrier against a further approach of the particles. For energy maxima between 1 k_BT and 10 k_BT, a transition from rapid to slow agglomeration is observed. There is only a very small probability for particles to overcome an energy barrier higher than 10 k_BT [Hunter, R. J. 1993]. However, in the presence of fluid motion, the collision energy is much higher than the thermal en-

ergy and agglomeration occurs more readily. The small secondary energy minimum beyond the energy maximum is not sufficient to capture any particles.

- For an intermediate ionic strength and a high or intermediate zeta potential, the secondary minimum can be deeper than -2 $k_B T$, so that particles are caught in the secondary minimum. The resulting agglomerates, which are here called secondary agglomerates, are less stable than primary agglomerates because of the shallow secondary energy minimum [Hunter, R. J. 1993, Lyklema, J. 2005].

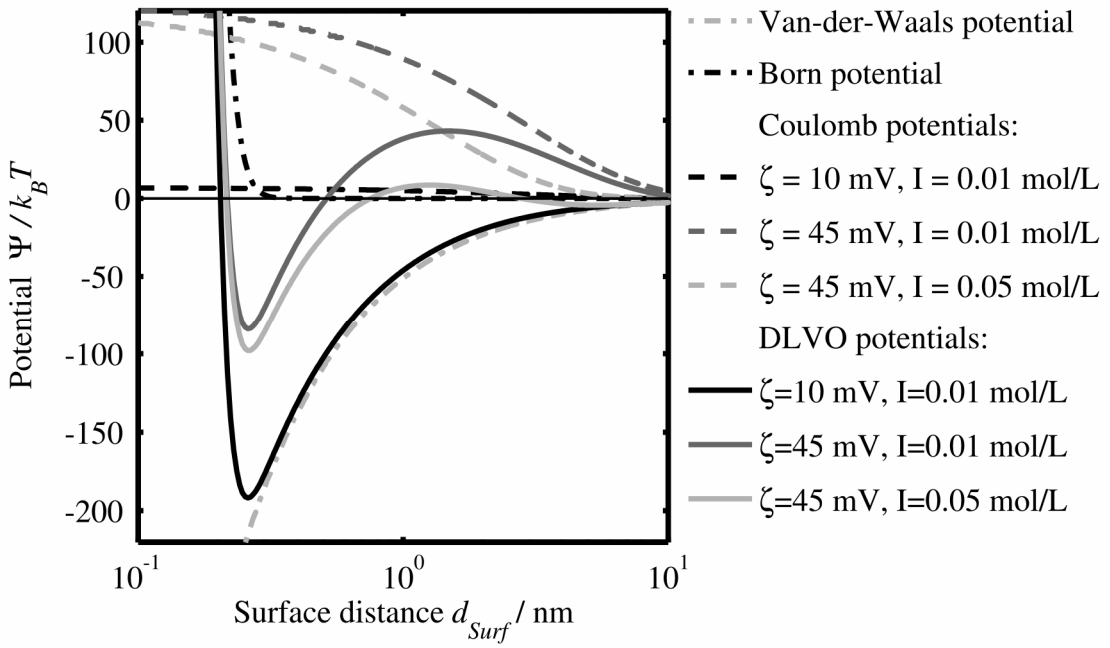

Figure 2-2: Interaction potentials Ψ for spherical particles with a diameter of 120 nm for illustrative combinations of zeta potential ζ and ionic strength I.

The DLVO theory explains how a stable suspension can be agglomerated by changing the pH value towards the IEP, thus reducing the zeta potential, or by adding ions, thus reducing the Debye length [Hunter, R. J. 1993, Lyklema, J. 2005]. Although the DLVO theory is still widely accepted 60 years after its publication, the literature discusses additional interaction forces to explain discrepancies between theoretical predictions and experimental observations on the stability, deposition, and adhesion of colloidal particles:

- The hydration force is a widely studied and controversially discussed non-DLVO force. It is probably caused by ordered layers of water molecules that form in a region of several molecular diameters from the interface and which

have to be squeezed of the closing gap between approaching surfaces [Liang, Y., et al. 2007, van Oss, C. J. 1993, Yu, C. J., et al. 2000].

- In a close gap between hydrophobic surfaces, water molecules have a limited ability to form clusters. The resulting increase of the molecules' free energy is referred to as osmotic interaction [Symons, M. C. R. 1989].
- Steric repulsion is caused by the increase of free energy associated with an overlapping of polymeric chain molecules on the surfaces of approaching particles [de Gennes, P. G. 1987, Liang, Y., et al. 2007].
- For non-spherical and rough particles, the interaction energies are reduced due to the increased effective surface distance. The effect can be quantified by surface element integration [Hoek, E. M. V. and Agarwal, G. K. 2006].

Spitzer proposes an alternative theory for interactions between colloids, which is based on a Maxwellian description of the ion distribution at charged surfaces. The model subdivides the particle interactions into regions of low potential at large distances, co-ion exclusion at intermediate distances, and high potential at small distances. This approach avoids the simplifications in the Poisson-Boltzmann equation, which is used in the classical approach [Spitzer, J. J. 2003]. However, this thesis is based on the classical DVLO theory.

2.3 Influence of agglomeration on the formation and pore structure of packed beds.

In the experiments presented in this study, the PBs are formed by filtration between two membranes. The pore structure of nanoporous PBs has a strong effect on the flow resistance and on the EHT since large pores constitute a significantly lower resistance against fluid flow and charge transport than small pores [Kovalsky, P., et al. 2007, Raha, S., et al. 2007]. The structure of a PB depends on the presence and size of agglomerates in the suspension from which the PB is formed. Filtration of agglomerated suspensions leads to loosely textured PBs with large pores between the agglomerates (see figure 2-3, left), which are accountable for the high permeability. The agglomerates can also be considered as large particles with an internal porosity [Antelmi, D., et al. 2001, Biggs, S. 2006, Cabane, B., et al. 2002, Guan, J., et al. 2001,

Madeline, J. B., et al. 2006, Schäfer, B. and Nirschl, H. 2008]. Even if the agglomerates have a relatively dense structure, their permeable edges keep them apart and can drastically reduce the PB's hydrodynamic resistance [Kim, A. S. and Yuan, R. 2005]. In contrast, PBs formed from stable suspensions have dense and homogeneous structures with low porosities $\Phi_{L,PB}$ and low permeabilities (see figure 2-3, right) [Park, P. K., et al. 2006].

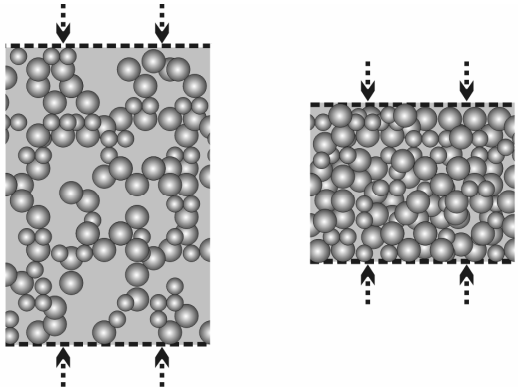

Figure 2-3: Illustration of the structure of a PB resulting from filtration of an agglomerated suspension (left) and a stable suspension (right).

The agglomeration and the agglomerate structure are also affected by the application of shear to the suspension: the diffuse arms of large agglomerates are easily sheared off, resulting in smaller and more compact agglomerates [Selomulya, C., et al. 2005, Biggs, S. 2006]. To exclude the influence of shear, the suspensions are prepared with identical stirrers and at identical rotational speed in this thesis.

The pore structure and the porosity further depend on the compressive load p_C, which acts on the PB [Antelmi, D., Cabane, B., Meireles, M. and Aimar, P. 2001, Kovalsky, P., Gedrat, M, Bushell, G., Waite and T, D. 2007, Lee, S. A., et al. 2003, Singh, G. and Song, L. 2006, Tiller, F. M., et al. 1987]. Nanoporous PBs are compressible even if the particles themselves are rigid since the particles remain mobile in PBs. PBs formed from agglomerated suspensions have a higher compressibility because the agglomerates can be deformed easily and can thus be considered as soft particles [Biggs, S. 2006, Guan, J., Amal, R. and Waite, T. D. 2001, Madeline, J. B., Meireles, M., Botet, R. and Cabane, B. 2006, Park, P. K., Lee, C. H. and Lee, S. 2006, Selomulya, C., Jia, X. and Williams, R. A. 2005]. A reduction of the inter-agglomerate porosity has a stronger effect on the hydraulic permeability than a reduction of the intra-agglomerate

porosity [Park, P. K., et al. 2006] because, for identical pressures differences, the velocity is higher in larger pores, as caused by the velocity profile of laminar flow.

For unagglomerated structures, it seems reasonable that the inter-particle distance depends on the equilibrium of the compression and the electrostatic repulsion between the particles. This hypothesis is supported by the finding that the compressibility of filter cakes from colloidal silica spheres decreases with increasing ionic strength in the regime below the critical coagulation concentration [Singh, G. and Song, L. 2006]. However, PBs without agglomerates are significantly less compressible because of the lack of large pores.

The local compressive load in a permeated PB results from the compressive load p_C and the pressure difference driving the liquid flow Δp, which exerts an additional drag force on the particles. Since each particle rests on top of another, the contact force between the particles increases along the direction of flow. Consequently, the compressive stress at the downstream side equals the compressive stress at the upstream side plus the pressure force that drives the flow [Kovalsky, P., et al. 2007, Wang, X. M., et al. 2008a, Wang, X. M., et al. 2008b]. However, this effect can be neglected here since the total compression is much higher than the driving pressure difference.

Current research on filtration is mainly aimed at understanding and optimizing the separation process for colloidal suspensions. A review of models for the cake filtration is presented in [Olivier, J., et al. 2007]. A popular approach is to model the filter cake as consisting of layers with individual compressive loads and porosities and to determine the relation of the local flow resistance to the local porosity experimentally [Alles, C. M. 2000, Erk, A., et al. 2006, Wang, X. M., Chang, S, Kovalsky, P., Waite and T, D. 2008a, Wang, X. M., Kovalsky, P and Waite, T. D. 2008b]. Bessiere treats the filtration of colloids as a transition from a dispersed state to a condensed state, namely the filter cake [Bessiere, Y., et al. 2008]. One of the main goals of research on filtration is to find an economic optimum between a low residual moisture of the filter cake and a short filtration time [Raha, S., et al. 2007]. This requires a material-specific customization of the operating conditions, for example by optimizing the geometry of the apparatus [Bessiere, Y., et al. 2008], by agglomerating the particles [Aspelund, M.

T., et al. 2008, Cho, M. H., et al. 2006, Rawlings, M. M., et al. 2006], or by controlling the temporal evolution of the filtration pressure [Alles, C. M. 2000, Blankert, B., et al. 2006]. New measurement techniques like nuclear magnetic resonance [Erk, A., et al. 2006] or small angle neutron scattering [Cabane, B., et al. 2002, Madeline, J. B., et al. 2006] give access to the influence of agglomeration and compression on the pore size distribution.

2.4 Pore structure evaluation

The structure of the agglomerates in the suspensions and in the PBs has a strong influence on the EHT. Both can be described with the pair correlation function G, which gives the probability density function for a particle to find another particle at a certain center-to-center distance d_C [Allen, M. P. and Tildesley, D. J. 1987]:

$$G(d_C) = \frac{V}{N^2}\left\langle \sum_n \sum_{n \neq m} \delta\left(d_C - \left|\boldsymbol{x}_m - \boldsymbol{x}_n\right|\right)\right\rangle, \qquad (2\text{-}9)$$

with the examination volume V, the number of particles in that volume N, and the positions $\boldsymbol{x}_m$ and $\boldsymbol{x}_n$ of the particles m and n. The Dirac delta function of a vector equals the factor of the Dirac delta functions of its components $\delta(\mathbf{x}) = \delta(x_1)\delta(x_2)\delta(x_3)$, each having the reciprocal dimension of its components. Accordingly, $\delta(\mathbf{x})$ has the dimension m^{-3} and $G(x)$ is dimensionless. The peaks of G indicate regular structures, for example a peak at one particle diameter originates from particles in direct contact and peaks at larger distances refer to more complex structures [Allen, M. P. and Tildesley, D. J. 1987]. An example is given in figure 4-9.

New measurement techniques such as small angle x-ray scattering allow to evaluate the structure of agglomerates and PBs. In the experiments, the incident light, as depicted by the wave number vector $\boldsymbol{k_0}$, is scattered in the sample. The scattered light, as depicted by the wave number vector $\boldsymbol{k}$, generates a radially symmetrical interference pattern on a detector behind the sample (see figure 2-4). Replacing the scattering angle 2Θ by the modulus of the scattering vector $q = |\boldsymbol{q}| = 4\pi \sin(\Theta)/\lambda_k$ makes the scattering pattern independent of the wave length λ_k [Wengeler, R., et al. 2007].

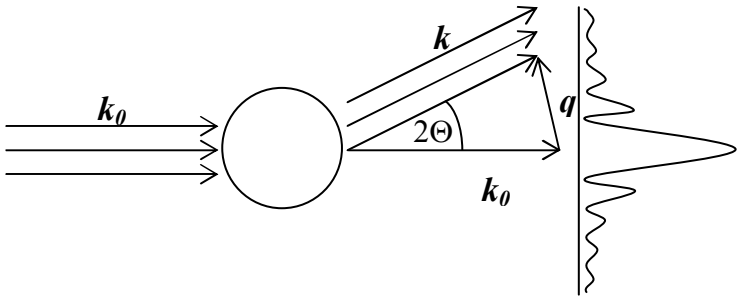

Figure 2-4: Scattering geometry with the incident beam represented by the wave number vector k_0, the scattered beam represented by k, the scattering vector q and the scattering angle 2Θ.

The experimental approach is limited to very thin or very dilute samples since the data is smeared if the light is scattered multiple times. Alternatively, the scattering pattern can be calculated if the positions and shapes of the particles are known, for example from a simulation. For monodisperse and spherical particles, the Debye formula gives the scattering intensity [Dingenouts, N. 1999, Wengeler, R., et al. 2007]

$$I_S(q) = I_0\left(N + 2\cdot\sum_{n=1}^{N-1}\sum_{m=n+1}^{N}\frac{\sin\left(q\left|\boldsymbol{x}_m-\boldsymbol{x}_n\right|\right)}{q\left|\boldsymbol{x}_m-\boldsymbol{x}_n\right|}\right). \qquad (2\text{-}10)$$

with the number of interconnected particles N, the single-particle scattering intensity [Dingenouts, N. 1999]

$$I_0(q) = \Delta\rho_{el}\frac{\pi d_P^3}{6}\left(3\frac{\sin\left(q\frac{d_P}{2}\right)-q\frac{d_P}{2}\cos\left(q\frac{d_P}{2}\right)}{\left(q\frac{d_P}{2}\right)^3}\right)^2, \qquad (2\text{-}11)$$

and the difference of the electron density $\Delta\rho_{el}$ between the particles and the liquid, which is normalized to 1 in this study. The negative slope of the linear section of $\log I_S(\log q)$ equals the fractal dimension of the system D_f, which is a is a significant structural parameter for agglomerated particles [Wengeler, R., et al. 2007].

2.5 Electrohydrodynamic transport

The flux of liquid $\boldsymbol{J}_L$ and charge $\boldsymbol{J}_{el}$ in nanoporous PBs depends on the gradients of the driving potentials, namely the pressure p and the electric potential Ψ_{el} [Lyklema, J. 1993]:

$$\boldsymbol{J}_L = -C_{11} \cdot \nabla p - C_{12} \cdot \nabla \Psi_{el}, \tag{2-12}$$

$$\boldsymbol{J}_{el} = -C_{21} \cdot \nabla p - C_{22} \cdot \nabla \Psi_{el}, \tag{2-13}$$

with the nabla operator ∇ and the material-specific coefficients C_{11} to C_{22}. All fluxes and gradients are defined in the direction of pressure-driven flow, which is from the top to the bottom of the PB. The coefficients depend on the physicochemical properties of the EDL and on the pore structure of the PBs, which itself depends on the properties of the EDL and the compression of the PBs. C_{11} is the hydraulic permeability as originally defined by Darcy and C_{22} equals the electric conductivity. The electroosmosis coefficient C_{12} and the streaming current coefficient C_{21} refer to the interrelation of mass and charge transport, which is caused by a dislocation of ions from the diffuse part of the EDL as explained below. These so-called electrokinetic effects are relevant only for systems with small dimensions and thus high specific surface areas [Lyklema, J. 1993, Delgado, A. V., et al. 2007]. In this study, Smoluchowski's assumption of a thin EDL (i.e. $\kappa d_P \gg 1$) applies: the number rated average particle diameter $d_{50,0}$ of the finest material is 24 nm and the minimum reciprocal Debye lengths κ is 0.4 nm^{-1}, as calculated with the ionic strength I = 0.02 mol/L and a temperature T = 295 K. Consequently, externally applied electric fields are not significantly distorted by the ion distribution in the EDLs and the electric potential in the PB can be considered as a linear function of the position [Lyklema, J. 1995]. Likewise, the local liquid pressure is a linear function of the position in the direction of permeation if the compression is significantly higher than the driving pressure difference.

Accordingly, the fluid flow $\dot{V}_L$ and the electric current I_{el} are expressed in macroscopic terms

$$\dot{V}_L = A_{PB}\boldsymbol{n}\boldsymbol{J}_L = -\frac{A_{PB}}{L_{PB}}\left(C_{11}\Delta p + C_{12}\Delta\Psi_{el}\right), \tag{2-14}$$

$$I_{el} = A_{PB}\boldsymbol{n}\boldsymbol{J}_E = -\frac{A_{PB}}{L_{PB}}\left(C_{21}\Delta p + C_{22}\Delta\Psi_{el}\right), \tag{2-15}$$

with the PB's cross sectional area A_{PB}, the normal vector on the cross sectional area $\boldsymbol{n}$, the externally applied voltage $\Delta\Psi_{el}$ and the PB's thickness L_{PB}. If the upstream and downstream sides of the PB are not electrically connected, the electric current I_{el} is zero during the hydraulic permeation and the streaming potential results as $\Delta\Psi_{Str}$. The streaming potential drives an electric current, the so-called counter-current, against the direction of permeation in order to compensate the streaming current. Additionally, the streaming potential evokes an electroosmotic backflow, which reduces the pressure-driven flow and appears as an increased viscosity of the liquid. This flow reduction is consequently called electroviscous effect [Lyklema, J. 1995, Delgado, A. V., et al. 2007]. The following subchapters discuss the influence of the physical properties on the four coefficients C_{11} to C_{22}, the streaming potential and the electroviscous effect.

2.5.1 Pressure-driven flow

Hydraulic permeation of porous structures occurs in many chemical engineering processes, such as filtration or fixed bed catalysis and in geological applications. It can be described by Darcy's fundamental equation

$$\dot{V}_L = -C_{11}\frac{A_{PB}}{L_{PB}}\Delta p. \tag{2-16}$$

The hydraulic permeability C_{11} as originally defined by Darcy [Darcy, H. 1856] was later identified as the quotient of a specific permeability C_{11}^* and the liquid's dynamic viscosity η. However, this separation of the liquid properties from the pore structure is problematic when investigating the EHT because the electroviscous flow retardation (see chapter 2.5.6) appears like an increase of the viscosity that depends on the pore structure. Consequently, the permeability is expressed in terms of C_{11} in this study.

The hydraulic permeability is inversely proportional to the mass-related filter cake resistance α as

$$C_{11} = \frac{1}{\alpha\eta\left(1-\Phi_{L,PB}\right)\rho_S}, \tag{2-17}$$

with the solid density ρ_S. It strongly depends on the pore geometry of the PB: Briefly, a larger pore size, as resulting from larger particles, a lower compression or the presence of agglomerates in the suspension, causes a higher permeability [Carman, P. C. 1937, Rumpf, H. and Gupte, A. R. 1971]. A number of models have been established for the permeability of macroporous PBs for different regimes of the particle size, the particle morphology, and the porosity of the PBs.

- The Carman-Kozeny equation is probably the most popular model, where the pore structure is represented by a hypothetical bundle of capillaries with the hydraulic diameter

$$d_{hydr} = 2/3 \cdot \Phi_{L,PB} \Big/ \left(1-\Phi_{L,PB}\right) d_{32} \tag{2-18}$$

  including the Sauter mean diameter d_{32} of the particles. The Hagen-Poiseuille equation for the flow in the capillaries yields [Carman, P. C. 1937]

$$C_{11}^{*} = \frac{\Phi_{L,PB}^{3}}{36 a_{CK}\left(1-\Phi_{L,PB}\right)^{2}} d_{32}^{2}, \tag{2-19}$$

  with the Carman-Kozeny coefficient a_{CK} in the range of 5.

- The Rumpf-Gupte model is an empirical model that is based on experiments in a wide range of the particle size (from 50 µm to 5 mm) and the porosity (from 0.35 to 0.7) [Rumpf, H. and Gupte, A. R. 1971]:

$$C_{11}^{*} = \frac{1}{5.6} \Phi_{L,PB}^{5.5} d_{32}^{2}. \tag{2-20}$$

- Happel and Brenner developed a model for the flow through a hypothetical array of identical cells, each containing one sphere of diameter d_{32} [Happel, J. and Brenner, H. 1983]:

$$C_{11}^{*} = \frac{1}{18}\left(\frac{3 - 4.5\Phi_{L,PB}^{1/3} + 4.5\Phi_{L,PB}^{5/3} - 3\Phi_{L,PB}^{2}}{3 + 2\Phi_{L,PB}^{5/3}} \frac{1}{\Phi_{L,PB}} \right) d_{32}^{2}. \tag{2-21}$$

These models for macroporous PBs assume a homogenous pore size distribution, which is not fulfilled for agglomerated structures, where the large pores between the agglomerates are accountable for the major part of the pressure-driven flow. The permeability increases with increasing agglomerate size and with decreasing fractal dimension of the agglomerates [Park, P. K., et al. 2006]. Agglomeration is thus an effective technique to enhance the filterability of colloidal suspensions [Aspelund, M. T., et al. 2008, Biggs, S. 2006, Guan, J., Amal, R. and Waite, T. D. 2001, Kim, A. S. and Yuan, R. 2005, Kim, A. S. and Yuan, R. 2006, Park, P. K., Lee, C. H. and Lee, S. 2006, Rawlings, M. M., et al. 2006, Selomulya, C., Jia, X. and Williams, R. A. 2005].

2.5.2 Electroosmotic flow

Electroosmotic flow is the liquid flow that is driven by an externally applied electric field. It can be used to pump liquids without any moving parts, for example in microfluidic chips [Chen, L., et al. 2007, Laser, D. J. and Santiago, J. G. 2004, Seibel, K., et al. 2008]. The counter-ions in the diffuse part of the EDL are accelerated by the Coulomb force. They drag the adjacent water molecules along, while the charged particles are fixed in the PB. The resulting relative velocity v_{rel} between the liquid and the solid phase is related to the difference of the electric potential $\Delta\Psi_{el}$ by the Helmholtz-Smoluchowski equation [Lyklema, J. 1995]

$$v_{rel} = \frac{\varepsilon_{rel}\varepsilon_0\zeta}{\eta}\Delta\Psi_{el}. \qquad (2\text{-}22)$$

In the simple example of a straight capillary with a thin EDL, the acceleration only acts in the region close to the walls, leading to a plug flow with a flow rate of

$$\dot{V}_L = -\frac{A_{Cap}}{L_{Cap}} C_{12,Cap}\Delta\Psi_{el}, \qquad (2\text{-}23)$$

with the cross sectional area A_{Cap}, the length L_{Cap}, and the electroosmotic coefficient for the capillary

$$C_{12,Cap} = \frac{\varepsilon_L\varepsilon_0\zeta}{\eta}. \qquad (2\text{-}24)$$

While electroosmosis is well understood for simple geometries, current research is aimed at understanding electroosmosis in microchannels with complex geometries [Barrot, C. and Colin, S. 2008, Xia, Z., et al. 2009], with surface roughness [Kang, S. and Suh, Y. K. 2009, Wang, M. R., et al. 2007, Yang, D. Y. and Liu, Y. 2008], and with inhomogeneous surface charge [Erickson, D. and Li, D. Q. 2002, Horiuchi, K., et al. 2007, Ren, L. Q. and Li, D. Q. 2001]. In the presence of surface heterogeneities, the overall electrokinetic coefficient is related to the surface-averaged zeta potential [Eykholt, G. R. 1997]. For porous structures, an empirical model relates the electroosmotic flow to the porosity $\Phi_{L,PB}$ of the PB [Delgado, A. V., et al. 2007]

$$\dot{V}_L = -\frac{A_{PB}}{L_{PB}} \frac{\varepsilon_{rel}\varepsilon_0 \zeta}{\eta} \Phi_{L,PB}^{2.5} \Delta\Psi_{el}. \qquad (2\text{-}25)$$

The flow rate $\dot{V}_L$ of electroosmosis decreases if it works against a pressure difference Δp since the latter causes a counter-flow in the pores [Chen, L. X., et al. 2003]:

$$\dot{V}_L = \frac{\Delta p_{EO,Max} - \Delta p}{\Delta p_{EO,Max}} \dot{V}_{EO,Max}, \qquad (2\text{-}26)$$

with the maximum flow rate $\dot{V}_{EO,Max}$ and maximum pressure difference $\Delta p_{EO,Max}$. For a given voltage, $\Delta p_{EO,Max}$ is proportional to the inverse square of the particle diameter and independent of the thickness of the PB. Typical operating conditions for electroosmotic micropumps from different studies are summarized in figure 2-5. Besides the low energy efficiency in the range of 1%, inherent problems encountered in electroosmotic micropumps are the formation of electrolytic gas at the electrodes and the temporal change of the pH value due to the electrode reactions, which causes an alteration of the flow rate [Brask, A., et al. 2006, Hu, J. S. and Chao, C. Y. H. 2007, Zeng, S. L., et al. 2001].

Electroosmosis is an important aspect in electrofiltration, where an external electric field keeps the charged particles away from the filter medium and thus reduces the formation of a filter cake. Furthermore, the permeation of the reduced filter cake is enhanced by electroosmosis [Hansen, H. K., et al. 2003, Larue, O., et al. 2006]. Also the suitability of electroosmosis for dewatering masonry is discussed in the literature [Bertolini, L., et al. 2007, Ottosen, L. M. and Rörig-Dalgård, I. 2007]. The plug flow

profile of electroosmotic flow seems favorable for washing processes, whereas pressure-driven flow with a parabolic flow profile hardly affects the impurities in narrow or intra-agglomerate pores. Preliminary experiments show that applying alternating electric fields can even help to remove ions from dead-end pores in the particles. Electroosmotic soil remediation is a similar application: an electric field accumulates the soluble contaminants such as heavy metal ions at the electrodes, from where they can be easily excavated [Chen, J. L., et al. 1999, Pamukcu, S. 1997, Rutigliano, L., et al. 2008]. Understanding the electroosmotic flow is also important for electrochromatography, where a voltage is applied to a porous system filled with a mobile phase that contains the solutes. The fluid is driven electroosmotically, while the solutes' relative velocities are influenced by electrical, hydrodynamic, and steric forces [Bartle, K. D. and Myers, P. 2001, Robson, M. M., et al. 1997, Wen, E., et al. 2001]. Electroosmosis also plays a fundamental role in many biochemical and biophysical processes, such as transport in ion channels [Wang, M., et al. 2008].

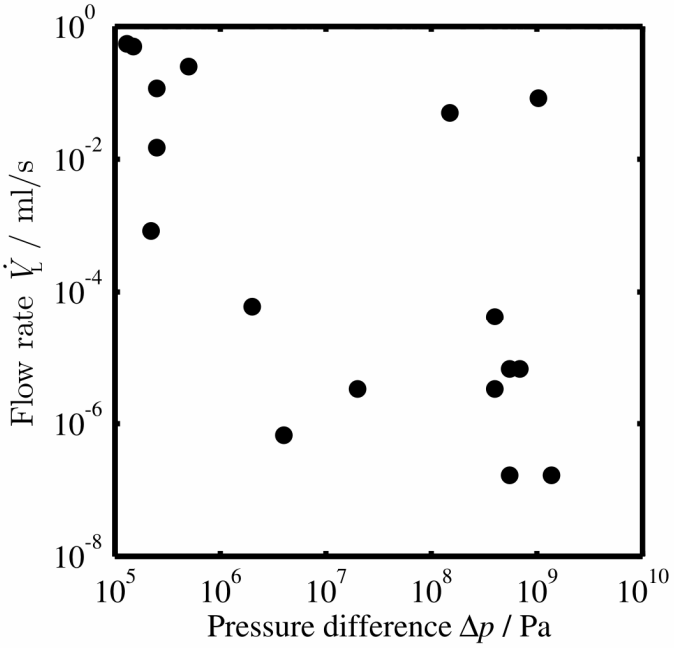

Figure 2-5: Typical operating conditions for electroosmotic micropumps investigated in different studies [Laser, D. J. and Santiago, J. G. 2004, Wang, X. Y., et al. 2009].

2.5.3 Streaming current

The streaming current I_{Str} is a charge transport that is generated in fine structures when the counter-ions are sheared off from the EDL by a pressure-driven liquid flow

$$I_{Str} = -C_{21} \frac{A_{PB}}{L_{PB}} \Delta p. \tag{2-27}$$

The streaming current coefficient C_{21} equals the electroosmosis coefficient C_{12} because of Onsager's relation for irreversible thermodynamics [Onsager, L. 1931, Brunet, E. and Ajdari, A. 2004]. The streaming current could be measured if the inlet area of the structure was externally connected to the outlet area by a low-resistance amperemeter [Delgado, A. V., et al. 2007]. However, it is not investigated in this study since the point electrodes are unsuitable for collecting the ions on the large cross sectional area of the PB.

The generation of streaming currents is almost exclusively used to characterize the surface charge of permeable materials like porous plugs, membranes, or capillaries [Zhang, Y., et al. 2005, Fievet, P., et al. 2006] and to monitor related phenomena such as the shift of the oil-water interface in reservoir engineering [Revil, A., et al. 2007]. Theoretically, the effect can be used to transform hydraulic energy into electric energy, but the low efficiency and the low power yield in the range of nanowatts limit the applicability to microfluidic applications [Olthuis, W., et al. 2005, Mirbozorgi, S. A., et al. 2007].

2.5.4 Electric conduction

Naturally, an electric potential difference $\Delta\Psi_{el}$ applied to a PB drives an electric current

$$I = -C_{22} \frac{A_{PB}}{L_{PB}} \Delta\Psi_{el} = -\frac{\Delta\Psi_{el}}{R_{el}}, \tag{2-28}$$

with the electric resistance R_{el}. For saturated and homogenous porous structures without surface conduction, Archie's law relates the bulk conductivity

$$C_{22} = C_{22,L} \cdot \Phi_{L,PB}^{a_{Ar}} \tag{2-29}$$

to the liquid conductivity $C_{22,L}$, with the material-specific exponent a_{Ar} in the order of 1.3 [Archie, G. E. 1942, Garcia-Gabaldon, M., et al. 2006, Roberts, J. N. and Schwartz, L. M. 1985, Tournelin, E. and Torres-Verdin, C. 2008]. The liquid conductivity depends on the concentrations c_i and the molar conductivities λ_i of the ionic species i, as described by Kohlrausch's law [Kolthoff, I. M. 2007]

$$C_{22,L} = \sum_i c_i \lambda_i . \tag{2-30}$$

The ionic conductivities are 34.96 mS·m²·mol^{-1} for oxonium ions, 7.35 mS·m²·mol^{-1} for potassium ions, 7.146 mS·m²·mol^{-1} for nitrate ions and 19.91 mS·m²·mol^{-1} for hydroxide ions [Atkins, P. W. and De Paula, J. 2006]. The dependency of the ionic conductivities λ_i on the concentration is neglected here because it only makes up to 3% for monovalent ions with concentrations of 0.02 mol/L [Kolthoff, I. M. 2007].

In the presence of EDLs, an additional surface conduction $C_{22,Surf}$ occurs. Surface conductivity must be considered for a correct interpretation of electrohydrodynamics since the charge transport behind the shear plane of the EDL does not contribute to the electroosmotic flow [Delgado, A. V., et al. 2007, Gupta, A. K., et al. 2007, Schäfer, B. and Nirschl, H. 2008]. The importance of surface conductivity is given by the Dukhin number [Lyklema, J. 1993]

$$Du = \frac{2C_{22,Surf}}{d_{Cap} C_{22,L}}, \tag{2-31}$$

with the capillary diameter d_{Cap} or another characteristic length to account for the influence of the system's specific surface area. For straight capillaries, the surface-to-volume ratio of $4/d_{Cap}$ yields [Lyklema, J. 1993]

$$C_{22} = \left(C_{22,L} + \frac{4}{d_{Cap}} C_{22,Surf} \right) = C_{22,L} \left(1 + 2Du \right). \tag{2-32}$$

The surface conductivity is accessible by combined measurements of streaming current and streaming potential in microchannels [Werner, C., et al. 2001] or by low-frequency dielectric dispersion in dilute suspensions [Jimenez, M. L., et al. 2007]. If the zeta potential of the particles is known, the Dukhin number can also be calculated

from the experimentally determined electroosmotic drag coefficient $\dot{V}_L/I_{el}$, which relates the electroosmotic flow to the electric current [Lyklema, J. 2003]

$$Du = -\frac{1}{2}\left(\frac{1}{C_{22,L}} \cdot \frac{\varepsilon_{rel}\varepsilon_0\zeta}{\eta\left(\dot{V}_L/I_{el}\right)} + 1 \right). \qquad (2\text{-}33)$$

The bulk conductivity of the boehmite particles is very small [Bruinink, J. 1972], so that its contribution can be neglected here.

2.5.5 Streaming potential

A streaming potential

$$\Delta\Psi_{Str} = -\frac{C_{21}}{C_{22}} \cdot \Delta p, \qquad (2\text{-}34)$$

is build up in a PB upon pressure-driven permeation if the streaming current (see 2.5.3) is not balanced by an external electric current. Equation (2-34) results from equation (2-13) if the net electric current in the PB I_{el} is set to zero. The streaming potential drives a counter-current against the pressure-driven flow to compensate the streaming current. It is important to make a correction for surface conduction (see above), since it reduces the potential needed to drive the counter-current [Delgado, A. V., et al. 2007, Schäfer, B. and Nirschl, H. 2008].

Measuring the streaming potential between an upstream and a downstream electrode is used for characterizing surfaces [Carlson, K. and Hall, M. 2008, Reischl, M., et al. 2008, Zhou, J. E., et al. 2009] or investigating related phenomena [Luxbacher, T., et al. 2008, Saunders, J. H., et al. 2008].

2.5.6 Electroviscous flow retardation

The streaming potential evokes an electroosmotic backflow against the hydraulic permeation. The reduced flow rate

$$\dot{V}_{red} = -\left(C_{11} - \frac{C_{12}\,C_{21}}{C_{22}} \right) \frac{A_{PB}}{L_{PB}} \Delta p. \qquad (2\text{-}35)$$

is obtained by inserting equation (2-34) into equation (2-12). The flow reduction appears to be caused by an increased liquid viscosity η_{app} and is thus called electrovis-

cous effect. The electroviscous retardation cannot be attributed to the liquid or to the PB since it originates from the interaction of both. It is not to be confused with the effect of EDLs on a suspension's viscosity, which is studied for example in [Carrique, F., et al. 2005, Ohshima, H. 2007b].

Theoretical and numerical treatments show that the increase of the apparent viscosity in microchannels is in the range of 1% for technically relevant conditions [Tang, G. H., et al. 2007, Mortensen, N. A. and Kristensen, A. 2008].

2.6 Simulation methods for colloidal systems

The EHT in nanoporous PBs involves many aspects that were simulated numerically, i.e. the agglomeration and filtration of suspensions, as well as liquid flow and electric current both driven by hydraulic and electrical gradients. However, comprehensive numerical studies are rarely performed. This chapter gives an overview of various simulation methods and their applicability to the various aspects of EHT in PBs. The simulations methods can be grouped into phenomenological models, continuum models (such as the finite volume and the finite element method), and particle-based methods (such as molecular dynamics, dissipative particle dynamics, and the lattice Boltzmann method). All numerical approaches reduce the complexity by introducing some simplifications.

2.6.1 Phenomenological models

Many numerical studies on filtration are based on Darcy's law and phenomenological equations for the local porosity and local permeability of the filter cake [Kocurek, J. and Palica, M. 2005, Konnur, R., et al. 2008, Olivier, J., Vaxelaire, J. and Vorobiev, E. 2007, Park, P. K., Lee, C. H. and Lee, S. 2006]. Kim et al. treat the agglomerates as solid cores with porous shells and determine the filter cake's permeability with Stokes' equation and Brinkman's extension of Darcy's law [Kim, A. S. and Yuan, R. 2005, Kim, A. S. and Yuan, R. 2006]. Lao replaces the pore system with a network of pipes and junctions and then calculates the flow in the tubes with the Hagen-Poiseuille equation [Lao, H.-W., et al. 2004].

2.6.2 Finite volume method

The finite volume method is probably the most familiar flow simulation tool to engineers, since it is the basis of commercial Navier-Stokes solvers such as FLUENT® or CFX®. The simulation space is mapped with a computational grid and the balances of mass and momentum are solved for each cell of the grid. This is a complex problem for irregular boundaries, such as the particle surfaces in PBs [Wachmann, B., et al. 1998]. The complexity increases further if the particles are mobile and interact with each other [Kalthoff, W., et al. 1997]. The finite volume method is applied to pressure-driven flow [Giraud, A., et al. 2007, Souders, D., et al. 2004, Weber, M. and Kimmich, R. 2002], electroosmotic flow [Hu, J. S. and Chao, C. Y. H. 2007, Markesteijn, A. P., et al. 2006, Patankar, N. A. and Hu, H. H. 1998, Souders, D., Khan, I., Yao, G. F., Incognito, A. and Corrado, M. 2004], streaming currents [Mirbozorgi, S. A., et al. 2007, Sheffer, M. R. and Oldenburg, D. W. 2007], streaming potentials [Mirbozorgi, S. A., et al. 2007, Sheffer, M. R. and Oldenburg, D. W. 2007], and electrically-driven currents [Weber, M. and Kimmich, R. 2002, Bharti, R. P., et al. 2008] in microchannels and porous structures.

2.6.3 Finite differences method

The finite differences method is similar to the finite volume method, but the differential formulation of the balance equations is not conservative. Finite differences methods have been applied to pressure-driven flow in statistically described porous structures, where the solid-liquid interaction is represented by a coupling term in the Navier-Stokes equation [Eisfeld, B. and Schnitzlein, K. 2005]. Another approach is to map the pore structures of real filter cakes, as obtained from magnetic resonance imaging [Yoon, H., et al. 2008]. The finite differences methods are also applied to pressure-driven flow in porous media [Yoon, H., et al. 2008], electric currents in porous media [Tabbagh, A., et al. 2002, Dalla, E., et al. 2004], and electroosmotic flow in microchannels [Hu, J. S., et al. 2007].

2.6.4 Molecular dynamics

Molecular dynamics (**MD**) is the state-of-the-art method for simulating discrete atoms or particles with Newton's equation of motion, mostly integrated with a Verlet algorithm [Chen, J. C. and Kim, A. S. 2004, Satoh, A. and Chantrell, R. W. 2006]. A detailed description of the MD method is given in chapter 4.2.1. It is similar to the discrete element method, but it is restricted to identically shaped particles [Feng, Y. T., et al. 2004]. The discrete element method is often used for simulating agglomeration and sedimentation of particles and filtration of suspensions [Lu, N., et al. 2008, Dong, K. J., et al. 2009]. Atomistic simulations of the solid-liquid interfaces are suitable to model the structure of EDLs on solid-liquid interfaces [Mattke, T. and Kecke, H. J. 1998, Mattke, T. 1999], but this is beyond the scope of studies on agglomeration and EHT. MD simulations can resolve the fluid flow and charge transport down to the molecular level, but the short time step of about 1 femtosecond limits the simulations to a few nanometers and nanoseconds [Freund, J. B. 2002, Kim, D. and Darve, E. 2006, Lorenz, C. D., et al. 2008, Wang, M., et al. 2008]. For larger systems, the atomistic simulation of the wall region with a thickness of several nm can be coupled to a continuum model for the bulk region [Qiao, R. and Aluru, N. R. 2004]. The time step can be increased by several orders of magnitude by omitting the water molecules and simply assuming that particles agglomerate if their distance is small enough [Olivi-Tran, N., et al. 2005], but this approach does not consider electrostatic interactions.

2.6.5 Monte Carlo simulations

In Monte Carlo simulations, the particles move according to a transition probability matrix, which is based on the repeated calculation of random numbers [Barcenas, M., et al. 2007]. The method is valuable for studying systems with a large number of coupled degrees of freedom, where a deterministic computation is too time-consuming. Monte Carlo simulations are used to predict the effect of DLVO interactions on filter cake structures [Kim, A. S. and Hoek, E. M. V. 2002]. Agglomeration can also be controlled by adding so-called inhibitor particles to the colloids [Barcenas, M., et al. 2007]. Monte Carlo simulations also permit to calculate the hydraulic permeability of porous media [Yu, B. M., et al. 2005].

2.6.6 Stokesian dynamics

In Stokesian dynamics**,** the particle motion is described by the Langevin equation

$$m_m \ddot{\boldsymbol{x}}_m(t) = \boldsymbol{F}_{hydr,m}(t) + \boldsymbol{F}_{inter,m}(t) + \boldsymbol{F}_{ext,m}(t) + \boldsymbol{F}_{rand,m}(t), \tag{2-36}$$

with the mass m_m, the acceleration $\ddot{\boldsymbol{x}}_m$, the hydrodynamic force $\boldsymbol{F}_{hydr,m}$, the sum of the inter-particle forces $\boldsymbol{F}_{inter,m}$, the sum of all external forces $\boldsymbol{F}_{ext,m}$ and the random Brownian force $\boldsymbol{F}_{rand,m}$ acting on the particle m. Stokesian dynamics includes the multiparticle hydrodynamic interactions, which is very important for non-equilibrium suspensions, but the numerical effort increases with the third power of the particle number [Brady, J. F. and Bossis, G. 1988]. This problem can be reduced by using accelerated Stokesian dynamics [Sierou, A. and Brady, J. F. 2001]. Stokesian dynamics is commonly used for simulation of agglomerated particles [Jones, R. B. 2001, Kutteh, R. 2003, Satoh, A. 2002, Satoh, A., et al. 2000].

2.6.7 Brownian dynamics

In Brownian dynamics, the hydrodynamic force in the Langevin equation is reduced to the Stokes' force, leading to

$$m_m \ddot{\boldsymbol{x}}_m(t) = -3\pi\eta d_P \dot{\boldsymbol{x}}_m(t) + \boldsymbol{F}_{inter,m}(t) + \boldsymbol{F}_{ext,m}(t) + \boldsymbol{F}_{rand,m}(t), \tag{2-37}$$

with the velocity $\dot{\boldsymbol{x}}_m$. Brownian dynamics is a useful tool for simulating agglomeration of colloidal suspensions [Chen, J. C. and Kim, A. S. 2004, Cordelair, J. and Greil, P. 2004, Hütter, M. 1999, Kim, J. C. and Auh, K. H. 1999, Melrose, J. R. and Hexes, D. M. 1993].

2.6.8 Dissipative particle dynamics

Dissipative particle dynamics is a mesoscopic off-lattice simulation technique, where the fluid is represented by clusters with continuous positions and discrete time steps. The method includes hydrodynamic interactions and Brownian motion. Like in Brownian dynamics, the acceleration of the particles is determined by pair interactions, random forces, and energy dissipation [Satoh, A. and Chantrell, R. W. 2006]. In comparison to Brownian dynamics and MD, the relatively soft inter-particle forces permit larger time steps and thus shorter simulation times [Groot, R. D. and Warren, P.

B. 1997] and the numerical effort for calculating the hydrodynamic interactions scales linearly with the particle number [Hecht, M. 2007]. DPD is successfully applied to the agglomeration of colloidal particles [Satoh, A. and Chantrell, R. W. 2006] and to EHT [Tang, G. H., et al. 2007, Duong-Hong, D., et al. 2008].

2.6.9 Stochastic rotation dynamics

Stochastic rotation dynamics (SRD) is a mesoscopic simulation method that includes thermal noise and hydrodynamic interactions [Hecht, M., Harting, J., Ihle, T. and Herrmann, H. J. 2005, Inoue, Y., et al. 2002, Malevanets, A. and Kapral, R. 1999, Padding, J. T. and Louis, A. A. 2004, 2006]. The method is also known as real-coded lattice gas or as multi-particle collision dynamics. The SRD particles represent clusters of fluid molecules in a regular lattice. In a propagation step, the continuous positions of the virtual fluid particles are calculated from their previous positions and velocities. Since the pointlike fluid particles cannot collide, they exchange momentum in a subsequent interaction step, which is based on a very simple algorithm that conserves mass, momentum, and energy: The fluid particles are sorted into cubic cells and the relative velocities of the particles within each cell are rotated stochastically. A detailed description of the method is given in chapter 4.2.2. SRD has been applied to colloidal suspensions [Boek, E. S., et al. 2008a, b, Dzwinel, W. and Yuen, D. A. 2002, Hecht, M., et al. 2006, Hecht, M., et al. 2007, Hecht, M., Harting, J., Ihle, T. and Herrmann, H. J. 2005, Winkler, R. G., et al. 2004] and EHT in confined geometries [Boek, E. S., et al. 2008, Duong-Hong, D., Wang, J.-S., Liu, G., Chen, Y., Han, J. and Hadjicon-stantinou, N. 2008, Efendiev, Y., et al. 2008, Madadi, M. and Mehrabi, M. 2006].

2.6.10 Lattice gas automata

In the lattice gas automata, the viscous fluid is substituted by mesoscopic particles that occupy the discrete nodes of a lattice. During a propagation step, the particles move along the lattice vectors, according to their discrete velocities. In the subsequent collision step, the particles exchange momentum. If the lattice is chosen carefully, lattice gas automata solve the Navier-Stokes equations [Frisch, U. 1989]. However, the occurrence of stochastic noise is a major disadvantage, which can be compensated by averaging over a large lattice and a long time. Lattice gas automata are used to

simulate the permeation and electrical conductivity of porous structures, for example reconstructed from magnetic resonance images of PBs [Kuntz, M., et al. 2000, Humby, S. J., et al. 2002].

2.6.11 Lattice Boltzmann method

In the lattice Boltzmann (LB) method, which is based on the lattice gas automata, the fluid is represented by particle populations that occupy the nodes of the lattice. The statistical description of the population densities with the Boltzmann equation solves the averaging problem of the lattice gas automata. The LB method is ideal for parallel computing since the Boltzmann equation only requires information of the nearest neighbor nodes [Aaltosalmi, U. 2005]. Since even complicated boundary conditions are easily implemented on the LB grid, the method is very popular for simulating flow in porous media [Aaltosalmi, U. 2005, Dardis, O. and McCloskey, J. 1998, Deshpande, A. P., et al. 2005, Manwart, C., et al. 2002, Nabovati, A. and Sousa, A. C. M. 2008, Quispe, J. R., et al. 2005, Schaap, M. G. and Lebron, I. 2004]. Also electroosmotic flow can be simulated with the LB method if the ion distribution in the EDL is calculated from the Poisson equation [Guo, Z., et al. 2005, Hlushkou, D., et al. 2006, Hlushkou, D., et al. 2005, Li, B. M. and Kwok, D. Y. 2003, 2004, Pagonabarraga, I., et al. 2005, Shi, Y., et al. 2008, Tang, G. H., et al. 2006, Wang, J., et al. 2006, Wang, M., et al. 2006]. The LB method was extended to include Brownian motion, which is important for the particle agglomeration [Ladd, A. J. C. and Verberg, R. 2001, Adhikari, R., et al. 2005].

3 Experiments

This chapter describes the apparatuses and the procedures used for preparing and executing the experiments. The materials include the particles, electrolyte solutions, and membranes. The presentation of the experimental results is accompanied by a detailed interpretation.

3.1 Experimental apparatuses

The measurements of the electrohydrodynamic transport (**EHT**) in nanoporous packed beds (**PBs**) are performed in an electro-compression-permeability cell. Filtration experiments in a Nutsche filter reveal the influence of the membranes on the EHT. The dependency of the EHT on the pH value is related to the particle charge, as measured with an AcoustoSizer II, and the agglomerate size, as measured by photon correlation spectroscopy. The solubility of the boehmite particles at high and at low pH values is determined with a photometer.

3.1.1 Electro-compression-permeability cell

The electro-compression-permeability cell shown in figure 3-1 is used for the formation, compression, and electrohydrodynamic permeation of nanoporous PBs. After filling the suspension onto the lower membrane in the non-conducting, tubular shell of the electro-compression-permeability cell, the upper membrane is placed on top of the suspension. The membrane must be kept dry during the assembly in order to offer the air in the tube a possibility to drain. The formation of the PB starts 10 min after finishing the preparation of the suspension: The plunger is pressed onto the upper membrane by a hydraulic piston and the fluid drains through the membranes, where the particles are retarded and form filter cakes. The filter cakes finally merge and are compressed between the membranes until the filtrate flow abates. Both membranes are supported by plastic structures with drainage channels and a coarse filter mesh between the membrane and the support structure makes the full cross sectional area of the membrane accessible to fluid flow and charge transport. The PBs are compressed homogenously since the friction between the particles and the shell is small, as achieved by the PB's low thickness-to-diameter ratio of 0.04 to 0.1 and the two-sided

filtration. Also the friction of the o-ring between the shell and the upper support structure is negligible if the o-ring is lubricated with Vaseline and free of particles.

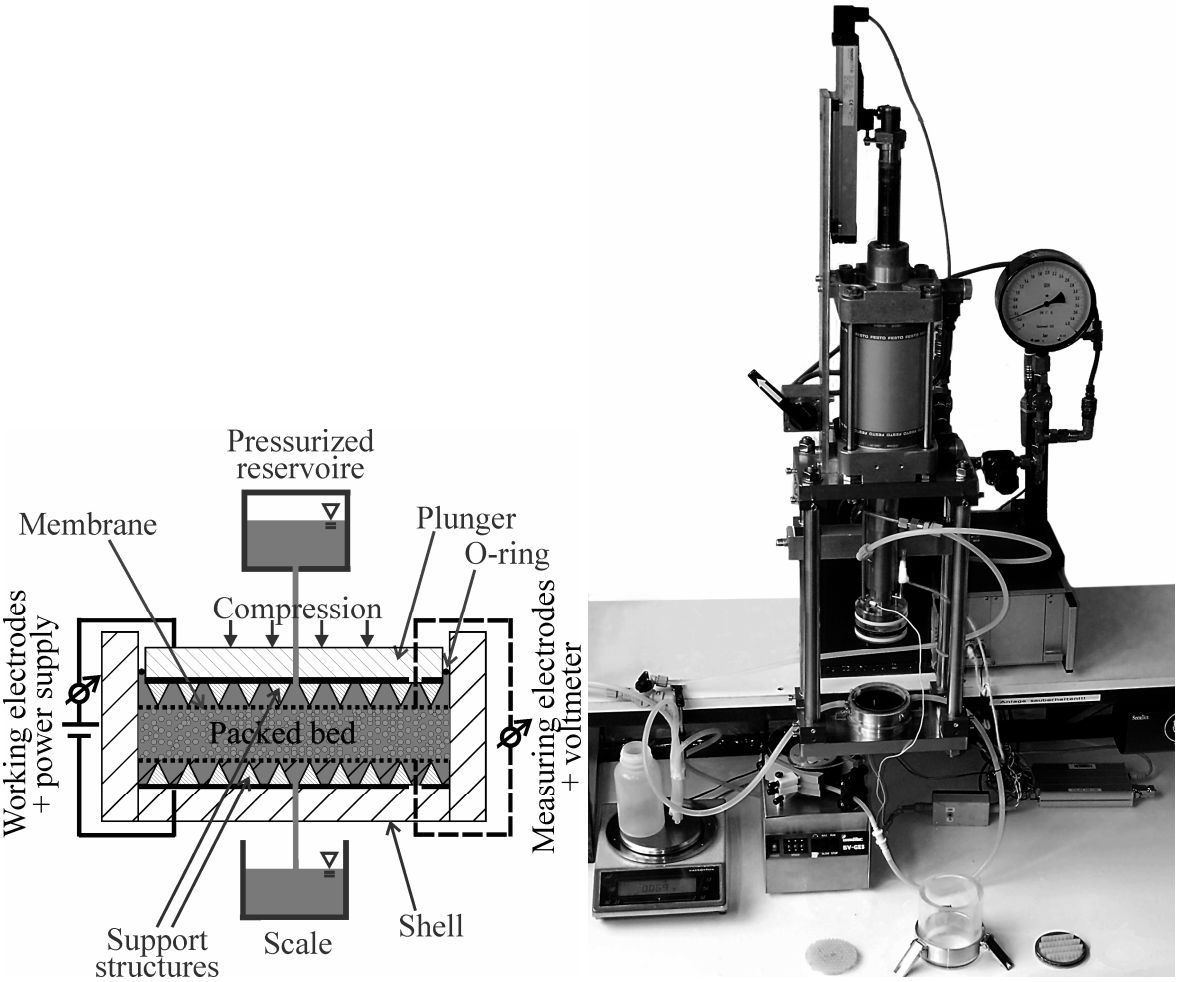

Figure 3-1: Principal sketch of the electro-compression-permeability cell (left). The photograph (right) shows the disassembled electro-compression-permeability cell with the lower support structure, the shell, the upper support structure in the front (from left to right).

After compressing the PB to its equilibrium thickness, as determined from the mass of the filtrate, the liquid reservoirs at the upstream and downstream side of the electro-compression-permeability cell are filled with an electrolyte solution that has the same pH value and ionic strength I as the initial suspension. A hydraulic pressure applied to the upside fluid reservoir drives the hydraulic permeation of the PB (as measured with a milligram scale and corrected for evaporation) and evokes a streaming potential. The latter is measured with a voltmeter that is connected to the measuring electrodes made from blank platinum. The voltmeter has a high electric resistance of 10 MΩ to keep the electric current low. It is not possible to measure streaming currents in the electro-compression-permeability cell since the electrodes do not cover

the cross sectional area of the PB. However, they allow for measuring the streaming potential.

In the second part of the experiment, a voltage is applied to the working electrodes. The electric field evokes an electric current, as measured with an amperemeter between the working electrodes. The electroosmotic flow is measured with the scale. The working electrodes are made from titanium and coated with iridium oxide to prevent oxidation. They have the same cross sectional area as the PB to generate a one-dimensional electric field. The electrodes exchange electrons with the solution via the anode reaction [Eid, N., et al. 2000]

$$2\,H_2O - 4\,e^- \rightarrow O_2 + 4\,H^+ \qquad (3\text{-}1)$$

and the cathode reaction

$$4\,H_2O + 4\,e^- \rightarrow 2\,H_2 + 4\,OH^-. \qquad (3\text{-}2)$$

These reactions cause two intrinsic problems of electroosmosis:

- Electrolytic gas displaces the electrolyte solution from the electro-compression-permeability cell to the liquid reservoir on the scale and thus biases the measurement of the flow rate.
- Oxonium and hydroxide ions formed at the electrodes migrate into the PB, and produce spatial gradients of the pH value and the particles' zeta potential [Eid, N., et al. 2000, Minerick, A. R., et al. 2002]. While this effect is desired for isoelectric focusing of proteins and enzymes [Work, T. S. and Burdon, R. H. 1983, Cabrera, C. R., et al. 2001], it renders the measurement of the EHT impossible.

Both problems are solved by using titanium electrodes and regularly switching the direction of the electric field. The reversal of the electric field makes each electrode work as cathode and anode for equal amounts of time. Since titanium has a high affinity for hydrogen atoms, the electrodes can store atomic hydrogen in the metal lattice during the cathode cycle and release it during the anode cycle [Ariyaratnam, S. V., et al. 1987, Qazi, J., et al. 2001]. This prevents the formation of hydrogen, oxygen, oxonium ions, and hydroxide ions. Testing the electrode reversal for hours without

formation of electrolytic gas proves its operability. Alternative methods for dealing with electrolysis are presented in the literature:

- Palladium electrodes can also store and release hydrogen reversibly [Mutlu, S., et al. 2002, Brask, A., et al. 2006], but palladium oxidizes rapidly and the dissolved palladium oxide changes the ionic strength of the solution in the pores.
- Sacrificial electrodes, for example made of iron, oxidize preferentially over water. This prevents electrolysis and keeps the pH value constant [Athmer, C. and Huntsman, B. 2009, Ho, S. V., et al. 1999, Shin, H.-S. and Lee, J.-K. 2006] but changes the ionic strength in the PB.
- Working below the decomposition voltage of water of 1.23 V prevents electrolysis, but the electroosmotic flow would be too low to for accurate measurements.
- The pH value in the PB can be stabilized with a buffer solution [Baur, L., et al. 2002, Yao, S. H., et al. 2003, Brask, A. 2005, Brask, A., et al. 2005], but the multivalent buffer ions increase the ionic strength. Furthermore, the buffer is depleted during the experiment [Brask, A. 2005].
- Ion exchange membranes between the electrode and the PB prevent the migration of oxonium and hydroxide ions into the PB and keep the pH value constant [Brask, A. 2005].

A part of the electric voltage applied to the working electrodes drops in the liquid between the working electrodes and the PB. The effective voltage is measured directly at the membranes with the measuring electrodes. Like every inert metal electrode, these platinum electrodes show an unavoidable measuring inaccuracy because of a concentration polarization: The potential of an electrode depends on the concentration of the ions at the electrode surface. The ion concentrations deviate from the concentrations in the bulk liquid since they are influenced by the electrode reactions and the transport of ions to the electrode surface by diffusion, migration, and convection [Bagotsky, V. S. 2005, Heister, K. 2005, Kaler, K. V. I. S. 2006]. The effect of polarization can vary from less than 1 mV to more than 2 V [Bagotsky, V. S. 2005].

However, it is possible to correct for the polarization effects by measuring the potentials during and after streaming [Heister, K. 2005].

Electrode polarization could be prevented by using electrodes of the second kind. These comprise a metal, a low soluble salt containing that metal's cations, and a solution containing anions of that salt, each separated by liquid junctions. However, these electrodes are not used in the electro-compression-permeability cell because they are very sensitive to air bubbles and to pressurization [Heister, K. 2005].

3.1.2 Nutsche filter

The Nutsche filter, which is used to characterize the filtration behavior of the suspensions, consists of a round tube with a diameter of 50 mm and a perforated plate at the lower end of the tube. The perforated plate is covered with a membrane. A coarse filter cloth between the membrane and the perforated plate makes the whole cross sectional area accessible to fluid flow. The outlet of the Nutsche filter can be hydraulically connected to the beaker on the scale, so that the permeate flow is continuous and not delayed. For the chemical analysis of the filtrate, the hydraulic connection is cut.

3.1.3 AcoustoSizer II for measuring the zeta potential

The zeta potential of the particles is measured by the electrosonic amplitude technique in an AcoustoSizer II (formerly Agilent Technologies, USA). Alternating electric fields with frequencies between 0.3 and 11 MHz evoke a vibration of the charged particles and thus generate a measurable ultrasound. The amplitude of the sound wave is determined by the surface charge, while the phase shift between the electric excitation and the acoustic response depends on the inertia of the particles and is thus related to the particle size [O'brien, R. W., et al. 1995, Hunter, R. J. 2001]. Alternative methods for measuring the zeta potential are disqualified because of certain draw-backs:

- In microelectrophoresis, the motion of charged individual particles in an electric field is observed with a microscope. The major disadvantages are the dependence on the observer's objectivity in selecting representative particles, the long measurement time during which the temperature or the pH value of the

fluid can change, and the occurrence of fluid motion in the sample cell [Johnson, P. R. 1999, Delgado, A. V., et al. 2007]. The first problems can be solved by using automatic image analysis [Noordmans, J., et al. 1993] or electrophoretic light scattering, where the electrophoretic motion of the particles is measured by laser Doppler velocimetry [Delgado, A. V., et al. 2007]. However, the sample has to be diluted.

- The colloid vibration potential is the electric voltage caused by a sound wave travelling in a suspension. The technique is analogous to the electrosonic amplitude technique, but requires knowledge of the suspensions complex electric conductivity [Ohshima, H. 2007a].
- The dielectric dispersion of a suspension refers to the dependence of the complex electric permittivity on the frequency of an applied electric field. The frequency spectrum is related to the surface characteristics, concentration, and geometry of the particles and the nature of the dispersion medium. Consequently, it is difficult to separate these effects [Delgado, A. V., Gonzalez-Caballero, E., Hunter, R. J., Koopal, L. K. and Lyklema, J. 2007, Jimenez, M. L., Arroyo, F. J., Carrique, F. and Delgado, A. V. 2007].

3.1.4 Nanotrac for agglomerate size measurement

The formation of agglomerates and the size of the agglomerates in a colloidal suspension depend on the particle charge and determine the pore structure of nanoporous PBs, which are formed by filtration of the suspension. Measuring the agglomerate size distribution is thus a crucial step for relating the composition of the suspension to the EHT phenomena.

The agglomerate size is determined by photon correlation spectroscopy, which is also called dynamic light scattering. In the Nanotrac® (Microtrac Inc., USA), the analyzed particles scatter the incident laser beam in all directions. The wavelength of the scattered light is shifted due to the Doppler effect. The shift reveals information about the Brownian motion and thus the size of the particles or agglomerates without needing a priori information [Trainer, M. N., et al. 1992]. The Nanotrac® is capable of measuring the size of particles and agglomerates in the range from 0.8 nm to 6.5 µm,

only limited by the sedimentation of the particles. In the backscattering geometry, the concentration of the suspensions is not limited by multiple scattering, but only by the requirement of unhindered particle motion.

A variety of other methods for particle and agglomerate size measurement is available, all with unacceptable disadvantages:

- Various apparatuses apply different modifications of dynamic light scattering, also interpreting the temporal fluctuation of the scattering intensity at a fixed angle. Unless a backscattering geometry is used, the sample concentration must be extremely low to prevent multiple scattering and the required dilution of the sample changes the agglomerate size.
- Static light scattering techniques determine the particle size distribution from the time-averaged light scattering. The scattering intensity, as measured on a detector behind the sample, is a pattern with distinct maxima and minima due to constructive and destructive interference. The accessible particle size range depends on the wavelength of the scattered light and on the measuring angles of the detector. The commercial HELOS® (Sympatec GmbH, Germany) uses static light scattering of a laser to measure particles diameters in the range from 0.1 µm to 8.75 mm [Sympatec 2009]. Small angle X-ray scattering is applicable to structures with dimensions between 0.5 nm and 500 nm [Beaucage, G., et al. 2004]. However, all static light scattering techniques are prone to multiple scattering, which requires extremely dilute samples.
- The particle size of highly concentrated suspensions can be determined with the electrosonic amplitude technique (see chapter 3.1.3). The phase shift of the electrosonic amplitude depends on the equilibrium between electric excitation and inertia against vibration. The suitability to measure the size of agglomerates seems dubious since the phase shift should depend on the specific surface, which is not expected to change during agglomeration. An increase of the particle size from 0.4 µm to 0.6 µm upon agglomeration is reported in [Mikkola, P., et al. 2004].

- Ultrasonic attenuation occurs in suspensions if the particle density differs from the solvent density. The frequency-spectra of the attenuation are strongly influenced by the presence of agglomerates, but the determination of the agglomerates size involves too many parameters [Babick, F. and Ripperger, S. 2004, Babick, F. 2005]. Another study reports that the mean diameter remained constant during electrostatic agglomeration, while only the standard deviation increased [Hinze, F. 2001].
- Analysis of images from scanning electron microscopy (**SEM**) and transmission electron microscopy requires strong dilution of the suspension and the sampling is not statistically representative.
- Sedimentation analysis with analytical centrifuges is not suitable for suspensions with high concentrations and with polydisperse agglomerates.

3.1.5 Photometer

A Cary 50 photometer made by Varian Inc., USA, is used to measure the concentration of the aluminium ions in the suspensions to verify that the dissolution of the particles does not change the ionic strength significantly. The photometer measures the sample's fluorescence at a wavelength $\lambda = 490$ nm, which reveals the concentration of the complex ion that is formed by aluminium ions and Alizarin Red S, a sodium salt of alizarinmonosulphonic acid [dos Santos, T. C. R., et al. 2003].

3.2 Materials

The investigated PBs are formed by filtration of colloidal suspensions. These consist of boehmite particles dispersed in electrolyte solutions of different electrochemical compositions. This chapter describes the particles, the electrolyte solution, the dispersion process, the suspension properties, and the membranes.

3.2.1 Particles

Most of the experiments are performed with boehmite particles in three different grades, namely Disperal®, Disperal 20®, and Disperal 40® (Sasol, Germany). The particles with a purity of 99.5% by mass are commonly used in applications that require a high dispersibility, such as sol-gel ceramics, catalysis, refractory materials,

rheology control and surface frictionizing [Sasol 2008]. Furthermore, Boehmite is an important resource for the production of alumina [Dash, B., et al. 2007]. The particles are easily dispersed by stirring in acidic solutions [Sasol]. In contrast, most other ceramic colloids require high-energy dispersion methods, such as ball mills [Perrin-Sarazin, F., et al. 2006, Kowalski, A. J., et al. 2008], rotor-stator systems [Baldyga, J., et al. 2008], high-pressure dispersion [Wengeler, R., et al. 2006, Sauter, C. and Schuchmann, H. P. 2008], or ultrasound [Pohl, M., et al. 2004]. The number-weighted mean diameter $d_{50,0}$ of the dispersed primary particles is 24 nm for Disperal®, 73 nm for Disperal 20®, and 130 nm for Disperal 40®. Figure 3-2 presents the number-rated particle size distributions q_0 of the different grades.

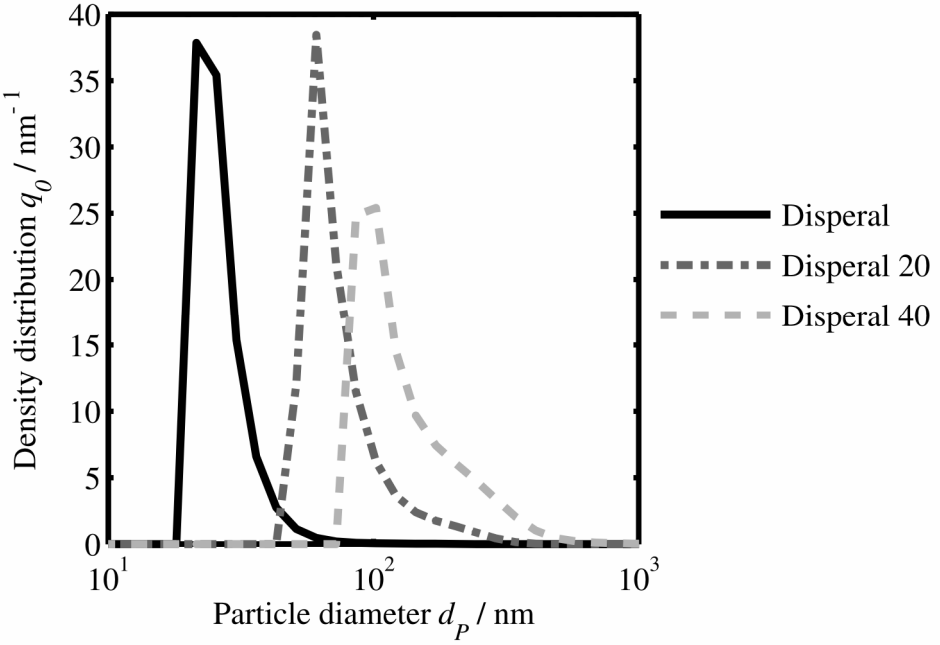

Figure 3-2: Particle size distribution q_0 of Disperal®, Disperal 20® and Disperal 40® dispersed at a pH value of 2.7, an ionic strength of 0.02 mol/L, and a solid mass concentration of 10%.

The SEM photographs of Disperal®, Disperal 20®, and Disperal 40® particles dispersed at a pH value of 2.7 are shown in figure 3-3. Although the particles have irregular shapes, they are closer to a spherical form than to a flat or needle-shaped form. Boehmite is the monohydrate of aluminium oxide, with the stochiometric formula γ-AlO(OH). It has an orthorhombic crystal structure [Bokhimi, X., et al. 2001, Brühne, S., et al. 2008] and a refractive index of 1.65 [de Gans, B.-J., et al. 2003]. The electric conductivity of $5.3 \cdot 10^{-5}$ S/m is negligible for the study of EHT [Bruinink, J.

1972]. The literature quotes different values for the Hamaker constant of boehmite in water, ranging from $3.67 \cdot 10^{-20}$ J to $6 \cdot 10^{-20}$ J [Jang, H. M., et al. 1996, Philipse, A. P. and Wierenga, A. M. 1998, Yang, C.-Y., et al. 2001, Yang, C. Y., et al. 2000].

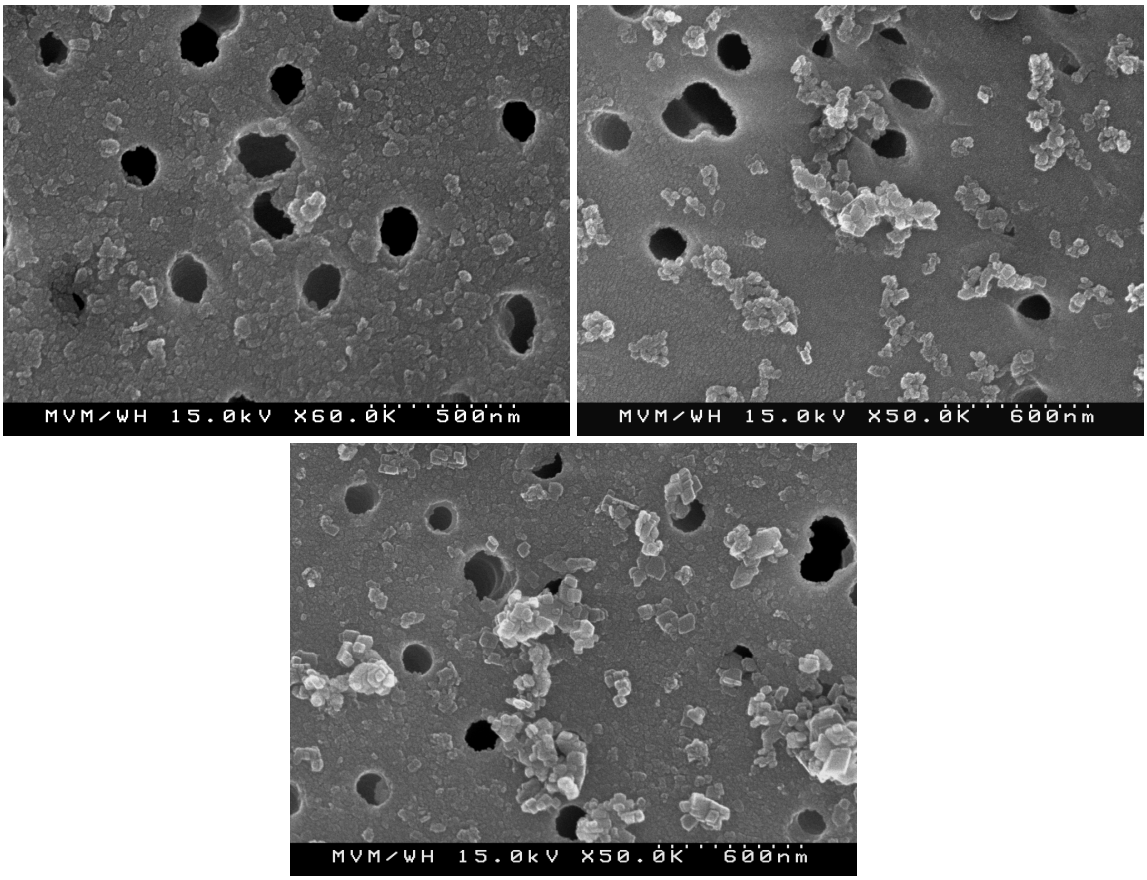

Figure 3-3: SEM photograph of Disperal® (top, left), Disperal 20® (top, right) and Disperal 40® (bottom) particles as filtered from suspensions at a pH value of 2.7.

Also the solubility of Boehmite in aqueous solutions is widely discussed in the literature, but most studies are restricted to high temperatures and high pH values [Benezeth, P., et al. 2001, Benezeth, P., et al. 2008, Palmer, D. A., et al. 2001, Palmer, D. A., et al. 2004, Panias, D., et al. 2001]. Figure 3-4 shows the equilibrium molality m_{Al} of aluminium ions in boehmite suspensions depending on the pH value for different temperatures. Although the electrolyte solution is different from the ones used in this study and extrapolation to room temperature is uncertain, the increased solubility at high and low pH values is obvious. For decreasing temperature, the solubility increases at low pH values and decreases at high pH values. Conveniently, the dissolution rate of boehmite strongly decreases with decreasing temperature [Panias, D., et al. 2001] and at a pH value of 14 and a temperature of 30°C the equilibrium of dissolution is not reached after 90 days [Palmer, D. A., et al. 2004].

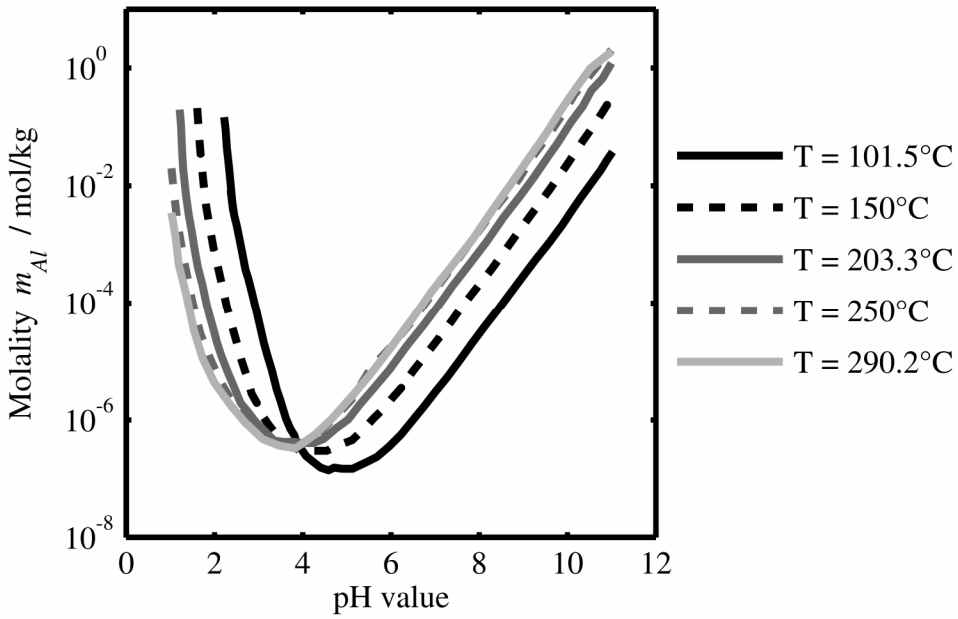

Figure 3-4: Equilibrium molality m_{Al} of aluminium ions in boehmite suspensions with a sodium chloride concentration of 0.03 mol/L depending on the pH value for different temperatures T [Bourcier, W. L., et al. 1993, Benezeth, P., et al. 2001].

Additional experiments were carried out with Aeroxide P25® (Evonik Degussa, Germany). These titanium dioxide particles have a purity of 99.5 %. The primary particles with a diameter of 21 nm form sintered aggregates during the production by flame synthesis. Figure 3-5 shows the irregular shape and the heterogeneous size distribution of these aggregates. The sample was prepared from a stable suspension with a pH value of 11.5, which is far from the isoelectric point (**IEP**) at a pH value of 6.9 [Hristovski, K., et al. 2008].

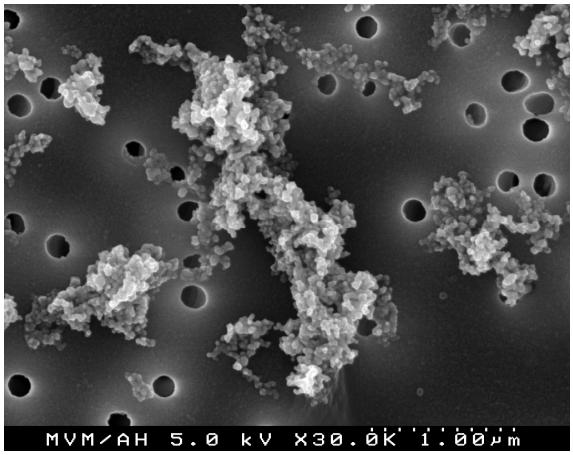

Figure 3-5: SEM photograph of Aeroxide P25®.

3.2.2 Electrolyte solutions

All electrolyte solutions are prepared with deionized water. The pH value and the ionic strength of the electrolyte solutions and the suspensions are adjusted by adding potassium nitrate (KNO_3, solid), nitric acid (HNO_3, 1 mol/L), and caustic potash (KOH, 1 mol/L). Potassium ions and nitrate ions are indifferent ions, meaning that they do not adsorb specifically on the particle surface.

For all experiments, the ionic strength of the electrolyte solution is at least 0.02 mol/L to screen the effect of aluminium ions dissolved from the particles. The concept of the EDL would be ill-defined if the ionic strength was too low [Delgado, A. V., et al. 2007].

3.2.3 Preparation of the suspensions

For each pH value and ionic strength, a new PB is formed by filtration of a suspension. The preparation of the suspensions starts with dissolving potassium nitrate in deionized water and lowering the pH value of the solution to 2.7 with nitric acid. 25g of particles are mixed with approximately 200 g of the potassium nitrate solution, which is chosen to finally obtain a suspension with a mass concentration of 10%. At the low pH value, the suspension is easily dispersed with the agitator F 520 75 (Krups, Germany), which is shown in figure 3-6 (left). The suspensions are stirred for 30 min s at a speed of 900 rpm in a beaker of 400 ml and the pH value is constantly readjusted with nitric acid.

Subsequently, the final pH value is adjusted by adding caustic potash (KOH, 1 mol/L) while the suspension is stirred with a modified special horseshoe mixer (see figure 3-6, right) for 30 min at a speed of 300 rpm. The mixer reaches the bottom as well as the wall of the beaker and has a helix form to evoke axial transport and provide a homogenous mixing, which is critical because the suspensions are pseudoplastic after agglomeration. Using a mixer with a small surface, for example a propeller mixer or the F 520 75, would lead to poor mixing and thus to an inhomogeneous distribution of the agglomerate size. A normal horseshoe mixer would cause a rotation of the suspension at a constant angular speed, so that shear and mixing would only occur in the gap between the glass and the mixer.

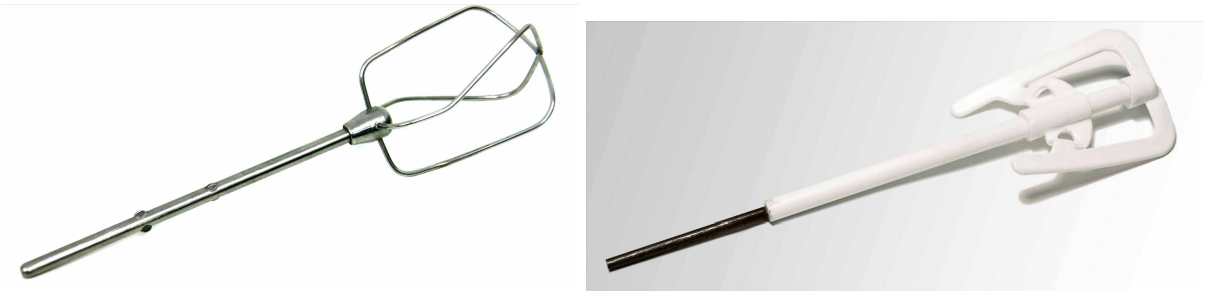

Figure 3-6: Agitator F 520 75 used for dispersing (left) and modified horseshoe mixer used for agglomeration (right).

The caustic potash is always injected into the zone of high velocity, which is located between the wall and the center of the beaker and the suspension is stirred for 30 min. The time for macroscopic homogenization of an unagglomerated suspension is in the range of 2 s, as can be seen by triggering the suspension with ink. After injecting the caustic potash, a visible change of viscosity is observed during 30 s, which is significantly slower than the time for homogenization. The pH value of the suspension is not modified after agglomeration since the mixing of a low viscosity flocculant into the high viscosity suspension might be inhomogeneous. The boehmite suspensions are not evacuated since no gas bubbles evolve during evacuation. The formation of the PB starts 10 min after finishing the stirring.

The Aeroxide P25® suspensions are prepared by mixing 25 g of the particles into 225 g of aqueous solutions with different concentrations of nitric acid or caustic potash. The suspensions are dispersed in an ultrasonic bath and evacuated in a vacuum desiccator at a pressure of 5 kPa for 5 min.

3.2.4 Membranes

The PBs are formed by filtration between two Ultipor® membranes (Pall, USA). These Nylon N6.6 membranes are hydrophilic, resistant to mechanical and chemical stress and have a nominal pore size of 0.1 µm [Pall 2009]. Particles that are smaller than the pores are retained due to bridge formation. A small amount of particles may pass the membrane before these bridges are formed, but this is not even visible in the filtrate. The membranes have a thickness of 0.12 mm and a porosity of 0.52, as determined gravimetrically. An SEM photograph of the membrane is shown in figure 3-7.

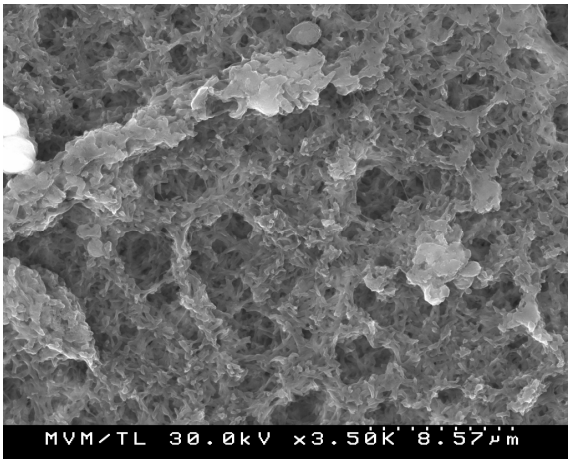

Figure 3-7: SEM photograph of the Ultipor® membrane.

Figure 3-8 shows the zeta potential of Ultipor® membranes depending on the pH value. It is negative above the IEP at a pH value of 6.2 and positive below. Unexpectedly, it decreases again for pH values below 4.

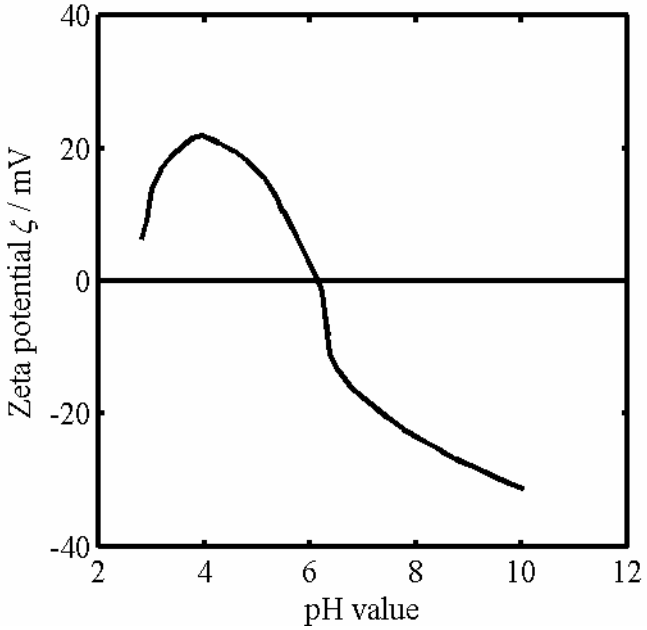

Figure 3-8: Zeta potential ζ of Ultipor® membranes depending on the pH value [Pall 1994].

The experiments on the hydraulic permeability of PBs consisting of titanium dioxide particles, Aeroxide P25®, were also performed with Ultipor® membranes, but with a larger nominal pore size of 0.2 µm and thus lower flow resistance.

3.3 Results

The experimental results presented in this chapter are structured in a similar way like the state-of-the-art in chapter 2. After verifying that the dissolution of the particles can be neglected in this study, the following subchapters cover the particle charge, the agglomeration of the particles, the resulting pore structure, and the EHT. A capillary model is introduced to describe the EHT phenomena. The confidence intervals are presented in the appendix.

3.3.1 Dissolution of boehmite in aqueous suspensions

The dissolution kinetics of boehmite particles depends on the temperature, the specific surface area of the particles, the pH value, and the ionic strength of the suspension. It is thus not feasible to extrapolate the dissolution behavior reported in the literature, e.g. in [Benezeth, P., et al. 2008, Palmer, D. A., et al. 2001, Panias, D., Asimidis, P. and Paspaliaris, I. 2001]. Here, the dissolution is examined with photometrically for the presumed worst cases, which are for the finest material and at the lowest and highest pH values. The measurement procedure is described in [1989]. The Disperal® suspensions are prepared as described in chapter 3.2.3. Since the suspensions are too turbid for spectroflourometric analysis, they are filtered in the Nutsche filter prior to the complexation. This also stops the dissolution of the particles at the time of filtration, namely 10 min, 6 h, or 24 h after the preparation. The dissolution time of 24 hours corresponds to the maximum duration of the experiments in the electro-compression-permeability cell. The filtrate is diluted with bidistilled water to reach the testing range of 0.01 mg/L to 0.5 mg/L.

The aluminium concentration in the filtrate increases over dissolution time (see table 3-1). The small decrease of the aluminium concentration that is observed after 6 h for pH values of 3.9 and 11.1 is attributed to experimental imprecision. While the aluminium concentration stays below $4 \cdot 10^{-5}$ mol/L at a pH value of 3.9 and 11.1, it is almost $2 \cdot 10^{-4}$ mol/L for pH 2.7. However, for the investigation of the EHT, the suspensions are kept at a pH value of 2.7 only for a few minutes during dispersion. The pH value is subsequently increased to at least 4 in order to reduce the dissolution.

Since the concentration of aluminium ions is much smaller than the concentration of potassium nitrate, which is at least 0.02 mol/L, the contribution of the dissolved ions to the ionic strength can be neglected in this study.

Table 3-1: Aluminium concentration $c_{Al^{3+}}$ in the filtrate depending on the suspension's aging time for different pH values at a potassium nitrate concentration of 0.02 mol/L.

pH value	$c_{Al^{3+}}$ after 10 min	$c_{Al^{3+}}$ after 6 h	$c_{Al^{3+}}$ after 24 h
2.7	$1.70 \cdot 10^{-4}$ mol/L	$1.70 \cdot 10^{-4}$ mol/L	$1.89 \cdot 10^{-4}$ mol/L
3,9	$2.36 \cdot 10^{-5}$ mol/L	$1.94 \cdot 10^{-5}$ mol/L	$3.15 \cdot 10^{-5}$ mol/L
11.1	$1.42 \cdot 10^{-5}$ mol/L	$9.49 \cdot 10^{-6}$ mol/L	$3.07 \cdot 10^{-5}$ mol/L

3.3.2 Zeta potential of the particles

The zeta potentials of the particles are measured with an AcoustoSizer II. Figure 3-9 shows the zeta potential of Disperal®, Disperal 20®, and Disperal 40® depending on the pH value of the suspensions for a constant ionic strength of 0.02 mol/L. The solid lines refer to measurements at a solid mass concentration of 10% and the dashed lines indicate the zeta potentials for a solid mass concentration of 5%. The Disperal® suspension has to be diluted because otherwise it would be too viscous for the measurements at high pH values. The influence of dilution on the zeta potential is relatively small, as can be seen from comparing the zeta potentials of Disperal 20® for solid mass concentrations of 5% and 10%. The different grades of boehmite show similar zeta potential curves due to their identical chemical composition. All materials have an IEP at a pH value of 9.4. At low pH values, the zeta potentials are around 60 mV. At high pH values, the absolute values of the zeta potential are lower. A higher particle charge would be expected at pH values beyond 12, but the particles would also dissolve faster. Only at low pH values, the zeta potential of Disperal® deviates from the zeta potential of Disperal 20® and Disperal 40®. However, this does not influence the stability of the suspensions significantly. The titania particles Aeroxide P25® have lower zeta potentials than the boehmite particles at all pH values and the IEP is located at a pH value of 6.9.

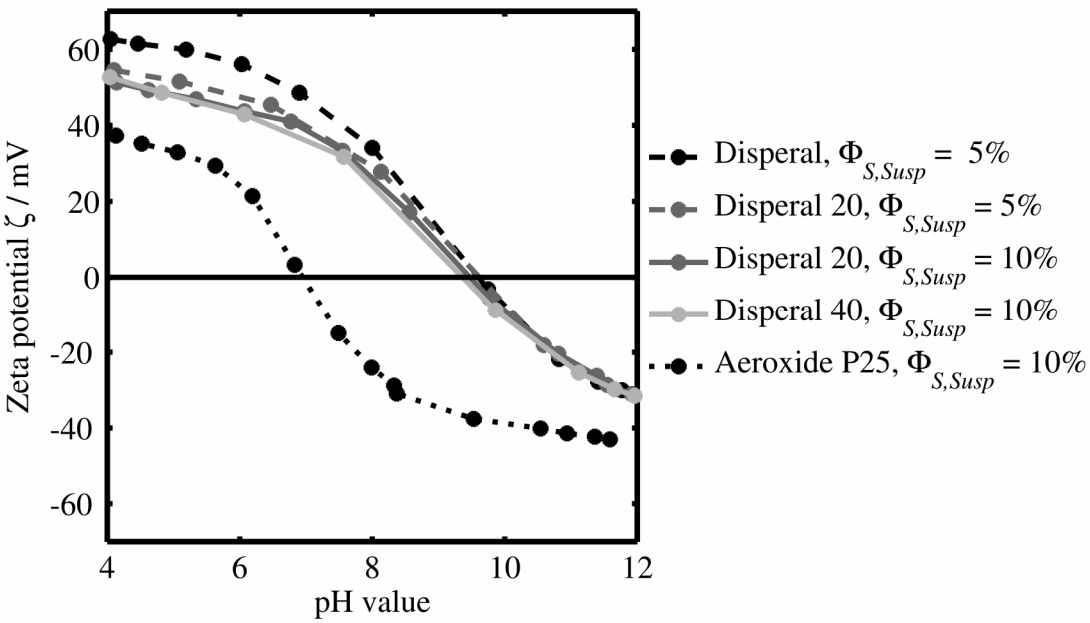

Figure 3-9: Zeta potential ζ depending on the pH value at an ionic strength of 0.02 mol/L for different materials and different solid mass concentrations $\Phi_{S,Susp}$.

The reduction of the zeta potential for increasing ionic strengths is presented in figure 3-10 for suspensions with a pH value of 4. Again, the zeta potentials of Disperal 20® and Disperal 40® are very similar, while it is higher for Disperal®. No dilution is required here, since the suspensions' viscosities increase less upon increasing the ionic strength than upon changing the pH value.

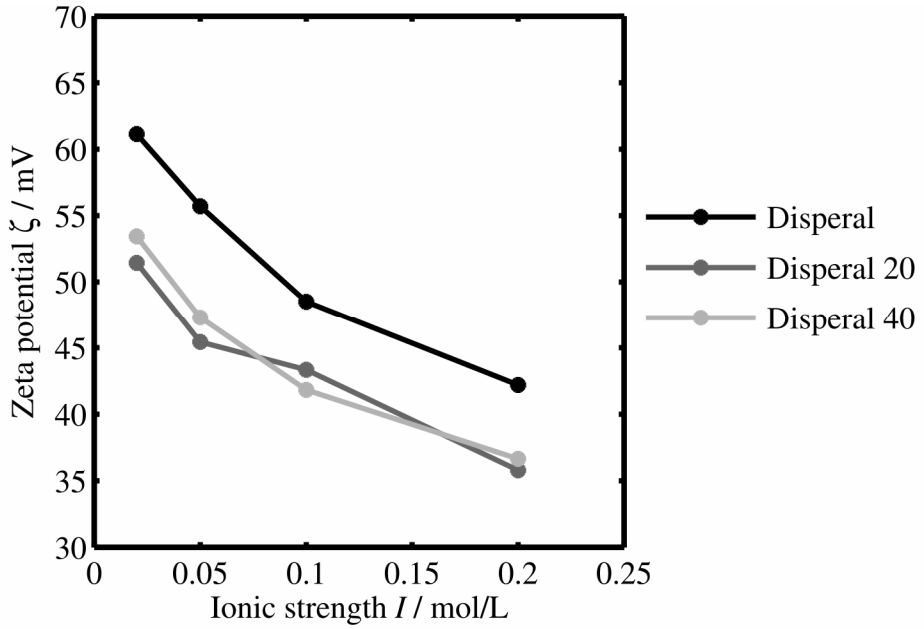

Figure 3-10: Zeta potential ζ depending on the ionic strength I at a pH value of 4 and a solid mass concentration $\Phi_{S,Susp}$ of 10% for different materials.

3.3.3 Agglomeration of suspensions

The agglomeration of the suspensions is examined by photon correlation spectroscopy in a Nanotrac®. It depends on the particle interactions and thus on the surface charge, which can be influenced by changing the pH value (see figure 3-11). The electrostatic Coulomb repulsion is strongest at low pH values, where the modulus of the zeta potential is highest. Increasing the pH value decreases the zeta potential, leading to an agglomeration of the particles. The number-weighted mean agglomerate size thus increases with increasing pH value until it reaches a constant level at a pH value of 8.5, where the zeta potential is about 22 mV and the resulting DLVO potential sets no energy barrier against agglomeration. A further increase of the pH value does not affect the agglomerates size. Even at a pH value of 11.5, where the zeta potential is -29 mV, the Coulomb repulsion is too weak to prevent agglomeration.

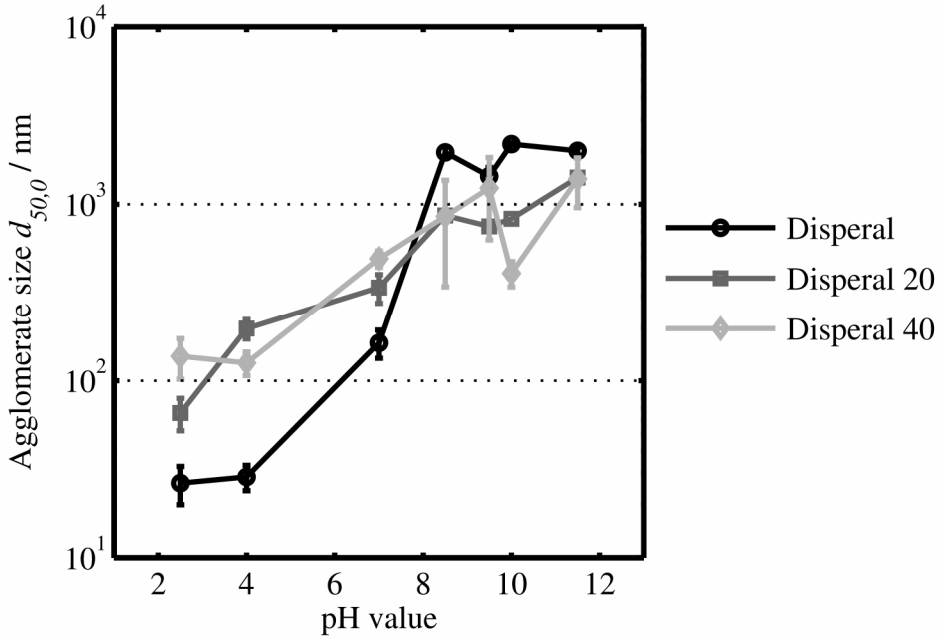

Figure 3-11: Number rated mean diameter $d_{50,0}$ of the particles and agglomerates in suspensions of different materials at an ionic strength of 0.02 mol/L for different materials.

3.3.4 Filtration behavior and membrane resistance

The filtration behavior of the suspensions and the membrane resistance are investigated with a simple Nutsche filter, which has the advantage of a fast and simple experimental procedure. The mass-related flow resistance of the filter cake is a meaningful indicator for the agglomeration of the particles and can be calculated from

the temporal evolution of the filtrate mass, as described by the differential equation [Alles, C. M. 2000]

$$\frac{dt}{dV_L} = -\frac{\eta\alpha\rho_S\Phi_{S,Susp}\left(1-\Phi_{L,PB}\right)}{\Delta p\, A_{PB}^2\left(1-\Phi_{L,PB}-\Phi_{S,Susp}\right)}V_L - \frac{\eta R_M}{A_{PB}\Delta p}, \tag{3-3}$$

with the time t, the volume of the filtrate V_L, the dynamic viscosity of the liquid η, the mass-related flow resistance of the PB α, the density of the solid ρ_S, the volumetric concentration of the solid in the suspension $\Phi_{S,Susp}$, the porosity of the PB $\Phi_{L,PB}$, the pressure difference Δp, the cross sectional area of the PB A_{PB}, and the membrane resistance R_M. The slope of the linear section of dt/dV_L as a function of V_L yields the mass-specific flow resistance of the filter cake α, while the intercept with the axis of ordinates represents the membrane resistance. For suspensions with low solid concentrations, equation (3-3) is approximated by

$$\frac{dt}{dV_L} = -\frac{\eta\alpha\rho_S\Phi_{S,Susp}}{\Delta p\, A_{PB}^2}V_L - \frac{\eta R_M}{A_{PB}\Delta p}, \tag{3-4}$$

which has the advantage of not requiring a measurement of the PB's porosity. The filtration experiment can thus be interrupted after a few minutes, since the mass-related flow resistance of the filter cake α is determined from the flow rate at the start of the filtration. Determining α from the integral function

$$\frac{t}{V_L} = -\frac{\eta\alpha\rho_S\Phi_{S,Susp}}{2\Delta p\, A_{PB}^2}V_L - \frac{\eta R_M}{A_{PB}\Delta p}, \tag{3-5}$$

instead of the differential equation (3-4) is less affected by disturbances of the scale that measures the filtrate, but has the disadvantage that the initial time and the initial volume must be accounted for. Figure 3-12 shows dt/dV_L (grey dots), t/V_L before correcting for the initial filtrate volume (black solid line), and t/V_L after correcting for the initial filtrate volume (black dashed line) as functions of the filtrate volume. Corresponding to equations (3-3) and (3-5), the slope of the linear section of dt/dV_L is twice the slope of the linear section of t/V_L.

The strong influence of disturbances of the scale on the function dt/dV_L is reflected by the dispersion of the values, whereas t/V_L is relatively smooth. Correcting for the

initial filtrate volume does hardly influence the slope of the linear section of t/V_L, so that the determination of the mass-related flow resistance is reliable.

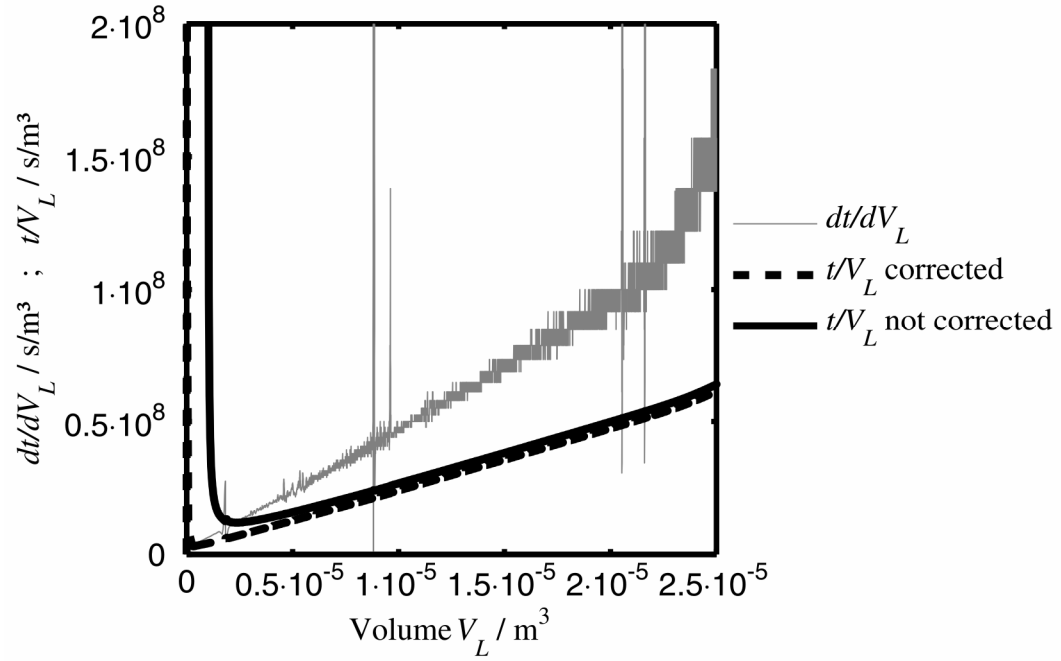

Figure 3-12: Filtration curves for a suspension of Disperal 40® at a pH value of 10 and an ionic strength of 0.02 mol/L.

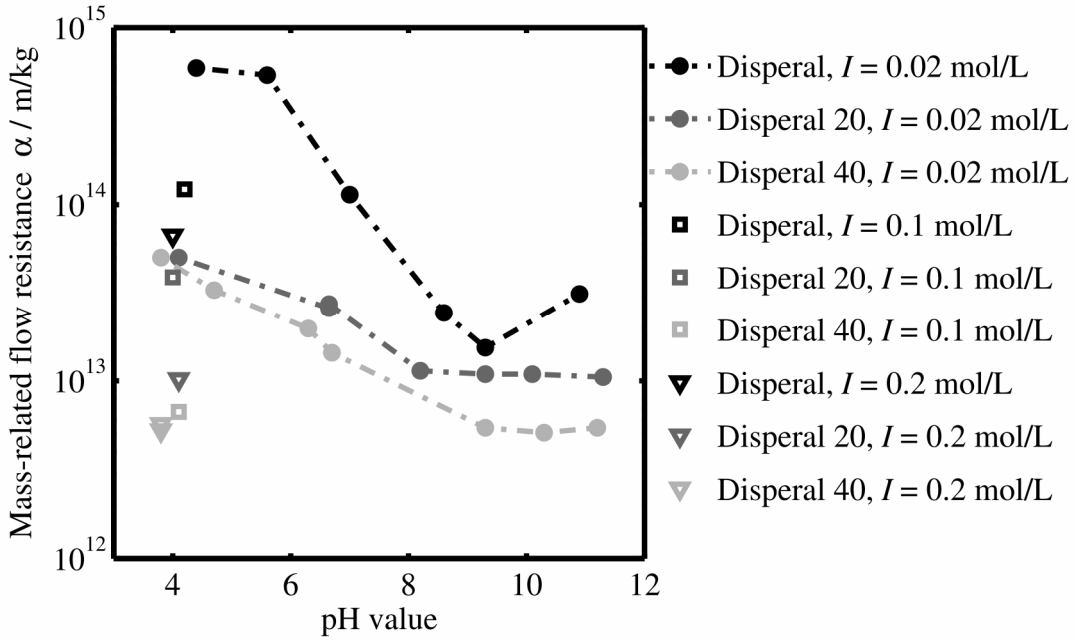

Figure 3-13: Mass-related flow resistance α of filter cakes depending on the pH value of the suspensions at different ionic strengths I for different materials.

For each material, the mass-related flow resistance shows a minimum at the IEP, where the particles agglomerate (see figure 3-13). The flow resistance increases with decreasing particle size, which is caused by the smaller pores. For pH values around 4,

increasing the ionic strength reduces the flow resistance of the filter cakes because of the agglomeration of the particles.

The membrane resistance is represented by the intersection of the axis of ordinates with the extrapolation of the linear section of the black dashed line in figure 3-12. However, this analysis is very sensitive to the correction for the initial volume and initial time, which causes the broad scattering in figure 3-14. The analysis is especially precarious for filter cakes with high flow resistances, where the contribution of the membrane resistance to the total flow resistance is very small, as is observed for Disperal® and Disperal 20® at low pH values. For the other cases, the membrane resistance is close to the membrane's resistance against permeation by pure water, which is $1.5 \cdot 10^{11}$ m^{-1}. The contribution of the membrane resistance to the total flow resistance of the PBs, which is between $2 \cdot 10^{13}$ m^{-1} and $2.4 \cdot 10^{15}$ m^{-1}, is below 1.5%. It is thus neglected in this study. The influence of the membrane on the streaming potential and on the electroosmotic flow is discussed in chapter 3.3.13.

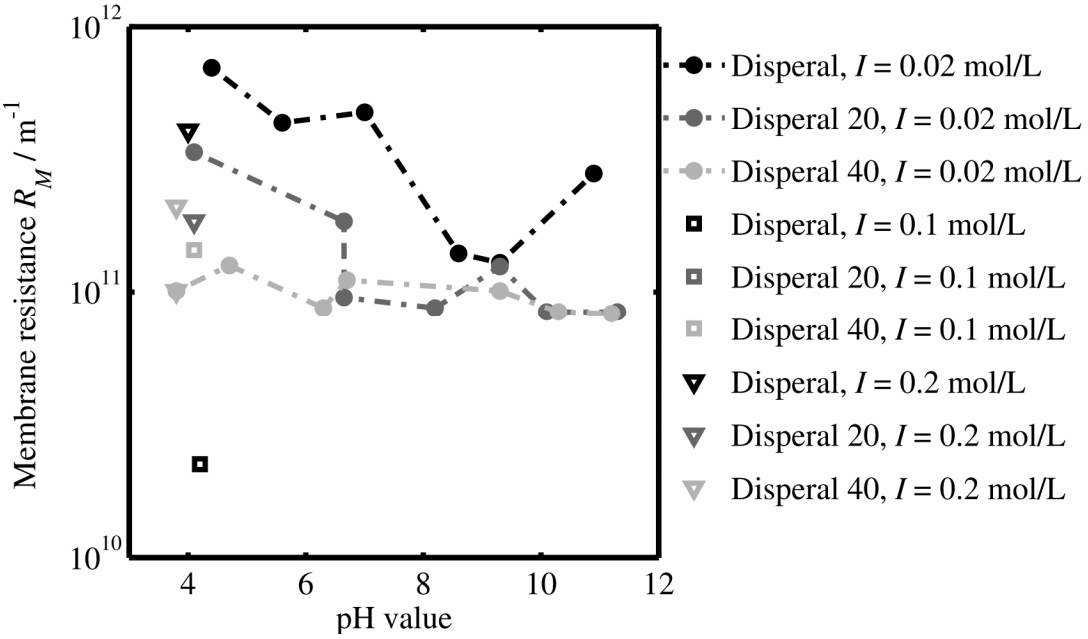

Figure 3-14: Flow resistance of the membranes R_M depending on the pH value of the suspensions at different ionic strengths I for different materials.

3.3.5 Porosity

The integral porosity $\Phi_{L,PB}$ is a measure for the pore structure of the PBs. Assuming a homogeneous compression, the porosity is a function of the thickness L_{PB} of the PB:

$$\Phi_{L,PB} = \frac{\left(L_{PB} A_{PB} - \frac{m_S}{\rho_S} \right)}{L_{PB} A_{PB}}, \qquad (3\text{-}6)$$

with the solid mass m_S, and the solid density ρ_S, and the cross sectional area A_{PB} of the PBs. The thickness of the PB determined with a position encoder on the plunger.

At an ionic strength of 0.02 mol/L, the porosity strongly depends on the pH value, on the compressive load, and on the size of the primary particles (see figure 3-15). The maximum around the IEP, which is at a pH value of 9.4, is caused by the agglomeration of the particles. The strongest change of porosity occurs between pH 4, where the zeta potential is 61 mV, and pH 8.5, where the zeta potential is 22 mV and the Coulomb repulsion is too weak to prevent agglomeration. The particles also agglomerate at a pH value of 12, where the zeta potential is -29 mV. As expected, a stronger compression results in a lower porosity at all pH values and for all particle sizes. The effect is relatively small at a pH value of 4, where the structure of the PB is very dense and homogenous. The high compressibility of agglomerated structures is caused by the deformation of the agglomerates and the resulting reduction of the inter-agglomerate pores. The highest compressibility is observed for Disperal 40® at a pH value of 7, possibly caused by the presence of highly deformable secondary agglomerates. For each pH value and for each compression, the PBs consisting of Disperal 20® have the highest porosities, followed by Disperal® and Disperal 40®. This observation cannot by explained by theoretical considerations for spherical particles. It has to be caused by the complicated interplay of particle morphology, DLVO interactions, and agglomerate structure. The systematic error caused by the deformation of the electro-compression-permeability cell is estimated to be below 1 %.

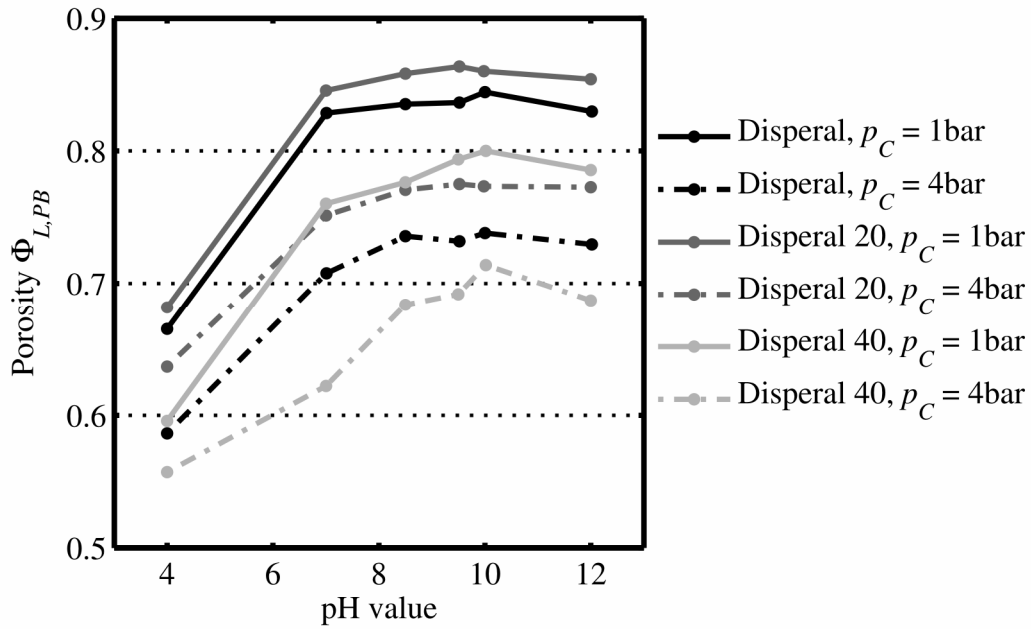

Figure 3-15: Porosity $\Phi_{L,PB}$ of the PBs depending on the pH value at an ionic strength of 0.02 mol/L for different compressive loads p_C and different materials.

Figure 3-16 shows the influence of the ionic strength on the porosity of the PBs at a pH value of 4. A higher ionic strength causes a shorter Debye length and thus a weaker electrostatic repulsion between the particles. Consequently, the particles agglomerate and the PBs formed at higher ionic strengths have a higher porosity. For Disperal 20® and Disperal 40®, the porosities are similar at 0.2 mol/L and 0.1 mol/L, where the particles are already fully agglomerated. Only for Disperal®, the porosities increase upon increasing the ionic strength to beyond 0.1 mol/L, because the ionic strength required for agglomeration increases with decreasing particle size. Like in figure 3-15, the higher compression causes a smaller porosity for all ionic strengths and all particle sizes and the change of the porosity is about the same in both compression steps. The influence of the compression is stronger at a high ionic strength due to the presence of deformable agglomerates. Again, the high porosity for Disperal 20® cannot be explained by theoretical considerations for spherical particles.

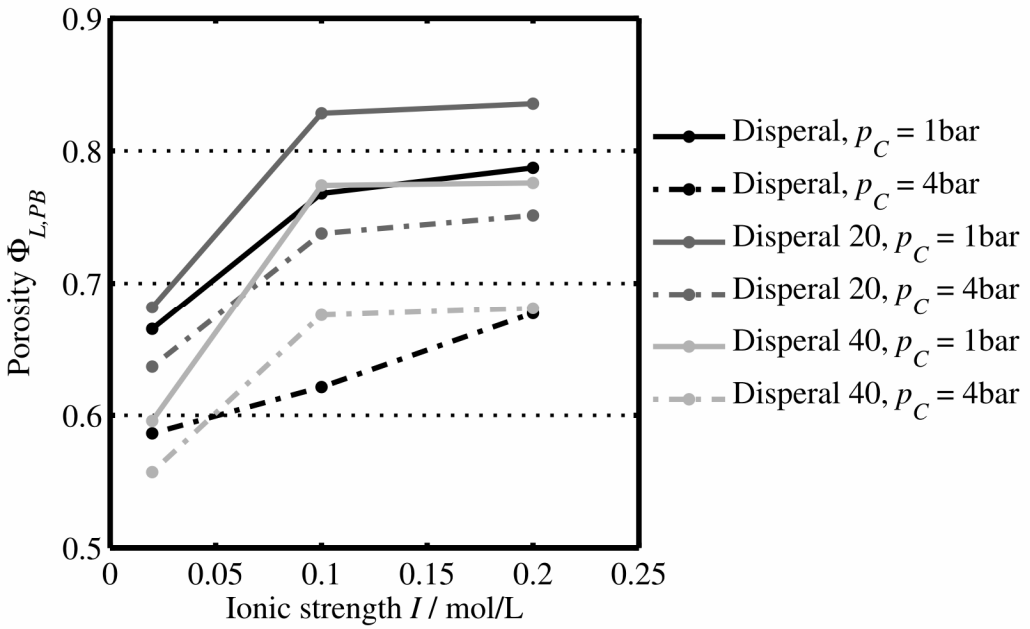

Figure 3-16: Porosity $\Phi_{L,PB}$ of the PBs depending on the ionic strength I at a pH value of 4 for different compressive loads p_C and different materials.

Experiments with Aeroxide P25® reveal a different behavior (see figure 3-17). The porosity of the PB is relatively high at all pH values and decreases only for pH values below the IEP, which is at a pH value of 6.9. The effect of increasing the compression is much smaller for Aeroxide P25® than for Disperal®, Disperal 20® and Disperal 40®, although the primary particle size of Aeroxide P25® is similar to the one of Disperal®. These differences are caused by the sintered aggregates of the Aeroxide P25® particles, which result from the flame synthesis and which cannot be broken even by ultrasound, rotor-stator systems or high-pressure dispersion [Teleki, A., et al. 2008].

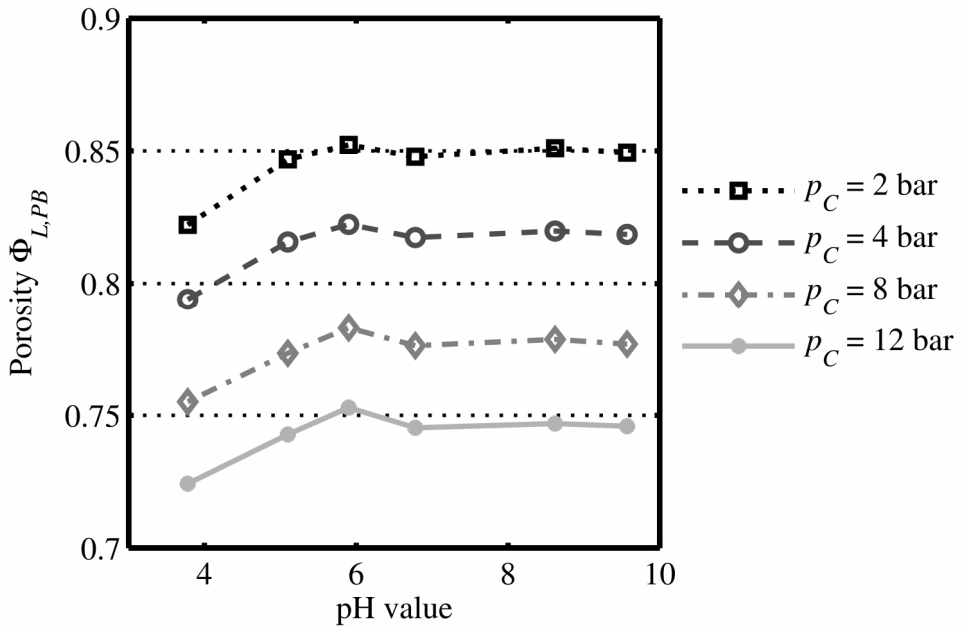

Figure 3-17: Porosity $\Phi_{L,PB}$ of PBs consisting of Aeroxide P25® depending on the pH value for different compressive loads p_C.

3.3.6 Pressure-driven flow

The hydraulic permeability C_{11} of a PB depends on its pore structure and is thus influenced by the electrochemical composition of the suspensions from which the PB is formed. For an ionic strength of 0.02 mol/L, the permeabilities have maxima around the IEP for all particle sizes and all compressive loads (see figure 3-18). These maxima correspond to the maxima of the porosities (see figure 3-15) and the reduction of the permeabilities beyond the IEP is relatively small. Increasing the compression leads to a decrease of the permeability for each pH value and for each particle size, which can be explained by the decreasing pore size. The flow rate decreases upon a reduction of the porosity although the pressure gradients increase when the pressure difference acts on a thinner PB.

The permeability also decreases with decreasing particle size, which cannot be explained by the different porosities: PBs consisting of Disperal 40® (with the highest particle size) have the lowest porosity, but the highest permeability. Disperal 20® and Disperal 40® have similar permeabilities, showing that the effect of the smaller particle size is almost compensated by the higher porosity observed for Disperal 20®. Disperal® has a significantly smaller permeability than Disperal 20®, although the porosities are similar.

Figure 3-19 shows the increase of the permeability with an increasing ionic strength, which is caused by the agglomeration of the particles. For Disperal 20® and Disperal 40®, the permeability is almost constant for ionic strengths above 0.1 mol/L, where the suspensions are fully agglomerated. The influences of the particle size and the compression are analogous to figure 3-18.

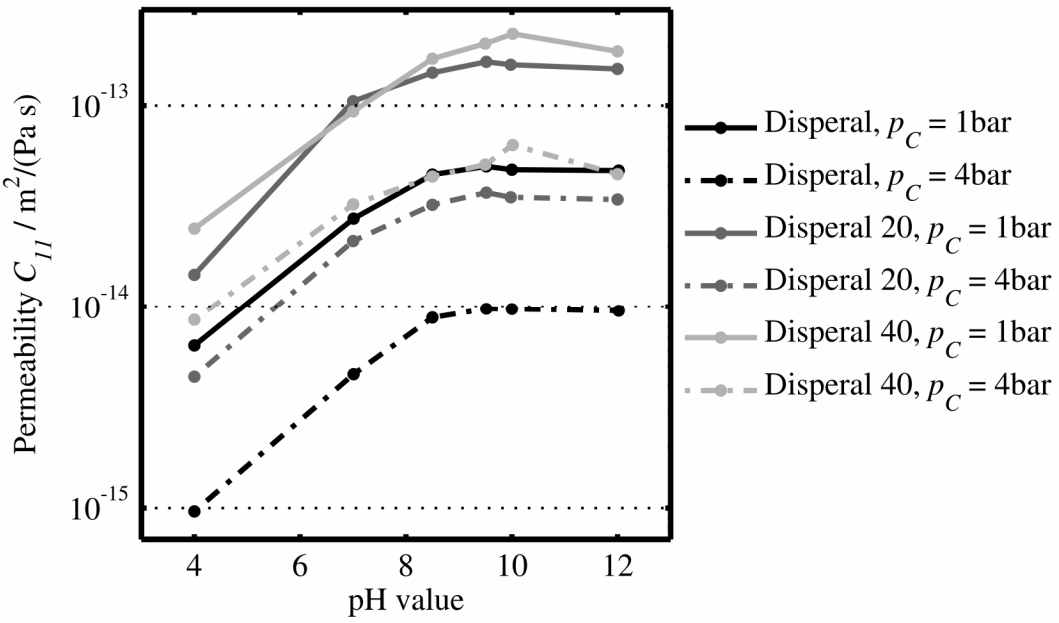

Figure 3-18: Permeability C_{11} of the PBs depending on the pH value at an ionic strength of 0.02 mol/L for different compressive loads p_C and different materials.

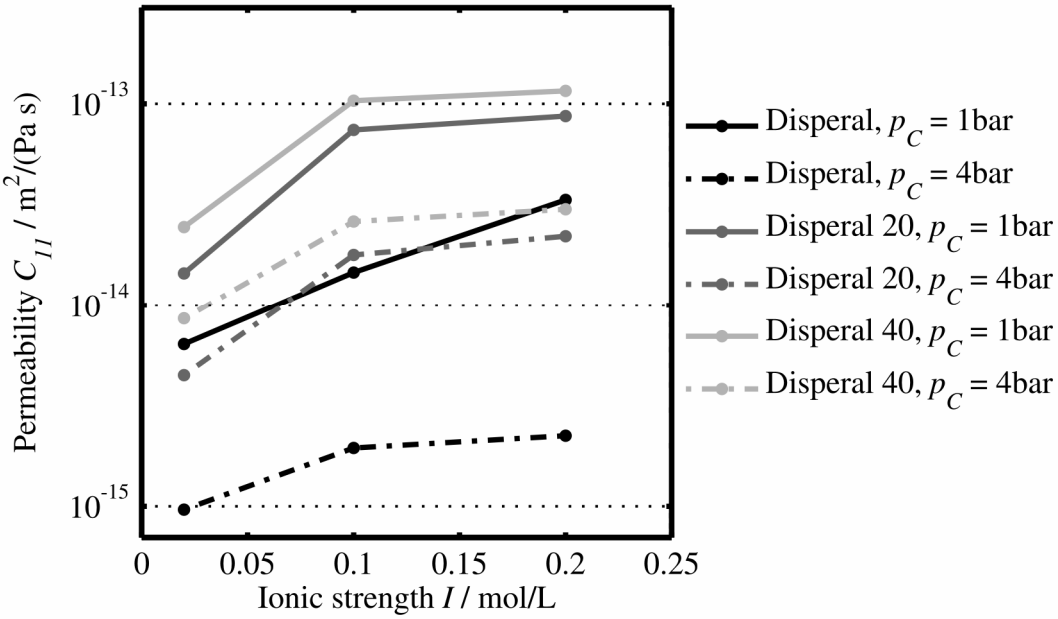

Figure 3-19: Permeability C_{11} depending on the ionic strength I at a pH value of 4 for different compressive loads p_C and different materials.

The permeability of PBs consisting of Aeroxide P25® is high for pH values above the IEP, which is at a pH value of 6.9 and decreases for pH values below the IEP (see figure 3-20). Like for the boehmite particles, a stronger compression causes a lower permeability. The logarithmic plots of the permeability are similar to the linear plots of the porosity, but the influence of the pH value on the permeability appears to be stronger than its influence on the porosity (compare figure 3-19): For the different compressive loads, the permeability ranges overlap, but the porosity ranges do not. A possible explanation is based on subdividing the porosity into the inter-aggregate and intra-aggregate porosity. The contribution of the intra- aggregate porosity to the permeability is small because the flow in the small pores within the aggregate is very slow. Increasing the compression mainly affects the inter-aggregate porosity, so that a small change of porosity has a strong effect on the permeability, while the intra-aggregate porosity can still be high.

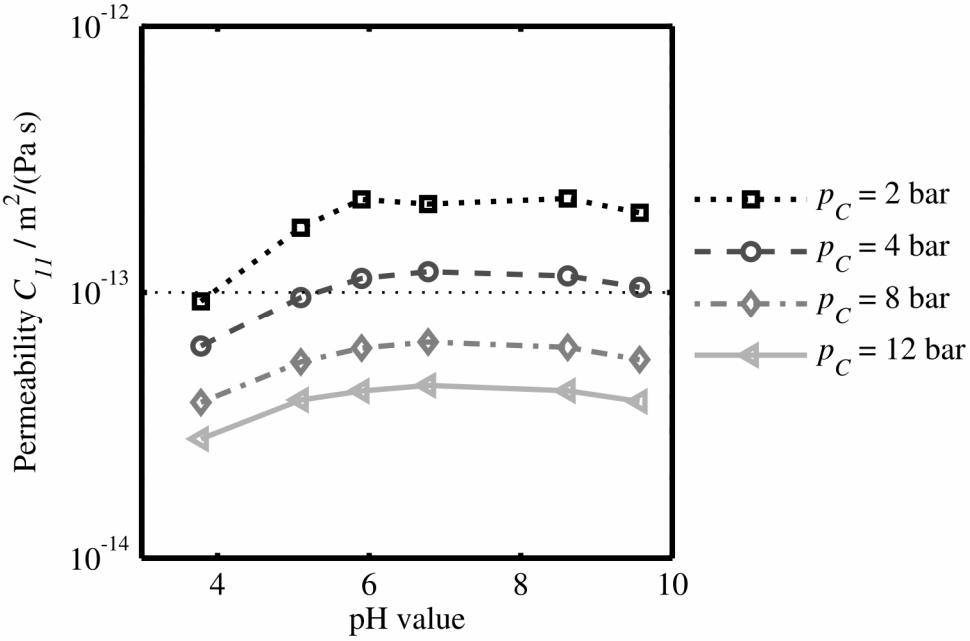

Figure 3-20: Permeability C_{11} of PBs consisting of Aeroxide P25® depending on the pH value at an ionic strength of 0.02 mol/L for different compressive loads p_C.

For each particle material, the permeability is an exponential function of the porosity (see figure 3-21) for different pH values, ionic strengths, and compressive loads

$$C_{11} = a \cdot e^{b \cdot \Phi_{L,PB}}, \qquad (3\text{-}7)$$

with the coefficients a and b as given in table 3-2. The coefficient b is similar for the different particle sizes, both for the simulation and for the experiments. The coefficient

a is highest for Disperal 40®, which is the coarsest material, followed by Aeroxide P25®, Disperal 20®, and Disperal®. Although Aeroxide P25® has the smallest primary particle size, its permeability is comparatively high because of the irregularly shaped, sintered aggregates, which lead to large inter-aggregate pores. Alternatively, the hydraulic permeability can be fitted to a power law function of the porosity

$$C_{11} = a\,\Phi_{L,PB}^{b}, \tag{3-8}$$

but the deviation is stronger than for the exponential fit. The fitting parameters are given in table 3-2. The exponents are significantly higher than the exponent of 5.5 that was found by Rumpf and Gupte [Rumpf, H. and Gupte, A. R. 1971]. This shows that the porosity has a stronger influence for smaller particles, which seems reasonable if you think of the PBs as an inhomogeneous structure with relatively large inter-agglomerate pores: Decreasing the porosity, for example by increasing the compressive load, primarily acts on the inter-agglomerate pores. Since these are accountable for the major part of the fluid flow, the permeability strongly decreases, although the intra-agglomerate porosity is still high.

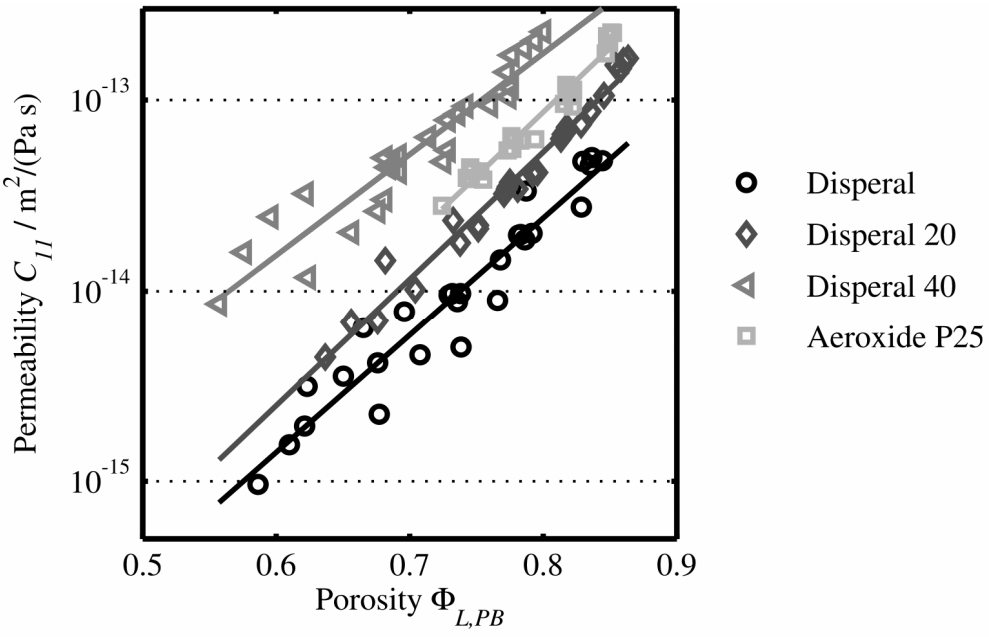

Figure 3-21: Permeability C_{11} of PBs consisting for of different materials as a function of the porosity $\Phi_{L,PB}$ for varying ionic strengths, pH values and compressive loads p_C.

Table 3-2: Fitting parameters for the permeability as a function of the porosity

Particle diameter	Exponential fit		Power law fit	
	a	*b*	*a*	*b*
30 nm	$3.5 \cdot 10^{-19}$	13.9	$2.2 \cdot 10^{-13}$	9.9
70 nm	$4{,}3 \cdot 10^{-19}$	14.7	$6.3 \cdot 10^{-13}$	10.9
120 nm	$2.1 \cdot 10^{-17}$	11.3	$8.5 \cdot 10^{-13}$	7.5

An exponential relation between the porosity and the permeability is also found in the results of the numerical simulations (see chapter 4.4.3).

3.3.7 Electric conduction

The electric conductivity C_{22} relates the electric current to the voltage measured at the measuring electrodes. It comprises the conductivity of the liquid and the conductivity of the surfaces and furthermore depends on the porosity of the PB. The liquid conductivity is calculated with equation (2-30), assuming that the liquid in the pores has the same pH value and ionic strength as the suspension from which the PB was formed. The liquid conductivity is nearly constant over a wide range of the pH value. The maximum at high pH values is caused by the high concentration of hydroxide ions (see figure 3-22). The calculated liquid conductivity is of course independent of the particle size and the compression.

The conductivity C_{22} of the PBs is a function of the porosity, the liquid conductivity, and the surface conductivity, which is discussed below. The PBs' conductivity is one order of magnitude smaller than the conductivity of the electrolyte solution because the particles themselves are non-conducting and the ions have to migrate through the porous structure. This can also be seen from the low conductivity of PBs at low pH values and at high compressive loads. Analogously, the conductivity is comparatively high for Disperal 20®, which is caused by the high porosity. Also at the IEP, the high porosity results in a high conductivity. Theoretically, the conductivity should increase further for pH values above the IEP, where porosity, liquid conductivity, and surface

conductivity are high. However, this is only observed for Disperal®. The unexpected behavior of Disperal 20® and Disperal 40® at a pH value of 12 can be explained by the measurement uncertainty of the effective voltage, which is caused by a polarization of the measuring electrodes during the experiments.

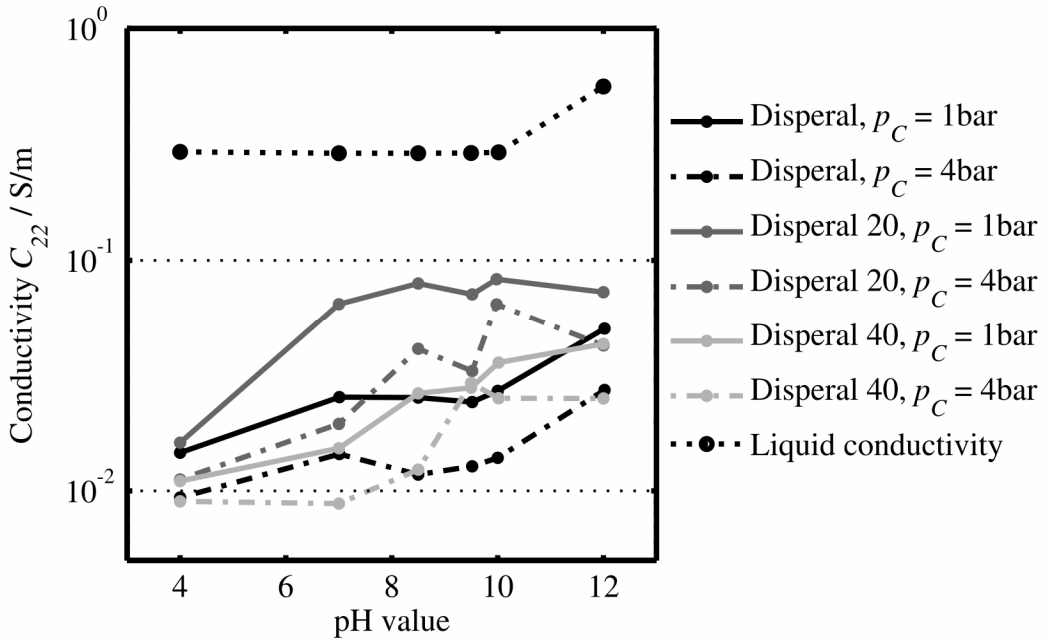

Figure 3-22: Electric conductivity C_{22} of the liquid and the PBs depending on the pH value at an ionic strength of 0.02 mol/L for different compressive loads p_C and different materials.

The contribution of surface conductivity is quantified by the Dukhin number, as defined in equation (2-31). It is relatively small at the IEP for each particle size and each compressive load (see figure 3-23). The perturbations are caused by the quotient of the zeta potential ζ and the electroosmotic flow $\dot{V}_L$ in equation (2-33). Since both are small near the IEP, a small measurement inaccuracy of the electroosmotic flow causes a large deviation of the Dukhin number. Furthermore, the electroacoustic measurements of the zeta potential of the particles in the suspensions possibly yield a different IEP than the electrohydrodynamic measurements on the densely packed particles in the PB. Consequently, the Dukhin numbers Du are more reliable at low pH values. The highest Dukhin numbers are observed for Disperal®, followed by Disperal 20® and Disperal 40®. This sequence indicates that surface conduction has a stronger contribution for finer structures with higher specific surface areas. A stronger compression of the PBs reduces the distance between neighboring particles, thus facilitating the charge transport on the surfaces.

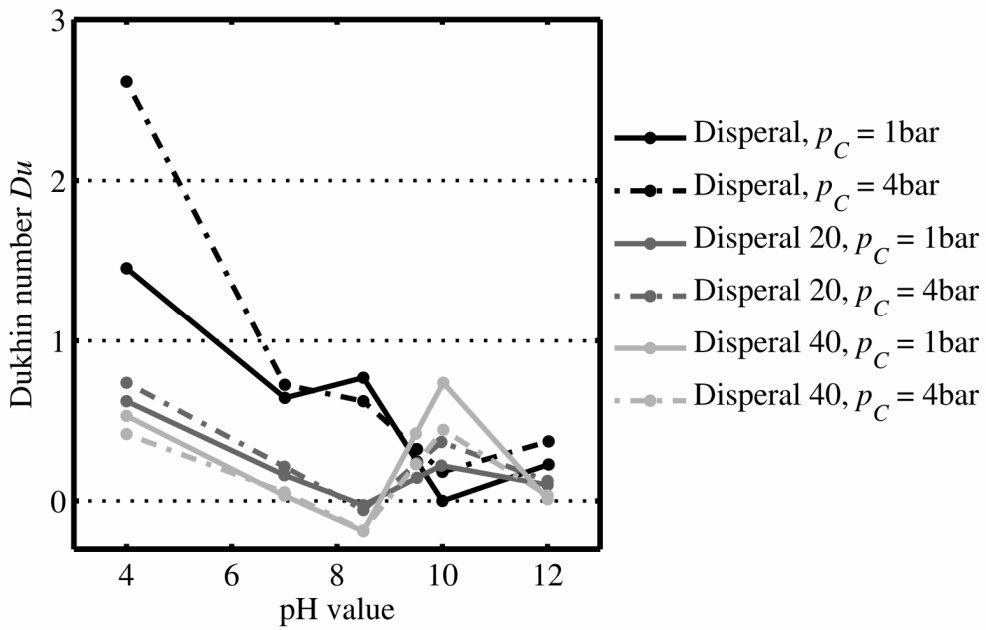

Figure 3-23: Dukhin number Du of the PBs depending on the pH value at an ionic strength of 0.02 mol/L for different compressive loads p_C and different materials.

The increase of the ionic strength effects a rising liquid conductivity and, as expected, an increased conductivity of the PBs (see figure 3-24). Their conductivity is lower at higher compression due to the lower porosity. The influence of the particle size on the conductivity is caused by the difference in porosity since the Dukhin number is relatively small at high ionic strengths (see figure 3-25). This also explains why both porosity and conductivity are highest for Disperal 20®. The conductivity is lower for Disperal® than for Disperal 40®, probably because the small pores for Disperal® restrict the motion of liquid and ions.

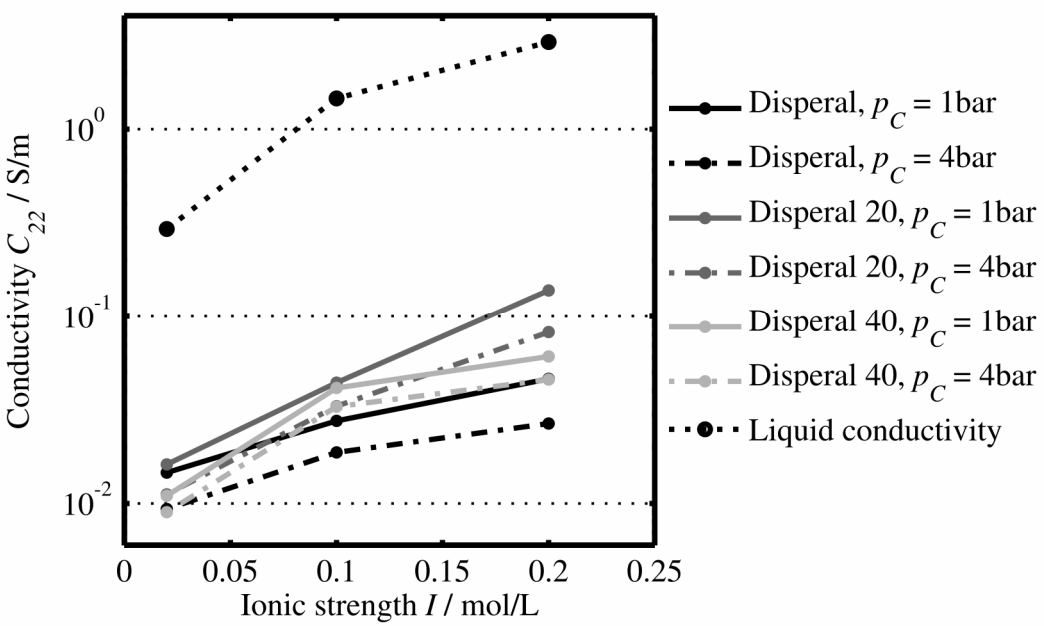

Figure 3-24: Electric conductivity C_{22} of the liquid and the PBs depending on the ionic strength I at a pH value of 4 for different compressive loads p_C and different materials.

As expected, the Dukhin number decreases for higher ionic strengths because of the increasing liquid conductivity (see figure 3-25). It becomes almost zero at an ionic strength of 0.2 mol/L. At a low ionic strength, the Dukhin number increases with increasing compression because the EDLs of neighboring particles overlap stronger when the particles get closer. The importance of surface conduction is again higher for smaller particles with higher specific surface area. At the highest ionic strengths, surface conduction is negligible. The negative values are caused by measuring inaccuracies, analogously to the perturbations around the IEP.

The distinction between surface and liquid conduction is important for the investigation of the electrokinetic effects and for the foundation of the capillary model, which is explained in the following.

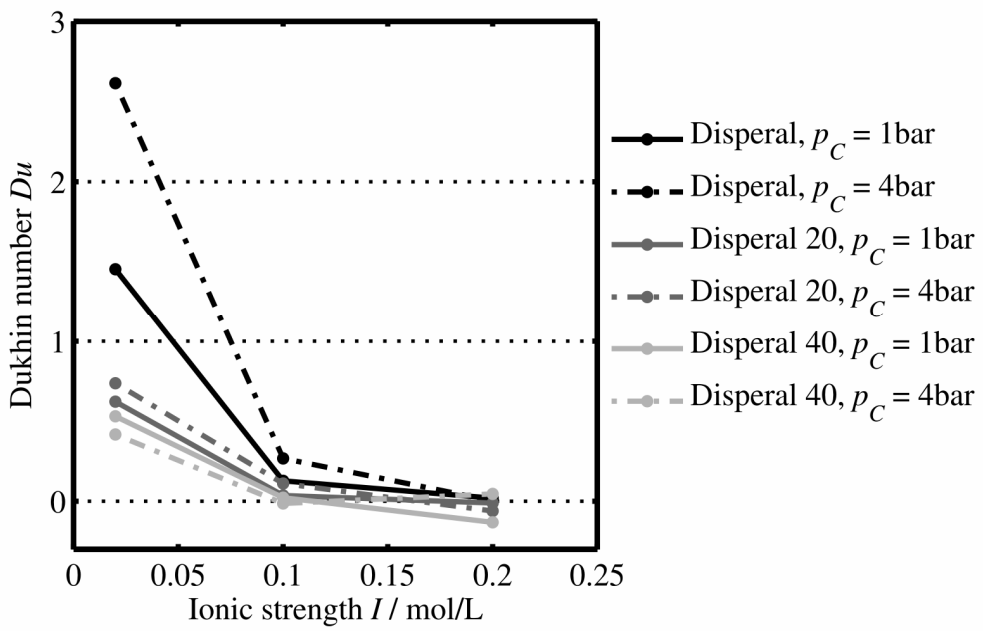

Figure 3-25: Dukhin number Du depending on the ionic strength I at a pH value of 4 for different compressive loads p_C and different materials.

3.3.8 Capillary model

While relations for the EHT are well established for simple geometries, explaining the phenomena in a PB is complicated because of the complex pore structure and because the pore structure itself also depends on the surface charge and the ion distribution in the EDL [Santiwong, S. R., et al. 2008, Schäfer, B. and Nirschl, H. 2008]. Many researchers describe the EHT with elaborate spherical cell models, for which the continuity and stokes equation are solved (see [Zholkovskij, E. K., et al. 2007] for a recent review). Others solve the Poisson-Boltzmann, continuity, and Stokes equations in porous simulation domains under the assumption of negligible surface conductivity [Gupta, A., et al. 2008] or apply molecular dynamics simulations [Marry, V., et al. 2003]. Due to their complexity, these models are not suitable for practical applications. This study presents a new method for analyzing the EHT. In analogy to the Carman-Kozeny model, the PBs are considered as theoretical sets of cylindrical capillaries with an experimentally determined geometry (see figure 3-26). The capillaries are longer and thinner than the PBs because the pores in the PBs are tortuous and a part of the PBs' cross sectional area is occupied by the particles.

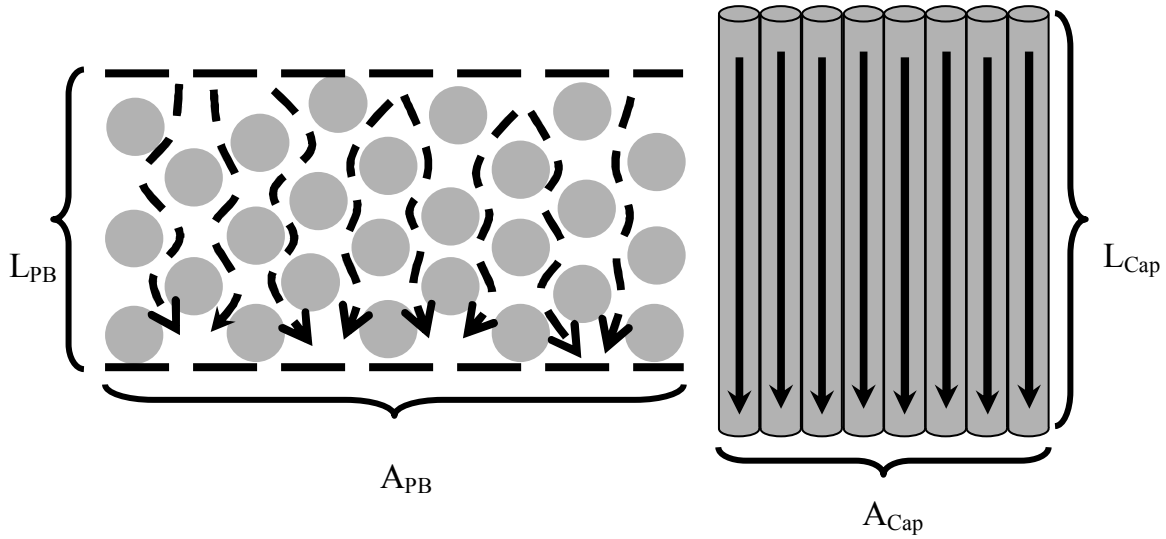

Figure 3-26: Illustration of the hypothetical capillary system for modeling the pore structure.

The electric current in the capillary bundle equals the electric current in the PB, leading to

$$C_{22,Cap}\frac{A_{Cap}}{L_{Cap}} = C_{22}\frac{A_{PB}}{L_{PB}}, \tag{3-9}$$

with the capillary bundle's conductivity $C_{22,Cap}$, cross sectional area A_{Cap}, and length L_{Cap}. Furthermore, the capillary bundle must have the same ratio of surface to liquid conductivity, i.e. the same Dukhin number Du, as the PB. The capillary conductivity then results from equation (2-32) as

$$C_{22,Cap} = C_{22,L}\left(1+2Du\right), \tag{3-10}$$

with the liquid conductivity $C_{22,L}$, which is defined above. The capillary geometry is quantified with the geometry ratio

$$R_{Geo} = \frac{A_{Cap}}{L_{Cap}}\frac{L_{PB}}{A_{PB}} = \frac{C_{22}}{C_{22,Cap}}. \tag{3-11}$$

At a low ionic strength of 0.02 mol/L, the capillary conductivity (see figure 3-27) is almost proportional to the Dukhin number (see figure 3-23) over a wide range of the pH value. The deviations at high pH values reflect the high liquid conductivity and the low surface conductivity. The capillary conductivity increases with increasing compression, whereas the total conductivity decreases (see figure 3-22). Also a reduction of the particle size causes a smaller pore size and thus higher capillary

conductivity. The perturbations at the IEP arise from the irregularities of the Dukhin number, which are explained above.

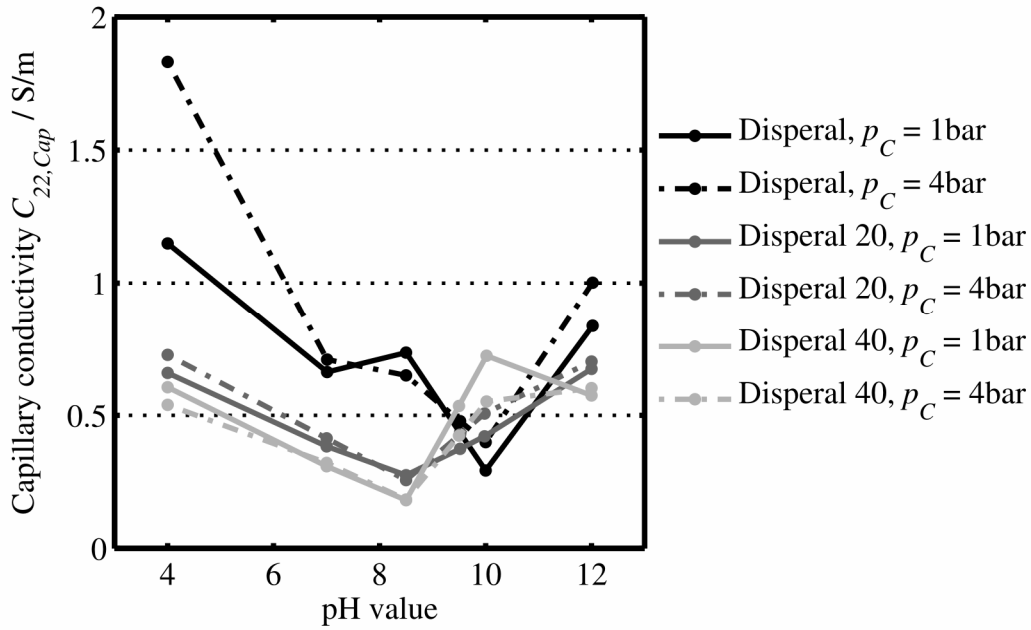

Figure 3-27: Electric conductivity $C_{22,Cap}$ of the hypothetical capillary system depending on the pH value at an ionic strength of 0.02 mol/L for different compressive loads p_C and different materials.

The geometry ratio is smaller than unity for all experiments because the path through the PB is tortuous and thus makes the capillaries longer and thinner than the PB (see figure 3-28). Decreasing the pH value from the IEP to 4 decreases the porosity and thus decreases the geometry ratio. Likewise, a stronger compression causes a lower porosity and lower geometry ratio. The geometry ratio also decreases with decreasing particle size, indicating that it is influenced by the pore size, not by the porosity. The perturbations of the geometry ratio at the IEP are caused by the irregularities of the Dukhin number.

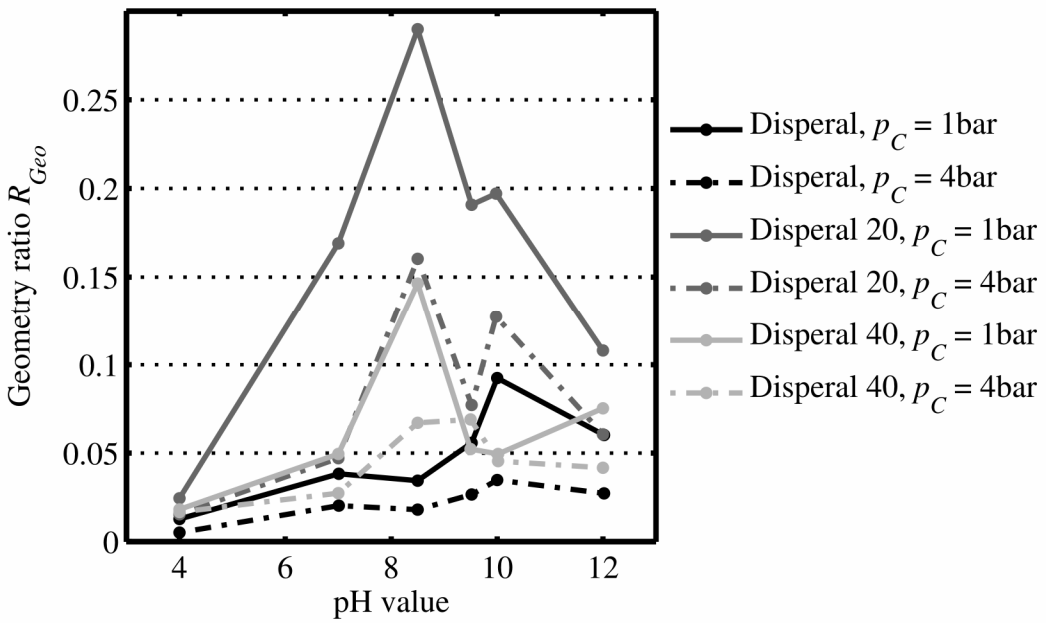

Figure 3-28: Geometry ratio R_{Geo} of the hypothetical capillary system depending on the pH value at an ionic strength of 0.02 mol/L for different compressive loads p_C and different materials.

At high ionic strengths, where liquid conduction is prevalent over surface conduction, the capillary conductivity is proportional to the ionic strength (see figure 3-29). The disproportionally high surface conductivity for Disperal® at low ionic strength and high compression is caused by the growing importance of surface conductivity. Like in figure 3-27, the capillary conductivity increases with compression, while the total conductivity of the PB decreases.

The geometry ratio as defined above also depends on the ionic strength (see figure 3-30). At a higher ionic strength, the geometry ratio is higher due to the larger pores. This is also reflected by the reduction of the geometry ratio upon increasing the compression and by the geometry ratio being highest for Disperal 20®. Although the porosity is higher for Disperal® than for Disperal 40®, its geometry ratio is lower. This corroborates that the geometry ratio depends on the pore size, not on the porosity. The low geometry ratio for Disperal 40® at an ionic strength of 0.2 mol/L and at a compression of 4 bar is caused by the deviation of the capillary conductivity.

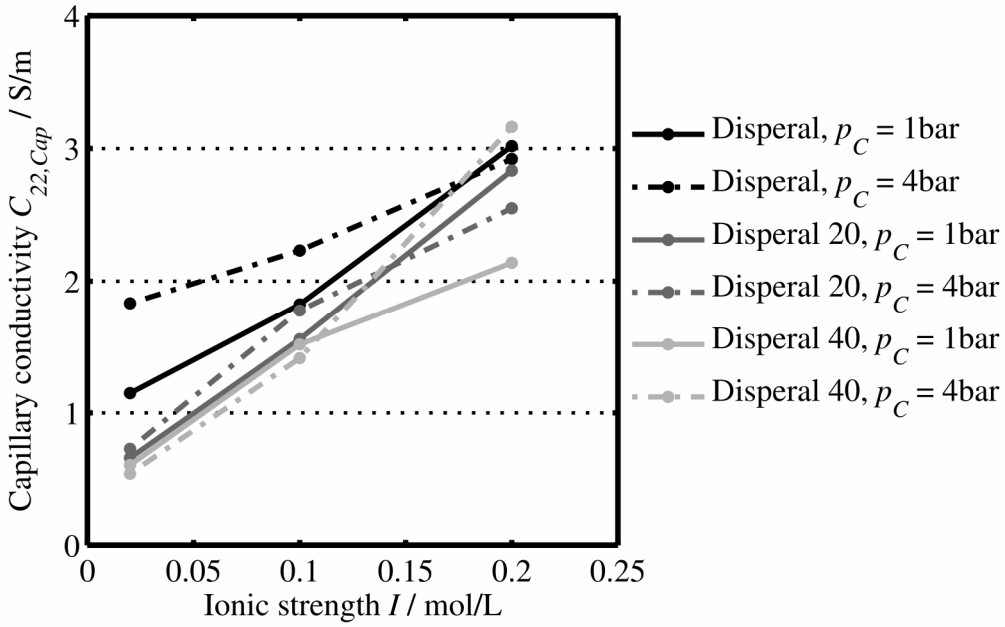

Figure 3-29: Electric conductivity $C_{22,Cap}$ of the hypothetical capillary system depending on the ionic strength I at a pH value of 4 for different compressive loads p_C and different materials.

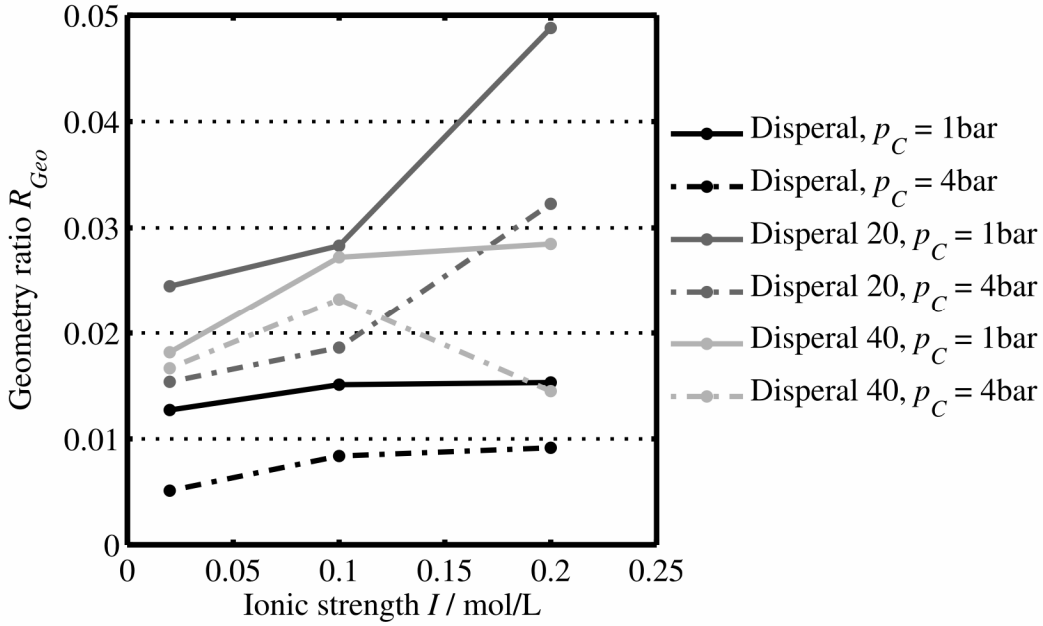

Figure 3-30: Geometry ratio R_{Geo} of the hypothetical capillary system depending on the ionic strength I at a pH value of 4 for different compressive loads p_C and different materials.

The capillary model can be used to calculate the electroosmosis coefficient, the streaming potential coefficient and the electroviscous effect. The results are compared to the measurements in the following chapters.

3.3.9 Electroosmotic flow

Knowing the geometry ratios, the electroosmotic flow in the PBs can be calculated from equations (2-23), (2-24), and (3-11) as

$$\dot{V}_L = \frac{A_{PB}}{L_{PB}} \frac{\varepsilon_{rel}\varepsilon_0\zeta}{\eta} \Delta\Psi_{el} \cdot R_{Geo}, \tag{3-12}$$

with the relative permittivity ε_{rel}, the vacuum permittivity ε_0, and the voltage $\Delta\Psi_{el}$. The electroosmosis coefficient consequently results as

$$C_{12} = \frac{\varepsilon_L\varepsilon_0\zeta}{\eta} R_{Geo}. \tag{3-13}$$

Alternatively, it can be determined experimentally from the temporal slope of the mass of the permeate on the scale related to the effective voltage at the measuring electrodes. Figure 3-31 shows the evolution of the electric current I_{el}, the electric potential difference $\Delta\Psi_{el}$, and the volume of the permeate V_L during the investigation of the electroosmotic flow. At the start, the volume of the liquid in the reservoir on the scale decreases because of evaporation. Subsequently, the electric field applied to the working electrodes drives an electroosmotic flow, as can be seen from the increasing volume. In the experiments, the electric current is controlled instead of the voltage at the working electrodes since a stable voltage does not produce a constant electroosmotic flow. The reversal of the electric current causes a reversal of the electroosmotic flow and a decreasing volume. At 180 s and 300 s, i.e. after applying the electric field in both directions for equal amounts of time, the volume on the scale correlates to the evaporation line, i.e. the extrapolation of the volume from the first 60 s. This proofs that no electrolytic gas is formed and the electroosmotic flow is independent of the flow direction. After increasing the electric current from 16 mA to 50 mA at 300 s, the volume increases more during one cycle than it decreases during the other, as can be explained by the formation of electrolytic gas: Hydrogen and oxygen formed on the working electrodes displace the electrolyte solution from the shell of the electro-compression-permeability cell to the liquid reservoir on the scale. Consequently, the measurements are analyzed only for currents of 16 mA, using the constant value of the electric potential difference, which is measured approximately 30 s after reversing the electric current.

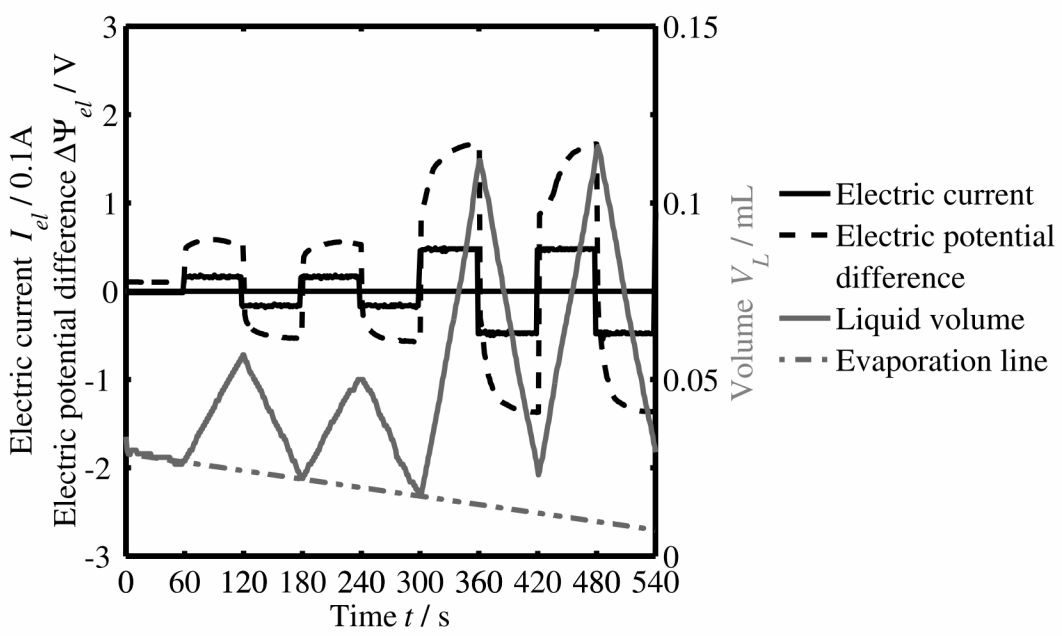

Figure 3-31: Electric current I_{el}, potential difference $\Delta\Psi_{el}$, and liquid volume V_L as measured during the electroosmosis.

For pH values below the IEP, the particles carry a positive surface charge. The negative counter-ions are driven towards the positive electrode, which is at the upper side of the PB for a positive gradient of the electric potential. Since the resulting flow is negative, C_{12} is negative below the IEP and positive above. The measurements agree well with the values calculated from the capillary model (see figure 3-32). The electroosmosis coefficient is reduced upon compression, as can be explained from the lower geometry ratio. Thinner and longer capillaries have a higher flow resistance and the driving gradients are smaller. Also the small modulus of the electroosmotic coefficient at low pH values is caused by the low geometry ratio. The maximum of the absolute value of C_{12} is caused by a relatively high geometry ratio and a relatively high zeta potential.

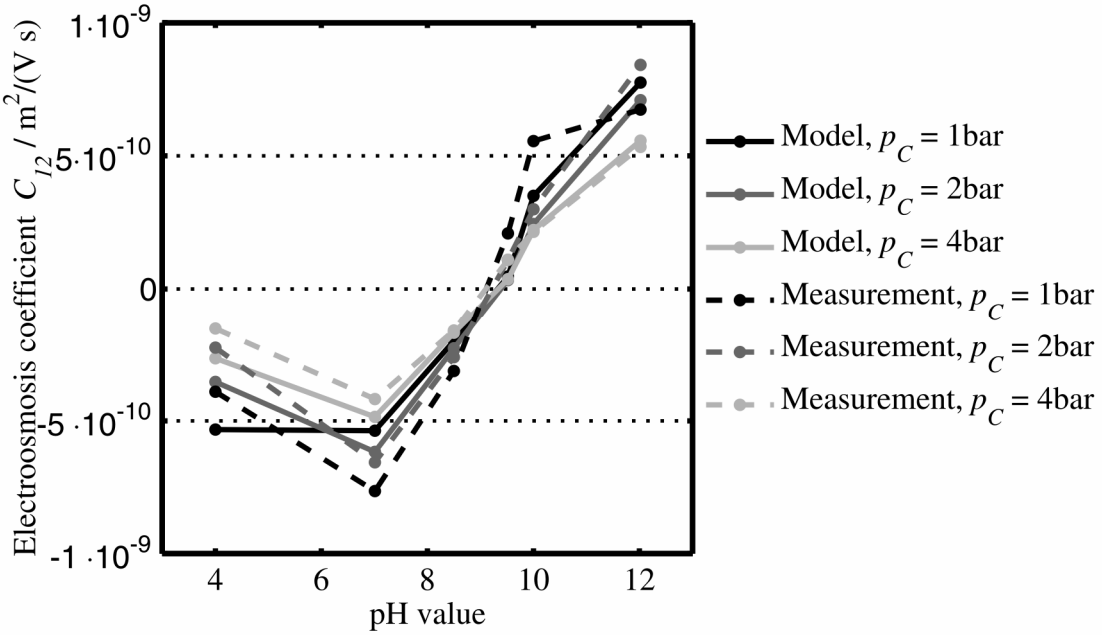

Figure 3-32: Electroosmosis coefficient C_{12} of the PBs consisting of Disperal® depending on the pH value at an ionic strength of 0.02 mol/L as resulting from calculations and measurements for different compressive loads p_C.

The same dependency of the electroosmosis coefficient on the pH value and on the compression is observed for Disperal 20® and Disperal 40® (see figure 6-1 and figure 6-2 in the appendix). Again, the model correlates well with the measurements. Since the geometry ratio is higher for Disperal 20® than for Disperal®, also a higher electroosmosis coefficient results. For Disperal 40®, the electroosmosis coefficient is higher than for Disperal® and smaller than for Disperal 20®, which is explained with the geometry ratio: A higher geometry ratio indicates thinner capillaries and smaller gradients. Increasing the ionic strength does not have a clear influence on the electroosmosis coefficient (see figure 3-33) because of two counteracting effects, namely a reduction of the zeta potential and an increased geometry ratio. Like for the variation of the pH value, the electroosmosis ratio is smallest for Disperal®, medium for Disperal 40® and highest for Disperal 20® (see figure 6-3 and figure 6-4 in the appendix). An increased compression results in a smaller absolute value of the electroosmosis coefficient due to the smaller geometry ratio.

The effects of varying the pH value, the ionic strength, the compressive load, and the particle size on the electroosmotic flow in PBs cam be explained with the capillary model.

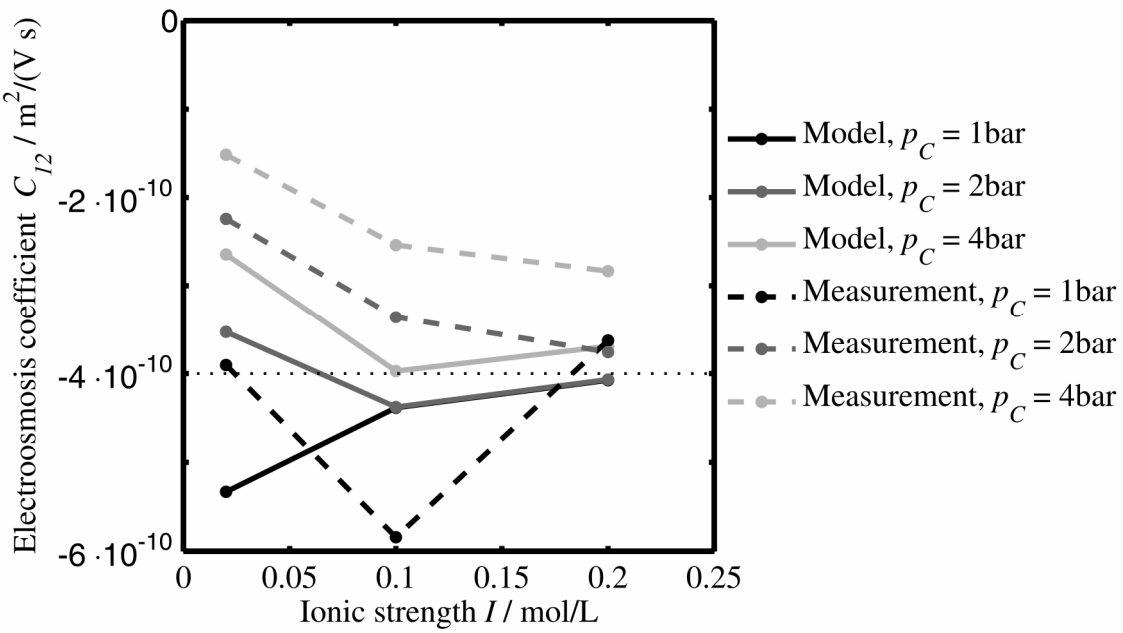

Figure 3-33: Electroosmosis coefficient C_{12} of the PBs consisting of Disperal® depending on the ionic strength I at a pH value of 4 as resulting from calculations and measurements for different compressive loads p_C.

3.3.10 Streaming current

The streaming current is the charge transport that results when a pressure-driven flow shears off the counter-ions from the charged particles in the PB. The streaming current is not measured in the electro-compression-permeability cell since the streaming current coefficient C_{21} equals the electroosmosis coefficient due to Onsager's relation of irreversible thermodynamics. Accurately measuring the streaming current would require collecting all ions on electrodes with a negligible concentration-polarization and negligible electric resistance. The electrodes should cover the faces of the PB and should be connected to an amperemeter with a picoampere resolution. This measurement technique is not implemented in the electro-compression-permeability cell.

3.3.11 Streaming potential

The streaming potential $\Delta\Psi_{Str}$ is the difference of the electric potential that builds up in the PB if its inlet and outlet face are not connected electrically, so that the net electric current I_{el} in equation (2-15) is zero. The streaming potential coefficient, which is defined as the ratio of the electric potential to the hydraulic potential, is then obtained with Onsager's relation and equations (3-13) as

$$C_{SP} = \frac{\Delta\Psi_{Str}}{\Delta p} = -\frac{C_{12}}{C_{22}} = -\frac{\varepsilon\varepsilon_0\zeta}{\eta C_{22,Cap}}. \qquad (3\text{-}14)$$

Alternatively, the streaming potential is measured with the point-shaped measuring electrodes in the electro-compression-permeability cell. As discussed in chapter 3.1.1, the measuring electrodes are prone to concentration polarization, leading to a potential difference between the measuring electrodes even without applying an external hydraulic or electrical gradient. Furthermore, the concentration polarization changes during the experiment (see figure 3-34). However, the streaming potential is identified as the step response of the electric potential difference $\Delta\Psi_{el}$ to a change of the externally applied pressure difference. The resulting streaming potential is proportional to the pressure step.

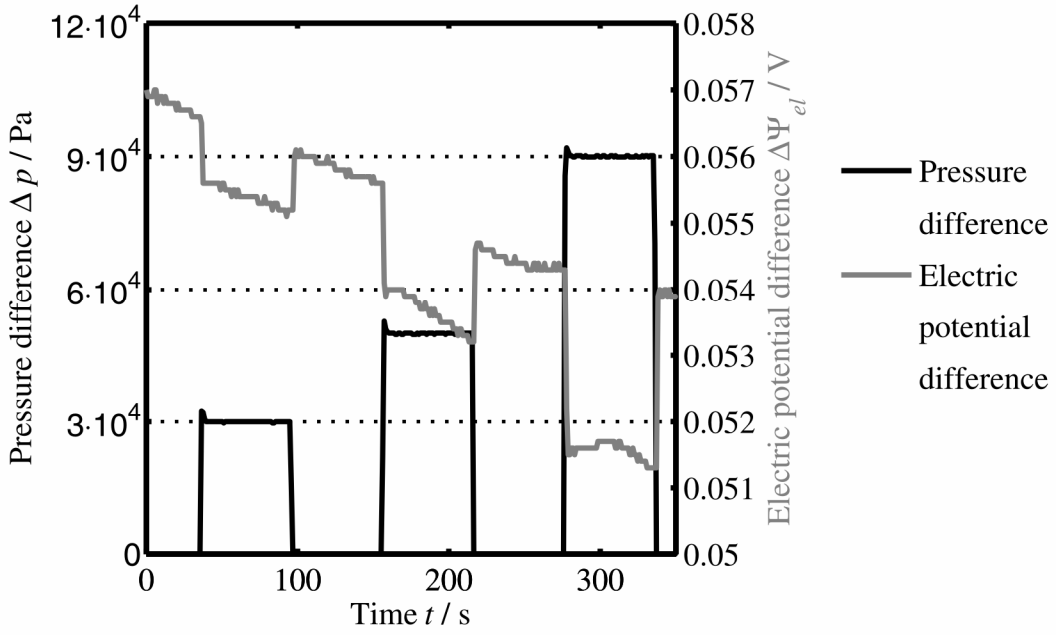

Figure 3-34: Pressure difference Δp and electric potential difference $\Delta\Psi_{el}$ as measured during the electroosmosis.

The measured streaming potential coefficients correlate with the predictions of the capillary model (see figure 3-35 and figure 3-36). The streaming potential coefficient depends on the pH value, similar to the electroosmosis coefficient, but with an opposite algebraic sign: Above the IEP, the positively charged counter-ions accumulate a positive charge at the downstream side of the PB when the ions are sheared off by the flow. A negative pressure gradient thus builds up a positive electric potential gradient.

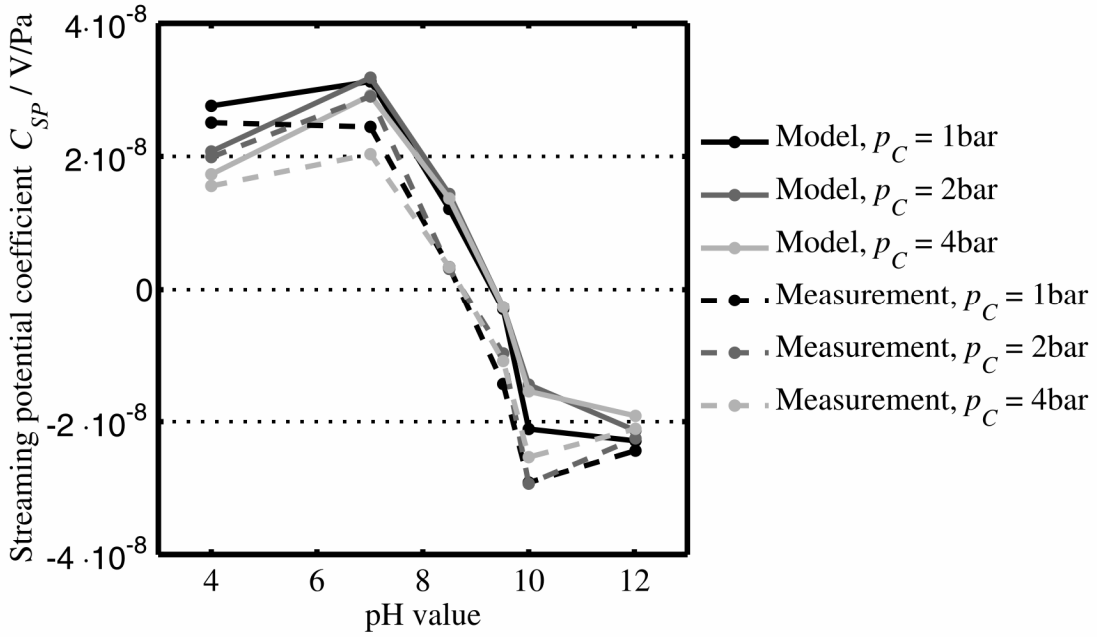

Figure 3-35: Streaming potential coefficient C_{SP} of the PBs consisting of Disperal® depending on the pH value at an ionic strength of 0.02 mol/L as resulting from calculations and measurements for different compressive loads p_C.

A stronger compression leads to a smaller modulus of the streaming potential coefficient (see figure 3-35) because of the characteristic functions of C_{12} and C_{22}. This also explains why the modulus of the quotient is smaller above the IEP than below. However, the dependency of the streaming potential coefficient on the compression is less pronounced than for the electroosmosis coefficient because both C_{12} and C_{22} decrease with increasing compression. The deviations between the measurements and the model are caused by measuring inaccuracies, probably caused by concentration polarization combined with small signals that are in the range of the voltmeter‘s accuracy. The streaming potential coefficient increases with increasing particle size, as can be seen from comparing the values for Disperal® and Disperal 20® (see figure 6-5 in the appendix). The streaming potential coefficient for Disperal 40® is similar to the one for Disperal 20® since the influence of the increasing particle size is compensated by the effect of the decreasing porosity (see figure 6-6 in the appendix).

The streaming potential coefficient decreases with increasing ionic strength because of the decreasing zeta potential and the increasing capillary conductivity (see figure 3-36). At higher ionic strengths, the Debye length is smaller, so that fewer ions are

dragged along by the fluid flow. Furthermore, the electric conductivity of the liquid is higher, so that a smaller electric field is sufficient to compensate the streaming current. Again, the compressive load has no strong influence on the streaming potential coefficient. The smallest streaming potential is observed for Disperal® and the coefficients are similar for Disperal 20® and Disperal 40® (see figure 6-7 and figure 6-8 in the appendix).

Also for the streaming potential, the capillary model explains the influences of changing the pH value, the ionic strength, the compression, and the particle size.

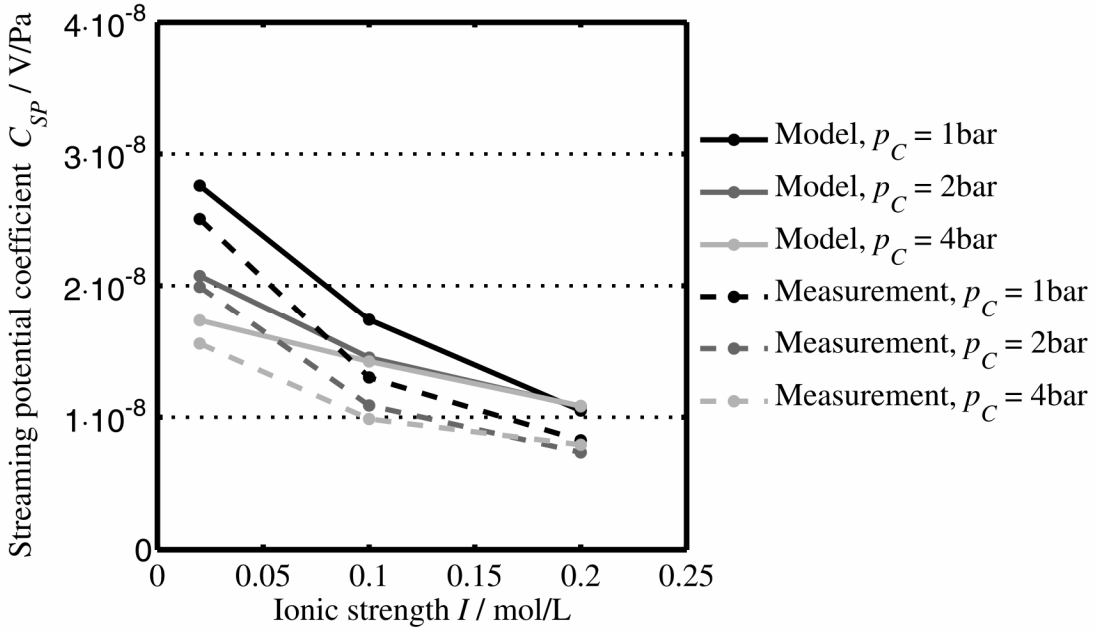

Figure 3-36: Streaming potential coefficient C_{SP} of the PBs consisting of Disperal® depending on the ionic strength I at a pH value of 4 as resulting from calculations and measurements for different compressive loads p_C.

3.3.12 Electroviscous flow retardation

The electroviscosity ratio is introduced to quantify the apparent increase of the permeate's viscosity, which is caused by the electrohydrodynamic effects. Imagine a PB that is hydraulically permeated while the faces are short-circuited by an external connection, so that no streaming potential and no electroosmotic backflow evolve. If the short-circuiting is now cut, the flow rate is reduced by the electroviscosity ratio

$$\frac{\eta_{app}}{\eta} = \frac{C_{11}}{C_{11} - \frac{C_{12} \cdot C_{21}}{C_{22}}}, \qquad (3\text{-}15)$$

with the apparent viscosity η_{app}. The calculated electroviscosity ratio has a minimum at the IEP, where it is close to the theoretical value of 1, meaning that the apparent viscosity equals the real viscosity of the liquid in the pores (see figure 3-37). Above and below the IEP, electroviscosity ratio increases because the pressure-driven flow is retarded by the electrokinetic effects. The electroviscosity ratio increase with increasing compression because a bigger part of the flow takes place within the EDL if the pores are smaller. This also explains why the electroviscosity ratio is smaller above the IEP then below. Theoretically, the electroviscosity ratio should be higher for smaller particles, but this is not evident from the data.

As expected, the electroviscosity ratio decreases with increasing ionic strength because of the decreasing Debye length and because of the increasing porosity (see figure 3-38). Again, the electroviscosity ratio increases with increasing compression and the particle size has no clear influence.

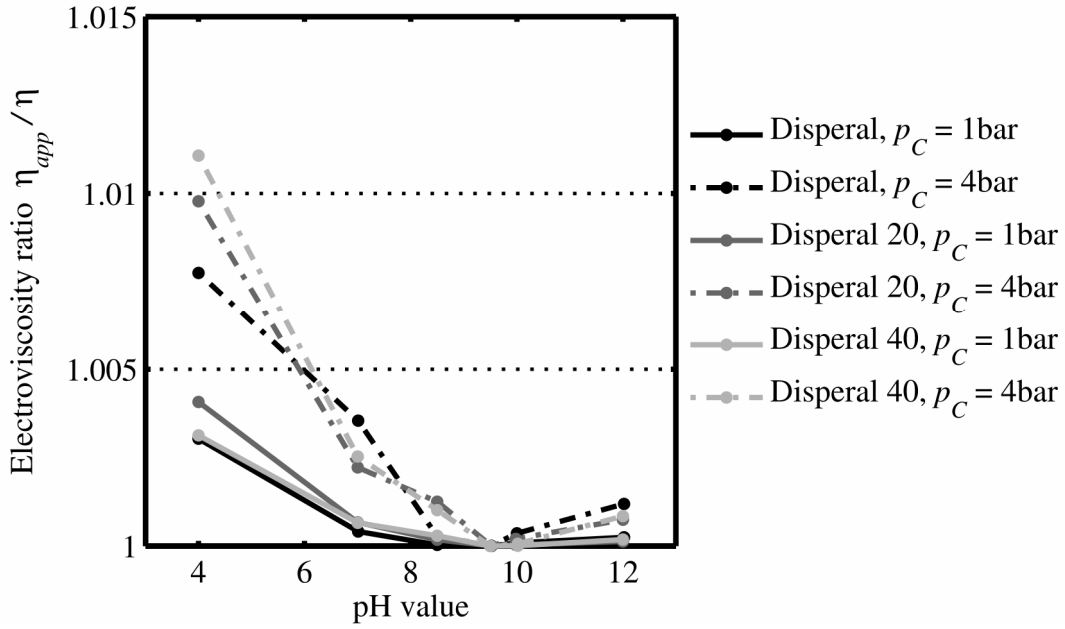

Figure 3-37: Electroviscosity ratio η_{app}/η for the PBs depending on the pH value at an ionic strength of 0.02 mol/L for different compressive loads p_C and different materials.

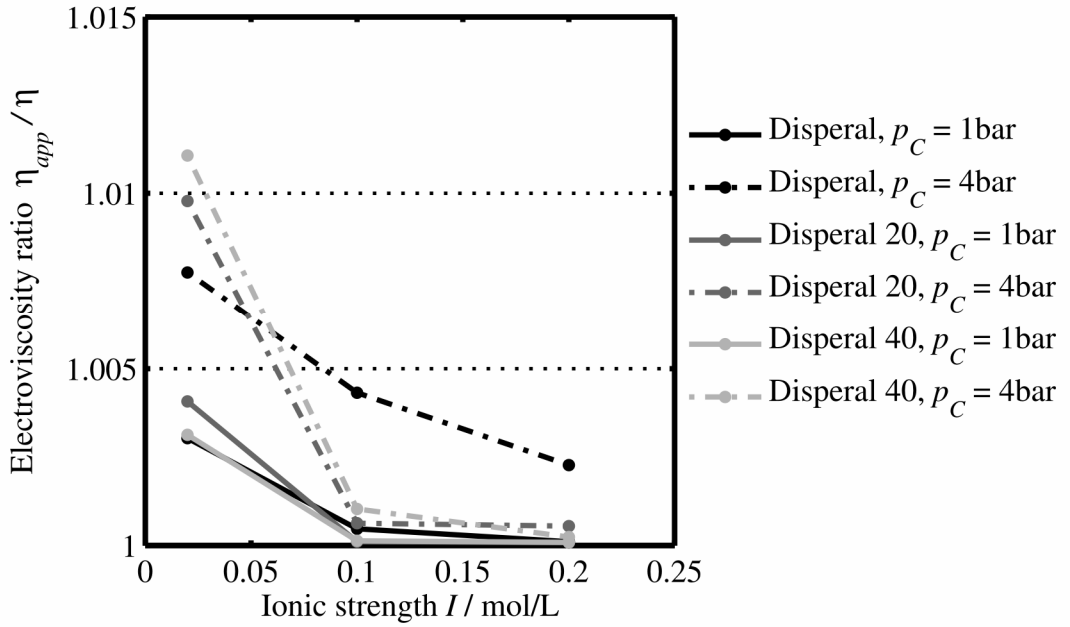

Figure 3-38: Electroviscosity ratio η_{app}/η for the PBs depending on the ionic strength I at a pH value of 4 for different compressive loads p_C and different materials.

Within the experimental range, the electroviscosity ratio is in the order of 1%. Its influence on the hydraulic permeability of the packed beds can thus be neglected in this study. However, it can be significantly stronger for smaller ionic strengths.

3.3.13 Influence of the membranes on the electrohydrodynamic transport

Inconveniently, the EHT in PBs cannot be investigated without the effect of the membranes. The influence of the membranes on the hydraulic permeability C_{11} can be neglected, as shown in chapter 3.3.4. The contribution to the electroosmotic flow, streaming current and streaming potential is evaluated by the following theoretical approach. The total streaming potential of the PB and the two membranes results from the superposition of their contributions as

$$\Delta\Psi_{Str} = \Delta\Psi_{Str,PB} + 2\Delta\Psi_{Str,M}, \tag{3-16}$$

with the streaming potential of the PB

$$\Delta\Psi_{Str,PB} = -\frac{\varepsilon_{rel}\varepsilon_0\zeta_{PB}}{\eta C_{22,L}\left(1+2Du_{PB}\right)}\Delta p_{PB}, \tag{3-17}$$

the streaming potentials of the membranes

$$\Delta\Psi_{Str,M} = -\frac{\varepsilon_{rel}\varepsilon_0\zeta_{M}}{\eta C_{22,L}\left(1+2Du_{M}\right)}\Delta p_{M}, \tag{3-18}$$

the zeta potentials ζ_M and ζ_{PB}, the Dukhin numbers Du_M and Du_{PB}, and the pressure differences Δp_M and Δp_{PB} for the membranes and the PB [Lyklema, J. 2006]. The zeta potentials of the membranes and the PB are in the same order of magnitude and the same is assumed for the Dukhin numbers. Since the ratio of the pressure differences equals the ratio of the flow resistances, the pressure difference in the membranes is negligible, as is the membranes' contribution to the streaming potential.

The situation is more complicated for the electroosmotic flow, where the layers can be thought of as pumps in a series connection. The flow rates in the layers

$$\dot{V}_L = \frac{\Delta p_{EO,Max} - \Delta p}{\Delta p_{EO,Max}} \dot{V}_{EO,Max}, \qquad (3\text{-}19)$$

are identical and the sum of the pressure differences of all three layers equals zero. For each layer, $\dot{V}_{EO,Max}$ and $\Delta p_{EO,Max}$ depend on the structure, the zeta potential and the ionic strength. This makes the estimation of each layer's contribution rather complicated. Instead, it is easier to reflect on the streaming current coefficient, which equals the electroosmosis coefficient due to Onsager's relation. The streaming current coefficient refers to the ions dragged along by the pressure-driven flow, which has the same flow rate in the layers. The streaming velocities should be similar due to the similar porosities of the layers. Since the Debye lengths of the layers are identical and the zeta potentials are in the same order of magnitude, the layers' contributions to the streaming current should be related to the layers' thicknesses. Since the membranes are much thinner than the PB, their contribution to the streaming potentials and thus electroosmotic flow should be negligible.

The electroviscous effect, which is caused by the electroosmotic counter-flow due to the streaming potential, is related to the product of these. The contribution of the membranes can be neglected since both factors are small.

3.4 Conclusions

The experimental results show that fluid flow and charge transport in nanoporous PBs are closely interrelated because of the formation of EDLs on the surface of the particles. This so-called EHT depends on the particle charge, the ionic strength, the compressive load, and the particle size. The porosities of the PBs, which are formed by

filtration of colloidal suspensions of boehmite particles with different particle sizes, are determined by the particle charge, the ionic strength of the suspension, and the compressive load acting on the PB. For a constant ionic strength of 0.02 mol/L, the porosity shows a maximum around the IEP, which is caused by the agglomeration of the particles. For a constant pH value of 4, the porosity increases with increasing ionic strength because of the shorter range of the electrostatic repulsion. However, for agglomerated suspensions, a further increase of the ionic strength has only a small effect. A stronger compression causes a lower porosity at all pH values, ionic strengths, and particle sizes. This effect is stronger for agglomerated structures, as attributed to a deformation of the agglomerates and a shrinking of the inter-agglomerate pores. For PBs consisting of Aeroxide P25®, the porosity is relatively high at all pH values, which is caused by the sintered agglomerates that cannot be broken during the dispersion. The sintered agglomerated also effect a lower compressibility in comparison to the boehmite particles.

For each material and particle size, the permeability C_{11} is an exponential function of the porosity and thus depends on the pH value, the ionic strength, and the compression. For colloidal particles, the porosity has a significantly stronger influence on the permeability than for macroscale particles, which seems reasonable if you think of the PBs as an inhomogeneous structure with relatively large inter-agglomerate pores: Decreasing the porosity, for example by increasing the compressive load, primarily acts on the inter-agglomerate pores. Since these are accountable for the major part of the fluid flow, the flow rate strongly decreases even if the intra-agglomerate porosity is still high. Furthermore, PBs consisting of smaller particle have a lower permeability because, assuming geometrical similarity, the pore size would be proportional to the particle size. The membranes' contribution the hydraulic resistance is found to be below 1.5% in this study.

The electric conductivity C_{22} of a PB decreases with decreasing porosity because the ions have to migrate through the porous structure. The conductivity comprises the liquid conductivity and the surface conductivity of the particles. The contribution of the surface conductivity, as quantified by the Dukhin number Du, is relatively small at the IEP, since the surface conductivity depends on the presence of an EDL. The

Dukhin number increases with decreasing particle size because of the increasing specific surface area. It also increases with increasing compression because of the reduced distance between the particles. A higher ionic strength causes a higher liquid conductivity and thus an increased conductivity of the PBs, while the Dukhin number is reduced.

A new capillary model is proposed to describe the EHT in complex porous structures. The PBs are represented by hypothetical sets of straight parallel capillaries with a cross-section-to-length ratio that is related to the geometry of the PBs by the geometry ratio. The geometry ratio and the conductivity of the capillaries are calculated by assuming that the electric current and the Dukhin number are equivalent to the PB. A stronger compression and a smaller particle size cause a reduction of the geometry ratio and an increased capillary conductivity. Increasing the ionic strength leads to an increased capillary conductivity and a higher geometry ratio.

The capillary model permits to predict the electroosmosis coefficient, which agrees with the measurements carried out in the electro-compression-permeability cell. The electroosmosis coefficient C_{12} is negative below the IEP and positive above. Its absolute value shows a maximum at a pH value of 7.5, which is caused by a relatively high geometry ratio and a relatively high zeta potential. C_{12} is reduced upon compression, as can be explained from the lower geometry ratio. Increasing the ionic strength does not have a clear influence on the electroosmosis coefficient because of two counteracting effects, namely the reduced driving force and the reduced hydraulic resistance. According to Onsager's relation, the electroosmosis coefficient equals the streaming current coefficient.

The streaming potential, which is identified as the step response of the electric potential difference to a change of the externally applied pressure difference, is proportional to the pressure step and agrees with the predictions of the capillary model. The streaming potential coefficient C_{21} depends on the pH value, similar to the electroosmosis coefficient, but with an opposite algebraic sign. It decreases with increasing ionic strength because of the decreasing zeta potential and the increasing

capillary conductivity. The modulus of the streaming potential coefficient increases with increasing particle size and decreasing compression.

The electroviscosity ratio η_{app}/η has a minimum at the IEP, where the apparent viscosity equals the real viscosity of the liquid in the pores. Above and below the IEP, the electroviscosity ratio increases because the pressure-driven flow is retarded by the electrokinetic effects. A stronger compression effects a higher electroviscosity ratio because a bigger part of the flow takes place within the EDLs if the pores are smaller. As expected, the electroviscosity ratio decreases with increasing ionic strength because of the decreasing Debye length and the higher liquid conductivity. Within the experimental range, the electroviscosity ratio is in the order of 1%.

Theoretical considerations show that also the membranes' effect on the electroosmotic flow, the streaming potential, and the electroviscous effect can be neglected.

4 Simulation

Although the formation and permeation of packed beds (**PBs**) are encountered in many processes such as filtration, the influence of the pore structure on the performance is not fully understood. The numerical simulation of the agglomeration of the particles, the filtration process, and the pressure-driven permeation of the PBs gives insight into the underlying physics and helps to comprehend the influence of the pH value, the ionic strength, the particle size, and the compressive load on the pore structure and the hydraulic permeability. However, simulations including full DLVO interactions and hydrodynamics are rarely performed because of the high computational demands. This limitation also determines the choice of the simulation methods, as explained below. Subsequently, the chosen simulation methods are explained in detail. The validation of the simulation methods is followed by the presentation of the numerical results.

4.1 Choice of the simulation methods

The simulation of the particle agglomeration should include Brownian motion and the inter-particle forces as described by the Derjaguin-Landau-Verwey-Overbeek (**DLVO**) theory. Furthermore, the simulation of the liquid phase should include thermal noise and reproduce the full hydrodynamics. The methods should be mathematically simple to allow for higher numbers of particles with limited simulation time capacity. These requirements limit the applicability of all simulation methods:

- Solving the balance equations with finite elements methods or finite differences methods requires a meshing of the computational domain, which is mathematically a complex problem for moving particles and for PBs [Harting, J., et al. 2006].
- Brownian dynamics includes Brownian motion, but the hydrodynamics is reduced to a simple Stokes force [Hütter, M. 1999, Kim, J. C. and Auh, K. H. 1999, Melrose, J. R. and Hexes, D. M. 1993].
- Dissipative particle dynamics comprises hydrodynamics and Brownian motion, but the calculation of the particle interactions is very time consuming [Hecht, M. 2007].

- Stokesian dynamics includes multiparticle hydrodynamic interactions, but the numerical effort increases with the third power of the particle number [Brady, J. F. and Bossis, G. 1988].
- The lattice Boltzmann (LB) method does not include Brownian motion intrinsically; however, some recent approaches also introduce thermal noise [Adhikari, R., Stratford, K., Cates, M. E. and Wagner, A. J. 2005, Usta, O. B., et al. 2005].
- Molecular dynamics (**MD**) simulations are ideal for simulating particle interactions, but simulations of suspensions that resolve the water molecules and ions are computationally far too demanding. Even if the water is replaced by a background friction and stochastic fluctuations and only the ions are simulated explicitly, the simulation would be limited to only a few colloidal particles by the power of today's computers.
- Stochastic rotation dynamics (**SRD**) includes thermal noise and hydrodynamic interactions, but it does not account for particle interactions.

Consequently, a combination of simulation methods is used:

- An MD simulation of the colloidal particles and inter-particle forces is coupled to an SRD simulation of the fluid to simulate the agglomeration of the particles and the formation of the PBs. MD is the standard tool for simulating the motion of discrete particles, based on Newton’s equation. Inter-particle forces are easily implemented and thermal fluctuations can be controlled with a simple Monte Carlo thermostat [Hecht, M., et al. 2005].
- The SRD simulation of the fluid is an efficient method for simulating hydrodynamics and Brownian motion in fluids that is easy to implement and has low demands for computational power. It is based on a robust algorithm that runs stable even for high particle concentrations and the resolution of the SRD hydrodynamics can be chosen within certain limits [Hecht, M., et al. 2005].
- Lattice Boltzmann simulations of the resulting PBs reveal their permeabilities. The LB method is the standard tool for fluid flow in porous structures. Even complex boundaries do not significantly increase the computational time since the boundary conditions are imposed locally [Chen, S., et al. 1994]. Further-

more, LB simulations are easy to parallelize because the Boltzmann equation only requires information of the nearest neighbor nodes [Aaltosalmi, U. 2005]. In the context of this study, the LB simulations can be seen as a Navier-Stokes solver based on a very simple algorithm that is capable to cope with complex flow domains [Benzi, R., et al. 1992, He, X. and Luo, L.-S. 1997, Dardis, O. and McCloskey, J. 1998]. LB simulations are applicable to liquid flow in nanoporous PBs since the relevant characteristic numbers, i.e. the Reynolds number Re, the Mach number Ma and the Knudsen number Kn, are well below one for both the experiment and the simulation.

The following subchapters give a detailed description of these methods and the boundary conditions used to implement the formation of PBs.

4.2 Simulation domain and boundary conditions

The simulation starts with 2000 solid particles stochastically distributed in the simulation space. To realize a mass concentration of 10%, which is consistent with the experiments, the system dimensions are set to 19.2 particle diameters in the horizontal directions and 76.8 particle diameters in the vertical direction, which is the direction of compression and permeation. The closed boundaries in the vertical direction exert a Hooke force on overlapping particles, while the boundaries in the horizontal directions are periodic.

The particles agglomerate until an equilibrium structure is reached (see figure 4-1, left). This is controlled by analyzing the temporal development of the pair correlation function G. Subsequently, the filtration starts by incrementally approaching the horizontal boundaries of the MD space towards each other and thus exerting a Hooke force on the particles. Consequently, the MD particles build up filter cakes on the top and bottom boundary conditions, like on the membranes in the electro-compression-permeability cell (see figure 4-1, center). The filter cakes finally merge and get compressed between the membranes until the Hooke force, which is carried by the particle network, reaches the desired compressive load p_C (see figure 4-1, right).

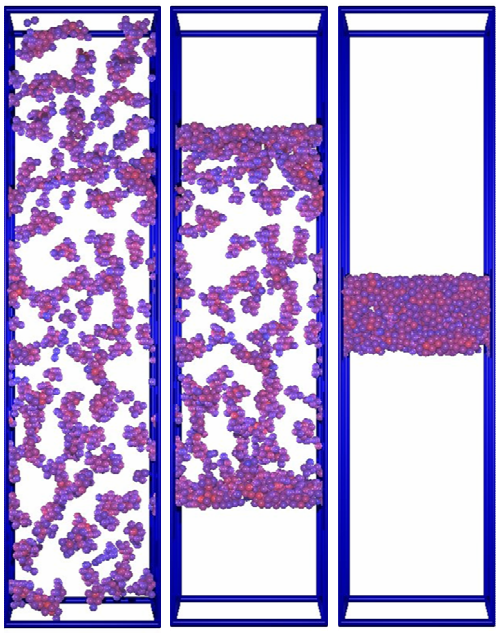

Figure 4-1: MD particles in the simulation space at different stages of the simulation (left: agglomeration, center: filtration, right: compression). The SRD particles and the MD boundaries are not visible.

After the PBs reach a constant thickness, the positions of the particles are fixed and PBs are mapped with a cubic lattice. The hydraulic permeabilities of the PBs are determined with Lattice Boltzmann simulations.

4.2.1 Molecular dynamics simulation of the solid particles

The motion of the colloidal solid particles is computed with an MD simulation, where Newton's equation of motion

$$\boldsymbol{F}_m = m_m \ddot{\boldsymbol{x}}_m, \tag{4-1}$$

is solved with a Velocity Verlet algorithm [Allen, M. P. and Tildesley, D. J. 1987], including the mass m_m and the acceleration $\ddot{\boldsymbol{x}}_m$ for each particle m. The force $\boldsymbol{F}_m$ includes the van-der-Waals attraction (see equation (2-6)), the Coulomb repulsion (see equation (2-7)), the contact force, the lubrication force (see below), the transversal friction forces, and gravity. In this study, a Hamaker constant is set to $4.76 \cdot 10^{-20}$ J [Hecht, M., et al. 2005]. The particle interaction are simplified by assuming spherical solid particles. To reduce the computational effort further, the MD simulation space is mapped with a cubic grid that has a cell length of two particle diameters and the particle interactions are restricted to MD particles in the same and adjacent cells. In

order to reduce the potential gradients and thus expand the simulation time step, the Born repulsion is replaced by the weaker Hertzian contact force, with the potential

$$\Psi_{Hertz} = K_{Hertz} \cdot \left(2d_p - d_C\right)^{2.5}, \qquad (4\text{-}2)$$

for $d_C = \left|\boldsymbol{x}_m - \boldsymbol{x}_n\right| < d_p$, with the center-to-center distance d_C, the particle diameter d_P, and the positions $\boldsymbol{x}_m$ and $\boldsymbol{x}_n$ of the particles m and n. In this study, the Hertz constant is arbitrarily set to 0.1, which makes the influence of the overlapping on the structure of the PB small. If the Hertz constant K_{Hertz} was determined from the realistic elastic modulus of the particles, the MD time step would still have to be very small since the particle collision has to be resolved with about 20 time steps to conserve energy and momentum. On the other hand, the Hertz constant has to be large enough so that the particles do not overlap more than approximately 0.1 particle radii [Harting, J., et al. 2006]. The above-mentioned forces are cut-off for surface-to-surface distances below 0.005 radii to circumvent the singularity of the van-der-Waals potential for direct contact. The gap between the cut-off radius and the particle surface is modeled by a Hooke law with a coefficient D_H of $7.7 \cdot 10^6$ N/m. The coefficient is chosen such that the potential is steadily differentiable at the transition point between the Hooke law and the DLVO potential.

Although the forces seem to be modeled arbitrarily, the stability of the suspensions against agglomeration is accurately described. This can be seen in figure 4-2, which compares the model potentials to the real potentials for illustrative combinations of zeta potential ζ and ionic strength I for a particle diameter of 30 nm. The potentials agree well in the distance range that determines the agglomeration, which is here above 1.015 d_P particle radii. For the stable suspension with a zeta potential of 60 mV and an ionic strength of 0.02 mol/L, the particles cannot overcome the energy barrier, so that they do not feel the deviation of the modeled potential from the DLVO potential Ψ_{DLVO} in the primary minimum. In the other examples, the particles form primary agglomerates. The stability of primary agglomerates is independent of the depth of the primary minimum as long as it is deeper than 10 $k_B T$ and no external shear forces are applied. The latter could lift particles out of an even deeper minimum.

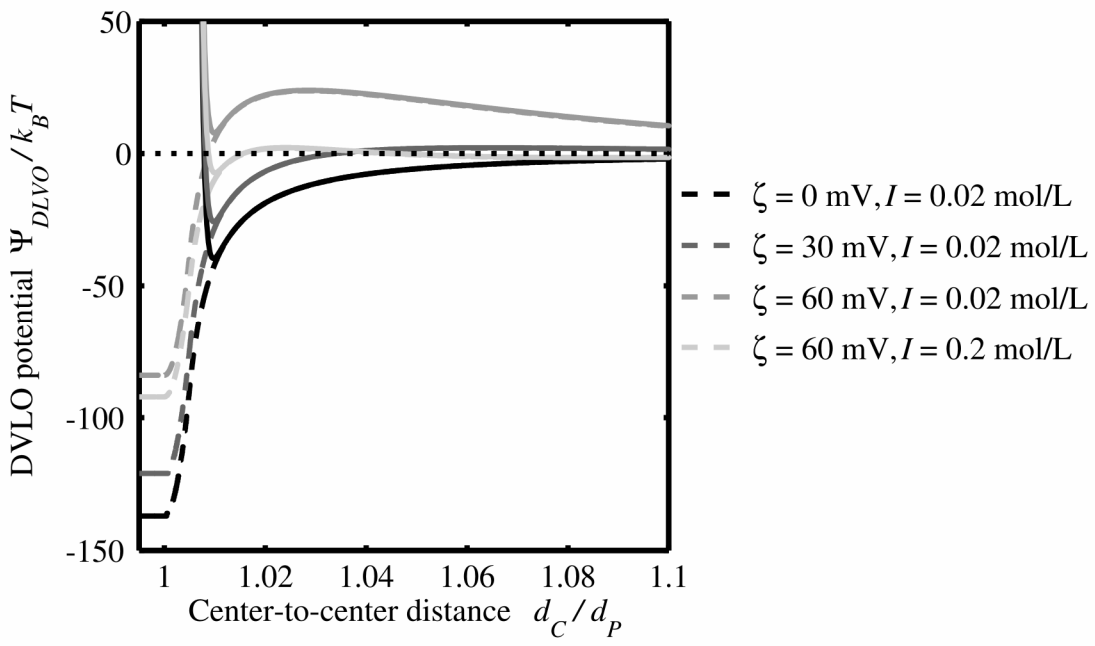

Figure 4-2: DLVO potentials Ψ_{DLVO} as predicted by the DLVO theory (solid lines) and as modeled in the simulations (dashed lines) for particles with a diameter of 30 nm at illustrative combinations of the zeta potential ζ and the ionic strength I.

Long-range hydrodynamic interactions between the particles act via the motion of the fluid particles that are simulated with the SRD simulation introduced in chapter 4.2.2. However, the SRD simulation does not account for the resistance of the fluid against being squeezed out of the closing gap between two approaching particles. This shortcoming is corrected by the dissipative lubrication force [Hecht, M., et al. 2007]

$$\boldsymbol{F}_{Lub} = -\boldsymbol{v}_{rel,\perp} \frac{6\pi\eta c_{Lub}}{d_C - d_P + r_{CO,i}} \left(\frac{d_P}{4}\right)^2, \qquad (4\text{-}3)$$

with the relative velocity $\boldsymbol{v}_{rel,\perp}$ projected on the connecting line between the particle centers and with the dynamic viscosity of the liquid η. The lubrication factor c_{Lub} is arbitrarily set to 0.2 and the inner cut-off radius $r_{CO,i}$ is set to 0.005 particle radii to circumvent the singularity for touching particles. Since the force decays for large particle distances, it is cut off for distances larger than the outer cut-off radius $r_{CO,o}$ of two particle radii to reduce the numerical effort.

The dissipative forces reduce the kinetic energy of the particles, while the reduction of the potential energy upon agglomeration releases kinetic energy. The resulting change of temperature would change the viscosity of the fluid. Therefore, the temperature of the MD particles is controlled by means of a Monte Carlo thermostat, which is

described in [Hecht, M., et al. 2005]. The thermostat is similar to one described in [Allen, M. P. and Tildesley, D. J. 1987], but it only scales the relative velocities while conserving the mean velocity in each SRD cell, which is introduced in the following.

4.2.2 Stochastic rotation dynamics simulation of the fluid

The SRD method introduced by Malevanets and Kapral [Malevanets, A. and Kapral, R. 1999] is used for simulating the fluid because it intrinsically contains thermal fluctuations, has low demands for computational time and is applicable to colloidal suspensions [Inoue, Y., et al. 2002, Winkler, R. G., et al. 2004, Hecht, M., et al. 2006, Padding, J. T. and Louis, A. A. 2006, Hecht, M., et al. 2007]. The fluid is coarse-grained to virtual fluid particles since a molecular resolution is not required. SRD is based on calculating the continuous position of these virtual fluid particles m at the time $t+\Delta t_{SRD}$ from the previous positions $\boldsymbol{x}_m(t)$ and velocities $\dot{\boldsymbol{x}}_m(t)$ as

$$\boldsymbol{x}_m(t+\Delta t_{SRD}) = \boldsymbol{x}_m(t) + \Delta t_{SRD}\dot{\boldsymbol{x}}_m(t) \tag{4-4}$$

Since the SRD particles are pointlike, they cannot collide. Instead, momentum is exchanged in the subsequent collective interaction step, which is depicted in figure 4-3. The SRD particles are sorted into cubic cells k with the mean velocity $\bar{\dot{\boldsymbol{x}}}_k$. The relative velocities of the particles $\dot{\boldsymbol{x}}_{m,rel}(t) = \dot{\boldsymbol{x}}_m(t) - \bar{\dot{\boldsymbol{x}}}_k(t)$ with respect to their average velocity are rotated according to [Ihle, T. and Kroll, D. M. 2003]

$$\dot{\boldsymbol{x}}_m(t) = \bar{\dot{\boldsymbol{x}}}_k(t) + \Omega_{SRD,k}(t)\cdot\left[\dot{\boldsymbol{x}}_m(t) - \bar{\dot{\boldsymbol{x}}}_k(t)\right]. \tag{4-5}$$

The rotation matrix $\Omega_{SRD,k}$ is stochastically chosen for each cell and time step. The calculation of the mean velocity realizes a momentum exchange between the fluid particles. The physical meaning of the mechanism becomes clear if you imagine a cell with nine particles having a mean velocity equal to zero. The fluid in the cell is at rest from a macroscopic point of view and the relative velocities of the particle represent their Brownian motion. If a particle enters the cell, it will set the other particles in motion by contributing to the mean velocity in the cell. The averaging of the velocities thus conserves the momentum in the cell. The high kinetic energy of the new particle is dissipated and thus increases the relative velocities of all particles in the cells and the local temperature.

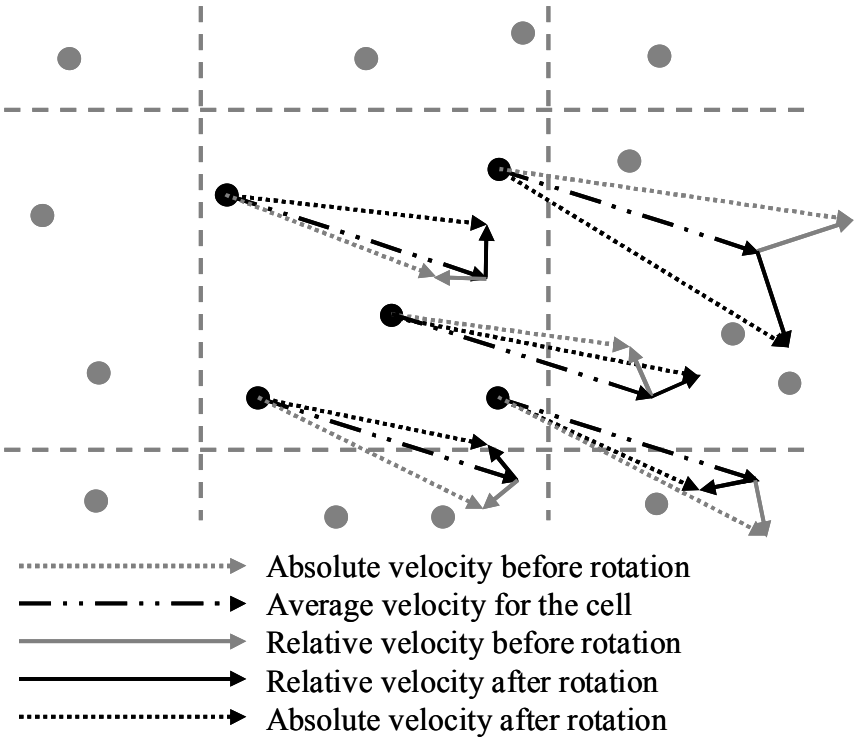

Figure 4-3: Illustration of the propagation and rotation step of the fluid particles in the SRD method.

To reduce the numerical effort, the rotations are restricted to angles of 90° or -90° around the three coordinate axes in this study, as described by the six possible rotation matrices

$$\begin{pmatrix} 1 & 0 & 0 \\ 0 & 0 & 1 \\ 0 & -1 & 0 \end{pmatrix}, \begin{pmatrix} 1 & 0 & 0 \\ 0 & 0 & -1 \\ 0 & 1 & 0 \end{pmatrix}, \begin{pmatrix} 0 & 1 & 0 \\ -1 & 0 & 0 \\ 0 & 0 & 1 \end{pmatrix}, \begin{pmatrix} 0 & -1 & 0 \\ 1 & 0 & 0 \\ 0 & 0 & 1 \end{pmatrix}, \begin{pmatrix} 0 & 0 & 1 \\ 0 & 1 & 0 \\ -1 & 0 & 0 \end{pmatrix}, \text{ and } \begin{pmatrix} 0 & 0 & -1 \\ 0 & 1 & 0 \\ 1 & 0 & 0 \end{pmatrix}.$$

This rotation is a mathematically simple means to exchange momentum between the fluid particles while conserving the total mass, energy, and momentum within each cell. However, other sets of rotation matrices would be possible as well.

The rotation does not affect the mean velocity of each cell, which represents the streaming velocity of the fluid, so that the total momentum and the kinetic energy of the streaming velocity are preserved. Further, the rotation preserves the local temperature in the cell, which is related to the sum of the squared relative velocities. However, energy would be exchanged between the SRD simulation and the MD simulation if the latter had a different temperature, but this is prevented by the thermostat in the MD simulation.

Realistic simulations have to be Galilean invariant, which means that observations are independent of the inertial frame of the observer. This is not fulfilled if the SRD cells are so large that most particles remain in their cell during the streaming step since the resulting correlation of neighboring particles over several time steps breaks if the particles are observed from a moving inertial system with a moving grid.

However, in SRD simulations these correlations are minimized if the length of the SRD cells L_{Cell} is chosen to be at most twice the mean free path of the particles

$$\lambda = \Delta t_{SRD} \sqrt{k_B T / m_{SRD}}, \tag{4-6}$$

with the Boltzmann constant k_B and the temperature $T =$ 295 K. The mass of one SRD particle is given by

$$m_{SRD} = \frac{L_{Cell}^3 \rho_L}{\bar{N}_k}, \tag{4-7}$$

where ρ_L denotes the liquid density and the average number of SRD particles per cell is set to $\bar{N}_k = 60$. Table 4-1 gives the lengths of the SRD cells L_{Cell} used in this study to restore Galilean invariance. Another possibility would be to shift the grid by random vectors with components in the interval between $-L_{Cell}/2$ and $L_{Cell}/2$ before the collision and shift it back after the collision [Ihle, T. and Kroll, D. M. 2003].

4.2.3 Coupling of the solid and fluid simulations

The MD simulation of the solid particles has to be coupled to the SRD simulation of the fluid, so that momentum is transferred between them. The literature discusses different coupling methods that conserve the global momentum:

- Implementing a no-slip boundary condition on the particle surface accurately resolves the local velocity field around the colloidal particles and thus reproduces the short-range hydrodynamic interactions [Inoue, Y., et al. 2002].
- Padding and Louis assume full-slip boundaries on the solid particles and make a correction by modifying the particles' hydrodynamic diameter [Padding, J. T. and Louis, A. A. 2006].

- The fastest and simplest coupling method is to include the solid particles from the MD simulation in the rotation step of the SRD simulation [Falck, E., et al. 2004]. The different masses m_m of the MD and SRD particles are considered by weighting factors when calculating the mean velocities in the cells

$$\dot{\bar{\boldsymbol{x}}}_k(t) = \sum_{m=1}^{N_k(t)} \dot{\boldsymbol{x}}_m(t) m_m \Big/ \sum_{m=1}^{N_k(t)} m_m , \qquad (4\text{-}8)$$

  with the number of fluid and solid particles $N_k(t)$ in the cell k [Hecht, M., et al. 2005]. This accurately reproduces long-range hydrodynamic interactions, as shown for example for sheared suspensions [Hecht, M., et al. 2006] and sedimenting particles [Hecht, M., et al. 2005].

In this study, the simple coupling method is used to reduce the computational effort. Since the coupling only acts between particles within the same cell, the cells must be of a similar size as the solid particles for the solid particles to have a realistic effect on the flow field: a smaller lattice constant would model smaller colloidal particles in the context of the SRD simulation. The cell lengths for the different particle diameters are given in table 4-1.

Since the SRD particles are allowed inside the MD particles, short-range hydrodynamic interactions are not reproduced. This is corrected for by the lubrication force introduced in chapter 4.2.1.

4.2.4 Scaling of the physical parameters

In order to maintain numerical stability, the time step of the simulation has to be significantly smaller then the time required for translating an MD particle by a distance of one diameter. Each force or process in the system has its own characteristic translation time, which depends on the particle diameter d_p as shown by the solid lines in figure 4-4. The smallest characteristic time limits the maximum time step to maintain numerical stability, even if the corresponding process is not the focus of the simulation. For example, the simulation of the macroscopic behavior of a colloidal suspension must also resolve the fast Brownian motion of the MD particles since the latter determines the particles' ability to overcome the energy barrier in the DLVO potential.

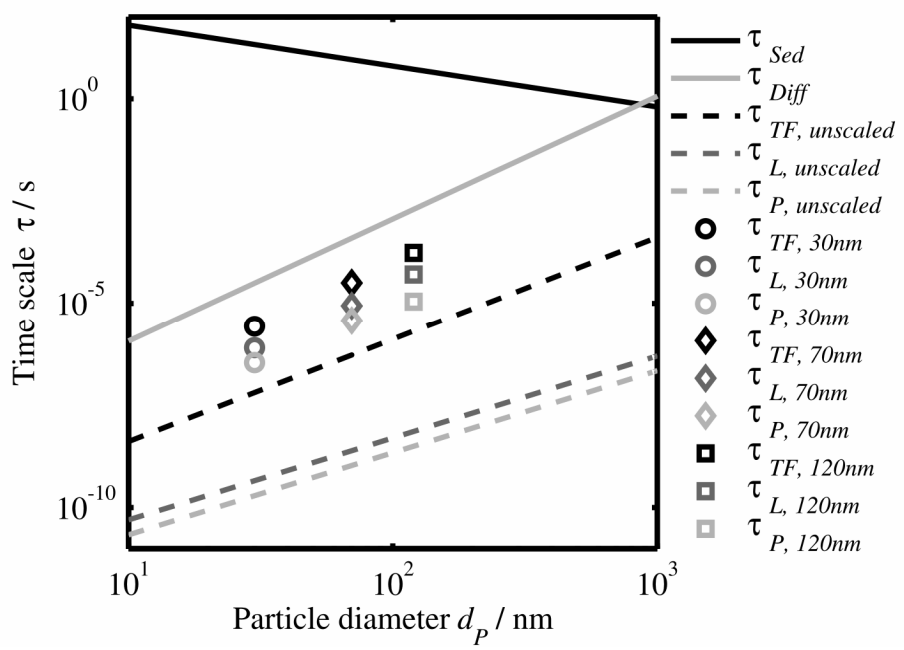

Figure 4-4: Characteristic time scales τ for different forces in the simulation depending on the particle diameter d_P (solid and dashed lines). The symbols give the characteristic times of the scaled forces for particle diameters of 30 nm (circles), 70 nm (diamonds), and 120 nm (squares). The variables are explained in the text below.

A sedimenting particle takes the time τ_{Sed} to cover a distance of one particle diameter. This characteristic time is reciprocal to the Stokes velocity v_{Sed} as

$$\tau_{Sed} = \frac{d_P}{v_{Sed}} = \frac{18\eta}{d_P g\left(\rho_S - \rho_L\right)}. \tag{4-9}$$

It is thus inversely proportional to the particle diameter, with the gravitational constant g and the particle density ρ_S. The time τ_{Diff} it takes a particle to diffuse a distance of one particle diameter depends on the diffusion constant $D = \left(k_b T\right)/\left(3\pi\eta d_P\right)$ and is proportional to the third power of the diameter [Einstein, A. 1956]:

$$\tau_{Diff} = \frac{d_P^2}{2D} = \frac{3\pi\eta d_P^3}{2k_B T}. \tag{4-10}$$

The average velocity of the particles' thermal fluctuations refers to a kinetic energy of $\frac{1}{2}mv^2 = 1.5k_B T$ [Wedler, G. 2007], leading to a characteristic time of

$$\tau_{TF} = \sqrt{\frac{d_P^5 \pi \rho_S}{18 k_B T}}. \tag{4-11}$$

The particle relaxation time

$$\tau_P = \frac{1}{18}\frac{d_P^2 \rho_S}{\eta} \tag{4-12}$$

is the time for a particle to adapt to the flow field of the surrounding fluid. The distortions of the liquid flow field relax with a characteristic time

$$\tau_L = \frac{d_P^2 \rho_L}{2\eta}. \tag{4-13}$$

In colloidal suspensions, the time scale covers a range from several nanoseconds (for the fast processes like momentum transport in the fluid) up to seconds for slow processes like sedimentation. Since the smallest characteristic time determines the maximum simulation time step needed to maintain numerical stability, the numerical effort increases for a decreasing particle size, thus limiting the simulation of colloidal suspensions. For a particle diameter of 30 nm, the resulting time scale difference of 10^{11} cannot be dealt with by today's algorithms and computers.

However, the characteristic times can be modified while maintaining the physical behavior of the suspension if the physical properties of the system are carefully scaled. The scaling must not change the sequence of the characteristic times or bring them close together, as explained in the following. Each time scale ratio represents a characteristic number of the system, for example the Archimedes number $Ar = (9\tau_L)/(2\tau_{Sed})$, the Schmidt number $Sc = \tau_{Diff}/\tau_L$, the Péclet number $Pe = \tau_{Sed}/\tau_{Diff}$. The major physical behavior of the system is not influenced by an alteration of the characteristic numbers as long as they remain much smaller or much larger than one, which means that the two corresponding forces do not compete.

In this study, the values for viscosity, temperature, gravity, and interaction potentials are carefully scaled for each particle diameter as described in the following: The viscous behavior of the fluid results from the stochastic rotation of the relative velocities and thus depends on the rotation algorithm and the simulation parameters.

For the rotation angles of ±90°, the viscosity of the SRD fluid is

$$\eta_{SRD} = \rho_L \left(\frac{L_{Cell}^2}{18\Delta t_{SRD}} \left(1 - \frac{1 - e^{-\bar{N}_k}}{\bar{N}_k} \right) + \frac{k_B T_{SRD} \Delta t_{SRD}}{4 m_{SRD}} \frac{\bar{N}_k + 2}{\bar{N}_k - 1} \right), \tag{4-14}$$

with the temperature T_{SRD} of the SRD fluid {Hecht, 2005 #298}.

To reproduce the realistic diffusion of the solid particles, the diffusion constant in the simulation

$$D_{MD} = \frac{k_B T_{SRD}}{6\pi \eta_{SRD} R}, \tag{4-15}$$

with the gas constant R is identified with the real diffusion constant given in table 4-1. With $\lambda = L_{Cell}/2$ to guarantee Galilean invariance, equations (4-6), (4-7), (4-14) , and (4-15) lead to the SRD time steps and scaling factors given in table 4-1 for each particle diameter. To preserve the sedimentation velocity and diffusion constant, the gravitational constant and the temperature are scaled by the same scaling factor as the viscosity. The DLVO interactions are scaled as well to maintain their ratio to the energy associated to the thermal fluctuations of particles. Consequently, the characteristic times τ_{TF} , τ_L , and τ_P change, while τ_{Sed} and τ_{Diff} remain the same. Also the ratio between τ_L and τ_P is kept constant and the ratios of τ_{TF} to τ_{Diff} and τ_L to τ_{TF} remain well below unity. The characteristic times of the scaled forces are shown for each particle diameter by the symbols in figure 4-4.

The resulting SRD time steps are too large to resolve the motion of the colloidal particles, so that a smaller time step is chosen for the MD simulations. This means that the extensive SRD calculation is applied less often than the MD calculation, which reduces the computational effort substantially.

Table 4-1: Simulation parameters for different particle diameters

Particle diameter d_P / nm	30	70	120
Length of the SRD cells L_{Cell} / nm	25	50	100
Diffusion constant D / m²/s	$1.44 \cdot 10^{-11}$	$6.17 \cdot 10^{-12}$	$3.60 \cdot 10^{-12}$
Scaling factor	$5.66 \cdot 10^{-4}$	$2.828 \cdot 10^{-4}$	$1.414 \cdot 10^{-4}$
SRD time step Δt_{SRD} / s	$1.25 \cdot 10^{-7}$	$1.10 \cdot 10^{-6}$	$8.50 \cdot 10^{-6}$
MD time step Δt_{MD} / s	$1 \cdot 10^{-10}$	$1 \cdot 10^{-9}$	$1 \cdot 10^{-9}$

4.2.5 Lattice Boltzmann simulation of the permeation

The lattice Boltzmann (LB) method is a mesoscopic approach to simulate the motion of a viscous fluid. The fluid is represented by an ideal gas, but the compressibility can be neglected for very small Mach numbers, which is fulfilled for the permeation of nanoporous packed beds. The LB method is based on the Boltzmann equation

$$\frac{\partial f}{\partial t} + \boldsymbol{e} \cdot \nabla f = \Omega_{LB}, \tag{4-16}$$

with the single-particle distribution function $f(\boldsymbol{x}, \boldsymbol{e}, t)$, which gives the probability to find a virtual fluid particle at the position $\boldsymbol{x}$, the velocity $\boldsymbol{e} = \partial \boldsymbol{x} / \partial t$, and the time t. The collision operator $\Omega_{LB}(\boldsymbol{x}, \boldsymbol{e}, t)$ mimics the viscous behavior of the fluid by exchanging momentum between the fluid particles while conserving total mass, momentum, and energy. In the Bhatnagar-Gross-Krook approximation [Bhatnagar, P. L., et al. 1954], which is used in this study, the collision operator

$$\Omega_{LB} = -\frac{1}{\tau_{LB}}\left(f - f_{Equ}\right) \tag{4-17}$$

relaxes the fluid towards equilibrium with the relaxation time τ_{LB}.

The equilibrium distribution function $f_{Equ}(\boldsymbol{x},\boldsymbol{e},t)$ is given by the Maxwell velocity distribution

$$f_{Equ} = \frac{\rho_{LB}}{(2\pi RT)^{1,5}} \exp\left(-\frac{(\boldsymbol{e}-\boldsymbol{v_{LB}})^2}{2RT} \right) \tag{4-18}$$

with the macroscopic velocity $\boldsymbol{v}_{LB}(\boldsymbol{x},t)$ and the density $\rho_{LB}(\boldsymbol{x},t)$ of the fluid, which are given below. The Maxell distribution is approximated by the second order Taylor expansion

$$\begin{aligned} f_{Equ} &= \frac{\rho_{LB}}{(2\pi RT)^{1,5}} \exp\left(-\frac{\boldsymbol{e^2}}{2RT} \right) \exp\left(\frac{(\boldsymbol{e}\cdot\boldsymbol{v_{LB}}) - \boldsymbol{v}_{LB}^2/2}{RT} \right) \\ &= \frac{\rho_{LB}}{(2\pi RT)^{1,5}} \exp\left(-\frac{\boldsymbol{e}^2}{2RT} \right) \left(1 + \frac{\boldsymbol{e}\cdot\boldsymbol{v}_{LB}}{RT} + \frac{(\boldsymbol{e}\cdot\boldsymbol{v}_{LB})^2}{2(RT)^2} - \frac{\boldsymbol{v_{LB}^2}}{2RT} \right). \end{aligned} \tag{4-19}$$

Using

$$\boldsymbol{e}\cdot\nabla f = \frac{\partial f}{\partial \boldsymbol{e}} = \lim_{\Delta t\to 0} \left(\frac{f(\boldsymbol{x}+\boldsymbol{e}\Delta t_{LB}, \boldsymbol{e}, t+\Delta t_{LB}) - f(\boldsymbol{x},\boldsymbol{e},t+\Delta t_{LB})}{\Delta t_{LB}} \right), \tag{4-20}$$

the Boltzmann equation is discretized in time, leading to

$$f(\boldsymbol{x}+\boldsymbol{e}\Delta t_{LB}, \boldsymbol{e}, t+\Delta t_{LB}) - f(\boldsymbol{x},\boldsymbol{e},t) = \Delta t_{LB}\Omega_{LB}, \tag{4-21}$$

with the time step Δt_{LB}. In this study, the fixed geometries of the PBs obtained from the MD and SRD simulation are mapped on a cubic lattice with the lattice constant Δx and the velocity space is discretized to the basic lattice vectors $\boldsymbol{e}_j$ in the directions j. The lattice has 128 nodes in each dimension, leaving fluid reservoirs below and above the PB, where the driving external force is applied and where the flow field adapts to the complex pore network [Narvaez, A., et al.]. In the D3Q19 lattice used in this study, the lattice vectors are the main lattice directions $\boldsymbol{e}_1$ to $\boldsymbol{e}_6$, the diagonals $\boldsymbol{e}_7$ to $\boldsymbol{e}_{18}$, and the rest vector $\boldsymbol{e}_{19}$ (see figure 4-5). The velocity field is described by the single-particle distribution functions $f_j(\boldsymbol{x},t)$, which gives the number density of particles moving along the lattice vector $\boldsymbol{e}_j$ as depicted by the grey polyhedron in figure 4-5.

The discrete form of the Boltzmann equation reads as [Narvaez, A., et al.]

$$f_j\left(\boldsymbol{x}+\boldsymbol{e}_j\Delta t_{LB},t+\Delta t_{LB}\right)-f_j\left(\boldsymbol{x},\boldsymbol{e},t\right)=\Delta t_{LB}\Omega_{LB,j}. \tag{4-22}$$

The no-slip boundary conditions on the particle surfaces are implemented with the so-called mid-grid bounce back condition: for lattice nodes inside the particles, the collision operator reflects the velocity distributions, so that the velocity at the border becomes zero [Manwart, C., et al. 2002, Aaltosalmi, U. 2005, Deshpande, A. P., et al. 2005]. For the fluid, the collision operator is

$$\Omega_{LB,j}=-\frac{1}{\tau_{LB}}\left(f_j\left(\boldsymbol{x},t\right)-f_{Equ,j}\left(\boldsymbol{x},t\right)\right)+\frac{w_j}{c_{S,LB}^2\rho_{LB}}\boldsymbol{e}_j\boldsymbol{b}\left(\boldsymbol{x},t\right), \tag{4-23}$$

with the relaxation time $\tau_{LB}\approx\Delta t_{LB}$, the discrete equilibrium distribution function [Narvaez, A., et al.]

$$f_{Equ,j}\left(\boldsymbol{x},t\right)=w_j\left(1+\frac{\boldsymbol{e}_j\cdot\boldsymbol{v}_{LB}}{c_{S,LB}^2}+\frac{\left(\boldsymbol{e}_j\cdot\boldsymbol{v}_{LB}\right)^2}{c_{S,LB}^4}-\frac{\boldsymbol{e}_j\cdot\boldsymbol{v}_{LB}}{c_{S,LB}^2}\right)\sum_{j=1}^{19}f_j\left(\boldsymbol{x},t\right), \tag{4-24}$$

the speed of sound

$$c_{S,LB}=\frac{\Delta x}{\sqrt{3}\Delta t_{LB}}, \tag{4-25}$$

the local density

$$\rho_{LB}\left(\boldsymbol{x},t\right)=\rho_0\sum_{j=1}^{19}f_j\left(\boldsymbol{x},t\right), \tag{4-26}$$

the reference density ρ_0, and the externally applied acceleration $\boldsymbol{b}\left(\boldsymbol{x},t\right)$. The lattice weights w_j to correct for the discrepancy between the different lengths of the lattice vectors have values of $\frac{1}{18}$ for $1\le j\le 6$, $\frac{1}{36}$ for $7\le j\le 18$, and $\frac{1}{3}$ for $j=19$ [Yu, H. and Girimaji, S. S. 2008].

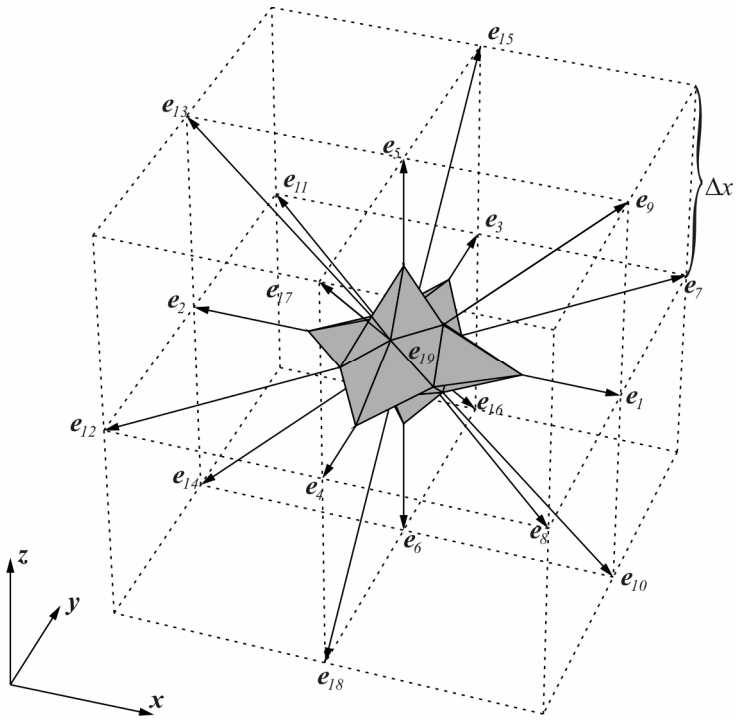

Figure 4-5: Computational lattice of a three-dimensional lattice Boltzmann simulation with the lattice constant Δx and the discrete lattice vectors e_j. The grey polyhedron gives the single-particle distribution functions f_j for each lattice vector.

The fluid's macroscopic velocity

$$\boldsymbol{v}_{LB}(\boldsymbol{x},t)=\frac{\sum_{j=1}^{19} f_j(\boldsymbol{x},t)\boldsymbol{e}_j}{\sum_{j=1}^{19} f_j(\boldsymbol{x},t)}+\frac{\Delta t_{LB}}{2\rho_{LB}(\boldsymbol{x},t)}\boldsymbol{b}. \tag{4-27}$$

is corrected for the external acceleration to satisfy the Navier-Stokes equation [Ginzburg, I. and d'Humières, D. 2003, Lallemand, P. and Luo, L.-S. 2003, Pan, C., et al. 2006]. The permeability of the PBs results from equation (2-16) with the fluid's mean velocity and with the difference of the pressure above and below the PB, which is calculated as

$$p(\boldsymbol{x},t)=c_{S,LB}^2\rho_{LB}(\boldsymbol{x},t). \tag{4-28}$$

4.3 Validation of the simulation

The formation of agglomerates, which dominates the filtration behavior of the suspension and the permeability of the PBs, depends on whether the kinetic energy of the particles is sufficient to overcome the energy maximum in the DLVO potential. The level, constancy, and distribution of the energy associated with thermal fluctua-

tions are thus crucial properties of the system. Figure 4-6 shows the distribution function F_i of the velocities v_i in the directions of the coordinate system i for unagglomerated particles with a diameter of 120 nm. The velocity distributions fluctuate around the Maxwell-Boltzmann distribution given by [Atkins, P. W. and De Paula, J. 2006]

$$F_i(v_i) = \sqrt{\frac{m_{MD}}{2\pi k_B T}} \exp\left(-\frac{m_{MD} v_i^2}{2 k_B T}\right), \tag{4-29}$$

with the mass of the MD particles m_{MD}, which is indicated by the solid line. The symmetry about the axis of ordinates shows that there is no macroscopic flow.

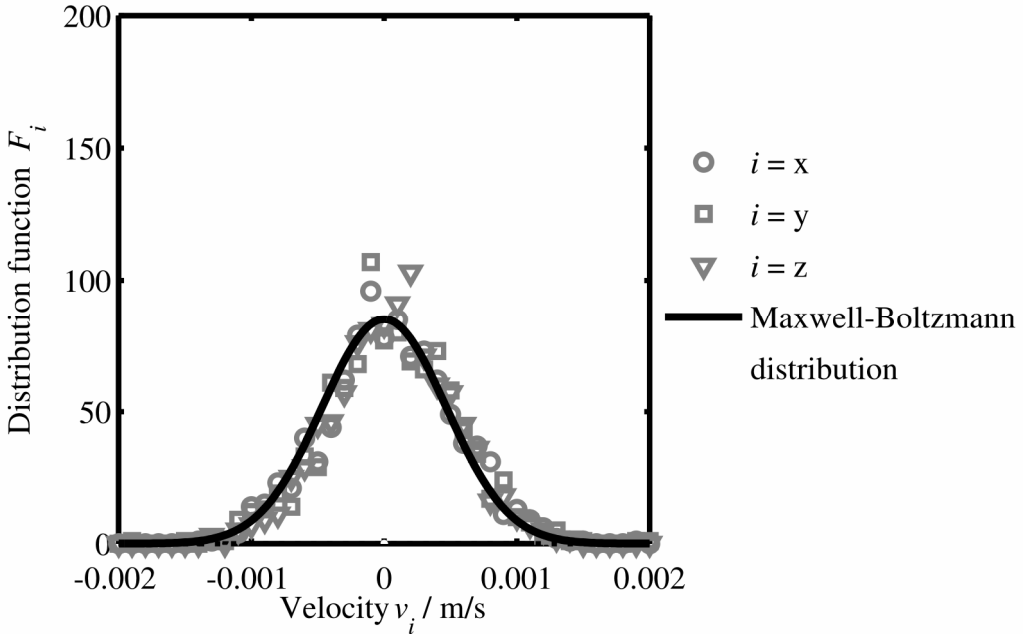

Figure 4-6: Distribution function F_i of the velocities v_i in direction i for unagglomerated particles with a diameter of 120 nm with a zeta potential of 60 mV at an ionic strength of 0.02 mol/L compared to the Maxwell-Boltzmann distribution.

The kinetic energy of the MD particles fluctuates around its equilibrium value of 1.5 $k_B T$. For 2000 particles the standard deviation equals 0.045 $k_B T$. Furthermore, the diffusion constant of the simulated solid particles

$$D_{MD} = \frac{\sum_{m=1}^{N_{MD}} \left(\boldsymbol{x}_m(t) - \boldsymbol{x}_m(t_0)\right)^2}{2 N_{MD} (t - t_0)}, \tag{4-30}$$

with the number of MD particles N_{MD} and the initial time t_0 corresponds to the Stokes-Einstein relation

$$D_{MD} = \frac{k_B T}{3\pi d_P \eta}. \tag{4-31}$$

Figure 4-7 shows the influence of varying the arbitrarily chosen simulation parameters on the porosity of PBs $\Phi_{L,PB}$. These consist of particles with a diameter of 30 nm primary agglomerated in the primary minimum, which represents the worst case within the domain of investigations. The investigated simulation parameters are multiplied by factors of 0.8 and 1.25, respectively, and the data points are shifted horizontally to enhance the clarity of the figure because the symbols would otherwise have the same horizontal positions. The variation of the Hertz constant K_{Hertz} and the time step for the MD simulations Δt_{MD} changes the porosity of the PBs by a few percent. This is less than the size of the 95% confidence intervals, which are based on five simulations with different seeds for the random number generator that distributes the solid particles at the beginning of the simulation and chooses the rotaton matrices. Primary agglomerates are not influenced by the parameters of the lubrication force since the latter does not act within the primary minimum.

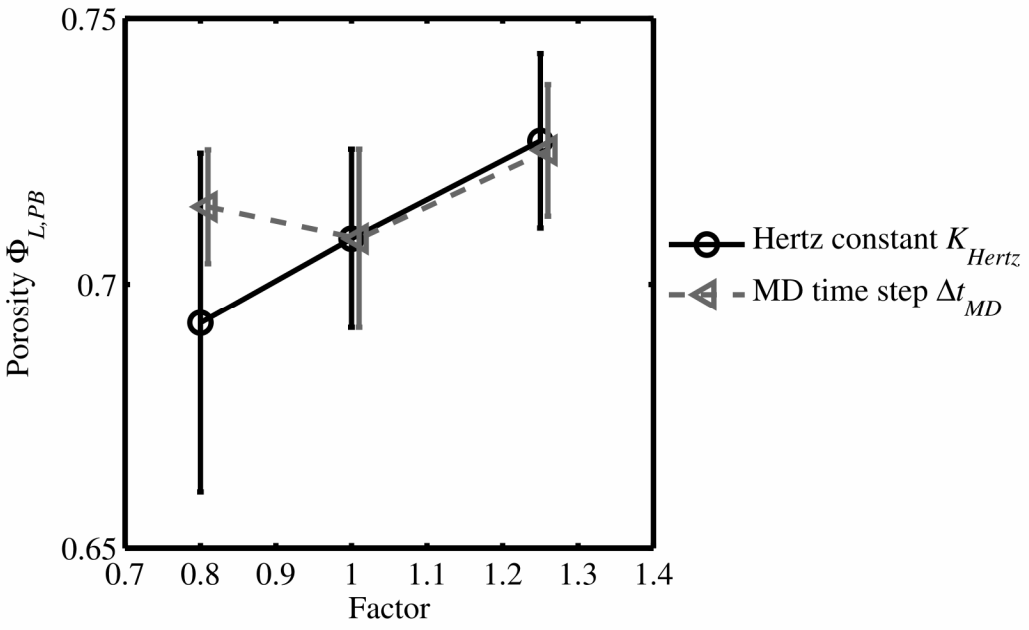

Figure 4-7: Influence of varying the arbitrarily chosen simulation parameters on the porosity $\Phi_{L,PB}$ of PBs that consist of primary agglomerates for a particle diameter of 30 nm. The data points are shifted horizontally to enhance the clarity of the figure.

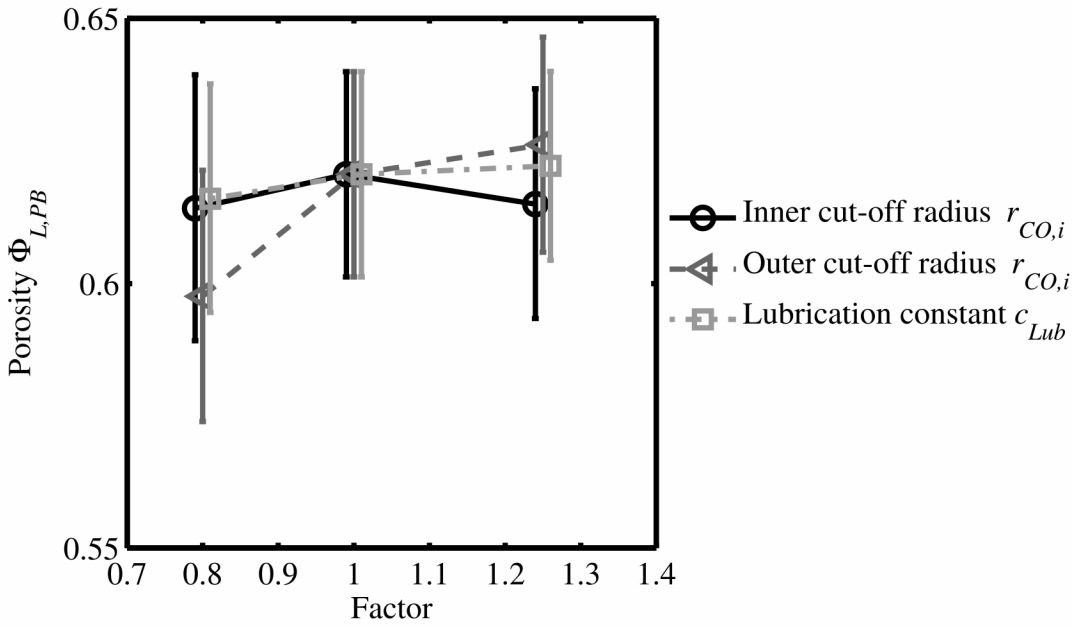

Figure 4-8: Influence of multiplying the arbitrarily chosen simulation parameters on the porosity $\Phi_{L,PB}$ of PBs consisting of primary agglomerates of particles with a diameter of 30 nm. The data points are shifted horizontally to enhance the clarity of the figure.

In contrast, the lubrication constant c_{Lub} and the inner and outer cut-off radius $r_{CO,i}$ and $r_{CO,o}$ of the lubrication force affect secondary agglomerates. The influence of multiplying the parameters by factors of 0.8 and 1.25 is shown in figure 4-8 for a particle diameter of 30 nm, which is again the worst case within the domain of investigations. The data points are again shifted horizontally because the symbols would otherwise have the same horizontal positions. The influence of the parameter variation is again smaller than the 95% confidence intervals that result from simulations with five different seeds for the random number generator. The parameters of the Hertz force do not influence secondary agglomerates since the Hertz force only acts on primary agglomerates. The MD time step is also uncritical for secondary agglomerates because the potential gradients in the secondary minimum are much smaller than the potetnial gradients in the primary minimum and the maximum MD time step is thus less restricted.

4.4 Results

The simulation methods introduced above are used to investigate the influence of the particle size, the particle charge, and the ionic strength on the agglomeration of particles and on the structure of PBs, which are formed by two-sided filtration of colloidal suspensions. The subsequent lattice Boltzmann simulations yield the permeabilities C_{11} of the PBs.

4.4.1 Agglomeration of colloidal particles

The agglomeration and agglomerate structure is quantified by means of the pair correlation function G, which is shown in figure 4-9 for the different particle diameters. The peaks indicate a high probability for a particle to find another particle at the specified center-to-center distance d_C and refer to the distance between the dark spheres in the sketches. Similar pair correlation functions are observed in Brownian dynamics simulations [Hütter, M. 2000]. The gap of G for d_C/d_P between 1 and 1.1 indicates a low probability of finding a particle in corresponding steep region of the DLVO potential. The extension of the first peaks to d_C/d_P less than one shows an unrealistic overlapping of the particles. This results from substituting the Born repulsion with a Hertz force in the DLVO interactions, which is done to reduce the gradient of the DLVO potential and thus increase the simulation time step. The resulting broadening of the peaks is especially pronounced for the small particles, since the penetration depth is related to the particle diameter. The broadening effect is accompanied by a smaller peak height since the integral has to be conserved.

The position of the peaks is further used to distinguish between primary and secondary agglomeration. For secondary agglomerates, the peaks of G are at larger distances than for primary agglomerates (see figure 4-10) because the secondary minimum is located at a larger surface distance. Furthermore, the peaks for secondary agglomerates are significantly broader due to the larger width of the secondary minimum. This also indicates a higher mobility of the particles in the agglomerates. Secondary agglomerates are thus less stable against deformation. For secondary agglomerates, the higher order peaks of G are less pronounced.

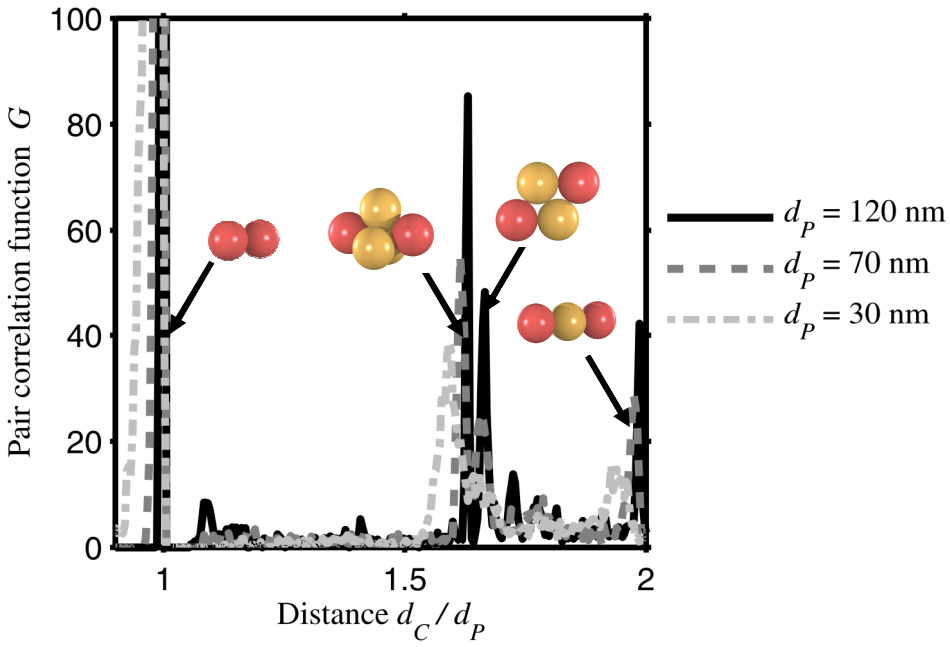

Figure 4-9: Pair correlation function G for particles of different particle diameters d_P. The peak positions refer to the distance between the dark spheres in the sketches.

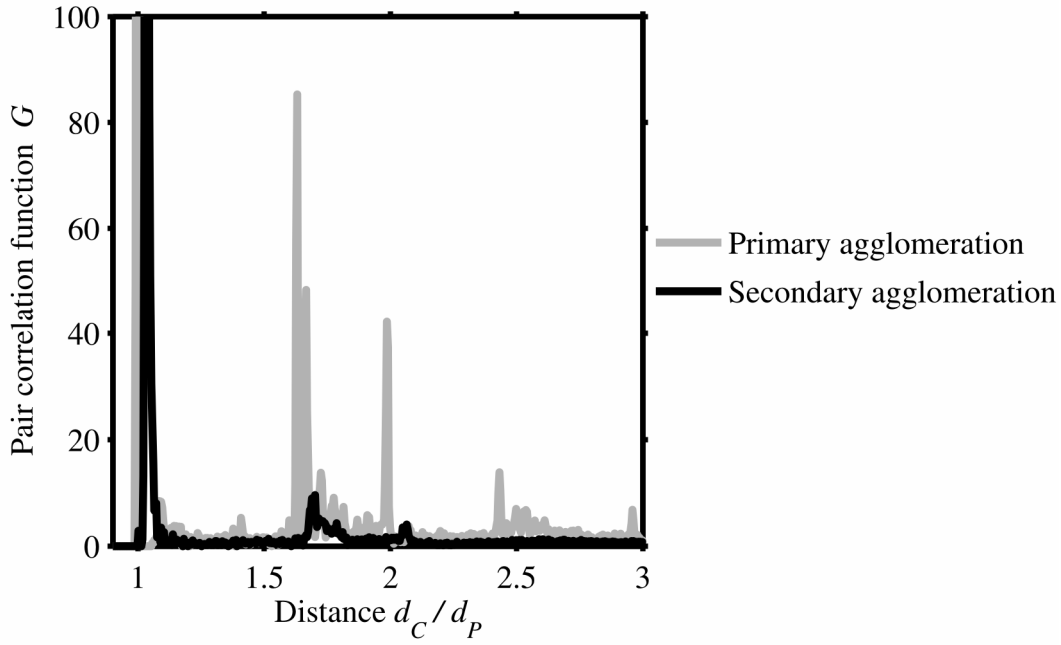

Figure 4-10: Pair correlation functions G for a particle diameter d_P of 120 nm in the presence of primary agglomerates (grey) and secondary agglomerates (black).

The stability diagram (see figure 4-11) shows the agglomeration behavior of suspensions with different particle diameters for all combinations of zeta potential ζ and ionic strength I.

- For combinations above and between the solid lines, the difference $\Delta\Psi_{DLVO}$ between the maximum and the secondary minimum of the DLVO potential is

smaller than 10 $k_B T$. The energy barrier should be overcome by at least some of the particles, which have a Boltzmann distributed kinetic energy [Atkins, P. W. and De Paula, J. 2006].

- Between the solid lines and the dashed lines, the energy barrier $\Delta\Psi_{DLVO}$ is higher than 10 $k_B T$ and the secondary minimum $\Psi_{DLVO,Min}$ is deeper than 2 $k_B T$. Consequently, some particles get caught in the secondary minimum and are referred to as secondary agglomerates.
- The suspensions are stable below the dashed lines, where the secondary minimum $\Psi_{DLVO,Min}$ is too shallow to retain the particles and the energy barrier $\Delta\Psi_{DLVO}$ is too high to be overcome. The particle size has a stronger influence on secondary agglomeration than on primary agglomeration.

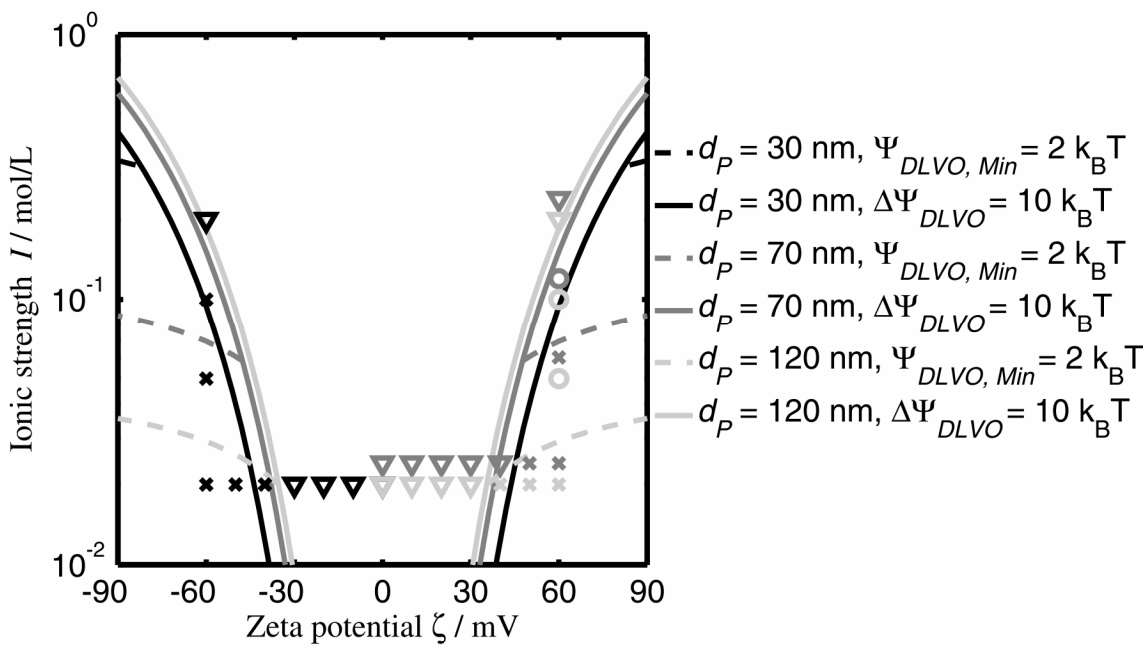

Figure 4-11: Stability diagram for different particle sizes d_P showing the regions of primary agglomeration (above and between the solid lines), secondary agglomeration (between the solid and the dashed lines) and stable suspensions (below the dashed lines). The symbols are explained in the text.

The symbols show the state of agglomeration observed in the simulations for particle diameters of 30 nm (black symbols), 70 nm (dark grey symbols), and 120 nm (light grey symbols). The data points for a diameter of 70 nm are shifted vertically for the sake of optical clarity because the symbols would otherwise have the same positions. Primary agglomerates are indicated by triangles, secondary agglomerates by circles

and unagglomerated suspensions by crosses. The agglomeration behavior observed in the simulations agrees with the stability diagram.

The simulations of the agglomeration and filtration start with statistically distributed particles, which move and agglomerate due to Brownian motion. Before the filtration starts, the agglomeration must come to an equilibrium state as controlled via the evolution of the pair correlation function (see figure 4-12). Starting from a completely irregular structure, the nearest-neighbor peaks evolve rapidly and the peaks for higher orders follow.

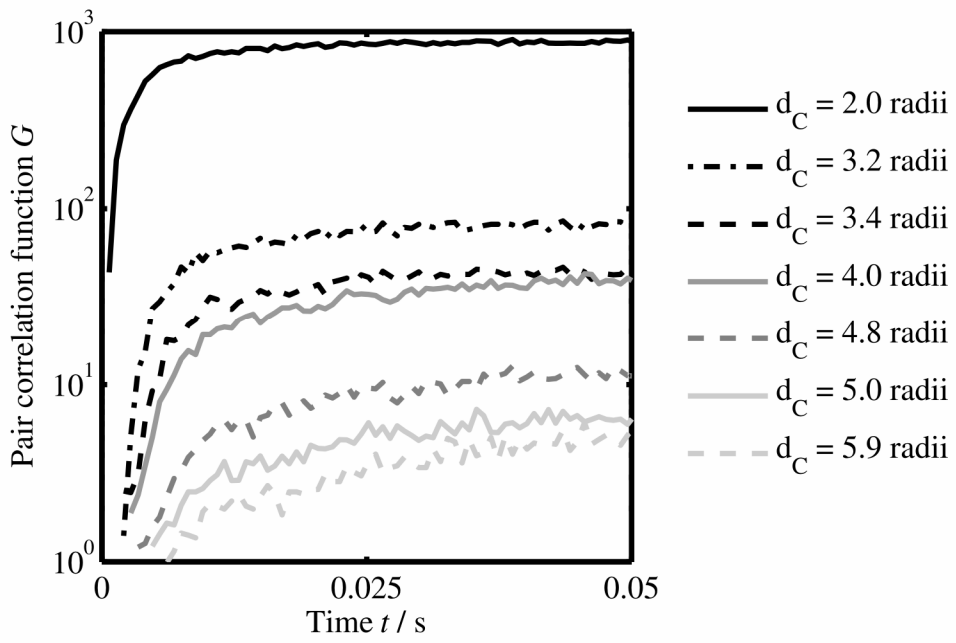

Figure 4-12: Evolution of the peak heights of the pair correlation function G for particles with a diameter of 120 nm at different center-to-center distances.

For a particle diameter of 120 nm, the agglomeration time prior to filtration is set to 30 ms, when the agglomeration is close to its equilibrium state (see figure 4-12). A longer agglomeration time would primarily increase the computational time. The agglomeration time is set to 0.65 ms for a particle diameter of 30 nm and to 4.4 ms for a particle diameter of 70 nm. The corresponding diagrams are presented in the appendix. For smaller particles, the agglomeration time is shorter because of the faster Brownian motion, but this also requires smaller time steps of the simulation.

In the simulation, the particles in the suspensions agglomerate before the formation of the packed beds by filtration of the suspension starts, which is analogous to the experiments described in chapter 3.

4.4.2 Structure of the packed beds

After the agglomeration reaches its equilibrium, the filtration starts by incrementally reducing the MD space. Filter cakes build up at the upper and lower boundaries of the MD simulation space until they eventually merge and get compressed. This procedure is controlled by the integrated force between the particles and the boundary planes to ensure a compression at a constant pressure. The structure of the PBs is evaluated in terms of its porosity $\Phi_{L,PB}$, which relates the liquid volume V_L to the total volume of the PB V_{PB}

$$\Phi_{L,PB} = 1 - \frac{\frac{1}{6}\pi d_P^3 N_{MD}}{A_{PB} L_{PB}}, \tag{32}$$

with the number of MD particles N_{MD} and the cross sectional area of the PB A_{PB}. The thickness of the PB L_{PB} should not be determined from the coordinates of the highest and lowest particles because the PBs can be rough and irregular if agglomerates are present. The resulting statistical uncertainty could be reduced by increasing the number of particles, but this would lead to an increased computational effort. Instead, the thickness of the PBs is calculated from the vertical coordinates $x_{z,m}$ of the particles as

$$L_{PB} = 4 \frac{\sum_{m=1}^{N_{MD}} \left| x_{z,m} - \sum_{m=1}^{N_{MD}} x_{z,m} / N_{MD} \right|}{N_{MD}} + d_P. \tag{33}$$

The porosity of the PB strongly depends on the ionic strength of the suspension (see figure 4-13), because the ions reduce the Debye length and thus shield the Coulomb repulsion. Accordingly, the porosity is relatively high for the agglomerated particles at an ionic strength of 0.2 mol/L and a zeta potential of 60 mV, which approximates the zeta potential of boehmite particles at a pH value of 4. An increasing compression results in a decreasing porosity since the lose agglomerate structure can be easily compressed by rearrangement of the particles. The agglomerates can be considered as deformable particles. This effect is stronger for smaller particles, probably because of the broader primary minimum and thus higher mobility within the agglomerates. However, the effect is not observable in experiments with irregular shaped particles and the author is not aware of experimental studies comparing ideally spherical particles with different particle sizes.

For an ionic strength of 0.1 mol/L and a zeta potential of 60 mV, only few primary agglomerates are formed because of the high energy barrier. Consequently, for lower ionic strengths agglomeration does not play a role anymore and the porosity is mainly determined by the nearest-neighbor distance of the particles. The latter depends on the equilibrium of compressive force on the PB and the electrostatic repulsion between the particles and thus decreases with increasing ionic strength and increasing compression. The influence of the compression on the porosity decreases with increasing ionic strength as long as it is kept below the critical coagulation concentration, which is also observed in experiments carried out with colloidal silica spheres [Singh, G. and Song, L. 2006].

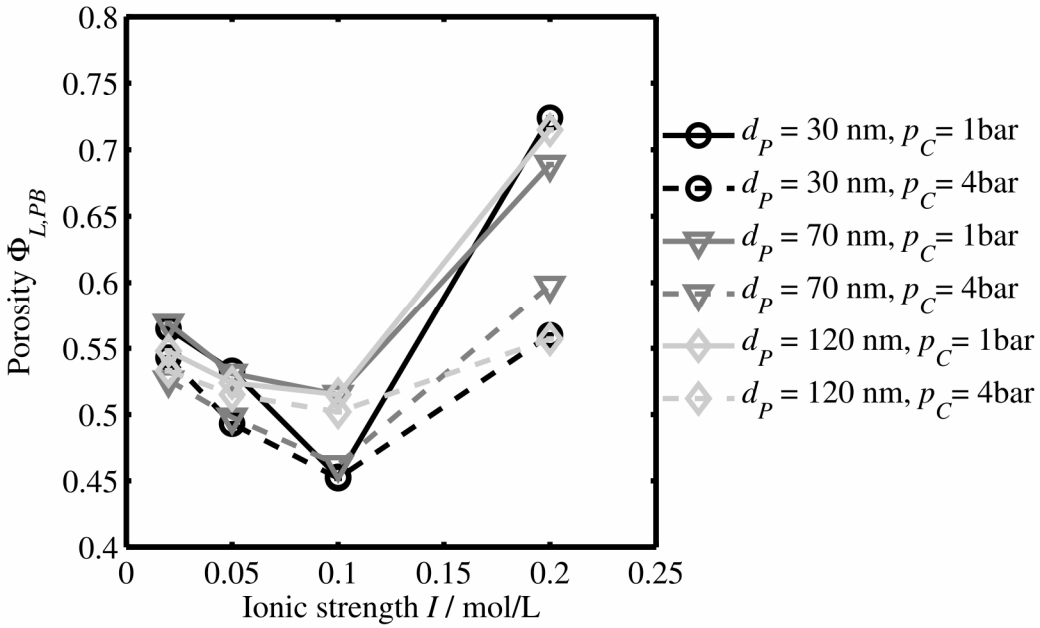

Figure 4-13: Porosity $\Phi_{L,PB}$ of the PBs depending on the ionic strength I at a zeta potential of 60 mV for different compressive loads p_C and different particle diameters d_P.

The behavior of the particles with diameters of 70 nm and 120 nm is similar, but not identical because they form secondary agglomerates at ionic strengths below 0.1 mol/L. These secondary agglomerates are much easier to deform than primary agglomerates because of the shallow and broad secondary minimum.

The porosity of the PBs also depends on the zeta potential of the particles (see figure 4-14). At low zeta potentials, the porosity is relatively high for all particle diameters and for all compressive loads because the particles are agglomerated. At a zeta

potential of 40 mV and beyond, only few agglomerates are formed because of the strong Coulomb repulsion. Consequently, agglomeration does not play a role anymore and the porosity is mainly determined by the nearest-neighbor distance of the particles, analogously to what happens when the ionic strength is decreased. A stronger compression again causes a lower porosity.

The error bars at a zeta potential of 0 mV indicate the 95% confidence intervals based on five simulations with different seeds for the random number generator, carried out for each particle diameter and each compressive load. These are the suspected worst cases, since the structures for stable suspensions are more regular.

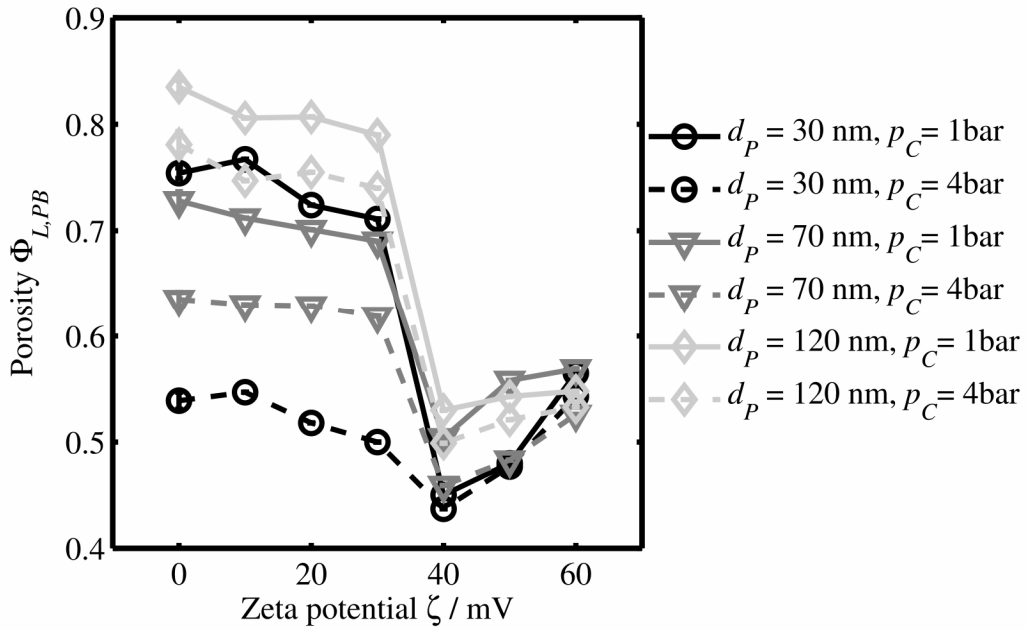

Figure 4-14: Porosity $\Phi_{L,PB}$ of the PBs depending on the zeta potential at an ionic strength of 0.02 mol/L for different compressive loads p_C and different particle diameters d_P.

The increase of the porosity for zeta potentials beyond 40 mV, which is shown in figure 4-14, is attributed to the strong repulsion between the particles. This is also reflected in the pair correlation function G shown in figure 4-15. The irregular pair correlation functions for the suspension with values close to zero indicate an even distribution of the particles in the suspension without agglomerates. During the filtration, when the MD space is reduced, the particles come closer and G increases over the whole distance range presented in figure 4-15. In the PB, the particles with a zeta potential of 60 mV form regular structures since they arrange in a local order to

maximize the nearest-neighbor distances. The smooth maxima and minima of G reveal the particles' relatively high mobility. The strong compression of 4 bar makes some of the particles overcome the high energy barrier in the DLVO potential of about 24 $k_B T$. The second peak at a distance of approximately 1.2 d_C/d_P refers to the equilibrium of the compression and the electrostatic repulsion. For a zeta potential of 50 mV, the energy maximum of the DLVO potential of 15 $k_B T$ is more probable to be overcome. The first peak is consequently higher than for a zeta potential of 60 mV and the second peak is lower. The peak at 2.3 particle radii disappears for particles with a zeta potential of 40 mV, where the maximum of the DLVO potential of 7.5 $k_B T$ is readily overcome by the compression. The peaks at higher orders refer to the next-nearest neighbors.

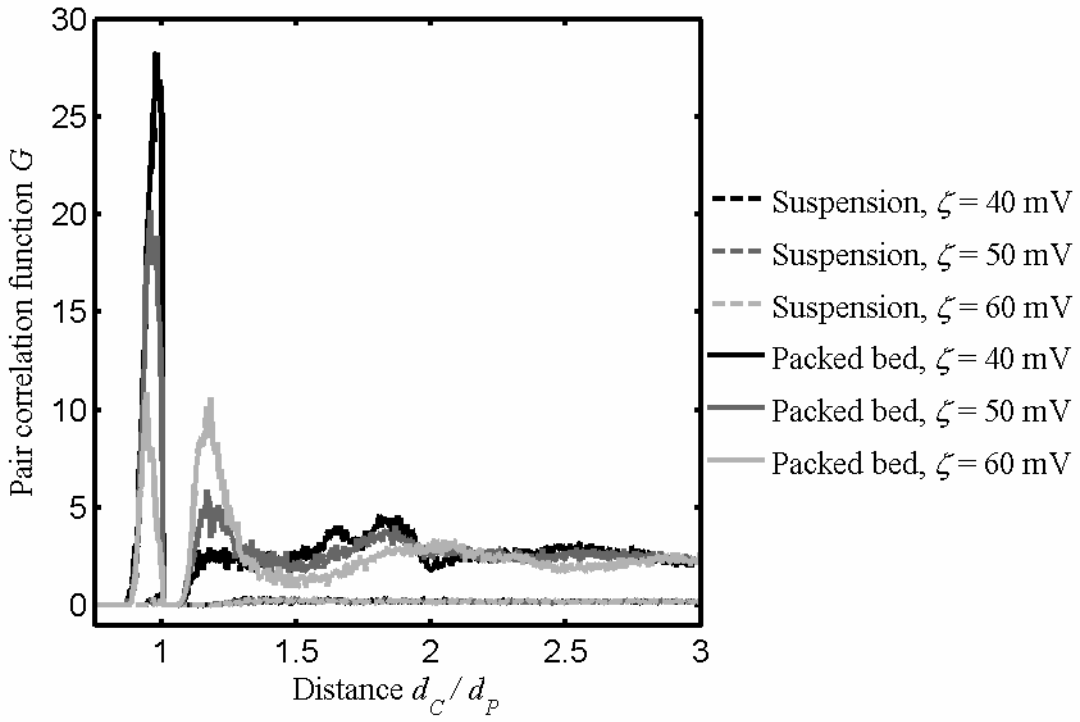

Figure 4-15: Pair correlation function G of the particles with a diameter of 30 nm in the suspensions (thin dashed lines close to the axis of abscissas) and in the PBs compressed with 4 bar (thick solid lines) for different zeta potentials ζ and at an ionic strength of 0.02 mol/L.

Although some of the particles occupy the primary minimum of the DLVO potential, they are not considered as agglomerated since there are no substructures in the PBs. The PB does not comprise large inter-agglomerates pores and the porosity of the PBs does not increase because of the overcoming of the energy barrier.

For a zeta potential of 0 mV, the particles agglomerate before the filtration starts, as indicated by the pronounced peaks of the pair correlation function for the suspension (see figure 4-16). The pair correlation function G increases during the filtration for almost each distance, similar to the unagglomerated particles. The peak below 1 d_C/d_P is broadened to the left side, indicating that the compression is balanced by the Hertz force. This effect is not expected in reality because the realistic Born potential is much steeper than the modeled Hertz potential. The other peaks are flattened upon the compression because particles belonging to neighboring agglomerates, for which there is no regularity, also contribute to the pair correlation function. The pair correlation functions for zeta potentials of 10 mV and 20 mV are not shown since they are almost identical to the ones for a zeta potential of 0 mV. For a zeta potential of 30 mV, the lower peaks of the pair correlation function indicate that less agglomerates are present in the suspension. However, the structure of the PB is similar to the ones for lower zeta potentials, probably because the compression supports the agglomeration.

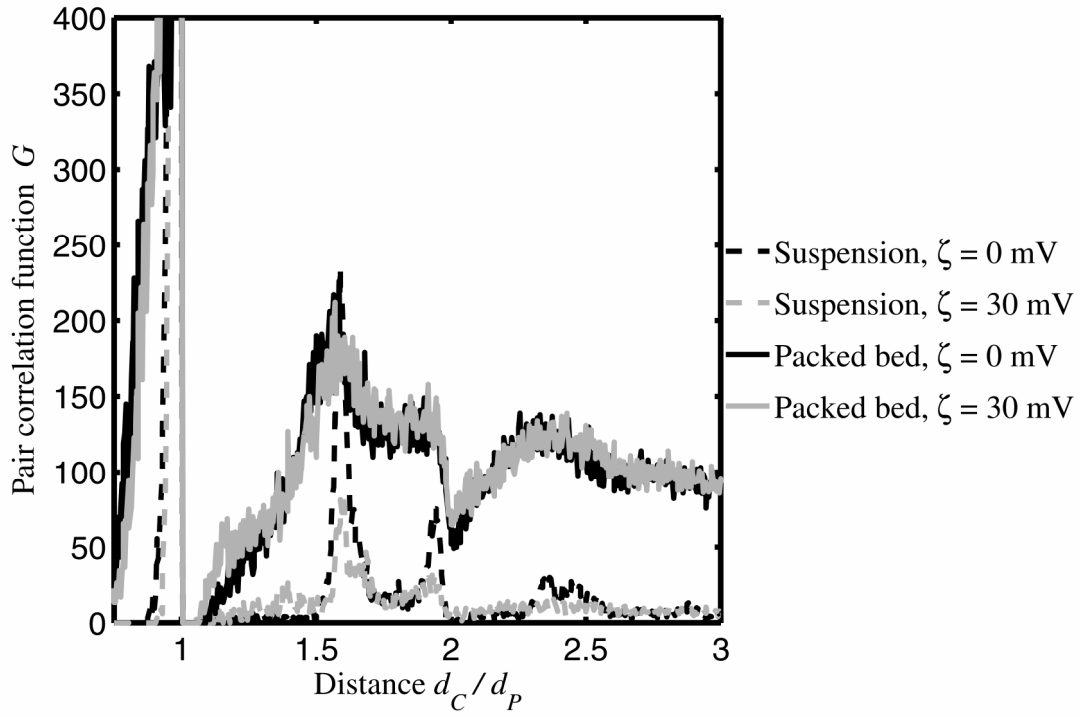

Figure 4-16: Pair correlation function G of the particles with a diameter of 30 nm and a zeta potential of 0 mV for the agglomerated suspension (black line) and in the PBs compressed with p_C = 4 bar (grey line).

Analyzing the pair correlation functions gives further insight into the structure of the PBs. This explains why the porosity of PBs increases with increasing zeta potential and with decreasing ionic strength as long as the particles do not agglomerate.

Another possibility to evaluate the structure of the PBs is to analyze their scattering curves as determined from the Debye formula (see equation (2-10) and (2-11). Figure 4-17 shows a comparison of scattering curves for agglomerated and stabilized particles in suspensions and in PBs. All scattering curves show distinct maxima for a high modulus of the scattering angle q because the particles are monodisperse and spherical. For the single particle, the scattering intensity $I_S(q)$ is almost constant in the low q range. It has a smooth transition (see the magnified section) to the Porod range, where the height of the maxima decreases according to

$$\lim_{q\to 0} I_S(q) = N\frac{C_P}{q^4}, \qquad (4\text{-}34)$$

with the Porod constant C_P and the number of particles in the examination volume N. The scattering intensity for the single particle is scaled by a factor of 2000, which is the total number of particles in the system, to make the scattering curves coincide in the high q range, which refers to small dimensions.

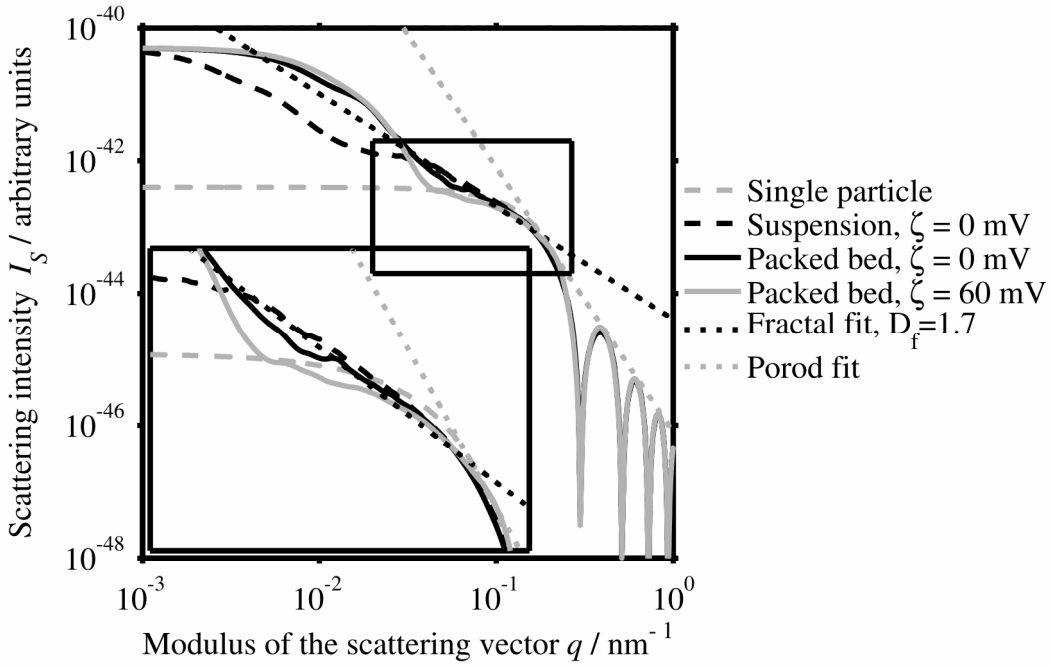

Figure 4-17: Scattering curves for suspensions (dashed lines) and PBs (solid lines) containing particles with a diameter of 30 nm. The black and grey lines refer to agglomerated and stabilized particles, respectively. The scattering curve of the single particle is scaled by a factor of 2000 so that the scattering curves coincide at high scattering angles.

The scattering curve is also calculated for all agglomerates in the simulation domain, which mimics unrealistic fixation between the agglomerates since the Debye formula

treats the floating agglomerates as a fixed porous system with a long range structure. The algorithm should thus only be applied to fixed structures such as single agglomerates. In experimental studies, this long-range interaction is cancelled out by the temporal averaging of the scattering patterns. However, the Debye formula should yield realistic short-range order within the agglomerates, so that deviations are only expected in the low q range. Consequently, it seems reasonable that the negative slope of the linear section (see the magnified section in figure 4-17) gives the fractal dimension D_f of the agglomerates. The resulting fractal dimension of 1.7 is close to the fractal dimension of 1.8, which is expected for diffusion limited cluster aggregation [Baron, P. A. and Willeke, K. 2001]. The same fractal dimension is found for the PB at a zeta potential of 0 mV, indicating that the filtration only slightly affects the short-range order of the particles in the agglomerates, which is also observed in experimental studies [Cabane, B., et al. 2002]. The scattering curves for the suspension and the PB deviate in the low q range, thus indicating the evolution of a long-range order between the agglomerates.

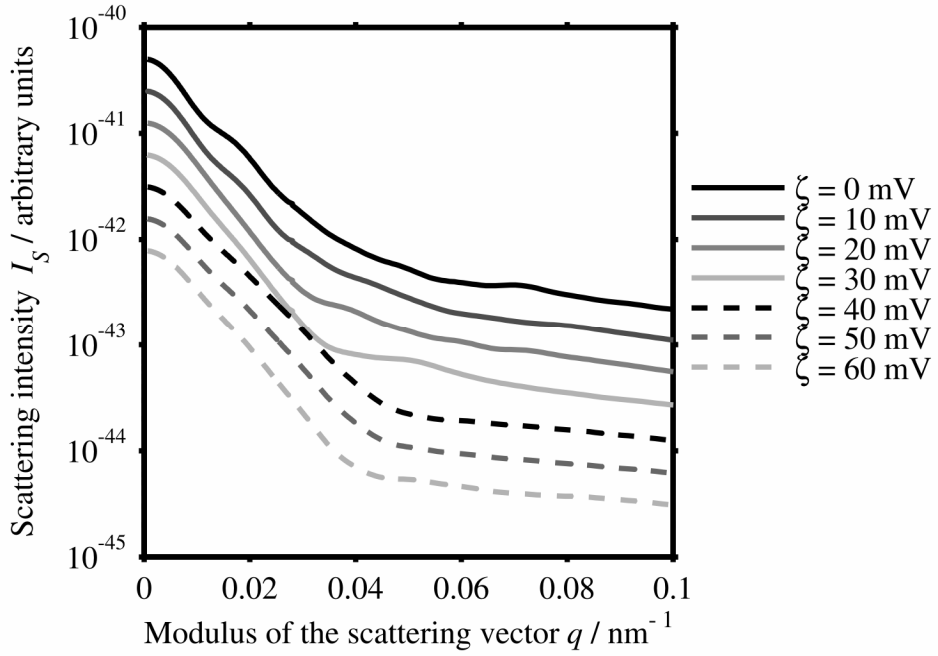

Figure 4-18: Scattering curves for PBs containing particles with a diameter of 30 nm. The curves are shifted vertically by factors of 2 to enhance the clarity of the figure.

The depression of the scattering curve for the PB consisting of highly charged particles at $q \approx 0.04$ nm^{-1} probably reflects the cylindrical form of the examination volume, which has a relatively homogenous electron density and can thus by seen as a

homogenous body. The depression does not occur for the agglomerated structures since these do not have a homgenous electron density.

For low scattering vectors, the scattering intensities are exponential functions of the scattering vector, as described by the Guinier law (figure 4-18). However, it makes no sense to determine the radius of gyration of the PBs since these do not reflect their structure. The bends of the scattering curves for zeta potentials of 40 mV and above reflect the form of the PB. Accordingly, the bend of the scattering curve is shifted to smaller values of q for higher zeta potentials due to the increasing thickness of the PBs. For unagglomerated structures with zeta potentials of 20 mV, the transition to the exponential behavior occurs at significantly smaller scattering angles and without a sharp bend, since the PBs have more heterogeneous electron density. The scattering curve for zeta potentials of 30 mV demands for further research.

Analyzing the scattering functions of PBs permits to distinguish between agglomerated and unagglomerated structures and gives further insight into the structure of PBs.

4.4.3 Permeability of the packed beds

The permeability of the PBs depends on the ionic strength of the suspension (see figure 4-19). This can be attributed to the changing pore size and the dependency of the mean velocity on the pore size in the regime of laminar flow. The logarithmic plots of the permeability (see figure 4-19) are similar in shape to the linear plots of the porosity (see figure 4-13). For an increasing ionic strength, the permeability first decreases because the particles come closer due to the smaller Debye length. Above 0.1 mol/L, where the particles agglomerate, the permeability increases significantly. Likewise, a higher compressive load results in a decreased permeability for all ionic strengths. The permeability increases for increasing particle size because the pores size is proportional to the particle size for an identical porosity.

Figure 4-20 shows the permeability for a variation of the zeta potential. Upon increasing the zeta potential up to 40 mV, the permeability decreases because of the decreasing porosity. Beyond 40 mV, the permeability increases again, especially for the smallest particles. The effect is again stronger for a weaker compression. The permeability also decreases with increasing compression and with decreasing particle

size. Again, the error bars are shown for the suspected worst cases, which are the PBs resulting from agglomerated particles with a zeta potential of 0 mV. The 95% confidence intervals are based on five simulations with different seeds for the random number generator, carried out for each particle diameter and each compressive load.

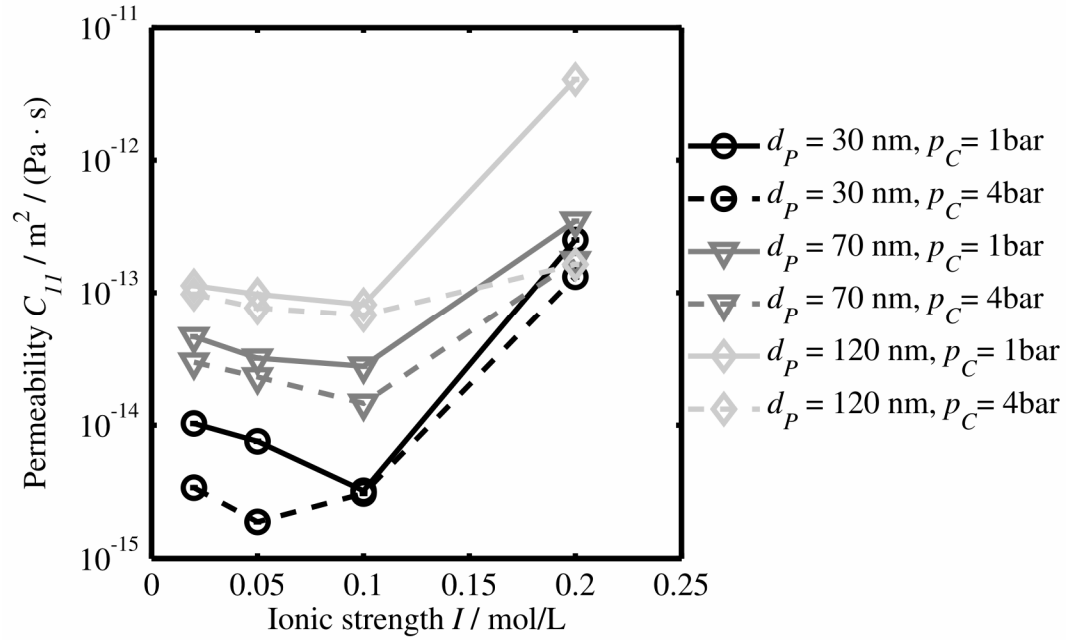

Figure 4-19: Permeability C_{11} of the PBs depending on the ionic strength I at a zeta potential of 60 mV for different compressive loads p_C and different particle diameters d_P.

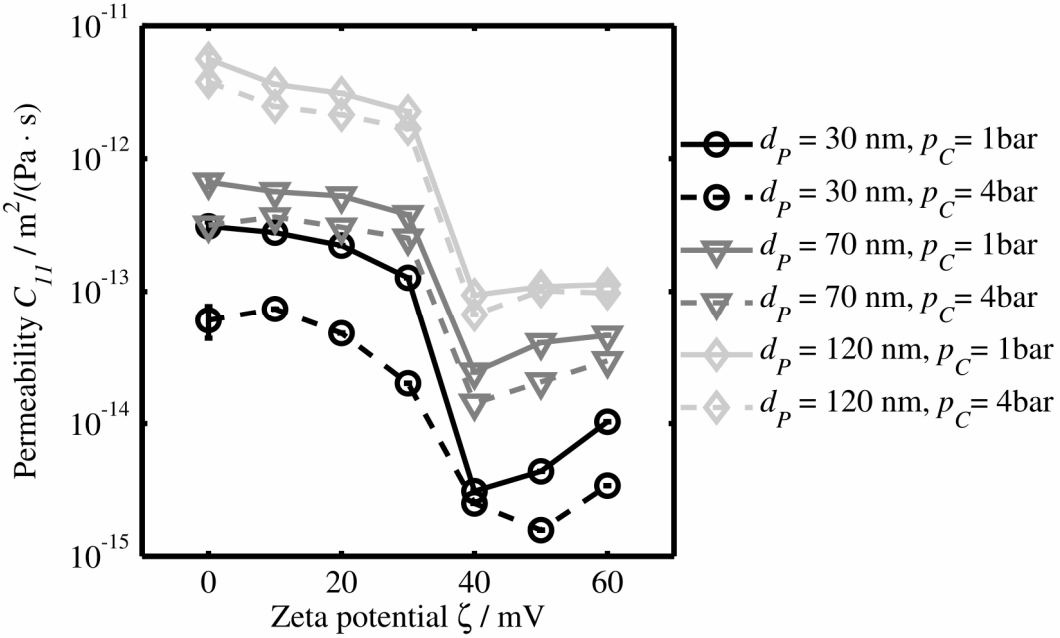

Figure 4-20: Permeability C_{11} of the PBs depending on the zeta potential ζ at an ionic strength of 0.02 mol/L for different compressive loads p_C and different particle diameters d_P.

The lattice Boltzmann (LB) simulations reveal that, for each particle size, the permeability of a packed bed is an exponential function of its porosity, which itself depends on the zeta potential, the ionic strength, and the compressive loads (see figure 4-21). A significant deviation from the exponential relation between the porosity and the permeability is found only for the 30 nm particles, where the simulated permeabilities are too high for porosities around 0.55. This indicates a stronger influence of the pore size heterogeneity on the permeability for smaller particles. Similar exponential relations between the porosity and the permeability are found in the experiments (see figure 3-21). While for the monodisperse spheres in the simulation, the regimes of stable and agglomerated particles can be clearly separated, the irregular shape of the particles in the experiments smoothes the transition between the agglomerated and unagglomerated state.

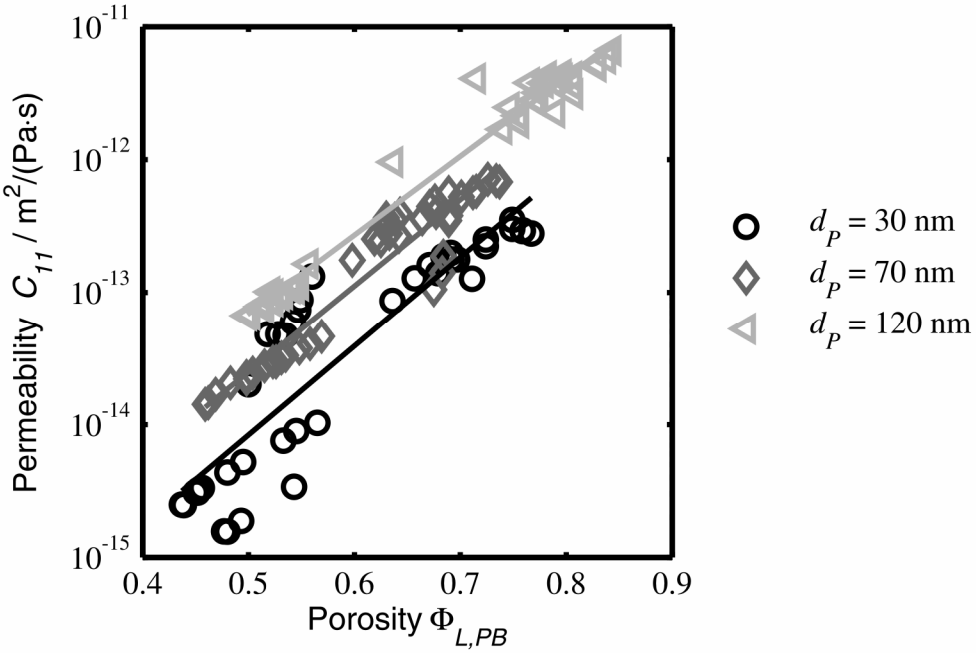

Figure 4-21: Permeability C_{11} of PBs consisting for of particles with different diameters d_P as a function of the porosity $\Phi_{L,PB}$ for varying ionic strengths, pH values and compressive loads as resulting from the simulation.

The simulated permeabilities are fitted to an exponential function of the porosity

$$C_{11} = a \cdot e^{b \cdot \Phi_{L,PB}}. \qquad (35)$$

The fitting parameters a and b are given in table 4-2 for the different particle sizes, together with the parameters describing the experiments. The parameter a reflects the higher permeability of packed beds composed of larger particles. The deviation of the

coefficient a between the simulations and the experiments is mainly attributed to the polydispersity and the non-spherical form of the particles in the experiment and the small system size in the simulations. The influence of the porosity, which is contained in the parameter b, is similar for the different particle sizes. The parameter b from the simulations is very close to the one from the experiments. Alternatively, the permeability can be fitted with a power-law function with exponents in around 9. This again shows the stronger influence of the porosity on the permeability for colloidal particles in comparison to macroscale particles, for which Rumpf and Gupte determined an exponent of 5.5 [Rumpf, H. and Gupte, A. R. 1971].

Table 4-2: Fitting parameters for the permeability as a function of the porosity

Particle diameter	Simulation		Experiment	
	a	*b*	*a*	*b*
30 nm	$3{,}7\cdot10^{-18}$	15,4	$3{,}5\cdot10^{-19}$	13.9
70 nm	$1{,}3\cdot10^{-17}$	15,2	$4{,}3\cdot10^{-19}$	14.7
120 nm	$7.4\cdot10^{-17}$	13.7	$2.1\cdot10^{-17}$	11.3

4.5 Conclusions

The agglomeration and filtration of colloidal particles are investigated with a simulation method that combines MD simulations of the solid particles with SRD simulations of the fluid. The MD simulation, which is based on solving Newton's equation of motion for the spherical solid particles with a Velocity Verlet algorithm, includes the van-der-Waals attraction, the Coulomb repulsion, the contact force, the lubrication force, the transversal friction forces, gravity, and a Monte Carlo thermostat. The SRD simulation of the fluid includes thermal noise, has low demands for computational time and is applicable to colloidal suspensions. The coarse-graining of the fluid in the SRD simulation involves a scaling of the suspension's physical properties, which permits to increase the computational time step by several orders of magnitude. An analysis of the relevant forces shows that the scaling does not change

the characteristic numbers significantly and the major physical behavior of the suspension is reproduced.

The applicability of the simulation methods is verified by comparing the thermal fluctuations to the Maxwell-Boltzmann distribution and checking the diffusion constant of the simulated particles against the Stoke-Einstein relation. The influence of varying the arbitrarily chosen simulation parameters on the porosity of PBs is smaller than the size of the 95% confidence intervals, which are based on five simulations with different seeds for the random number generator.

The agglomeration of the particles is analyzed by means of the pair correlation function G, which indicates the probability for the particles to find other particles at a certain center-to-center distance. The position of the peaks is further used to distinguish between primary and secondary agglomeration, which is compared to the stability diagram, and to determine the time for the agglomeration to reach equilibrium.

After the agglomeration, the suspensions are filtered by incrementally approaching the horizontal boundaries of the MD space towards each other. Like in the experiments, the porosity of the simulated PBs depends on the ionic strength, the zeta potential and the compression of the PBs. Agglomerated particles, as resulting from a high ionic strength or a low zeta potential, lead to PBs with a high porosity and a high compressibility. The investigation of the agglomerate structure via light scattering patterns shows that the short-range order of the agglomerates is only slightly changed during the filtration and that stabilized particles form regular, almost crystalline structures. The charged particles form regular structures since they try to maximize the nearest-neighbor distances, as can also be seen from the pair correlation function. The porosity of the crystalline PBs increases with increasing particle charge and decreasing ionic strength since the distance between the particles reflects the equilibrium between the Coulomb repulsion and the compression of the packed bed. A similar behavior is also observed in experiments on colloidal silica spheres [Singh, G. and Song, L. 2006], but not for irregularly shaped boehmite particles. A strong compression of the PBs makes some of the particles overcome high energy barriers in the DLVO potential. However, these particles are not considered as agglomerated since there is no substructure of the

PBs and the overcoming of the energy barrier does not cause a higher porosity of the PBs.

The permeabilities of the resulting PBs are determined by lattice Boltzmann simulations, which are the standard method for simulating fluid flow in porous structures. Like in the experiments, the permeability of the PBs is an exponential function of the porosity for each particle size and the PBs consisting of larger particles have higher permeabilities at identical porosities. Like in the experiments, an exponential relation between the porosity and the permeability of the PBs is found in the simulations and the exponential coefficients are almost identical for the simulations and experiments on particles with different diameters.

5 Summary and future prospects

5.1 Summary

Fluid flow and charge transport in nanoporous packed beds (**PBs**) are closely interrelated due to the presence of electrochemical double layers (**EDLs**) on the solid-liquid interfaces and can be driven both by hydraulic and electrical gradients. For each of the investigated materials, namely Disperal ®, Disperal 20®, Disperal 40® and Aeroxide P25®, the hydraulic permeability is found to be an exponential function of the porosity (see figure 5-1), which itself depends on the compression acting on the PB and on the agglomeration of the particles. The latter is controlled by the particle charge and the ionic strength of the suspension. For the different grades of boehmite particles, the permeability decreases with decreasing particle size. In spite of the small size of the primary particles, PBs consisting of Aeroxide P25® have a relatively high permeability because of the large pores between the indestructible agglomerates.

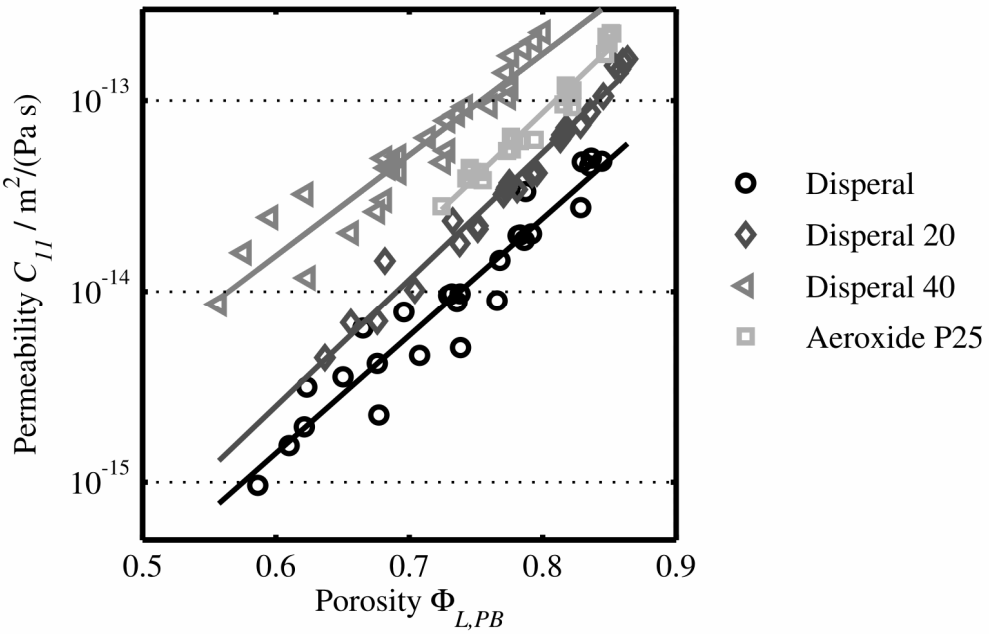

Figure 5-1: Permeability C_{11} of PBs consisting for of different materials as a function of the porosity $\Phi_{L,PB}$ for varying ionic strengths, pH values and compressive loads.

As fluid flow and charge transport in porous structures are closely interrelated, it is difficult to examine them separately. Especially the charge transport mechanism has a strong influence on the EHT. The separation between surface and liquid conduction permits to determine the parameters of a new capillary model for the electrohydrody-

namic cross effects, which is based on replacing the porous structures of the PBs by a hypothetical set of straight, parallel capillaries. The capillary model describes the influence of the particle charge, the ionic strength, and the compression on the interrelation of mass and charge transport and agrees well with the experimental results (see figure 5-2). The model helps to separate the structural and physicochemical influences and explains why the EHT coefficients can decrease with increasing modulus of surface charge if the porosity decreases substantially. The electroviscous retardation of the pressure driven flow amounts to only a few percent in the range of this study.

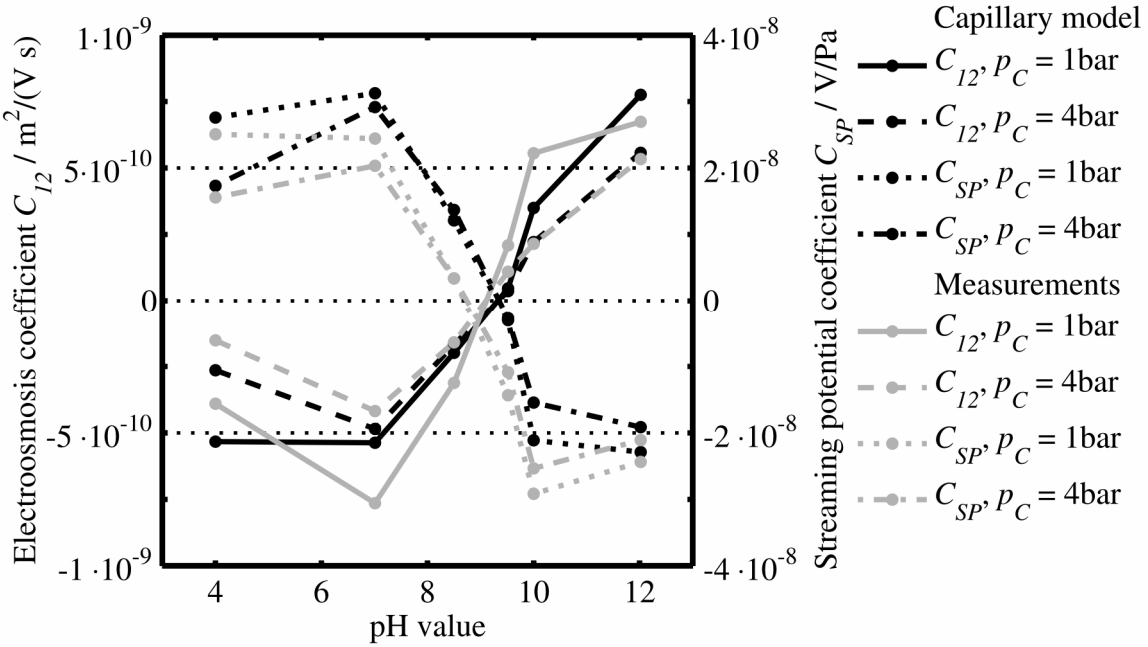

Figure 5-2: Electroosmosis coefficient C_{12} and streaming potential coefficient C_{SP} of the PBs depending on the pH value at an ionic strength of 0.02 mol/L at different compressive loads. The black lines refer to the capillary model and light grey lines to the measurements.

The numerical simulation includes the agglomeration of the particles, the filtration of the suspensions, and the compression of the resulting PBs. The computational effort is minimized with a combination of molecular dynamics and stochastic rotation dynamics. This permits to simulate 2000 colloidal particles with DVLO interactions, Brownian motion and the full hydrodynamics of the suspension. The filtration and the compression of the PBs only slightly changes the short-range order of the agglomerated particles, as indicated by the pair correlation function and the scattering curves. For highly charged particles, the strong repulsion between results in regular structures,

where the inter-particle distance reflects the equilibrium between the repulsion and the compression. A very strong compression can even make the particles overcome high energy barriers of more than 20 $k_B T$.

Lattice Boltzmann simulations yield the permeability of the PBs. For each particle size, it is an exponential function of the porosity (see figure 5-3). The exponential coefficients resulting from the simulations are almost identical to the experimental ones.

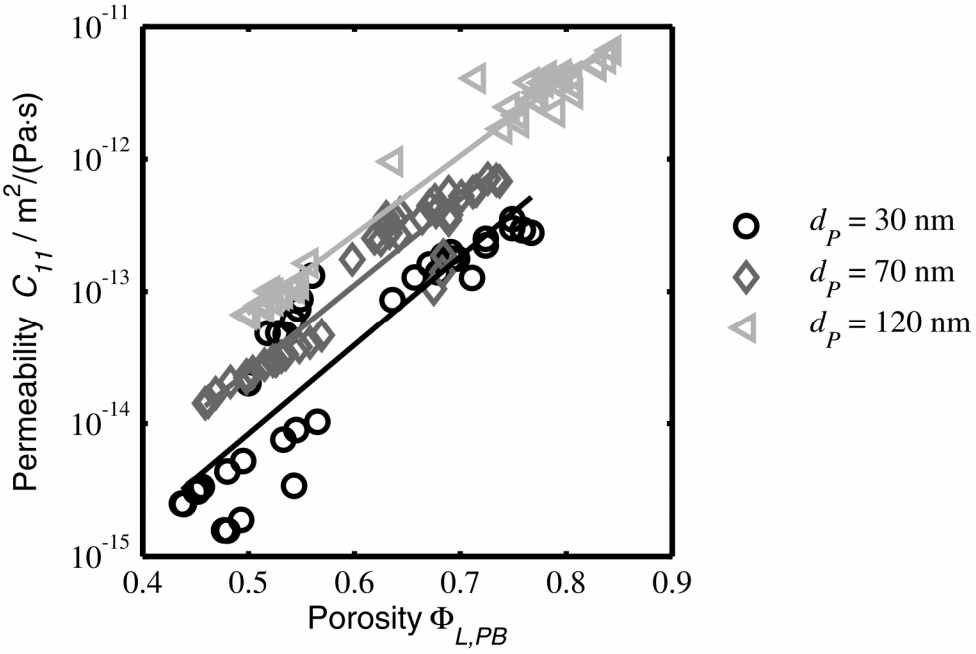

Figure 5-3: Permeability C_{11} of PBs consisting for different particle diameters d_P depending on the porosity $\Phi_{L,PB}$. The porosity is determined by the ionic strength, the pH value and the compressive load.

5.2 Future prospects

While both the experimental and the numerical approach offer perspectives of further research, the main effort should be made to combine them in a common regime of investigations. Since a simulation of irregularly shaped particles and their interactions is far too demanding today and in the next years, one should do experiments with spherical particles, for example latex or silica particles. Commercially available and affordable suspensions of these particles are often stabilized sterically, so that self-made latex particles seem preferable. These do not have to be monodisperse since the simulation can be extended to polydisperse particles. In addition to comparing the

mass and charge transport between the experiments and the simulations, it seems possible to determine the structure of the PBs by small angle neutron scattering if the particles are deuterated in order to increase the contrast between the particles and the liquid [Hahn, K., et al. 1986].

The knowledge on transport in nanoporous structures should be converted into technological processes, for example electrowashing of PBs, which is a new and promising technique for removing ions from dead-end pores within the particles. An alternating voltage extricates the ions from the pores and a pressure-driven flow drags them out of the packed bed. Preliminary experiments showed an increase of the washing efficiency by a factor of 7, which makes the process commercially interesting. Electrohydrodynamic transport and electrowashing should also be investigated for porous systems containing different non-aqueous liquids.

The lattice Boltzmann simulations of the fluid transport in PBs are currently extended to include electroosmotic flow. Electroosmosis is driven by the Coulomb force acting on the counter ions in the diffuse part of the electrochemical double layer. This force is implemented in the momentum balance

$$\rho_L \frac{\partial \boldsymbol{v}}{\partial t} + \rho_L \left(\boldsymbol{v} \cdot \nabla \right) \boldsymbol{v} = -\nabla p + \eta \nabla^2 \boldsymbol{v} + \rho_{el} \nabla \Psi_{el}, \qquad (5\text{-}1)$$

with the density ρ_L, the velocity $\boldsymbol{v}$, the time t, the pressure p, the viscosity η, the charge density ρ_{el} and the electric potential Ψ_{el}. In the regime of Smoluchowski's assumption of a thin electrochemical double layer, the driving gradient of the electric potentials is approximated by the externally applied field $\nabla \Psi_{el} = \Delta \Psi_{el} / L_{PB}$, with the externally applied voltage $\Delta \Psi_{el}$ and the thickness of the packed bed L_{PB}. According to the Poisson equation, the charge density is $\rho_e = \varepsilon_0 \varepsilon_{rel} \nabla^2 \Psi_{el}$, with the vacuum permittivity ε_0, the relative permittivity ε_{rel}, and the electric potential in the electrochemical double layer resulting from equation (2-3). The resulting body force is implemented via the external acceleration $\boldsymbol{b}$ in the collision operator of the lattice Boltzmann simulations, see equation (4-23). This method also yields the streaming current in the PBs. Implementing the electric conduction would complete a numerical approach to the interrelation of mass and charge transport in nanoporous structures.

6 Appendix

6.1 Complementing experimental results

6.1.1 Electroosmotic flow

The influence of the pH value and the compression on the electroosmosis coefficient for PBs consisting of Disperal 20® and Disperal 40® is presented in figure 6-1 and figure 6-2, respectively. Also for these materials, the predictions of the capillary model agree well with the measurements.

As for Disperal® (see figure 3-32), the electroosmosis coefficient is reduced upon compression because of the lower geometry ratio. This also explains the maximum of the absolute value of C_{12} at pH 7, where both the geometry ratio and the zeta potential are relatively high. Further, the modulus of the electroosmotic coefficient is smaller at low pH values than at high pH values. The geometry ratio also explains why the electroosmosis coefficient for Disperal 20® is higher than for Disperal 40®.

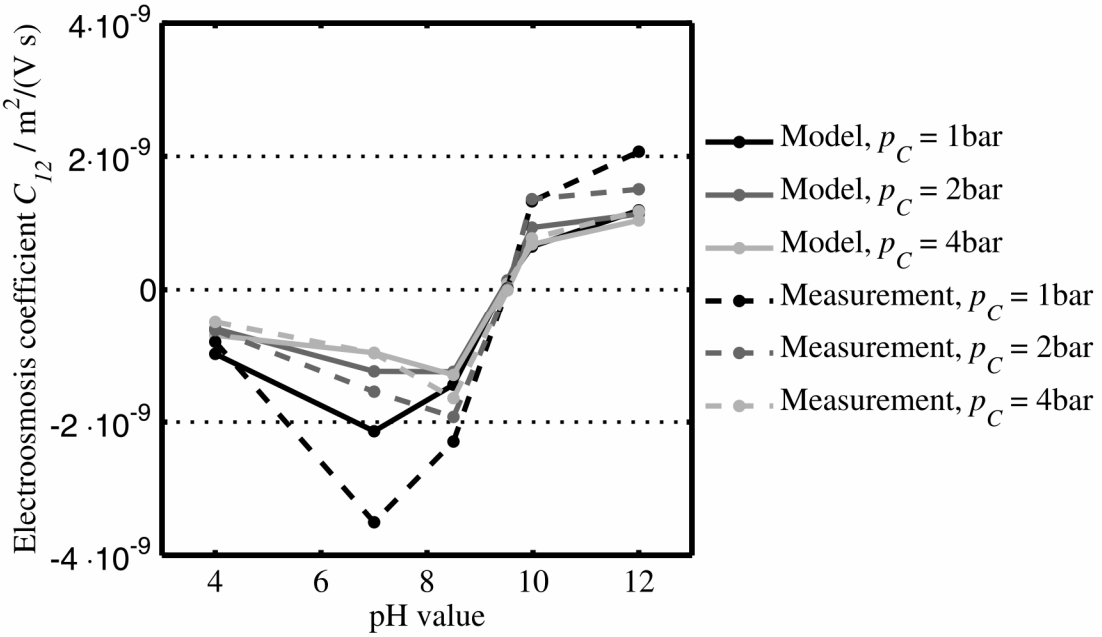

Figure 6-1: Electroosmosis coefficient C_{12} of the PBs consisting of Disperal 20® depending on the pH value for different compressive loads p_C at an ionic strength of 0.02 mol/L.

The effect of increasing the ionic strength on the electroosmosis coefficient for PB consisting of Disperal 20® and Disperal40® (see figure 6-3 and figure 6-4) is smaller than the influence of changing the pH value because of the counteracting effects of a

decreasing Debye length and decreasing hydraulic resistance. The electroosmosis coefficient decreases with decreasing geometry ratio, as caused by a stronger compression or variation of the particle material.

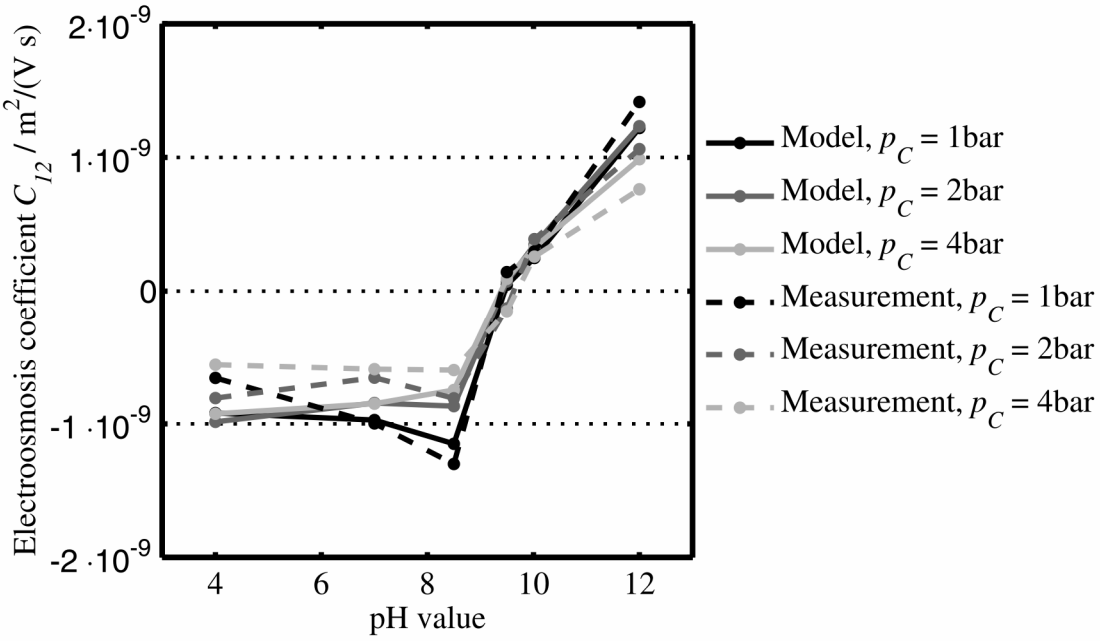

Figure 6-2: Electroosmosis coefficient C_{12} of the PBs consisting of Disperal 40® depending on the pH value for different compressive loads p_C at an ionic strength of 0.02 mol/L.

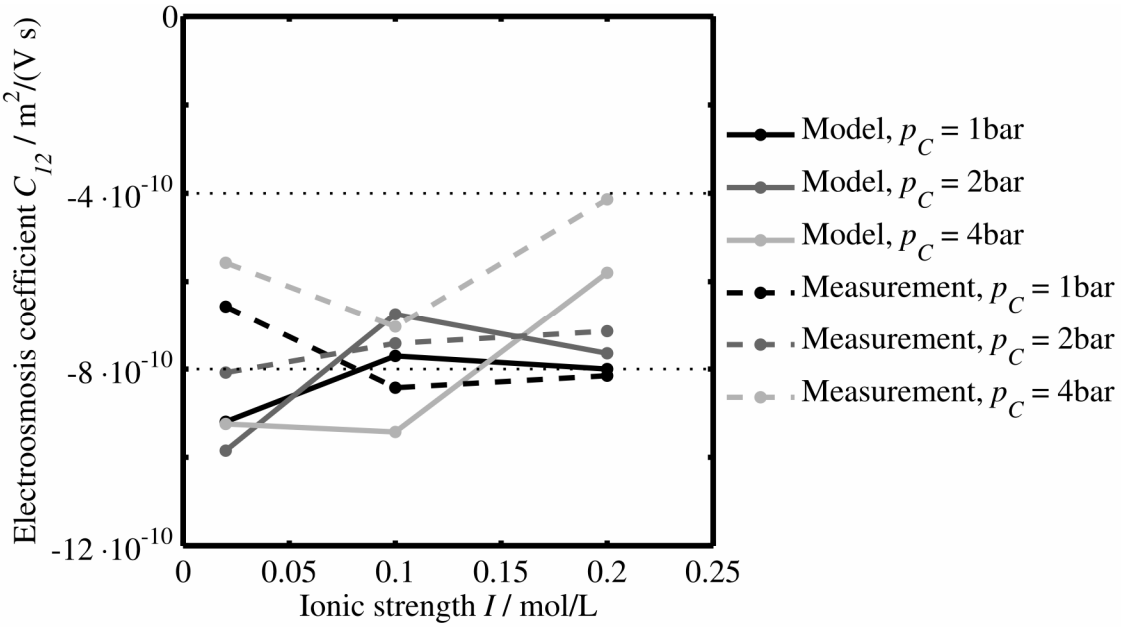

Figure 6-3: Electroosmosis coefficient C_{12} of the PBs consisting of Disperal 20® depending on the ionic strength I at a pH value of 4 for different compressive loads p_C.

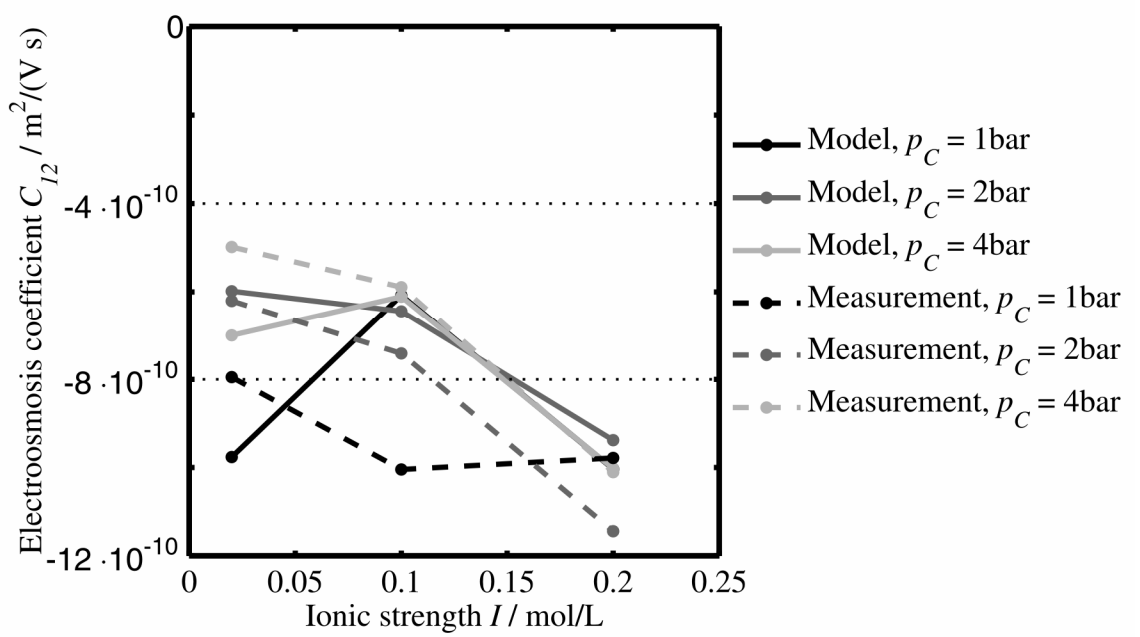

Figure 6-4: Electroosmosis coefficient C_{12} of the PBs consisting of Disperal 40® depending on the ionic strength I at a pH value of 4 for different compressive loads p_C.

6.1.2 Streaming potential

The influence of the pH value and the compression on the streaming potential coefficient for Disperal 20® and Disperal 40® (see figure 6-5 and figure 6-6) is similar to the influence for Disperal® (see figure 3-35). The higher streaming potential coefficient for Disperal 20® in comparison to Disperal® is attributed to the larger particles, while this effect is compensated by the lower decreasing porosity when comparing Disperal 40® to Disperal 20®.

The streaming potential coefficient for Disperal 20® and Disperal 40® (see figure 6-7 and figure 6-8) also decreases with increasing ionic strength, like for Disperal® (see figure 3-36). The smallest streaming potential is observed for Disperal® and the coefficients are similar for Disperal 20® and Disperal 40® because the effect of the particle size is compensated by the effect of porosity.

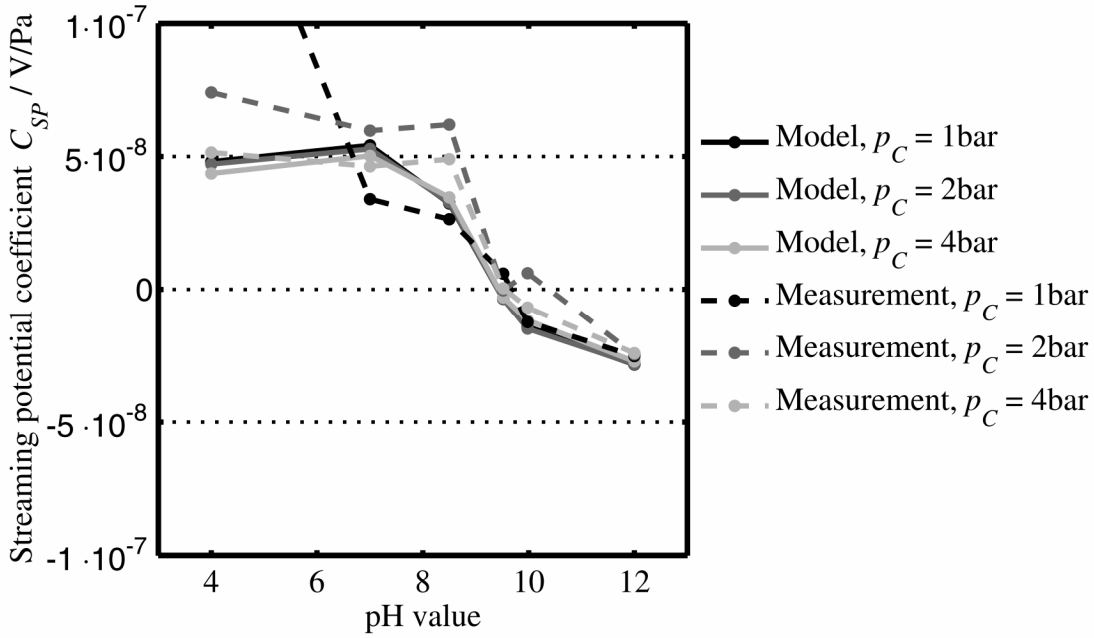

Figure 6-5: Streaming potential coefficient C_{SP} of the PBs consisting of Disperal 20® depending on the pH value for different compressive loads p_C at an ionic strength of 0.02 mol/L.

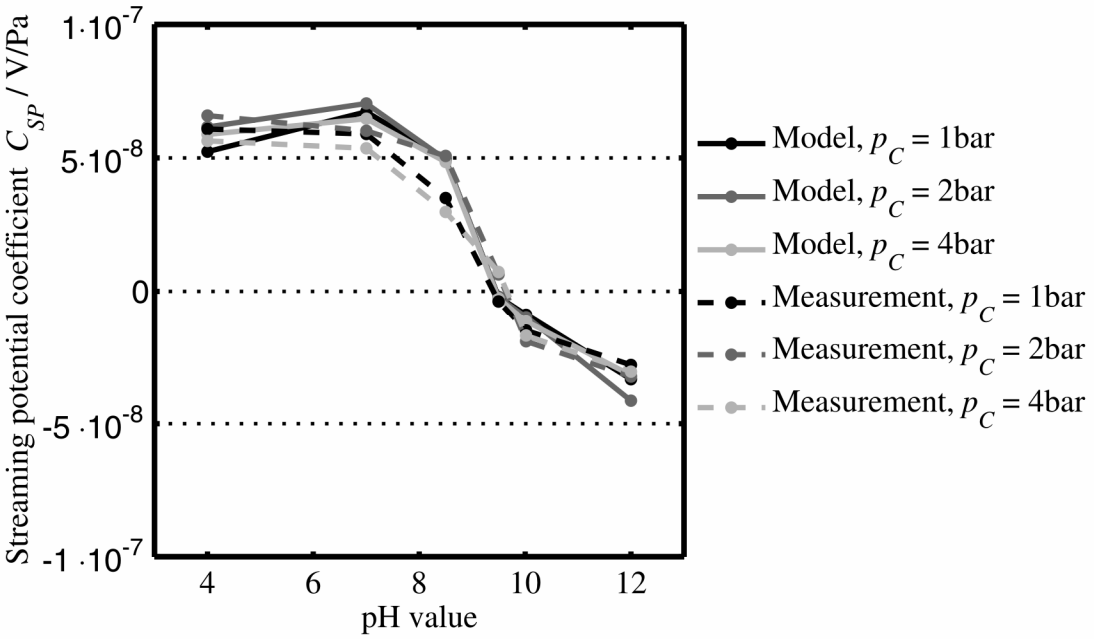

Figure 6-6: Streaming potential coefficient C_{SP} of the PBs consisting of Disperal 40® depending on the pH value for different compressive loads p_C at an ionic strength of 0.02 mol/L. The solid lines indicate the predictions of the capillary model; the dashed lines show the measured values.

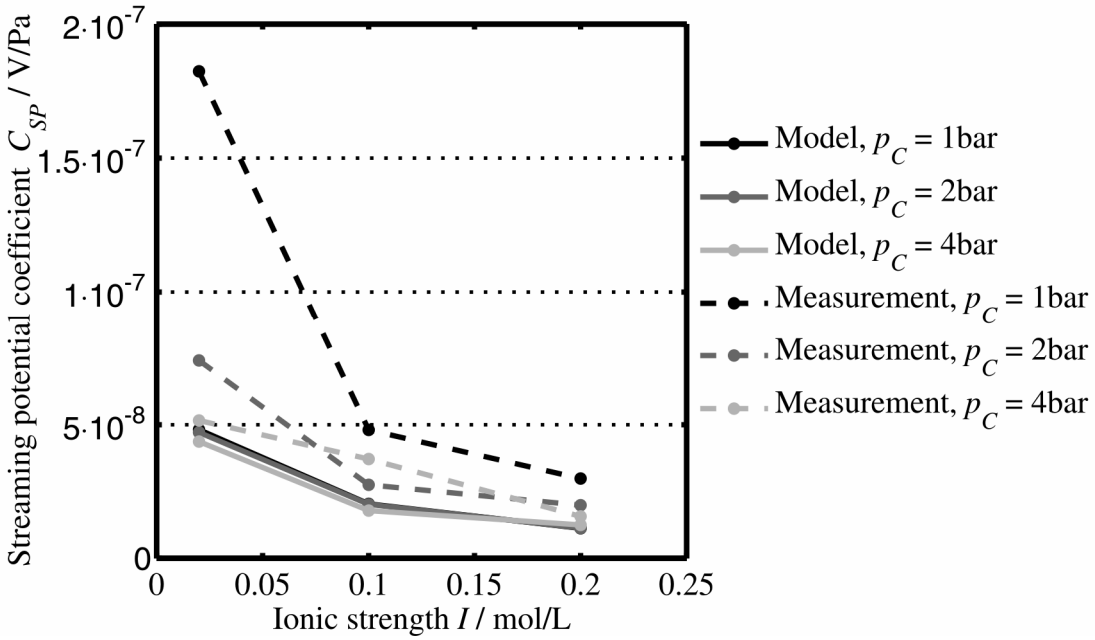

Figure 6-7: Streaming potential coefficient C_{SP} of the PBs consisting of Disperal 20® depending on the ionic strength I for different compressive loads p_C at a pH value of 4. The solid lines indicate the predictions of the capillary model; the dashed lines show the measured values.

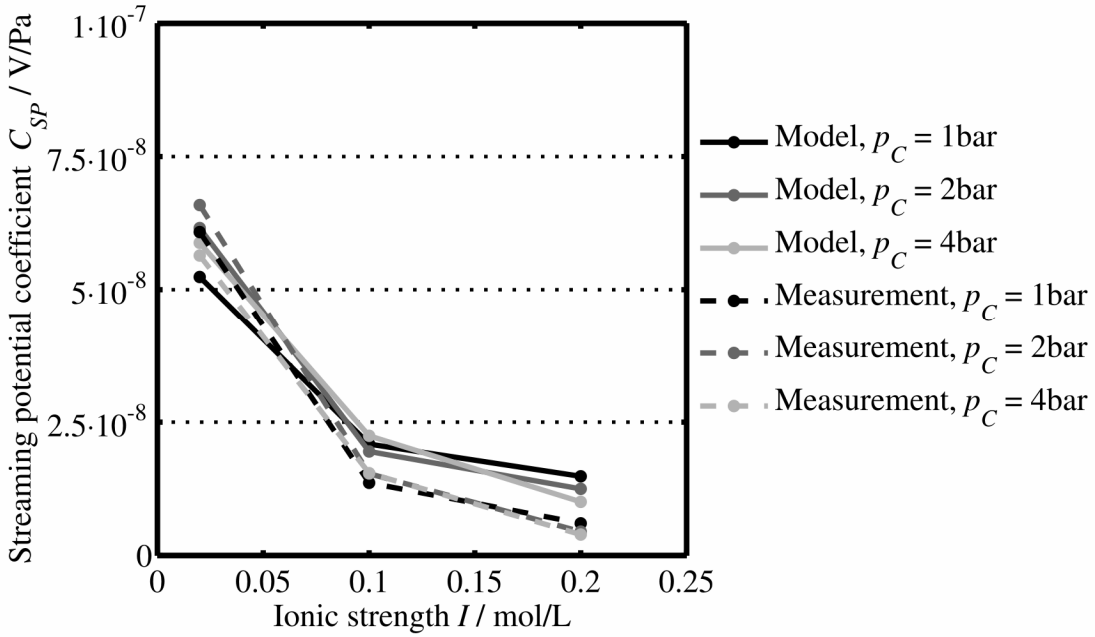

Figure 6-8: Streaming potential coefficient C_{SP} of the PBs consisting of Disperal 40® depending on the ionic strength I for different compressive loads p_C at a pH value of 4. The solid lines indicate the predictions of the capillary model; the dashed lines show the measured values.

6.1.3 Confidence Intervals

The following tables give the 95% confidence intervals for the EHT coefficients as measured and as calculated with the capillary model.

Table 6-1: 95% confidence intervals for the permeability C_{11} in m²/(Pa s)

		Disperal			Disperal			Disperal		
pH value	I	1bar	2bar	4bar	1bar	2bar	4bar	1bar	2bar	4bar
4	0,02	[5.97E-15; 6.81E-15]	[2.95E-15; 3.34E-15]	[7.86E-16; 1.14E-15]	[1.30E-14; 1.59E-14]	[6.47E-15; 7.22E-15]	[4.40E-15; 4.55E-15]	[2.30E-14; 2.60E-14]	[1.45E-14; 1.75E-14]	[7.83E-15; 9.32E-15]
7,01	0,02	[1.87E-14; 3.63E-14]	[8.37E-15; 9.50E-15]	[4.46E-15; 4.75E-15]	[9.96E-14; 1.11E-13]	[4.05E-14; 4.30E-14]	[2.07E-14; 2.18E-14]	[7.71E-14; 1.10E-13]	[4.46E-14; 5.50E-14]	[3.06E-14; 3.41E-14]
8,5	0,02	[4.11E-14; 4.98E-14]	[1.80E-14; 1.91E-14]	[8.52E-15; 9.09E-15]	[1.42E-13; 1.50E-13]	[6.13E-14; 6.39E-14]	[3.15E-14; 3.30E-14]	[1.60E-13; 1.83E-13]	[7.67E-14; 8.02E-14]	[4.32E-14; 4.57E-14]
9,52	0,02	[4.46E-14; 5.54E-14]	[1.91E-14; 2.05E-14]	[9.48E-15; 9.99E-15]	[1.61E-13; 1.70E-13]	[7.01E-14; 7.39E-14]	[3.63E-14; 3.79E-14]	[1.92E-13; 2.15E-13]	[9.06E-14; 9.50E-14]	[4.99E-14; 5.21E-14]
10	0,02	[4.08E-14; 5.55E-14]	[1.96E-14; 2.06E-14]	[9.41E-15; 1.00E-14]	[1.53E-13; 1.66E-13]	[6.68E-14; 7.02E-14]	[3.47E-14; 3.56E-14]	[2.14E-13; 2.41E-13]	[1.36E-13; 1.43E-13]	[6.27E-14; 6.50E-14]
12,02	0,02	[4.48E-14; 5.07E-14]	[1.87E-14; 2.06E-14]	[9.36E-15; 9.70E-15]	[1.44E-13; 1.61E-13]	[6.44E-14; 6.77E-14]	[3.35E-14; 3.50E-14]	[1.77E-13; 1.96E-13]	[8.27E-14; 8.61E-14]	[4.51E-14; 4.65E-14]
4,01	0,1	[1.16E-14; 1.76E-14]	[3.69E-15; 4.67E-15]	[1.80E-15; 2.10E-15]	[7.15E-14; 7.72E-14]	[3.33E-14; 3.52E-14]	[1.76E-14; 1.82E-14]	[1.00E-13; 1.07E-13]	[4.47E-14; 5.03E-14]	[2.58E-14; 2.65E-14]
4,01	0,2	[3.27E-14; 3.42E-14]	[4.77E-15; 5.34E-15]	[2.14E-15; 2.35E-15]	[8.48E-14; 8.95E-14]	[4.02E-14; 4.22E-14]	[2.16E-14; 2.26E-14]	[1.08E-13; 1.24E-13]	[5.32E-14; 5.60E-14]	[2.97E-14; 3.05E-14]

Table 6-2: 95% confidence intervals for the electric conductivity C_{22} in S/m

		Disperal			Disperal			Disperal		
pH value	I	1bar	2bar	4bar	1bar	2bar	4bar	1bar	2bar	4bar
4	0,02	[1.34E-02; 1.58E-02]	[1.07E-02; 1.22E-02]	[8.89E-03; 9.83E-03]	[1.32E-02; 1.91E-02]	[9.26E-03; 9.47E-03]	[9.11E-03; 1.33E-02]	[9.42E-03; 1.26E-02]	[6.73E-03; 1.24E-02]	[8.35E-03; 9.64E-03]
7,01	0,02	[2.24E-02; 2.84E-02]	[1.50E-02; 2.70E-02]	[1.12E-02; 1.77E-02]	[6.28E-02; 6.67E-02]	[2.47E-02; 3.35E-02]	[1.59E-02; 2.30E-02]	[1.33E-02; 1.73E-02]	[8.08E-03; 1.10E-02]	[8.02E-03; 9.59E-03]
8,5	0,02	[2.14E-02; 2.92E-02]	[1.50E-02; 2.25E-02]	[1.14E-02; 1.21E-02]	[6.94E-02; 8.98E-02]	[3.25E-02; 7.10E-02]	[2.87E-02; 5.37E-02]	[1.98E-02; 3.30E-02]	[1.46E-02; 1.82E-02]	[1.16E-02; 1.30E-02]
9,52	0,02	[2.09E-02; 2.75E-02]	[1.32E-02; 1.64E-02]	[1.06E-02; 1.50E-02]	[6.73E-02; 7.55E-02]	[4.30E-02; 6.45E-02]	[2.91E-02; 3.69E-02]	[2.68E-02; 2.91E-02]	[1.46E-02; 4.89E-02]	[1.80E-02; 4.05E-02]
10	0,02	[2.26E-02; 3.15E-02]	[1.57E-02; 2.56E-02]	[9.88E-03; 1.79E-02]	[8.03E-02; 8.56E-02]	[8.16E-02; 9.16E-02]	[5.78E-02; 7.13E-02]	[2.96E-02; 4.22E-02]	[3.81E-02; 4.15E-02]	[2.13E-02; 2.90E-02]
12,02	0,02	[3.74E-02; 6.34E-02]	[2.78E-02; 4.93E-02]	[2.15E-02; 3.31E-02]	[5.56E-02; 9.03E-02]	[3.84E-02; 7.16E-02]	[2.88E-02; 5.63E-02]	[3.48E-02; 5.17E-02]	[2.17E-02; 3.55E-02]	[2.17E-02; 2.86E-02]
4,01	0,1	[2.69E-02; 2.83E-02]	[2.07E-02; 2.65E-02]	[1.66E-02; 2.09E-02]	[3.72E-02; 5.11E-02]	[3.32E-02; 4.07E-02]	[3.09E-02; 3.53E-02]	[3.23E-02; 5.04E-02]	[1.95E-02; 4.43E-02]	[2.19E-02; 4.38E-02]
4,01	0,2	[3.85E-02; 5.40E-02]	[3.04E-02; 4.27E-02]	[2.14E-02; 3.20E-02]	[1.16E-01; 1.61E-01]	[8.63E-02; 1.16E-01]	[7.33E-02; 9.12E-02]	[5.08E-02; 7.10E-02]	[5.43E-02; 6.01E-02]	[4.35E-02; 4.83E-02]

Table 6-3: 95% confidence intervals for the Dukhin number Du

		Disperal			Disperal			Disperal		
pH value	I	1bar	2bar	4bar	1bar	2bar	4bar	1bar	2bar	4bar
4	0,02	[1.35E+00; 1.56E+00]	[1.94E+00; 2.27E+00]	[2.46E+00; 2.77E+00]	[5.84E-01; 6.58E-01]	[6.21E-01; 6.68E-01]	[7.23E-01; 7.48E-01]	[3.64E-01; 6.96E-01]	[3.22E-01; 4.30E-01]	[4.12E-01; 4.22E-01]
7,01	0,02	[4.08E-01; 8.78E-01]	[6.00E-01; 6.45E-01]	[6.66E-01; 7.82E-01]	[1.55E-01; 1.66E-01]	[1.73E-01; 1.81E-01]	[2.04E-01; 2.21E-01]	[2.77E-02; 3.75E-02]	[7.80E-03; 1.00E-02]	[5.11E-02; 5.63E-02]
8,5	0,02	[6.01E-01; 9.36E-01]	[5.01E-01; 6.34E-01]	[5.33E-01; 7.09E-01]	[-2.82E-02; -2.45E-02]	[-3.29E-02; -2.87E-02]	[-5.84E-02; -5.65E-02]	[-1.92E-01; -1.86E-01]	[-1.99E-01; -1.80E-01]	[-1.88E-01; -1.80E-01]
9,52	0,02	[1.92E-01; 2.99E-01]	[3.03E-01; 3.74E-01]	[2.77E-01; 3.68E-01]	[1.34E-01; 1.52E-01]	[1.10E-01; 1.23E-01]	[2.05E-01; 2.64E-01]	[3.77E-01; 4.62E-01]	[2.62E-01; 4.20E-01]	[1.90E-01; 2.67E-01]
10	0,02	[-8.12E-04; -3.02E-04]	[2.10E-01; 2.51E-01]	[1.56E-01; 2.08E-01]	[2.08E-01; 2.32E-01]	[1.74E-01; 1.91E-01]	[3.24E-01; 4.08E-01]	[6.73E-01; 7.99E-01]	[5.02E-01; 7.33E-01]	[3.86E-01; 4.99E-01]
12,02	0,02	[2.06E-01; 2.49E-01]	[2.53E-01; 3.07E-01]	[3.42E-01; 4.00E-01]	[8.48E-02; 1.14E-01]	[9.68E-02; 1.09E-01]	[1.18E-01; 1.30E-01]	[9.84E-03; 1.12E-02]	[-1.10E-01; -6.69E-02]	[2.83E-02; 4.16E-02]
4,01	0,1	[9.70E-02; 1.58E-01]	[2.13E-01; 2.92E-01]	[2.19E-01; 3.16E-01]	[3.28E-02; 3.93E-02]	[3.77E-02; 4.31E-02]	[1.03E-01; 1.19E-01]	[2.07E-02; 2.40E-02]	[5.51E-02; 6.44E-02]	[-1.47E-02; -1.26E-02]
4,01	0,2	[3.01E-03; 3.67E-02]	[4.65E-03; 6.92E-03]	[2.87E-03; 3.42E-03]	[-1.38E-02; -9.91E-03]	[-1.86E-02; -1.64E-02]	[-6.58E-02; -5.56E-02]	[-1.70E-01; -9.31E-02]	[-6.16E-02; -6.09E-02]	[3.56E-02; 5.42E-02]

Table 6-4: 95% confidence intervals for the capillary conductivity $C_{22,Cap}$ in S/m

		Disperal			Disperal			Disperal		
pH value	I	1bar	2bar	4bar	1bar	2bar	4bar	1bar	2bar	4bar
4	0,02	[1.06E+00; 1.23E+00]	[1.41E+00; 1.65E+00]	[1.72E+00; 1.94E+00]	[6.20E-01; 6.99E-01]	[6.49E-01; 6.98E-01]	[7.15E-01; 7.39E-01]	[4.16E-01; 7.96E-01]	[4.42E-01; 5.89E-01]	[5.33E-01; 5.46E-01]
7,01	0,02	[4.20E-01; 9.05E-01]	[6.28E-01; 6.74E-01]	[6.53E-01; 7.66E-01]	[3.70E-01; 3.96E-01]	[3.84E-01; 4.01E-01]	[3.97E-01; 4.30E-01]	[2.62E-01; 3.55E-01]	[2.58E-01; 3.32E-01]	[3.06E-01; 3.37E-01]
8,5	0,02	[5.75E-01; 8.96E-01]	[5.46E-01; 6.92E-01]	[5.58E-01; 7.43E-01]	[2.56E-01; 2.94E-01]	[2.53E-01; 2.91E-01]	[2.52E-01; 2.61E-01]	[1.78E-01; 1.83E-01]	[1.71E-01; 1.89E-01]	[1.80E-01; 1.87E-01]
9,52	0,02	[2.68E-01; 5.99E-01]	[4.40E-01; 5.36E-01]	[4.05E-01; 5.52E-01]	[3.50E-01; 3.98E-01]	[3.39E-01; 3.78E-01]	[3.87E-01; 4.67E-01]	[5.02E-01; 5.68E-01]	[4.21E-01; 5.58E-01]	[3.89E-01; 4.58E-01]
10	0,02	[1.58E-01; 4.26E-01]	[3.89E-01; 4.66E-01]	[3.43E-01; 4.55E-01]	[3.98E-01; 4.44E-01]	[3.80E-01; 4.18E-01]	[4.49E-01; 5.65E-01]	[6.62E-01; 7.86E-01]	[5.32E-01; 7.76E-01]	[4.81E-01; 6.22E-01]
12,02	0,02	[7.58E-01; 9.15E-01]	[8.11E-01; 9.84E-01]	[9.24E-01; 1.08E+00]	[5.76E-01; 7.73E-01]	[6.39E-01; 7.17E-01]	[6.70E-01; 7.35E-01]	[5.37E-01; 6.12E-01]	[3.49E-01; 5.76E-01]	[4.87E-01; 7.16E-01]
4,01	0,1	[1.39E+00; 2.26E+00]	[1.85E+00; 2.53E+00]	[1.83E+00; 2.64E+00]	[1.42E+00; 1.70E+00]	[1.47E+00; 1.68E+00]	[1.65E+00; 1.90E+00]	[1.41E+00; 1.63E+00]	[1.50E+00; 1.75E+00]	[1.31E+00; 1.52E+00]
4,01	0,2	[4.58E-01; 5.58E+00]	[2.36E+00; 3.51E+00]	[2.67E+00; 3.18E+00]	[2.37E+00; 3.30E+00]	[2.63E+00; 2.97E+00]	[2.34E+00; 2.76E+00]	[1.51E+00; 2.76E+00]	[2.53E+00; 2.56E+00]	[2.51E+00; 3.82E+00]

Table 6-5: 95% confidence intervals for the geometry ratio R_{Geo}

		Disperal			Disperal			Disperal		
pH value	I	1bar	2bar	4bar	1bar	2bar	4bar	1bar	2bar	4bar
4	0,02	[1.06E-02; 1.48E-02]	[6.24E-03; 8.73E-03]	[4.51E-03; 5.71E-03]	[1.79E-02; 3.11E-02]	[1.33E-02; 1.45E-02]	[1.18E-02; 1.89E-02]	[9.86E-03; 2.65E-02]	[1.04E-02; 2.67E-02]	[1.51E-02; 1.83E-02]
7,01	0,02	[1.98E-02; 5.69E-02]	[2.19E-02; 4.26E-02]	[1.41E-02; 2.65E-02]	[1.58E-01; 1.80E-01]	[6.13E-02; 8.68E-02]	[3.66E-02; 5.76E-02]	[3.56E-02; 6.34E-02]	[2.33E-02; 4.14E-02]	[2.36E-02; 3.12E-02]
8,5	0,02	[2.16E-02; 4.72E-02]	[2.06E-02; 3.99E-02]	[1.49E-02; 2.12E-02]	[2.32E-01; 3.47E-01]	[1.16E-01; 2.64E-01]	[1.15E-01; 2.05E-01]	[1.12E-01; 1.81E-01]	[7.65E-02; 1.06E-01]	[6.20E-02; 7.25E-02]
9,52	0,02	[2.70E-02; 8.47E-02]	[2.40E-02; 3.65E-02]	[1.80E-02; 3.53E-02]	[1.71E-01; 2.11E-01]	[1.16E-01; 1.84E-01]	[6.08E-02; 9.37E-02]	[4.75E-02; 5.70E-02]	[2.54E-02; 1.04E-01]	[3.97E-02; 9.84E-02]
10	0,02	[3.50E-02; 1.50E-01]	[3.23E-02; 6.41E-02]	[1.98E-02; 4.99E-02]	[1.81E-01; 2.13E-01]	[1.96E-01; 2.38E-01]	[1.01E-01; 1.54E-01]	[3.78E-02; 6.13E-02]	[4.68E-02; 7.48E-02]	[3.37E-02; 5.74E-02]
12,02	0,02	[3.90E-02; 8.14E-02]	[2.68E-02; 5.91E-02]	[1.93E-02; 3.52E-02]	[6.66E-02; 1.50E-01]	[5.19E-02; 1.10E-01]	[3.82E-02; 8.31E-02]	[5.57E-02; 9.50E-02]	[3.16E-02; 9.19E-02]	[2.80E-02; 5.54E-02]
4,01	0,1	[1.13E-02; 1.90E-02]	[7.79E-03; 1.38E-02]	[5.90E-03; 1.09E-02]	[2.13E-02; 3.53E-02]	[1.95E-02; 2.75E-02]	[1.60E-02; 2.12E-02]	[1.93E-02; 3.52E-02]	[1.15E-02; 2.77E-02]	[1.37E-02; 3.27E-02]
4,01	0,2	[-2.48E-04; 3.09E-02]	[7.90E-03; 1.70E-02]	[6.53E-03; 1.18E-02]	[3.16E-02; 6.60E-02]	[2.86E-02; 4.36E-02]	[2.60E-02; 3.85E-02]	[1.54E-02; 4.15E-02]	[2.12E-02; 2.37E-02]	[1.09E-02; 1.81E-02]

Table 6-6: 95% confidence intervals for the electroosmosis coefficient C_{12} in m²/(V s) as resulting from the capillary model

		Disperal			Disperal			Disperal		
pH value	I	1bar	2bar	4bar	1bar	2bar	4bar	1bar	2bar	4bar
4	0,02	[-6.20E-10; -4.46E-10]	[-4.12E-10; -2.94E-10]	[-2.95E-10; -2.33E-10]	[-1.24E-09; -7.13E-10]	[-6.25E-10; -5.72E-10]	[-8.61E-10; -5.38E-10]	[-1.34E-09; -4.99E-10]	[-1.42E-09; -5.52E-10]	[-1.01E-09; -8.36E-10]
7,01	0,02	[-7.96E-10; -2.78E-10]	[-8.14E-10; -4.20E-10]	[-6.33E-10; -3.37E-10]	[-2.28E-09; -2.00E-09]	[-1.45E-09; -1.03E-09]	[-1.17E-09; -7.45E-10]	[-1.25E-09; -6.98E-10]	[-1.08E-09; -6.09E-10]	[-9.66E-10; -7.32E-10]
8,5	0,02	[-2.73E-10; -1.25E-10]	[-2.99E-10; -1.54E-10]	[-1.97E-10; -1.38E-10]	[-1.73E-09; -1.16E-09]	[-1.73E-09; -7.59E-10]	[-1.65E-09; -9.29E-10]	[-1.42E-09; -8.82E-10]	[-1.01E-09; -7.30E-10]	[-8.05E-10; -6.88E-10]
9,52	0,02	[2.27E-11; 7.14E-11]	[2.68E-11; 4.08E-11]	[2.49E-11; 4.88E-11]	[1.20E-10; 1.48E-10]	[1.09E-10; 1.73E-10]	[7.04E-11; 1.09E-10]	[4.26E-11; 5.10E-11]	[2.85E-11; 1.17E-10]	[5.32E-11; 1.32E-10]
10	0,02	[1.32E-10; 5.68E-10]	[1.64E-10; 3.25E-10]	[1.26E-10; 3.18E-10]	[5.95E-10; 7.03E-10]	[8.41E-10; 1.02E-09]	[5.38E-10; 8.21E-10]	[1.90E-10; 3.08E-10]	[2.67E-10; 4.27E-10]	[2.42E-10; 4.12E-10]
12,02	0,02	[5.02E-10; 1.05E-09]	[4.43E-10; 9.75E-10]	[3.95E-10; 7.19E-10]	[7.34E-10; 1.65E-09]	[7.27E-10; 1.54E-09]	[6.57E-10; 1.43E-09]	[9.03E-10; 1.54E-09]	[6.31E-10; 1.84E-09]	[6.63E-10; 1.31E-09]
4,01	0,1	[-5.51E-10; -3.26E-10]	[-5.60E-10; -3.16E-10]	[-5.15E-10; -2.79E-10]	[-7.59E-10; -4.57E-10]	[-7.53E-10; -5.36E-10]	[-6.96E-10; -5.26E-10]	[-9.95E-10; -5.46E-10]	[-9.54E-10; -3.95E-10]	[-1.33E-09; -5.57E-10]
4,01	0,2	[-8.22E-10; 6.59E-12]	[-5.55E-10; -2.58E-10]	[-4.75E-10; -2.63E-10]	[-1.36E-09; -6.50E-10]	[-1.13E-09; -7.43E-10]	[-1.20E-09; -8.09E-10]	[-1.17E-09; -4.34E-10]	[-8.07E-10; -7.21E-10]	[-7.23E-10; -4.36E-10]

Table 6-7: 95% confidence intervals for the electroosmosis coefficient C_{12} in m²/(V s) as resulting from the measurements

		Disperal			Disperal			Disperal		
pH value	I	1bar	2bar	4bar	1bar	2bar	4bar	1bar	2bar	4bar
4	0,02	[-4.04E-10; -3.76E-10]	[-2.41E-10; -2.08E-10]	[-1.66E-10; -1.38E-10]	[-9.01E-10; -6.89E-10]	[-7.38E-10; -5.03E-10]	[-5.79E-10; -4.18E-10]	[-7.43E-10; -5.71E-10]	[-9.02E-10; -7.14E-10]	[-5.81E-10; -5.34E-10]
7,01	0,02	[-1.05E-09; -4.83E-10]	[-8.18E-10; -4.94E-10]	[-5.10E-10; -3.26E-10]	[-3.60E-09; -3.41E-09]	[-1.79E-09; -1.30E-09]	[-1.11E-09; -8.22E-10]	[-1.09E-09; -9.05E-10]	[-7.52E-10; -5.56E-10]	[-6.32E-10; -5.50E-10]
8,5	0,02	[-4.11E-10; -2.14E-10]	[-2.98E-10; -2.22E-10]	[-1.78E-10; -1.41E-10]	[-2.60E-09; -1.99E-09]	[-2.45E-09; -1.39E-09]	[-2.05E-09; -1.24E-09]	[-1.61E-09; -9.91E-10]	[-8.96E-10; -7.22E-10]	[-6.25E-10; -5.71E-10]
9,52	0,02	[1.06E-10; 3.13E-10]	[6.69E-11; 1.52E-10]	[7.48E-11; 1.46E-10]	[-1.81E-10; 2.25E-10]	[-3.89E-11; 5.21E-11]	[-6.47E-11; 4.49E-11]	[-3.47E-10; 6.32E-10]	[-1.83E-10; -7.59E-11]	[-1.95E-10; -1.08E-10]
10	0,02	[2.45E-10; 8.67E-10]	[2.21E-10; 3.78E-10]	[1.43E-10; 2.87E-10]	[1.09E-09; 1.57E-09]	[1.20E-09; 1.52E-09]	[7.50E-10; 7.94E-10]	[2.40E-10; 3.54E-10]	[3.07E-10; 4.71E-10]	[2.36E-10; 2.83E-10]
12,02	0,02	[6.39E-10; 7.10E-10]	[5.65E-10; 1.12E-09]	[3.91E-10; 6.78E-10]	[1.50E-09; 2.65E-09]	[1.12E-09; 1.90E-09]	[7.73E-10; 1.58E-09]	[1.21E-09; 1.62E-09]	[8.49E-10; 1.28E-09]	[7.17E-10; 8.06E-10]
4,01	0,1	[-6.25E-10; -5.44E-10]	[-3.88E-10; -2.84E-10]	[-2.83E-10; -2.24E-10]	[-1.26E-09; -7.50E-10]	[-8.00E-10; -6.82E-10]	[-6.37E-10; -5.42E-10]	[-9.78E-10; -7.06E-10]	[-9.71E-10; -5.12E-10]	[-8.91E-10; -5.16E-10]
4,01	0,2	[-6.95E-10; -2.98E-11]	[-4.33E-10; -3.19E-10]	[-3.29E-10; -2.38E-10]	[-1.39E-09; -5.66E-10]	[-1.33E-09; -9.59E-10]	[-1.09E-09; -9.34E-10]	[-9.40E-10; -6.91E-10]	[-7.51E-10; -6.76E-10]	[-4.77E-10; -3.50E-10]

Table 6-8: 95% confidence intervals for the streaming potential coefficient C_{21} in V/Pa as resulting from the capillary model

		Disperal			Disperal			Disperal		
pH value	I	1bar	2bar	4bar	1bar	2bar	4bar	1bar	2bar	4bar
4	0,02	[2.56E-08; 2.97E-08]	[1.91E-08; 2.24E-08]	[1.63E-08; 1.84E-08]	[4.52E-08; 5.10E-08]	[4.54E-08; 4.89E-08]	[4.29E-08; 4.44E-08]	[3.60E-08; 6.88E-08]	[5.28E-08; 7.04E-08]	[5.81E-08; 5.96E-08]
7,01	0,02	[1.98E-08; 4.27E-08]	[3.07E-08; 3.30E-08]	[2.69E-08; 3.15E-08]	[5.24E-08; 5.61E-08]	[5.18E-08; 5.40E-08]	[4.83E-08; 5.23E-08]	[5.71E-08; 7.74E-08]	[6.16E-08; 7.92E-08]	[6.16E-08; 6.78E-08]
8,5	0,02	[9.47E-09; 1.47E-08]	[1.27E-08; 1.61E-08]	[1.17E-08; 1.56E-08]	[3.02E-08; 3.47E-08]	[3.04E-08; 3.50E-08]	[3.41E-08; 3.53E-08]	[4.85E-08; 5.01E-08]	[4.69E-08; 5.20E-08]	[4.75E-08; 4.96E-08]
9,52	0,02	[-4.16E-09; -1.86E-09]	[-2.94E-09; -2.42E-09]	[-3.15E-09; -2.31E-09]	[-3.72E-09; -3.27E-09]	[-3.84E-09; -3.45E-09]	[-3.34E-09; -2.77E-09]	[-2.19E-09; -1.93E-09]	[-2.57E-09; -1.94E-09]	[-2.81E-09; -2.39E-09]
10	0,02	[-3.08E-08; -1.14E-08]	[-1.57E-08; -1.31E-08]	[-1.76E-08; -1.33E-08]	[-1.50E-08; -1.34E-08]	[-1.57E-08; -1.42E-08]	[-1.31E-08; -1.04E-08]	[-9.55E-09; -8.04E-09]	[-1.15E-08; -7.92E-09]	[-1.30E-08; -1.01E-08]
12,02	0,02	[-2.51E-08; -2.08E-08]	[-2.34E-08; -1.93E-08]	[-2.06E-08; -1.76E-08]	[-3.26E-08; -2.43E-08]	[-2.99E-08; -2.66E-08]	[-2.86E-08; -2.60E-08]	[-3.55E-08; -3.12E-08]	[-5.16E-08; -3.12E-08]	[-3.79E-08; -2.58E-08]
4,01	0,1	[1.32E-08; 2.15E-08]	[1.22E-08; 1.68E-08]	[1.16E-08; 1.68E-08]	[1.85E-08; 2.22E-08]	[1.89E-08; 2.15E-08]	[1.66E-08; 1.92E-08]	[1.94E-08; 2.24E-08]	[1.80E-08; 2.10E-08]	[2.07E-08; 2.42E-08]
4,01	0,2	[1.59E-09; 1.94E-08]	[8.67E-09; 1.29E-08]	[9.90E-09; 1.18E-08]	[9.36E-09; 1.30E-08]	[1.06E-08; 1.20E-08]	[1.14E-08; 1.35E-08]	[1.05E-08; 1.92E-08]	[1.24E-08; 1.25E-08]	[7.96E-09; 1.21E-08]

Table 6-9: 95% confidence intervals for the streaming potential coefficient C_{21} in V/Pa as resulting from the measurements

		Disperal			Disperal			Disperal		
pH value	I	1bar	2bar	4bar	1bar	2bar	4bar	1bar	2bar	4bar
4	0,02	[2.29E-08; 2.72E-08]	[1.78E-08; 2.20E-08]	[1.52E-08; 1.60E-08]	[1.74E-07; 1.91E-07]	[7.07E-08; 7.75E-08]	[4.47E-08; 5.84E-08]	[5.51E-08; 6.65E-08]	[5.88E-08; 7.30E-08]	[3.71E-08; 7.58E-08]
7,01	0,02	[2.33E-08; 2.56E-08]	[2.69E-08; 3.11E-08]	[1.87E-08; 2.19E-08]	[-1.35E-07; 2.03E-07]	[2.90E-08; 9.05E-08]	[2.81E-08; 6.46E-08]	[5.28E-08; 6.53E-08]	[4.64E-08; 7.39E-08]	[4.41E-08; 6.32E-08]
8,5	0,02	[2.61E-09; 4.20E-09]	[8.98E-10; 5.34E-09]	[2.34E-09; 4.44E-09]	[-1.12E-07; 1.65E-07]	[-1.87E-08; 1.43E-07]	[1.35E-08; 8.46E-08]	[2.73E-08; 4.27E-08]	[-3.43E-09; 1.05E-07]	[2.72E-08; 3.23E-08]
9,52	0,02	[-1.48E-08; -1.39E-08]	[-1.00E-08; -9.47E-09]	[-1.21E-08; -9.69E-09]	[-1.03E-07; 1.15E-07]	[-2.69E-08; 2.62E-08]	[-2.47E-08; 2.56E-08]	[-1.37E-08; 6.06E-09]	[-8.28E-09; 2.11E-08]	[-4.47E-09; 1.90E-08]
10	0,02	[-3.03E-08; -2.81E-08]	[-3.03E-08; -2.84E-08]	[-2.61E-08; -2.46E-08]	[-1.82E-08; -6.59E-09]	[-3.67E-08; 4.90E-08]	[-1.98E-08; 5.92E-09]	[-2.32E-08; -6.75E-09]	[-1.16E-07; 7.76E-08]	[-2.85E-08; -5.35E-09]
12,02	0,02	[-2.62E-08; -2.25E-08]	[-2.39E-08; -2.11E-08]	[-2.28E-08; -1.94E-08]	[-2.62E-08; -2.43E-08]	[-2.54E-08; -2.38E-08]	[-2.50E-08; -2.33E-08]	[-2.94E-08; -2.64E-08]	[-3.37E-08; -3.10E-08]	[-3.16E-08; -2.93E-08]
4,01	0,1	[1.25E-08; 1.35E-08]	[1.01E-08; 1.16E-08]	[9.38E-09; 1.04E-08]	[-5.64E-08; 1.53E-07]	[1.08E-08; 4.42E-08]	[1.36E-09; 7.29E-08]	[1.29E-09; 2.59E-08]	[-5.07E-09; 3.57E-08]	[2.67E-09; 2.82E-08]
4,01	0,2	[6.97E-09; 9.53E-09]	[5.94E-09; 8.75E-09]	[6.38E-09; 9.46E-09]	[6.74E-09; 5.29E-08]	[-1.23E-08; 5.19E-08]	[-2.98E-09; 3.42E-08]	[-2.68E-08; 3.89E-08]	[-1.62E-08; 2.51E-08]	[-1.28E-08; 2.07E-08]

6.2 Complementing numerical results

The temporal evolution the pair correlation function reflects the formation of agglomerates prior to the filtration. Therefore, the filtration is started only when the peak heights of the pair correlation function remain constant. The evolution of the peak heights is shown in figure 6-10 and figure 6-9 for particles with a diameter of 30 nm and 70 nm, respectively. The filtrations are started after 0.65 ms for a particle diameter of 30 nm and after 4.4 ms for a particle diameter of 70 nm, where the peaks have almost reached a constant height. Longer agglomeration times would hardly affect the results, but only increase the numerical effort. The agglomerate time decreases with the decreasing particle diameter, also the time step of the simulation has to be reduced.

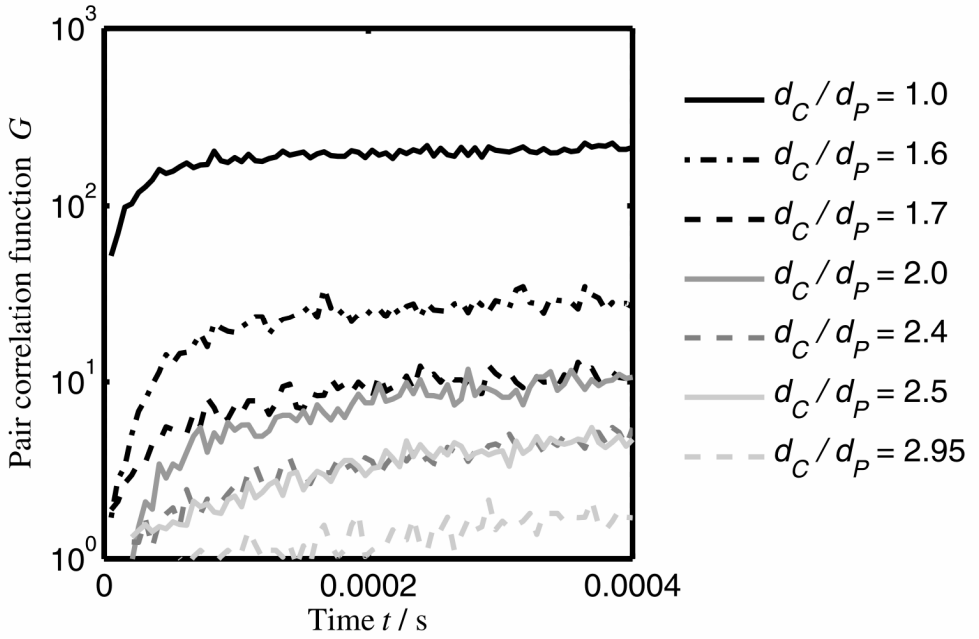

Figure 6-9: Evolution of the peak heights of the pair correlation function G for particles with a diameter of 30 nm at different center-to-center distances.

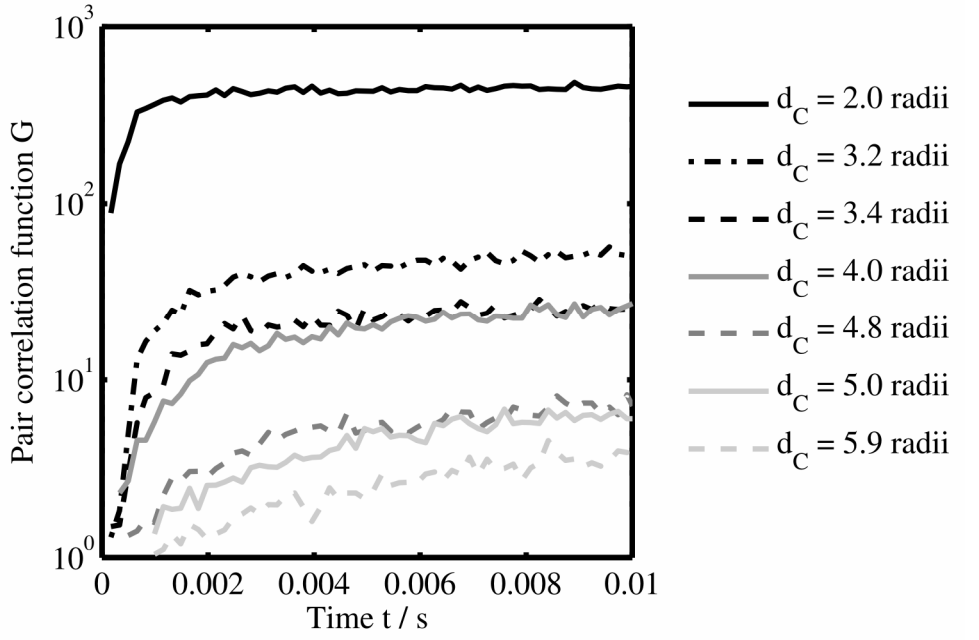

Figure 6-10: Evolution of the peak heights of the pair correlation function G for particles with a diameter of 70 nm at different center-to-center distances.

6.3 Nomenclature

Vectors are denoted by bold letters.

6.3.1 Latin symbols

a	Coefficient
a_{Ar}	Archie coefficient
A_{Cap}	Cross sectional area of the capillaries
a_{CK}	Carman-Kozeny coefficient
A_H	Hamaker constant
A_{PB}	Cross sectional area of the PB
Ar	Archimedes number
b	Coefficient
$\boldsymbol{b}$	Externally applied acceleration
c_i	Concentration of ion i
$c_{Al^{3+}}$	Concentration of Al^{3+} ions
c_{Lub}	Lubrication factor
$c_{S,LB}$	Speed of sound in the lattice Boltzmann simulations
C_{11}	Hydraulic permeability
C_{11}^*	Darcy permeability
C_{12}	Electroosmosis coefficient
$C_{12,Cap}$	Electroosmosis coefficient for the capillary model
C_{21}	Streaming current coefficient
C_{22}	Electric conductivity
$C_{22,Cap}$	Electric conductivity for the capillary system
$C_{22,L}$	Electric conductivity of the liquid
$C_{22,Surf}$	Electric conductivity of the surfaces
C_P	Porod constant
C_{SP}	Streaming potential coefficient
d_{32}	Sauter diameter
$d_{50,0}$	Number rated average particle diameter
d_{hydr}	Hydraulic diameter
d_C	Center-to-center distance
d_{Cap}	Diameter of the capillaries
d_P	Particle diameter
d_{Surf}	Surface-to-surface distance
D	Diffusion constant
D_f	Fractal dimension
D_H	Hooke constant

D_{MD} Diffusion constant for the MD particles

Du Dukhin number

Du_M Dukhin number for the membrane

Du_{PB} Dukhin number for the PB

e Elementary charge

$\boldsymbol{e}$ Microscopic velocity in lattice Boltzmann simulations

$\boldsymbol{e}_j$ Discretized microscopic velocity in the direction j

f Single-particle distribution function

f_j Single-particle distribution function for the direction j

f_{Equ} Equilibrium distribution function

$f_{Equ,j}$ Equilibrium distribution function for the direction j

$\boldsymbol{F}_{ext,m}$ Sum of external forces acting on particle m

$\boldsymbol{F}_{hydr,m}$ Hydraulic force acting on particle m

$\boldsymbol{F}_{inter,m}$ Sum of inter-particle forces acting on particle m

F_j Boltzmann distribution function for the direction j

$\boldsymbol{F}_m$ Force on particle m

$\boldsymbol{F}_{rand,m}$ Random force acting on particle m in Brownian dynamics

F_F Faraday constant

$\boldsymbol{F}_{Lub}$ Lubrication force

g Gravitational constant

G Pair correlation function

I Ionic strength

I_0 Single-particle scattering intensity

I_{el} Electric current

I_S Scattering intensity

I_{Str} Streaming current

$\boldsymbol{J}_{el}$ Charge flux

$\boldsymbol{J}_L$ Liquid flux

$\boldsymbol{k}$ Wave number vector of the scattered light

$\boldsymbol{k}_0$ Wave number vector of the incident light

k_B Boltzmann constant

K_{Hertz} Hertz constant

Kn Knudsen number

L_{Cap} Length of the capillary bundle

L_{Cell} Length of the SRD cells

L_{PB} Thickness of the PB

m_m Mass of the particle m

m_{Al} Molality of aluminium ions

m_{MD} Mass of one MD particle

m_S Mass of solids

m_{SRD} Mass of one SRD particle

Ma Mach number

$\boldsymbol{n}$ Normal vector in the direction of permeation

N Number of particles

N_k Number of particles in SRD cell k

$\bar{N}_k$ Average number of SRD particles per cell

N_{MD} Number of MD particles

p Pressure

p_{Comp} Compressive load

Pe Péclet number

q Modulus of the scattering vector

$\boldsymbol{q}$ Scattering vector

q_0 Number-rated particle size distribution

$r_{CO,i}$ Inner cut-off radius

$r_{CO,o}$ Outer cut-off radius

R Gas constant

R_{el} Electric resistance

R_{Geo} Geometry ratio

R_M Hydraulic resistance of the membrane

Re Reynolds number

S Surface atom

Sc Schmidt number

t Time

t_0 Initial time

T Temperature

T_{SRD} Temperature of the SRD fluid

v_i Velocity in direction i

v_{rel} Relative velocity

$\boldsymbol{v}_{rel,\perp}$ Relative velocity projected on the connecting line between the particle centers

$\boldsymbol{v}_{LB}$ Macroscopic velocity

v_{Sed} Stokes velocity

V Examination volume

$\dot{V}_{red}$ Reduced volumetric flux

$\dot{V}_{EO,\max}$ Maximum volumetric flux due to electroosmosis

V_L Volume of the liquid

$\dot{V}_L$ Volumetric flux of the liquid

V_{PB} Volume of the PB

w_j Lattice weights

$\boldsymbol{x}$ Position

$\bar{\dot{\boldsymbol{x}}}_k$ Mean velocity of the particles in the cell k

$\boldsymbol{x}_m$, $\boldsymbol{x}_n$ Positions of particles m and n

$\dot{\boldsymbol{x}}_m$, $\dot{\boldsymbol{x}}_n$ Velocities of particles m and n

$\ddot{\boldsymbol{x}}_m$ Acceleration of particle m

$\dot{\boldsymbol{x}}_{m,rel}$ Relative velocity of particle m

$x_{z,m}$ Vertical coordinate of the particle m

z_i Valency of ionic species i

6.3.2 Greek symbols

∇ Nabla operator

α Mass-related hydraulic resistance

δ Dirac delta function

Δp Pressure difference

$\Delta p_{EO,Max}$ Maximum pressure difference due to electroosmosis

Δp_M Pressure difference in the membrane

Δp_{PB} Pressure difference in the PB

Δt_{LB} Time step in the LB simulation

Δt_{MD} Time step in the MD simulation

Δt_{SRD} Time step in the SRD simulation

Δx Lattice constant

$\Delta \rho_{el}$ Difference in electron density

$\Delta \Psi_{el}$ Electric potential difference

$\Delta \Psi_{DLVO}$ Difference between the maximum and the secondary minimum of the DLVO potential

$\Delta \Psi_{Str}$ Streaming potential

$\Delta \Psi_{Str,M}$ Streaming potential of the membrane

$\Delta \Psi_{Str,PB}$ Streaming potential of the PB

ε_0 Vacuum permittivity

ε_{rel} Relative permittivity

$\Phi_{L,PB}$ Porosity of the PB

$\Phi_{S,Susp}$ Volume fraction of the solids in the suspension

η Dynamic viscosity of the liquid

η_{app} Apparent dynamic viscosity of the liquid

η_{SRD} Dynamic viscosity of the SRD fluid

κ Reciprocal Debye length

λ Mean free path of the SRD particles

λ_i Molar conductivity of ionic species i

λ_k Wave length

Θ Scattering angle

ρ_0 Reference density

ρ_L Density of the liquid

ρ_{LB} Density of the liquid in the LB simulations

ρ_S Solid density

σ_0 Charge density of the particle surface

σ_d Charge density of the diffuse layer

σ_i Charge density of the inner Helmholtz plane

τ_{Diff} Diffusion time

τ_L Liquid relaxation time

τ_{LB} Liquid relaxation time in the LB simulation

τ_P Particle relaxation time

τ_{Sed} Sedimentation time

τ_{TF} Thermal fluctuation time

Ω_{LB} Collision operator in lattice Boltzmann simulations

$\Omega_{LB,j}$ Collision operator for lattice vector j

$\Omega_{SRD,k}$ Rotation matrix for cell k in the SRD simulation

Ψ Potential

Ψ_0 Electric potential at the particle surface

Ψ_d Electric potential at the start of the diffuse layer

Ψ_{el} Electric potential

Ψ_i Electric potential at the inner Helmholtz plane

$\Psi_{DLVO,Min}$ Depth of the secondary minimum of the DLVO potential

Ψ_{vdW} Van-der-Waals potential

Ψ_{Born} Born potential

Ψ_{Coul} Coulomb potential

Ψ_{DLVO} Derjaguin-Landau-Verwey-Overbeek potential

Ψ_{Hertz} Hertz potential

ζ Zeta potential

ζ_M Zeta potential of the membrane

ζ_{PB} Zeta potential of the PB

6.3.3 Fixed indices

el	electric	*Cap*	Capillary
hydr	hydraulic	*L*	Liquid
i	Index for the ionic species and the coordinate directions	*Max*	Maximum
		Min	Minimum
j	Index for the lattice vectors	*P*	Particle
k	Index for the cells	*PB*	Packed bed
m	Index for the particles	*S*	Solid
n	Index for the particles	*Surf*	Surface

6.3.4 Abbreviations

DLVO Derjaguin-Landau-Verwey-Overbeek

EDL Electrochemical double layer

EHT Electrohydrodynamic transport

IEP Isoelectric point

MD Molecular dynamics

PB Packed bed

SEM Scanning electron microscopy

SRD Stochastic rotation dynamics

6.4 References

Aaltosalmi, U. (2005), "*Fluid flow in porous media with the lattice-Boltzmann method*", Ph.D. thesis, University of Jyväskylä, Finland.

Adhikari, R.; Stratford, K.; Cates, M. E.; Wagner, A. J. (2005), "*Fluctuating lattice Boltzmann*", Europhysics Letters 71 (3), p. 473.

Allen, M. P.; Tildesley, D. J. (1987), "*Computer simulation of liquids*", Clarendon Press: Oxford, UK.

Alles, C. M. (2000), "*Prozeßstrategien für die Filtration mit kompressiblen Kuchen*", Ph.D. thesis, University of Karlsruhe (TH), Germany.

Ariyaratnam, S. V.; Surplice, N. A.; Adem, E. H. (1987), "*Solubility of hydrogen in titanium wires and films at 300 K*", Journal of Materials Science Letters 6 (11), p. 1349.

Atkins, P. W.; De Paula, J. (2006), "*Atkins' Physical chemistry*", Oxford University Press: Oxford, UK.

Babick, F. (2005), "*Schallspektroskopische Charakterisierung von submikronen Emulsionen*", Ph.D. thesis, University of Dresden, Germany.

Babick, F.; Ripperger, S. (2004), "*Schallspektroskopische Charakterisierung konzentrierter Emulsionen*", Chemie Ingenieur Technik 76 (1-2), p. 30.

Bagotsky, V. S. (2005), "*Fundamentals of Electrochemistry*", John Wiley & Sons: New York, USA.

Baldyga, J.; Orciuch, W.; Makowski, L.; Malik, K.; Ozcan-Taskin, G.; Eagles, W.; Padron, G. (2008), "*Dispersion of nanoparticle clusters in a rotor-stator mixer*", Industrial & Engineering Chemistry Research 47 (10), p. 3652.

Barcenas, M.; Douda, J.; Duda, Y. (2007), "*Temperature dependence of the colloidal agglomeration inhibition: Computer simulation study*", Journal of Chemical Physics 127 (11), p. 114706.

Baron, P. A.; Willeke, K. (2001), "*Aerosol Measurement: Principles, Techniques and Applications*", John Wiley and Sons: New York, USA.

Barrot, C.; Colin, S. (2008), "*Electroosmotic flow in tree-shaped microchannel networks*", Proceedings of the 6th international conference of nanochannels, microchannels, and minichannels, p. 419.

Beaucage, G.; Kammler, H. K.; Mueller, R.; Strobel, R.; Agashe, N.; Pratsinis, S. E.; Narayanan, T. (2004), "*Probing the dynamics of nanoparticle growth in a flame using synchrotron radiation*", Nature Materials 3 (6), p. 370.

Benezeth, P.; Palmer, D. A.; Wesolowski, D. J. (2001), "*Aqueous high-temperature solubility studies. II. The solubility of boehmite at 0.03 m ionic strength as a function of temperature and pH as determined by in situ measurements*", Geochimica et Cosmochimica Acta 65 (13), p. 2097.

Benzi, R.; Succi, S.; Vergassola, M. (1992), "*The lattice Boltzmann equation: theory and applications*", Physics Reports 222 (3), p. 145.

Bertolini, L.; Coppola, L.; Gastaldi, M.; Redaelli, E. (2007), "*Electroosmotic transport in porous construction materials and dehumidification of masonry*", Construction and Building Materials 23 (1), p. 254.

Bessiere, Y.; Fletcher, D. F.; Bacchin, P. (2008), "*Numerical simulation of colloid dead-end filtration: Effect of membrane characteristics and operating conditions on matter accumulation*", Journal of Membrane Science 313 (1-2), p. 52.

Bharti, R. P.; Harvie, D. J. E.; Davidson, M. R. (2008), "*Steady flow of ionic liquid through a cylindrical microfluidic contraction-expansion pipe: Electroviscous effects and pressure drop*", Chemical Engineering Science 63 (14), p. 3593.

Bhatnagar, P. L.; Gross, E. P.; Krook, M. (1954), "*A Model for Collision Processes in Gases. I. Small Amplitude Processes in Charged and Neutral One-Component Systems*", Physical Review 94 (3), p. 511.

Biggs, S. (2006), "*Aggregate Structures and Solid-Liquid Separation Processes*", Kona 24, p. 41.

Blankert, B.; Betlem, B. H. L.; Roffel, B. (2006), "*Dynamic optimization of a dead-end filtration trajectory: Blocking filtration laws*", Journal of Membrane Science 285 (1-2), p. 90.

Bocquet, L.; Trizac, E.; Aubouy, M. (2002), "*Effective charge saturation in colloidal suspensions*", The Journal of Chemical Physics 117 (17), p. 8138.

Bokhimi, X.; Toledo-Antonio, J. A.; Guzman-Castillo, M. L.; Hernandez-Beltran, F. (2001), "*Relationship between Crystallite Size and Bond Lengths in Boehmite*", Journal of Solid State Chemistry 159 (1), p. 32.

Bourcier, W. L.; Knauss, K. G.; Jackson, K. J. (1993), "*Aluminum hydrolysis constants to 250[degrees]C from boehmite solubility measurements*", Geochimica et Cosmochimica Acta 57 (4), p. 747.

Brady, J. F.; Bossis, G. (1988), "*Stokesian Dynamics*", Annual Review of Fluid Mechanics 20 (1), p. 111.

Brask, A. (2005), "*Electroosmotic micropumps*", Ph.D. thesis, University of Copenhagen, Denmark.

Brask, A.; Snakenborg, D.; Kutter, J. P.; Bruus, H. (2006), "*AC electroosmotic pump with bubble-free palladium electrodes and rectifying polymer membrane valves*", Lab on a Chip 6 (2), p. 280.

Brühne, S.; Gottlieb, S.; Assmus, W.; Alig, E.; Schmidt, M. U. (2008), "*Atomic Structure Analysis of Nanocrystalline Boehmite AlO(OH)*", Crystal Growth und Design 8 (2), p. 489.

Bruinink, J. (1972), "*Proton migration in solids*", Journal of Applied Electrochemistry 2 (3), p. 239.

Brunet, E.; Ajdari, A. (2004), "*Generalized Onsager relations for electrokinetic effects in anisotropic and heterogeneous geometries*", Physical Review E 69 (1), p. 016306.

Cabane, B.; Meireles, M.; Aimar, P. (2002), "*Cake collapse in frontal filtration of colloidal aggregates: mechanisms and consequences*", Desalination 146 (1-3), p. 155.

Cabrera, C. R.; Finlayson, B.; Yager, P. (2001), "*Formation of natural pH gradients in a microfluidic device under flow conditions: model and experimental validation*", Analytical chemistry 73 (3), p. 658.

Carman, P. C. (1937), "*Fluid flow through a granular bed*", Trans. Inst. Chem. Eng. 15, p. 150.

Carrique, F.; Garcia, S.; P; Ruiz-Reina, E. (2005), "*Electroviscous effect of moderately concentrated colloidal suspensions: Stern-layer influence*", Journal of Physical Chemistry B 109 (51), p. 24369.

Chen, J. C.; Kim, A. S. (2004), "*Brownian Dynamics, Molecular Dynamics, and Monte Carlo modeling of colloidal systems*", Advances in Colloid and Interface Science 112 (1-3), p. 159.

Chen, L. X.; Guan, Y. F.; Ma, J. P.; Shu, X.; Tan, F. (2003), "*Theory, controls parameter and application of the packed-bed electroosmotic pump*", Chinese Science Bulletin 48 (23), p. 2572.

Chen, S.; Doolen, G. D.; Eggert, K. G. (1994), "*Lattice-Boltzmann Fluid Dynamics - a versatile tool for multiphase and other complicated flows*", Los Alamos Science 22, p. 98.

Dalla, E.; Cassiani; G; Brovelli, A.; Pitea; D (2004), "*Electrical conductivity of unsaturated porous media: Pore-scale model and comparison with laboratory data*", Geophysical Research Letters 31 (5), p. L05609.1.

Darcy, H. (1856), "*Les Fontaines Publiques de la Ville de Dijon*", Dalmont: Paris, France.

Dardis, O.; McCloskey, J. (1998), "*Lattice Boltzmann scheme with real numbered solid density for the simulation of flow in porous media*", Physical Review E 57 (4), p. 4834.

Dash, B.; Tripathy, B. C.; Bhattacharya, I. N.; Das, S. C.; Mishra, C. R.; Pani, B. S. (2007), "*Effect of temperature and alumina/caustic ratio on precipitation of boehmite in synthetic sodium aluminate liquor*", Hydrometallurgy 88 (1-4), p. 121.

de Gans, B.-J.; Kita, R.; Muller, B.; Wiegand, S. (2003), "*Negative thermodiffusion of polymers and colloids in solvent mixtures*", The Journal of Chemical Physics 118 (17), p. 8073.

de Gennes, P. G. (1987), "*Polymers at an interface: a simplified view*", Advances in Colloid and Interface Science 27 (3-4), p. 189.

Delgado, A. V.; Gonzalez-Caballero, E.; Hunter, R. J.; Koopal, L. K.; Lyklema, J. (2007), "*Measurement and interpretation of electrokinetic phenomena*", Journal of Colloid and Interface Science 309, p. 194.

Derjaguin, B. V.; Landau, L. (1941), "*Theory of the Stability of Strongly Charged Lyophobic Sols and of the Adhesion of Strongly Charged Particles in Solutions of Electrolytes*", Acta Phys. Chim. URSS 14, p. 633.

Deshpande, A. P.; Srikanth, A.; Praveen, N. (2005), "*Quantitative estimation of permeability with lattice Boltzmann simulations: Representative porous media from composite processing*", Canadian Journal of Chemical Engineering 83 (5), p. 808.

DIN (1989), "*DIN 38409-9 - Photometrische Bestimmung von Aluminium*", in: Beuth: Berlin, Germany.

Dingenouts, N. (1999), "*Röntgenkleinwinkelstreuung als Methodik der Strukturanalyse teilgeordneter kolloidaler Systeme*", Ph.D. thesis, University of Karlsruhe (TH), Germany.

Dong, K. J.; Zou, R. P.; Yang, R. Y.; Yu, A. B.; Roach, G. (2009), "*DEM simulation of cake formation in sedimentation and filtration*", Minerals Engineering In Press, Corrected Proof.

dos Santos, T. C. R.; Aucélio, R. Q.; Campos, R. C. (2003), "*Spectrofluorometric Method for the Determination of Aluminum with Alizarin Red PS*", Microchimica Acta 142 (1), p. 63.

Duong-Hong, D.; Wang, J.-S.; Liu, G.; Chen, Y.; Han, J.; Hadjiconstantinou, N. (2008), "*Dissipative particle dynamics simulations of electroosmotic flow in nanofluidic devices*", Microfluidics and Nanofluidics 4 (3), p. 219.

Eid, N.; Elshorbagy, W.; Larson, D.; Slack, D. (2000), "*Electro-migration of nitrate in sandy soil*", Journal of Hazardous Materials 79 (1-2), p. 133.

Einstein, A. (1956), "*Investigations on the theory of the Brownian movement*", Dover Publications: Mineola, USA.

Eisfeld, B.; Schnitzlein, K. (2005), "*A new pseudo-continuous model for the fluid flow in packed beds*", Chemical Engineering Science 60 (15), p. 4105.

Erk, A.; Hardy; E, H.; Althaus, T.; Stahl, W. (2006), "*Filtration of colloidal suspensions - MRI investigation and numerical simulation*", Chemical Engineering and Technology 29 (7), p. 828.

Eykholt, G. R. (1997), "*Development of pore pressures by nonuniform electroosmosis in clays*", Journal of Hazardous Materials 55 (1-3), p. 171.

Falck, E.; Lahtinen, J. M.; Vattulainen, I.; Ala-Nissila, T. (2004), "*Influence of hydrodynamics on many-particle diffusion in 2D colloidal suspensions*", The European Physical Journal E: Soft Matter and Biological Physics 13 (3), p. 267.

Feng, Y. T.; Han, K.; Owen, D. R. J. (2004), "*Discrete element simulation of the dynamics of high energy planetary ball milling processes*", Materials Science and Engineering A 375-377, p. 815.

Fievet, P.; Sbaï, M.; Szymczyk, A.; Magnenet, C.; Labbez, C.; Vidonne, A. (2006), "*Tangential streaming potential as a tool in the characterisation of microporous membranes*", Desalination 199 (1-3), p. 18.

Freund, J. B. (2002), "*Electro-osmosis in a nanometer-scale channel studied by atomistic simulation*", Journal of Chemical Physics 116 (5), p. 2194.

Frisch, U. (1989), "*Lattice gas automata for the Navier-Stokes equations: a new approach to hydrodynamics and turbulence*", Physica Scripta 40 (3), p. 423.

Groot, R. D.; Warren, P. B. (1997), "*Dissipative particle dynamics: Bridging the gap between atomistic and mesoscopic simulation*", The Journal of Chemical Physics 107 (11), p. 4423.

Gupta, A.; Coelho, D.; Adler, P. M. (2008), "*Universal electro-osmosis formulae for porous media*", Journal of Colloid and Interface Science 319 (2), p. 549.

Gupta, A. K.; Coelho, D.; Adler, P. M. (2007), "*Influence of the Stern layer on electrokinetic phenomena in porous media*", Journal of Colloid and Interface Science 316 (1), p. 140.

Hahn, K.; Ley, G.; Schuller, H.; Oberthür, R. (1986), "*On particle coalescence in latex films*", Colloid & Polymer Science 264 (12), p. 1092.

Hamaker, H. C. (1937), "*The London-van der Waals attraction between spherical particles*", Physica 4, p. 1058.

Hansen, H. K.; Kristensen, I. V.; Ottosen, L. M.; Villumsen, A. (2003), "*Electroosmotic dewatering of porous materials - Experiences with chalk, iron hydroxide and biomass sludges, and wet fly ash*", Journal of Chemical Engineering of Japan 36 (6), p. 689.

Happel, J.; Brenner, H. (1983), "*Low Reynolds number hydrodynamics*", Springer: The Hague, Netherlands.

Harting, J.; Hecht, M.; Herrmann, H. J.; McNamara, S. (2006), "*Computer Simulation of Particle Suspensions*", Springer: Berlin, Springer.

He, X.; Luo, L.-S. (1997), "*Lattice Boltzmann Model for the Incompressible Navier–Stokes Equation*", Journal of Statistical Physics 88 (3), p. 927.

Hecht, M. (2007), "*Simulation of pelloids*", Ph.D. thesis, University of Stuttgart, Germany.

Hecht, M.; Harting, J.; Bier, M.; Reinshagen, J.; Herrmann, H. J. (2006), "*Shear viscosity of claylike colloids in computer simulations and experiments*", Physical Review E 74 (2), p. 021403.

Hecht, M.; Harting, J.; Herrmann, H. J. (2007), "*Stability diagram for dense suspensions of model colloidal Al2O3 particles in shear flow*", Physical Review E 75 (5), p. 051404.

Hecht, M.; Harting, J.; Ihle, T.; Herrmann, H. J. (2005), "*Simulation of claylike colloids*", Physical Review E 72 (1), p. 011408.

Heister, K. (2005), "*Coupled transport in clayey materials with emphasis on induced electrokinetic phenomena*", Ph.D. thesis, University of Utrecht, Netherlands.

Hinze, F. (2001), "*Beitrag zur Charakterisierung hochkonzentrierter Suspensionen mit submikronen Partikeln mittels Ultraschallspektroskopie*", Ph.D. thesis, Technical University of Dresden, Germany.

Hoek, E. M. V.; Agarwal, G. K. (2006), "*Extended DLVO interactions between spherical particles and rough surfaces*", Journal of Colloid and Interface Science 298 (1), p. 50.

Hristovski, K.; Westerhoff, P.; Crittenden, J. (2008), "*An approach for evaluating nanomaterials for use as packed bed adsorber media: A case study of arsenate removal by titanate nanofibers*", Journal of Hazardous Materials 156 (1-3), p. 604.

Hu, J. S.; Chao, C. Y. H.; F Hu, J. S.; Chao, C. Y. H. (2007), "*Numerical study of electroosmotic (EO) flow in microfabricated EO pump with overlapped electrical double layer (EDL)*", International Journal of Refrigeration 30 (2), p. 290.

Hütter, M. (2000), "*Local Structure Evolution in Particle Network Formation Studied by Brownian Dynamics Simulation*", Journal of Colloid and Interface Science 231 (2), p. 337.

Humby, S. J.; Biggs; M, J.; Tuzun, U. (2002), "*Explicit numerical simulation of fluids in reconstructed porous media*", Chemical Engineering Science 57 (11), p. 1955.

Hunter, R. J. (1993), "*Introduction to modern colloid science*", Oxford University Press: Oxford, UK.

Hunter, R. J. (2001), "*Measuring zeta potential in concentrated industrial slurries*", Colloids and Surfaces A: Physicochemical and Engineering Aspects 195 (1-3), p. 205.

Ihle, T.; Kroll, D. M. (2003), "*Stochastic rotation dynamics. I. Formalism, Galilean invariance, and Green-Kubo relations*", Physical Review E 67 (6), p. 066705.

Inoue, Y.; Chen, Y.; Ohashi, H. (2002), "*Development of a Simulation Model for Solid Objects Suspended in a Fluctuating Fluid*", Journal of Statistical Physics 107 (1), p. 85.

Israelachvili, J. N. (1992), "*Intermolecular and surface forces*", 2nd ed.; Academic Press: London, UK.

Jimenez, M. L.; Arroyo, F. J.; Carrique, F.; Delgado, A. V. (2007), "*Surface conductivity of colloidal particles: Experimental assessment of its contributions*", Journal of Colloid And Interface Science 316 (2), p. 836.

Johnson, P. R. (1999), "*A comparison of streaming and microelectrophoresis methods for obtaining the zeta potential of granular porous media surfaces*", Journal of Colloid and Interface Science 209 (1), p. 264.

Kalthoff, W.; Schwarzer, S.; Herrmann, H. J. (1997), "*Algorithm for the simulation of particle suspensions with inertia effects*", Physical Review E 56 (2), p. 22342242.

Kerisit, S.; Ilton, E. S.; Parker, S. C. (2006), "*Molecular Dynamics Simulations of Electrolyte Solutions at the (100) Goethite Surface*", The Journal of Physical Chemistry B 110 (41), p. 20491.

Kim, A. S.; Hoek, E. M. V. (2002), "*Cake structure in dead-end membrane filtration: Monte Carlo simulations*", Environmental Engineering Science 19 (6), p. 373.

Kim, A. S.; Yuan, R. (2005), "*A new model for calculating specific resistance of aggregated colloidal cake layers in membrane filtration processes*", Journal of Membrane Science 249 (1-2), p. 89.

Kim, A. S.; Yuan, R. (2006), "*Cake resistance of aggregates formed in the diffusion-limited-cluster-aggregation (DLCA) regime*", Journal of Membrane Science 286 (1-2), p. 260.

Kim, D.; Darve, E. (2006), "*Molecular dynamics simulation of electro-osmotic flows in rough wall nanochannels*", Physical Review E 73 (5), p. 051203.

Kolthoff, I. M. (2007), "*Acid Base Indicators*", Kolthoff Press

Kovalsky, P.; Gedrat; M; Bushell, G.; Waite; T, D. (2007), "*Compressible cake characterization from steady-state filtration analysis*", AICHE Journal 53 (6), p. 1483.

Kowalski, A. J.; Watson, S.; Wai, K. (2008), "*Dispersion of nanoparticle clusters by ball milling*", Journal of Dispersion Science and Technology 29 (4), p. 600.

Kuntz, M.; Mareschal; J, C.; Lavallee, P. (2000), "*Numerical estimation of electrical conductivity in saturated porous media with a 2-D lattice gas*", Geophysicists 65 (3), p. 766.

Ladd, A. J. C.; Verberg, R. (2001), "*Lattice-Boltzmann Simulations of Particle-Fluid Suspensions*", Journal of Statistical Physics 104 (5), p. 1191.

Lao, H.-W.; Neeman, H. J.; Papavassiliou, D. V. (2004), "*A pore network model for the calculation of non-Darcy flow coefficients in fluid flow through porous media*", Chemical Engineering Communications 191 (10), p. 1285.

Larue, O.; Wakeman, R. J.; Tarleton, E. S.; Vorobiev, E. (2006), "*Pressure electroosmotic dewatering with continuous removal of electrolysis products*", Chemical Engineering Science 61 (14), p. 4732.

Laser, D. J.; Santiago, J. G. (2004), "*A review of micropumps*", Journal of Micromechanics and Microengineering 14 (6), p. 35.

Liang, Y.; Hilal; N; Langston, P.; Starov; V (2007), "*Interaction forces between colloidal particles in liquid: Theory and experiment*", Advances in Colloid and Interface Science 134-35, p. 151.

Lorenz, C. D.; Crozier; P, S.; Anderson, J. A.; Travesset; A (2008), "*Molecular dynamics of ionic transport and electrokinetic effects in realistic silica channels*", Journal of Physical Chemistry C 112 (27), p. 10222.

Lu, N.; Anderson, M. T.; Likos, W. J.; Mustoe, G. W. (2008), "*A discrete element model for kaolinite aggregate formation during sedimentation*", International Journal for Numerical and Analytical Methods in Geomechanics 32 (8), p. 965.

Luxbacher, T.; Pusic; T; Petrinic, I. (2008), "*Monitoring the Washing Efficiency of Stained Cotton Fabrics by Streaming Potential Measurement*", 4th International Textile, Clothing & Design Conference, Dubrovnik, Croatia, p. 825.

Lyklema, J. (1993), "*Fundamentals of interface and colloid science*", Vol. 1. Fundamentals, Academic Press: London, UK.

Lyklema, J. (1995), "*Fundamentals of interface and colloid science*", Vol. 2. Solid-liquid interfaces, Academic Press: London, UK.

Lyklema, J. (2003), "*Electrokinetics after Smoluchowski*", Colloids and Surfaces A 222 (1-3), p. 5.

Lyklema, J. (2005), "*Fundamentals of interface and colloid science*", Vol. 4. Particulate colloids, Elsevier: Amsterdam, Netherlands.

Lyklema, J. (2006) "Personal Communication", Karlsruhe, Germany, 15.03.2006

Madeline, J. B.; Meireles, M.; Botet, R.; Cabane, B. (2006), "*The role of interparticle forces in colloidal aggregates: local investigations and modelling of restructuring during filtration*", Water Science and Technology 53 (7), p. 25.

Malevanets, A.; Kapral, R. (1999), "*Mesoscopic model for solvent dynamics*", The Journal of Chemical Physics 110 (17), p. 8605.

Manwart, C.; Aaltosalmi, U.; Koponen, A.; Hilfer, R.; Timonen, J. (2002), "*Lattice-Boltzmann and finite-difference simulations for the permeability for three-dimensional porous media*", Physical Review E 66 (1), p. 016702.

Marry, V.; Dufreche, J. F.; Jardat, M.; Meriguet, G.; Turq, P.; Grun, F. (2003), "*Dynamics and transport in charged porous media*", Colloids and Surfaces A 222 (1-3), p. 147.

Mattke, T. (1999), "*Modellierung elektrochemischer Doppelschichten mit Hilfe der Molekulardynamik*", Ph.D. thesis, Otto-von-Guericke-Universität Magdeburg, Germany.

Mattke, T.; Kecke, H. J. (1998), "*Molecular dynamic simulations of single, interacting, and sheared double layers - 2. Influence of system properties, overlap, and shear*", Journal of Colloid and Interface Science 208 (2), p. 562.

Mikkola, P.; Ylha, P.; Levanen, E.; Rosenholm, J., B. (2004), "*Effect of impurities on dispersion properties of alpha-alumina powder*", Ceramics International 30 (2), p. 291.

Minerick, A. R.; Ostafin, A. E.; Chang, H.-C. (2002), "*Electrokinetic transport of red blood cells in microcapillaries*", Electrophoresis 23 (14), p. 2165.

Mirbozorgi, S. A.; Niamand, H.; Renksizbulut, M.; F Mirbozorgi, S. A. (2007), "*Streaming electric potential in pressure-driven flows through reservoir-connected microchannels*", Journal of Fluids Engineering 129 (10), p. 1346.

Mortensen, N. A.; Kristensen, A. (2008), "*Electroviscous effects in capillary filling of nanochannels*", Applied Physics Letters 92 (6), p. 063110.

Mutlu, S.; Yu, C.; Selvaganapathy, P.; Frantisek, S.; Carlos, H. M.; Jean, M. J. F. (2002), "*Micromachined porous polymer for bubble free electro-osmotic pump*", 15th IEEE International Conference on Micro Electro Mechanical Systems, Las Vegas, USA, p. 19.

Narvaez, A.; Zauner, T.; Raischel, F.; Harting, J.; Hilfer, R. (2009), "*Calibration of lattice Boltzmann simulation for flow in porous media*", in preparation.

Noordmans, J.; Kempen, J.; Busscher, H. J. (1993), "*Automated Image Analysis to Determine Zeta Potential Distributions in Particulate Microelectrophoresis*", Journal of Colloid and Interface Science 156 (2), p. 394.

O'brien, R. W.; Cannon, D. W.; Rowlands, W. N. (1995), "*Electroacoustic Determination of Particle Size and Zeta Potential*", Journal of Colloid and Interface Science 173 (2), p. 406.

Ohshima, H. (2007a), "*Colloid vibration potential in a suspension of spherical colloidal particles*", Colloids and Surfaces B: Biointerfaces 56 (1-2), p. 16.

Ohshima, H. (2007b), "*Primary electroviscous effect in a moderately concentrated suspension of charged spherical colloidal particles*", Langmuir 23 (24), p. 12061.

Olivi-Tran, N.; Lenormand, P.; Lecomte, A.; Dauger, A. (2005), "*Molecular Dynamics approach of sol-gel transition: Comparison with experiments*", Physica A 354, p. 10.

Olivier, J.; Vaxelaire, J.; Vorobiev, E. (2007), "*Modelling of Cake Filtration: An Overview*", Separation Science and Technology 42 (8), p. 1667.

Olthuis, W.; Schippers, B.; Eijkel, J.; van den Berg, A. (2005), "*Energy from streaming current and potential*", Sensors and Actuators B 111-112, p. 385.

Onsager, L. (1931), "*Reciprocal Relations in Irreversible Processes. II*", Physical Review 38 (12), p. 2265.

Ottosen, L. M.; Rörig-Dalgård, I. (2007), "*Drying brick masonry by electro-osmosis*", 6th Symposium on Electrokinetic Remediation, Vigo, Spain.

Padding, J. T.; Louis, A. A. (2006), "*Hydrodynamic interactions and Brownian forces in colloidal suspensions: Coarse-graining over time and length scales*", Physical Review E 74 (3), p. 031402.

Pall (1994), "*'N66' Posidyne Filter Guide - Product Specification Sheet*", 1994.

Pall (2009), "*Ultipor® Nylon 6,6 and N6,6 Posidyne® Membrane - Product specification sheet*", 2009.

Palmer, D. A.; Benezeth, P.; Wesolowski, D. J. (2004), "*Experimental Studies of the Solubilities of Aluminum Oxy-Hydroxy Phases to 300°C*", http://www.ornl.gov/~webworks/cppr/y2001/pres/120198.pdf (23.07.09).

Panias, D.; Asimidis, P.; Paspaliaris, I. (2001), "*Solubility of boehmite in concentrated sodium hydroxide solutions: model development and assessment*", Hydrometallurgy 59 (1), p. 15.

Park, P. K.; Lee, C. H.; Lee, S. (2006), "*Permeability of Collapsed Cakes Formed by Deposition of Fractal Aggregates upon Membrane Filtration*", Environmental Science Technology 40 (8), p. 2699.

Perrin-Sarazin, F.; Sepehr, M.; Bouaricha, S.; Denault, J. (2006), "*Potential of Ball Milling to Improve Clay Dispersion in Nanocomposites*", 8th International Symposium on Polymer Physics, Boucherville, Canada, p. 651.

Pohl, M.; Hogekamp, S.; Hoffmann, N. Q.; Schuchmann, H. P. (2004), "*Dispersion and deagglomeration of nanoparticles with ultrasound*", Chemie Ingenieur Technik 76 (4), p. 392.

Qazi, J.; Rahim, J.; Fores, F.; Senkov, O.; Genc, A. (2001), "*Phase transformations in Ti-6Al-4V- x H alloys*", Metallurgical and Materials Transactions A 32 (10), p. 2453.

Qiao, R.; Aluru, N. R. (2004), "*Multiscale Simulation of Electroosmotic Transport Using Embedding Techniques*", International Journal for Multiscale Computational Engineering 2 (2), p. 173.

Raha, S.; Khilar, K. C.; Kapur, P. C.; Pradip (2007), "*Regularities in pressure filtration of fine and colloidal suspensions*", International Journal of Mineral Processing 84 (1-4), p. 348.

Revil, A.; Linde, N.; Cerepi, A.; Jougnot, D.; Matthai, S.; Finsterle, S.; F Revil, A.; Matthaei, S. (2007), "*Electrokinetic coupling in unsaturated porous media*", Journal of Colloid and Interface Science 313 (1), p. 315.

Rumpf, H.; Gupte, A. R. (1971), "*Influence of porosity and particle size distribution in resistance law of porous flow*", Chemie Ingenieur Technik 43 (6), p. 367.

Santiwong, S. R.; Guan; J; Waite, T. D. (2008), "*Effect of ionic strength and pH on hydraulic properties and structure of accumulating solid assemblages during microfiltration of montmorillonite suspensions*", Journal of Colloid and Interface Science 317 (1), p. 214.

Sasol (2008), "*Disperal/Dispal high purity dispersible aluminas - Product specification sheet*", 2008.

Satoh, A.; Chantrell, R. W. (2006), "*Application of the dissipative particle dynamics method to magnetic colloidal dispersions*", Molecular Physics 104 (20-21), p. 3287.

Saunders, J. H.; Jackson; M, D.; Pain, C. C. (2008), "*Fluid flow monitoring in oilfields using downhole measurements of electrokinetic potential*", Geophysics 73 (5), p. 165.

Sauter, C.; Schuchmann, H. P. (2008), "*Material-protecting high pressure dispersion with high pressure post feeding (HPPF)-System*", Chemie Ingenieur Technik 80 (3), p. 365.

Schäfer, B.; Nirschl, H. (2008), "*Physicochemical influences on electrohydrodynamic transport in compressible packed beds of colloidal boehmite particles*", Journal of Colloid and Interface Science 318 (2), p. 457.

Selomulya, C.; Jia, X.; Williams, R. A. (2005), "*Direct prediction of structure and permeability of flocculated structures and sediments using 3D tomographic imaging*", Chemical Engineering Research and Design 83 (A7), p. 844.

Sheffer, M. R.; Oldenburg, D. W. (2007), "*Three-dimensional modelling of streaming potential*", Geophysical Journal International 169 (3), p. 839.

Sierou, A.; Brady, J. F. (2001), "*Accelerated Stokesian Dynamics simulations*", Journal of Fluid Mechanics 448, p. 115.

Singh, G.; Song, L. (2006), "*Cake Compressibility of Silica Colloids in Membrane Filtration Processes*", Industrial und Engineering Chemistry Research 45 (22), p. 7633.

Spitzer, J. J. (2003), "*A consistent alternative to the DLVO theory*", Journal of Adhesion 79 (10), p. 893.

Symons, M. C. R. (1989), "*Liquid water - the story unfolds*", Chemistry in Britain 25, p. 491.

Sympatec (2009), "*Particle size analysis with laser diffraction 0.1 µm - 8750 µm - Product specification sheet*", 2009.

Tabbagh, A.; Panissod, C.; Guerin, R.; Cosenza, P. (2002), "*Numerical modeling of the role of water and clay content in soils' and rocks' bulk electrical conductivity*", Journal of Geophysical Research-Solid Earth 107 (B11), p. 9.

Tang, G. H.; Li; Z; He, Y. L.; Zhao; C, Y.; Tao, W. Q. (2007), "*Experimental observations and lattice Boltzmann method study of the electroviscous effect for liquid flow in microchannels*", Journal of Micromechanics and Microengineering 17 (3), p. 539.

Teleki, A.; Wengeler, R.; Wengeler, L.; Nirschl, H.; Pratsinis, S. E. (2008), "*Distinguishing between aggregates and agglomerates of flame-made TiO2 by high-pressure dispersion*", Powder Technology 181 (3), p. 292.

Trainer, M. N.; Freud, P. J.; Leonardo, E. M. (1992), "*High-concentration submicron particle size distribution by dynamic light scattering*", American Laboratory 24, p. 34.

Verwey, E. J. W.; Overbeek, J. T. G. (1948), "*Theory of the Stability of Lyophobic Colloids*", Elsevier: Amsterdam, Netherlands.

Wachmann, B.; Kalthoff, W.; Schwarzer, S.; Herrmann, H. J. (1998), "*Collective drag and sedimentation: comparison of simulation and experiment in two and three dimensions*", Granular Matter 1 (2), p. 75.

Wang, M.; Chen, S. Y. (2008), "*On applicability of Poisson-Boltzmann equation for micro- and nanoscale electroosmotic flows*", Communications in Computational Physics 3 (5), p. 1087.

Wang, M.; Liu; J; Chen, S. (2008), "*Electric potential distribution in nanoscale electroosmosis: from molecules to continuum*", Molecular Simulation 34 (5), p. 509.

Wang, X. M.; Chang; S; Kovalsky, P.; Waite; T, D. (2008a), "*Multiphase flow models in quantifying constant pressure dead-end filtration and subsequent cake compression - 1. Dilute slurry filtration*", Journal of Membrane Science 308 (1-2), p. 35.

Wang, X. M.; Kovalsky; P; Waite, T. D. (2008b), "*Multiphase flow models in quantifying constant pressure dead-end filtration and subsequent cake compression - 2. Concentrated slurry filtration and cake compression*", Journal of Membrane Science 308 (1-2), p. 44.

Wang, X. Y.; Wang, S., L.; Gendhar, B.; Cheng, C.; Byun, C. K.; Li, G., B.; Zhao, M. P.; Liu, S., R. (2009), "*Electroosmotic pumps for microflow analysis*", Trends in Analytical Chemistry 28 (1), p. 64.

Weber, M.; Kimmich, R. (2002), "*Maps of electric current density and hydrodynamic flow in porous media: NMR experiments and numerical simulations*", Physical Review E 66 (2), p. 026306.

Wedler, G. (2007), "*Lehrbuch der physikalischen Chemie*", Wiley-VCH: Weinheim, Germany.

Wengeler, R.; Teleki, A.; Vetter, M.; Pratsinis, S. E.; Nirschl, H. (2006), "*High-Pressure Liquid Dispersion and Fragmentation of Flame-Made Silica Agglomerates*", Langmuir 22 (11), p. 4928.

Wengeler, R.; Wolf, F.; Dingenouts, N.; Nirschl, H. (2007), "*Characterizing Dispersion and Fragmentation of Fractal, Pyrogenic Silica Nanoagglomerates by Small-Angle X-ray Scattering*", Langmuir 23 (8), p. 4148.

Werner, C.; Zimmermann, R.; Kratzmuller, T. (2001), "*Streaming potential and streaming current measurements at planar solid/liquid interfaces for simultaneous*

determination of zeta potential and surface conductivity", Colloids and Surfaces A 192 (1-3), p. 205.

Winkler, R. G.; Mussawisade, K.; Ripoll, M.; Gompper, G. (2004), "*Rod-like colloids and polymers in shear flow: a multi-particle-collision dynamics study*", Journal of Physics: Condensed Matter 16 (38), p. 3941.

Work, T. S.; Burdon, R. H. (1983), "*Isoelectric focusing: theory, methodology and applications*", Elsevier: Amsterdam, Netherlands.

Xia, Z.; Mei; R, W.; Sheplak, M.; Fan; Z (2009), "*Electroosmotically driven creeping flows in a wavy microchannel*", Microfluidics and Nanofluidics 6 (1), p. 37.

Yoon, H.; Zhang; C, Y.; Werth, C. J.; Valocchi; A, J.; Webb, A. G. (2008), "*Numerical simulation of water flow in three dimensional heterogeneous porous media observed in a magnetic resonance imaging experiment*", Water Resources Research 44 (6), p. W06405.

Yu, B. M.; Zou, M. Q.; Feng, Y. J. (2005), "*Permeability of fractal porous media by Monte Carlo simulations*", International Journal of Heat and Mass Transfer 48 (13), p. 2787.

Yu, H.; Girimaji, S. S. (2008), "*Study of axis-switching and stability of laminar rectangular jets using lattice Boltzmann method*", Computers & Mathematics with Applications 55 (7), p. 1611.

Zhang, Y.; Xu, T.; Fu, R. (2005), "*Modeling of the streaming potential through porous bipolar membranes*", Desalination 181 (1), p. 293.

Zholkovskij, E. K.; Masliyah, J. H.; Shilov, V. N.; Bhattachalgee, S.; F Zholkovskij, E. K.; Masliyah, J. H.; Shilov, V. N.; Bhattachalgee, S. (2007), "*Electrokinetic phenomena in concentrated disperse systems: General problem formulation and spherical cell approach*", Advances in Colloid and Interface Science 134-35, p. 279.